MULTI-SCALE DATA FUSION FOR SURFACE METROLOGY

by

Suresh Kumar Ramasamy

A dissertation submitted to the faculty of
The University of North Carolina at Charlotte
in partial fulfillment of the requirements
for the degree of Doctor of Philosophy in
Mechanical Engineering

Charlotte

2011

Approved by:

_____
Dr. Jayaraman Raja

_____
Dr. Brian D. Boudreau

_____
Dr. Faramarz Farahi

_____
Dr. Robert J. Hocken

_____
Dr. Stuart T. Smith

_____
Dr. Peter L.Schmidt

ABSTRACT

SURESH KUMAR RAMASAMY. Multi-scale data fusion for surface metrology. (Under the direction of DR. JAYARAMAN RAJA)

The major trends in manufacturing are miniaturization, convergence of the traditional research fields and creation of interdisciplinary research areas. These trends have resulted in the development of multi-scale models and multi-scale surfaces to optimize the performance. Multi-scale surfaces that exhibit specific properties at different scales for a specific purpose require multi-scale measurement and characterization. Researchers and instrument developers have developed instruments that are able to perform measurements at multiple scales but lack the much required multi-scale characterization capability. The primary focus of this research was to explore possible multi-scale data fusion strategies and options for surface metrology domain and to develop enabling software tools in order to obtain effective multi-scale surface characterization, maximizing fidelity while minimizing measurement cost and time. This research effort explored the fusion strategies for surface metrology domain and narrowed the focus on Discrete Wavelet Frame (DWF) based multi-scale decomposition. An optimized multi-scale data fusion strategy ‘FWR method’ was developed and was successfully demonstrated on both high aspect ratio surfaces and non-planar surfaces. It was demonstrated that the datum features can be effectively characterized at a lower resolution using one system (Vision CMM) and the actual features of interest could be characterized at a higher resolution using another system (Coherence Scanning Interferometer) with higher capability while minimizing the measurement time.

ACKNOWLEDGEMENTS

I would like to express my sincere gratitude to Dr. Jayaraman Raja for his support and guidance during my doctoral work. I thank Dr. Brian D. Boudreau for being the external advisor and helping me maintain a delicate balance between work and research. I thank Dr. Faramarz Farahi, Dr. Peter L. Schmidt, Dr. Robert J. Hocken, and Dr. Stuart T. Smith for agreeing to serve on my committee.

Thanks to Mr. Claudiu Guisca (NPL), Dr. Don Cohen (Michigan Metrology), Dr. Jimmie Miller (UNCC), Mr. Manas Lakshmipathy (Zygo Corp.) and Dr. Peter de Groot (Zygo Corp.) for their valuable suggestions on the section detailing the adjustment procedures for a Coherence Scanning Interferometer. Thanks to Dr. Chris Wichern (Nanofocus AG), Dr. Laura Shaw (University Erlangen-Nuremberg), Ms. Rose Peet (RPC Photonics), Mr. John Bradford (Makino Micromachining Technologies) and Mr. Tatsuya Sugihara (Osaka University) for providing me with data samples. I would like to thank past students of the Center of Precision Metrology Dr. Bala Muralikrishnan, Dr. Trichy M. Kethara Pasupathy and Dr. Ritwik Verma for their valuable suggestions throughout my research work. I thank Hutchinson Technology Incorporated for providing me with instruments and data samples that were valuable to my research work. Special thanks to my friends Melissa and Niraj for their suggestions and proof reading this report.

I would like to thank my wife, Haritha, for the countless days she had to motivate me and keep me in on-track with my research. I will always be thankful and indebted to my parents Mrs. R. Kalarani and Mr. K. Ramasamy for their unwavering support and patience.

DEDICATION

To my Parents, Teachers and Guardian Angels.

My parents always strived to make a better life for me and sacrificed a lot so that I could make a life of my own. They taught the core of me and enabled me to pursue my dreams.

Whenever I felt my life was at crossroads, the Lord has blessed with a teacher or a guardian angel to guide me and move forward. Without them I would just be a stranded soul staring at the abyss.

அகர முதல எழுத்தெல்லாம் ஆதி
பகவன் முதற்றே உலகு.

- திருவள்ளுவர்

As "A" is the first letter in the alphabet, so is God the starting point of all that exists.

TABLE OF CONTENTS

LIST OF TABLES

LIST OF FIGURES

CHAPTER 1: INTRODUCTION

Surface characterization plays an important part in ensuring that products function safely and reliably, as intended. Novel methods to correlate surface texture to functional requirements [1] and to select manufacturing systems and measurement instruments for a specific surface function [2] have resulted in emphasis for the surface metrology field. A benefit of surface characterization is nowhere more apparent than in the ongoing change in warranties on many consumer products. As recently as two decades ago, cars didn't come with engine and power train warranties. Surface metrology tools have enabled the characterization of honed engine liners and wear studies of gear blocks [3], now, warranties on those products are taken for granted. Elsewhere in personal computers, the frequency of hard disk failures and crashes has reduced to below parts-per-million levels. Here again, surface metrology tools have played a vital role in characterizing head lift finishes and hard particle cleaning. The advancement and application of surface metrology has always been an enabling driver in the commercialization and improvement of the reliability of products within the progressive periods – automobiles, semi-conductors and the current nano-technology era. In order to better understand the future needs in surface metrology, a deeper look at the emerging technology trends is necessary.

1.1. Emerging Technology Trends

Manufacturing technology has undergone a sea of change during the last two decades and has evolved into new domains and scales. The trends can be broadly summarized in to these three categories: (a). Miniaturization where macro- and micro-scale phenomena meet, (b). Convergence leading to interdisciplinary research fields, and (c). Development of multi-scale surfaces.

1.1.1. Miniaturization

Taniguchi [4] accurately predicted that miniaturization would be the key driver in taking precision machining to new levels as witnessed in the semiconductor processing industry. This trend is nowhere more clearly expressed than by Moore's law in the semiconductor industry and its consequent evolution into micro- / nano-technology. Miniaturization has evolved into lab-on-chip concepts, biomaterial surfaces and other nano-technology instrumentation. Lab-on-chip concepts have materialized the possibility of testing for an entire set of biological pathogens in a single chip [5].

Carneiro et al [6] describe how the current miniaturization trend has come to a transition region between the macro- and micro-scale phenomena, where the atomic world starts and continuum mechanics ends, highlighting the lack of theoretical models to explain the probe to part interactions in this regime. Whitehouse [7] compared the relative importance of forces, depending on the scale, and showed that at smaller scales, inertial force is dominated by damping and elastic forces, which is a function of surface area and surface roughness. Surface roughness also impacts wear, friction, adhesion, light scattering and corrosion to name a few. He also illustrated the concept of classifying shape/form, waviness and roughness changes according to the regime, as

shown in Figure 1.1.1. [Some images shown in the figures of this chapter have been taken from the reference publication mentioned in the figure captions.] This effect could also be visualized differently as a meeting point between a top-down approach, where products are being consistently miniaturized and bottom-up approach, where molecules are used to assemble a mechanical, chemical or biological system. It can be seen, that depending on application and field of study, the line of demarcation between shape and roughness gets blurry.

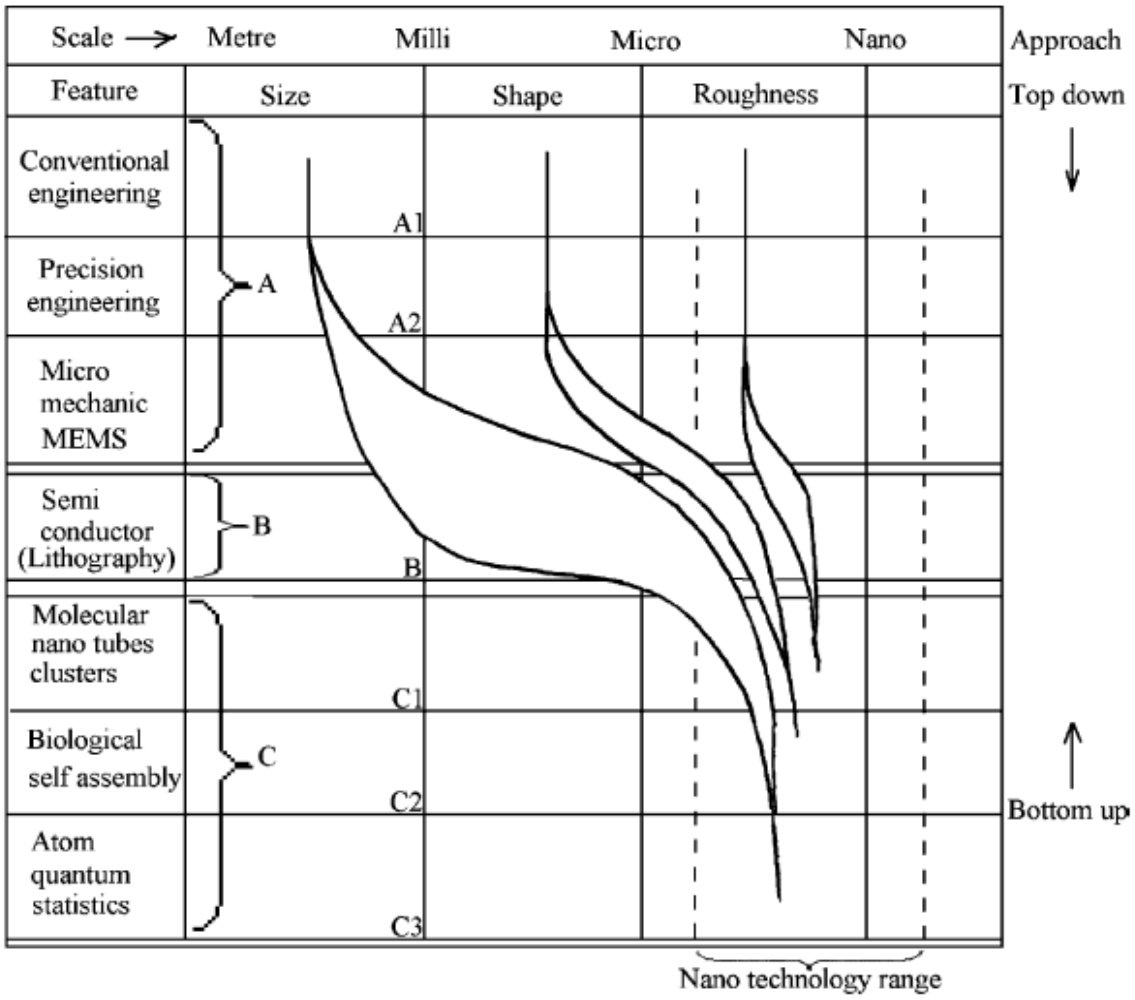

FIGURE 1.1.1: Feature categories in macro and micro scale regimes. [7]

At the micro- and nano- metrology levels, dimension, shape, roughness all play a critical role in defining the functional property and product reliability, so measurements have to be made in multiple scales.

Top-down approach is widely prevalent in Micro-Electro-Mechanical-Systems (MEMS), Micro-Opto-Electro-Mechanical-Systems (MOEMS) and hard disk drive suspensions. Typical products are fabricated on the meso- to micro-scale, yet nano-scale surface roughness and surface defects deeply impact product performance. Typical MEMS and MOEMS products have 100 nm size features spread over a several square mm or even cm area. These parts are traditionally manufactured in step-and-repeat patterns on a single panel or wafer to reduce costs, as shown in figure 1.1.2. Precise tools are required to measure the micro-scale features within the part and meso-scale tools are needed to measure the overall flatness of the panel or wafer and also the positional variation of individual patterns.

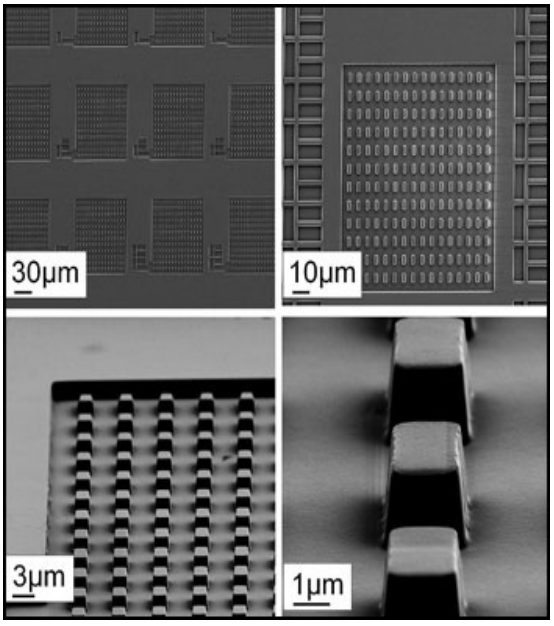

FIGURE 1.1.2: A typical patterned surface. [8]

A typical hard disk drive suspension has 100 µm features spread over a distance of several mm, as shown in figure 1.1.3. Many of the standard vision systems are on the limits of their capability to match the sub- 10 µm level positional requirements of these critical features, which are 5 to 10 mm apart from the 100 – 1000 µm datum features.

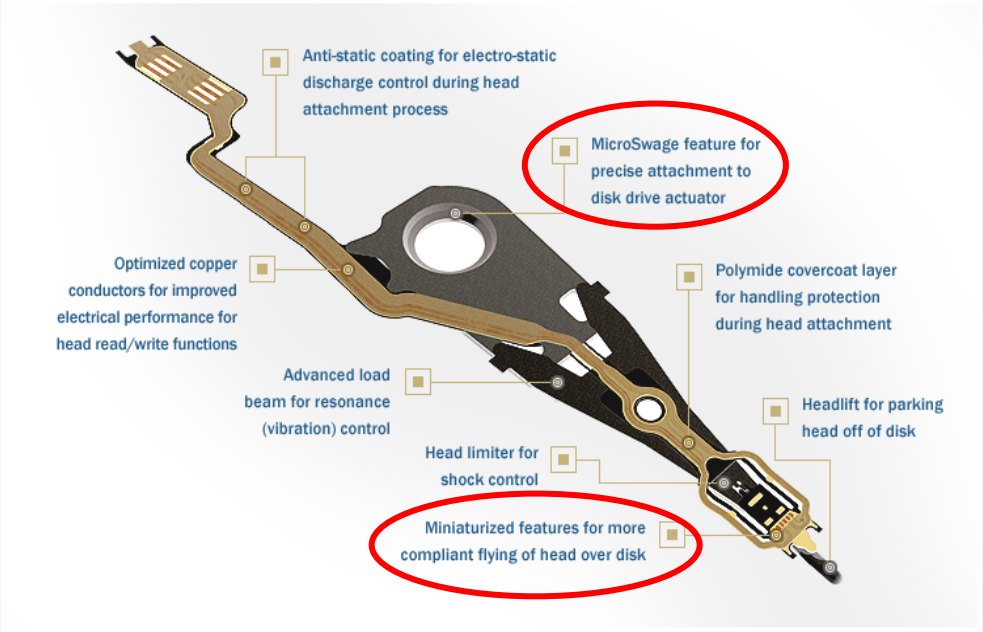

FIGURE 1.1.3: A typical hard disk drive suspension showing the spread of micrometer level features across several mm. [9]

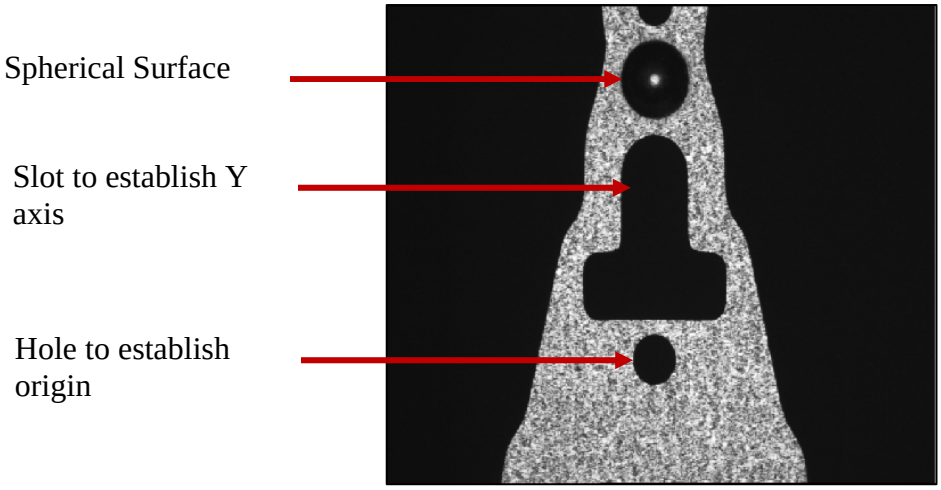

FIGURE 1.1.4: Feature of interest and datum features on a hard disk drive suspension sub-component.

Figure 1.1.4 shows a specific area of interest on a sub-component of a hard disk drive suspension. The location of the apex of the spherical surface (approx. 200 µm spherical radius) needs to be measured with respect to the datum structure established by the hole (approx. 100 µm diameter) and slot. The spherical surface requires 3D characterization in order to calculate the apex while for the datum features only require 2D characterization. This is a typical example of a product requiring multi-technology characterization with the main emphasis of measurement cost reduction while retaining data fidelity.

Miniaturization, driven by the need for cost reduction has enabled existing processing methods to produce more parts within the same space and minimal processing equipment modification. With miniaturization, the measurement requirements do not scale accordingly and existing measurement systems cannot handle these tighter requirements when compared to the process equipment. The added requirement of handling multi-technology characterization has resulted in the development of instruments stacked with multiple technology sensors, which will be explained in detail in section 1.2.1.

1.1.2. Convergence of Fields

Miniaturization and convergence of macro- and micro-scale phenomena have enabled the major traditional science fields to move closer. Convergence of fields has blurred the envelopes between various primary fields like biology, chemistry, and physics. Exploratory research demands interdisciplinary knowledge of mechanical, optical properties, molecular properties and in some cases, multi-scale surface properties. For example, a successful lab-on-chip design requires expertise in four domains: micro-

biology, micro-fluidics, micro-tribology and micro-optics. This situation is well portrayed in figure 1.1.5, which illustrates how the research fields traditionally involved with macro-scales have evolved to deal with smaller scales and some fields traditionally dealing with nano-scales have evolved upwards to evaluate macro-scale phenomena . Both of these evolution trends have come to cross-roads with the micro- / nano-technology domain where all the scales are important. These multi-scale and multi-disciplinary research demands measurement tools equipped with multiple technologies, which will be explained in detail in section 1.2.1.

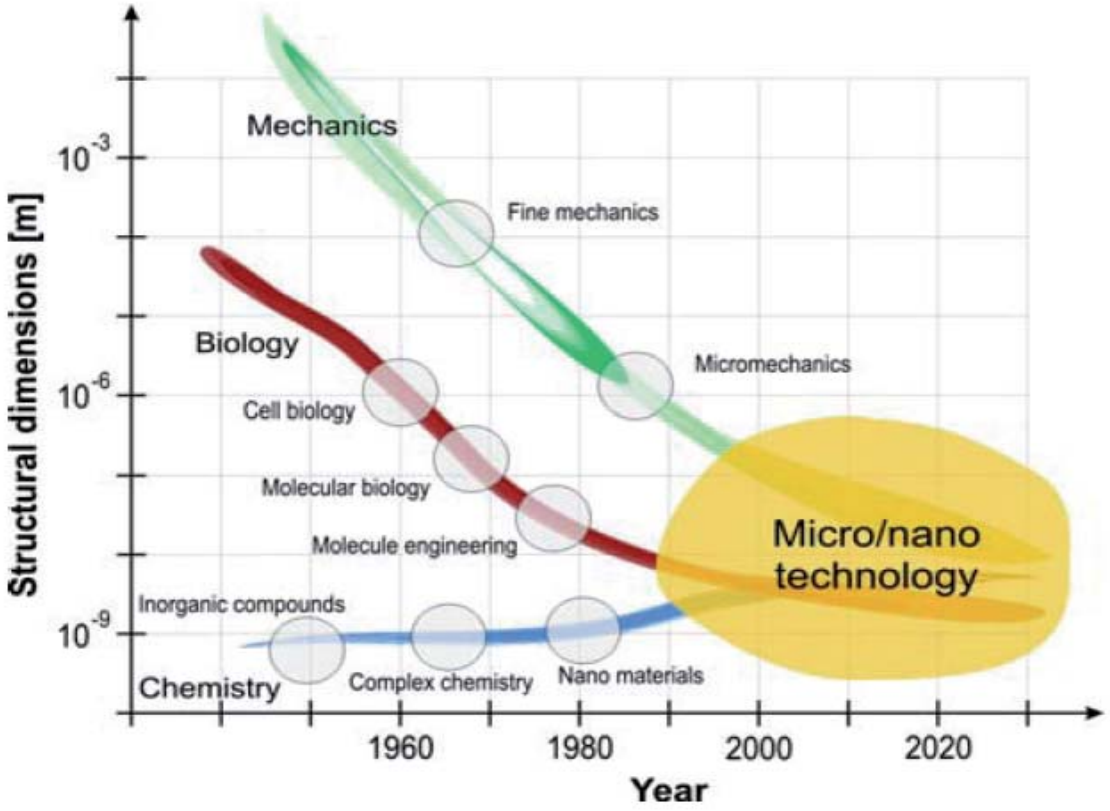

FIGURE 1.1.5: Convergence of traditional scientific fields into micro- / nano-technology. [10]

The following sections describe some of the new products from diverse interdisciplinary fields along with their needs for development of new metrology tools.

1.1.2.1. Bio-medical

Blunt et al [11] detail the role of tribology and metrology in the development of new bio- materials for hip implants. Medical adhesive surfaces, bio-compatible implant surfaces, bio-absorbable drug-eluting stents, micro rough surfaces on titanium screws for effective bone re-growth (shown in figure 1.1.6) are some of the examples.

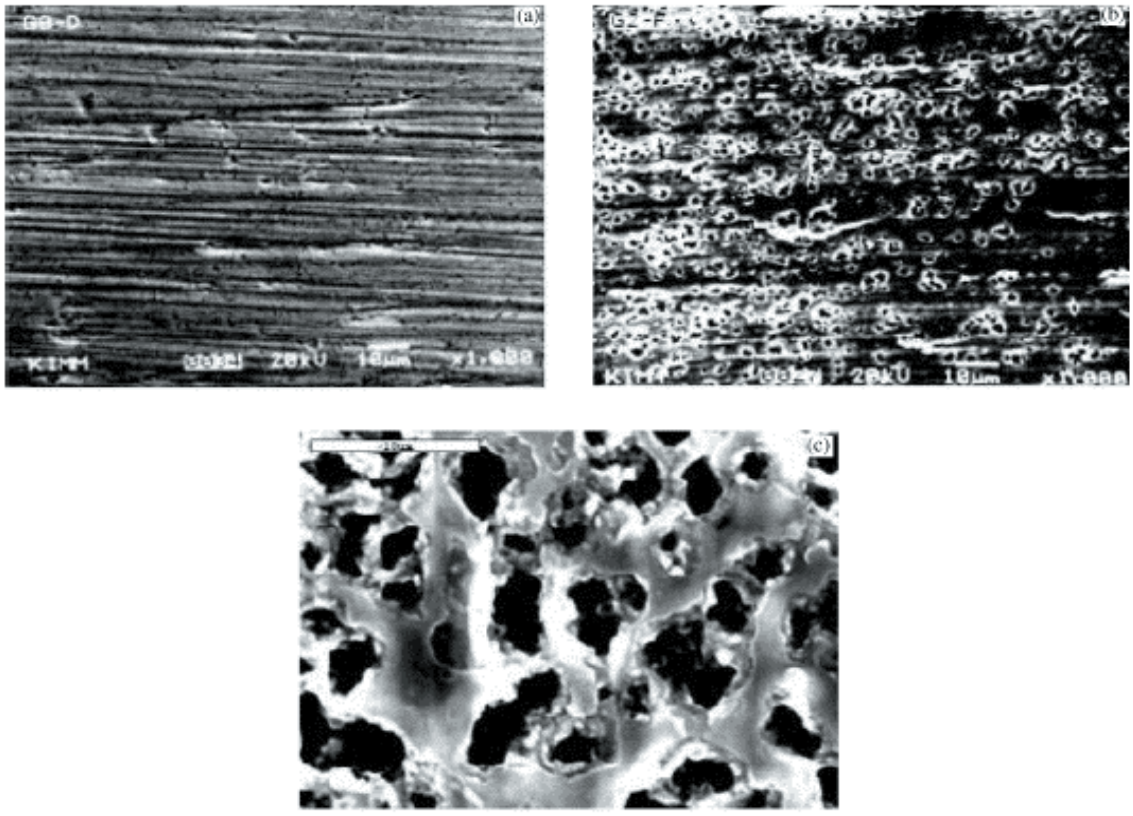

FIGURE 1.1.6: Micro-rough surface on titanium screws. [12]

Development of these new devices and surfaces, demand metrology tools with ultra-precision positioning systems and multi-functional sensors for the measurement of both biological and mechanical properties. Extensive research interest is shown in

surface and sub-surface layers of catheters, design of hydrophobic surfaces and wear of implants [13]. Various publications [14-16] demonstrate the use of integrated systems that have complimenting technologies – combining Confocal Microscopy, Atomic Force Microscopy (AFM), Fluorescence Microscopy, etc.

Knowledge of surfaces at different scales helps in better understanding on how different sizes and types of cells interact with each other and how bio-molecules get absorbed onto surfaces. Recent tissue culture studies [17-19] have shown the importance of roughness and patterns of the base structure over the growth of tissues and dendrites, leading to the new studies on importance of scaffold characterization. These studies are highly dependent on AFM measurements but recent studies [20] have shown that AFM derived roughness parameters are highly sensitive to the scan point density. In order to overcome these errors induced due to just changing the density of points to cover wide ranges, there is growing interest to develop integrated systems to cover the macro-, meso- and micro-scales in a single setup [21]. Development of multi-scale models in tissue growth is still in its infancy and new Computed Tomography (CT) equipment [22] are being developed for understanding and developing multi-scale models. There is a growing need for multi-scale surface measurement tools to understand the correlation between force impact and muscular and neurological reactions at different scales.

1.1.2.2. Micro-fluidics

Micro-fluidics plays a significant role in lab-on-chip concepts. These micro-surface patterns (shown in figure 1.1.7) are commonly etched on large formats and then sliced into multiple parts, similar to the manufacturing of silicon wafer patterns. The function of these surfaces relies on micro-scale phenomena for fluid transportation and

delivery. These surfaces have high aspect ratio and surfaces actually involved in fluid transportation need to be analyzed separately requiring efficient segmentation techniques.

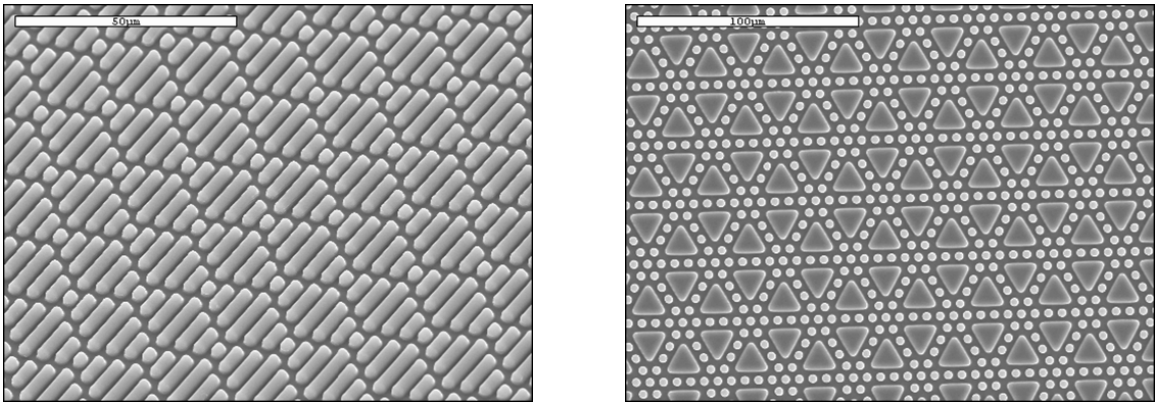

FIGURE 1.1.7: Typical micro-fluidics surface patterns. [23]

1.1.2.3. Micro- and Nano-tribology

Holmberg et al [24] show the evolution of tribology to cater to multi-scale wear, as shown in Figure 1.1.8. Four decades ago, contact mechanics studies had relied on statistical average parameters derived from single-scale models [25, 26], but with computational capability reaching new heights, the studies have now started to utilize actual 3-D surface topography measurements [27] and have led to new multi-scale models [28]. Metrology tools enabling multi-scale measurement play a vital role in the development of multi-scale models [29, 30].

New patterned surfaces are being developed trying to utilize the interesting play of surface roughness on friction over different scales – textured surfaces could be used to increase friction in meso-scale and macro-scale, but reduce friction in micro-scale. Plant cuticles and insects' endo-skeletal and wing patterns are being studied extensively in the Biomimetics [31 - 34] field to develop new multi-scale patterned surfaces. The

successful development of multi-scale surfaces needs development of hardware and software tools to effectively characterize them.

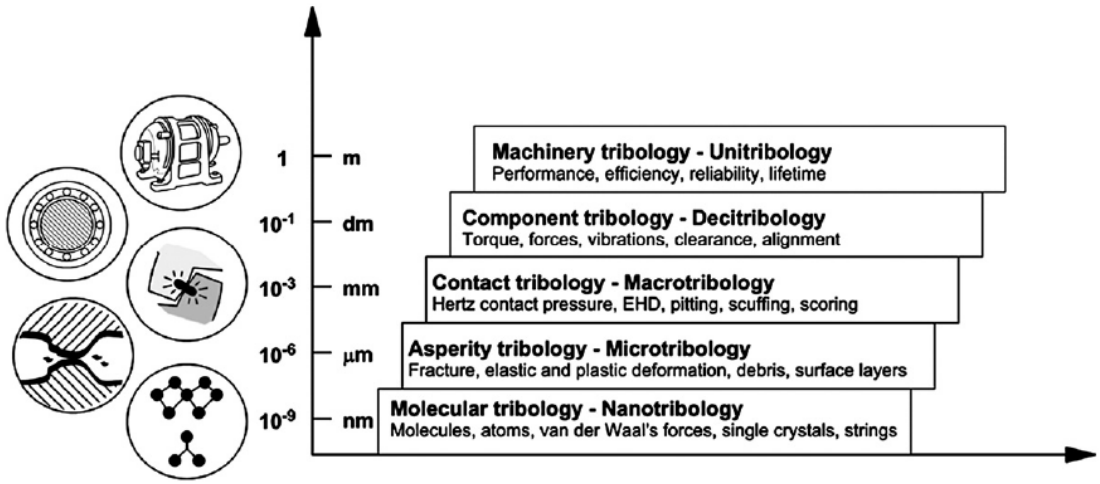

FIGURE 1.1.8: Tribology at different scales. [24]

The inter-disciplinary research fields discussed so far, like bio-medical, micro-fluidics and nano-tribology, have all shown the recent development of multi-scale surfaces and the resulting need for multi-scale surface characterization. A brief introduction of multi-scale surfaces and the commonly used classification are described in the next section.

1.1.3. Multi-scale Surfaces

Most naturally occurring surfaces are inherently multi-scale in nature, exhibiting specific properties at different scales for a specific purpose. When the surface looks the same at more than two scales, they are called fractals. Fractal geometry was introduced by Mandelbrot [35] to describe irregular objects and mathematically describe the natural and intrinsic properties of surface topography information, such as self-similar, self-affinities and invariance to scale. Studies on dental wear [36] and fractured surfaces [37]

have shown the fractal nature of those surfaces. Naturally formed surfaces – both additive and subtractive typically exhibit fractal nature. Machined surfaces (human induced – both additive and subtractive) normally have a deterministic pattern [38] and might show fractal nature at some scales [39]. Conventional machined surfaces have roughness, waviness and form, representing different scales [40] as shown in figure 1.1.9.

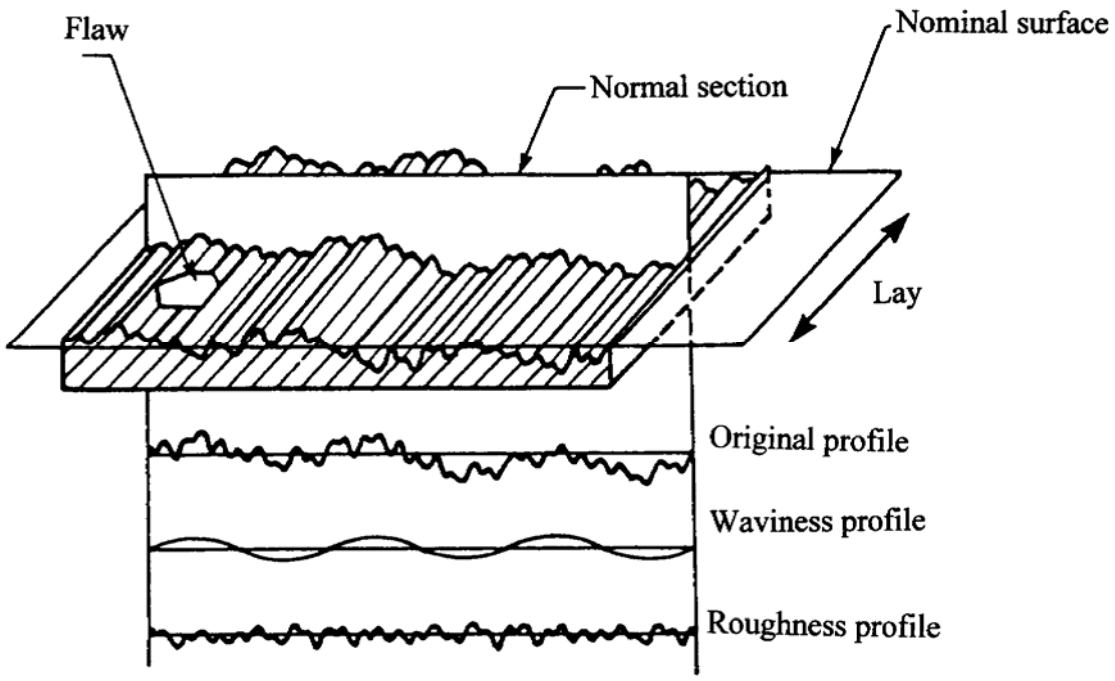

FIGURE 1.1.9: Separation of roughness, waviness and form from the original profile. [42]

Waviness and form on surfaces obtained using traditional machining processes are normally due to machine tool guide way errors and vibration. Roughness is mainly a function of cutting tool geometry and is the intended functional surface obtained from either a single-step or multi-step process [41]. With the rapid evolution of new designer surfaces for MEMS, micro-fluidics etc, traditional methods of separation of surface into roughness, waviness and form, and using only roughness data for characterization is not

effective. Non-conventional machining processes are used to generate these high aspect ratio surfaces, and the surface needs to be characterized at multiple scales.

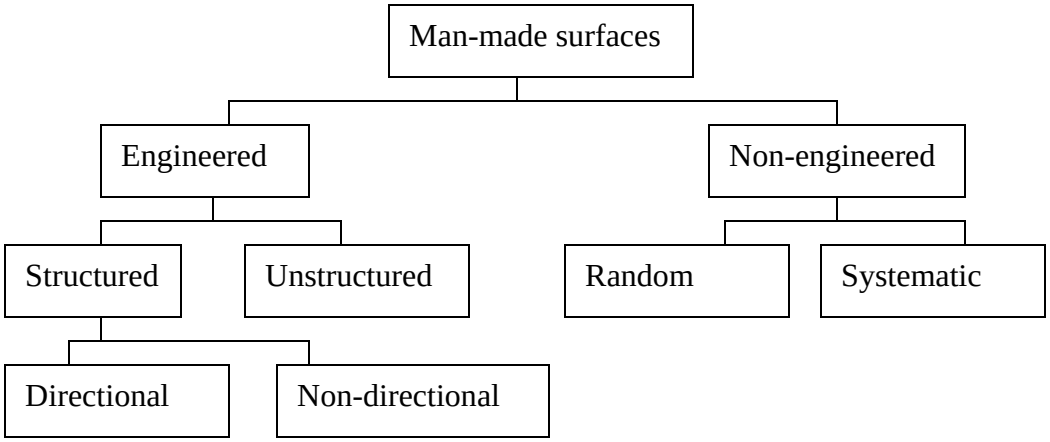

FIGURE 1.1.10: Classification of man-made surfaces (Based on [43]).

The brief description (as shown in figure 1.1.10) for classification of engineered surfaces [43, 44] is as follows:

- *Non-Engineered Surfaces*—surfaces produced as a direct consequence of the manufacturing process where little or no attempt is made to influence surface character. Most of the conventionally machined surfaces fall into this category.
- *Random Surfaces*—surfaces produced by random and pseudo-random processes often with the specific intention of removing systematic features. Casting, polishing and burnishing are some of the processes that result in these kind of surface. Figure 1.1.11 shows a typical surface generated using lapping process.
- *Systematic Surfaces*—surfaces exhibiting some repetitive features which are a consequence of the natural constraints of the process by which they have been produced. Turning and Blanchard grinding are some of the processes that result in

this kind of surface. Figure 1.1.12 shows a typical surface obtained from a turning process.

- *Engineered Surfaces*—surfaces produced in specific ways that deliberately alter surface and sub-surface layers to give a specific functional performance.
- *Unstructured Surfaces*—surfaces where a deliberate attempt has been made to impart texture through semi-control of the manufacturing process without achieving a deterministic pattern as shown in figure 1.1.13. Shot blasting and peening result in this kind of surface.

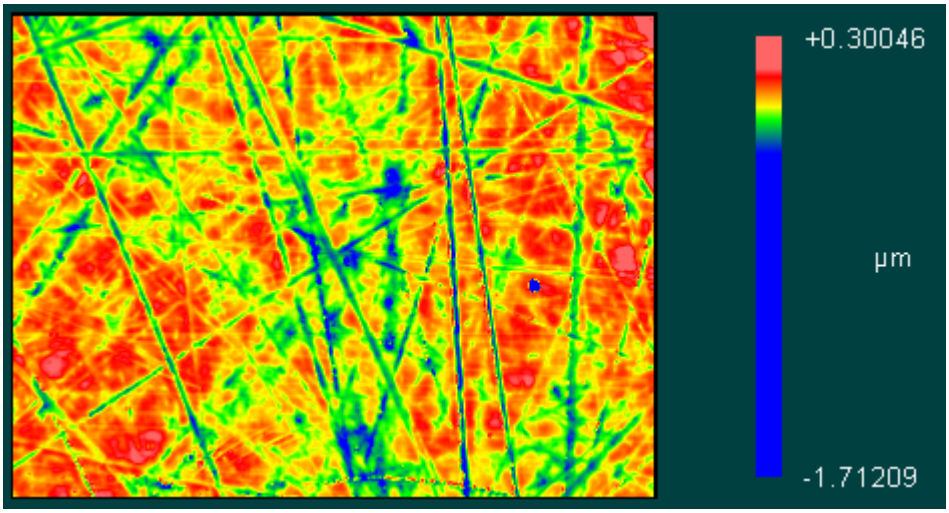

FIGURE 1.1.11: Surface obtained from lapping.

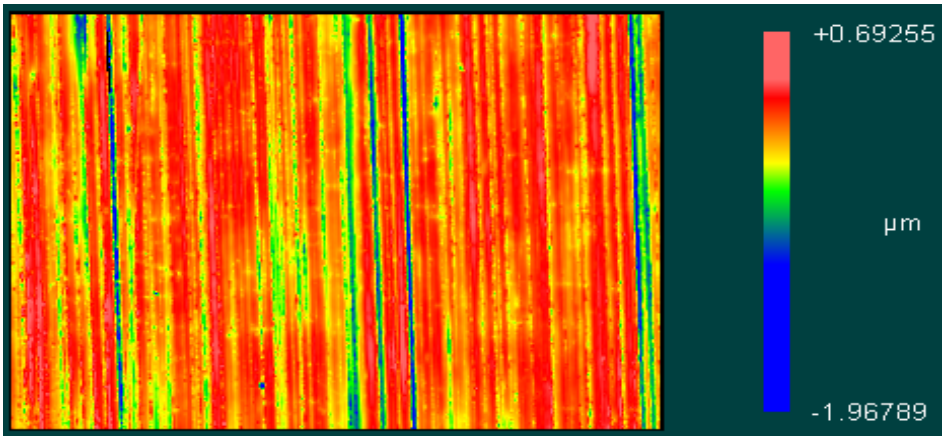

FIGURE 1.1.12: Systematic surface obtained from turning process.

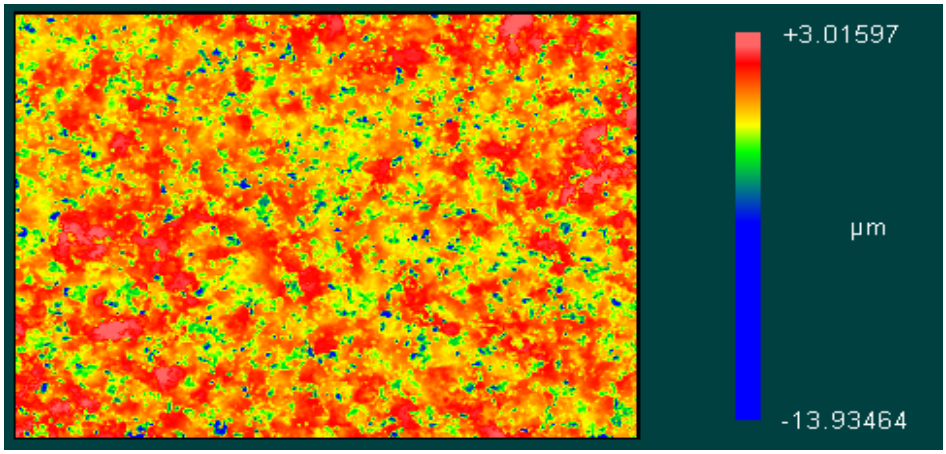

FUGURE 1.1.13: Typical unstructured surface obtained from shot blasting.

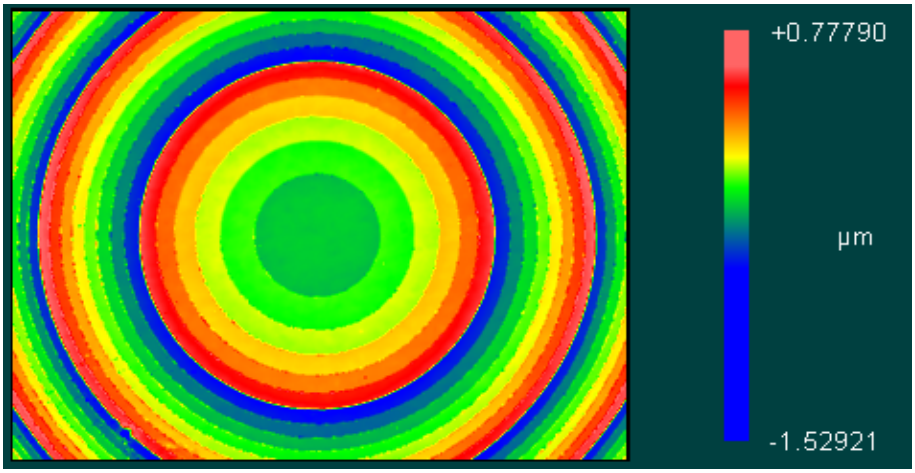

FIGURE 1.1.14: Structured surface of a beam shaper optic.

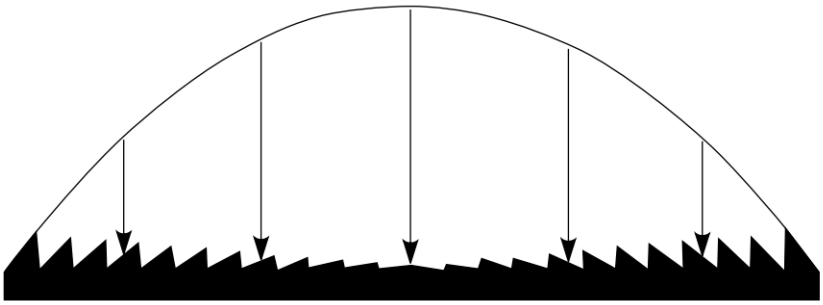

FIGURE 1.1.15: Cross-section of a Fresnel lens [45].

- *Structured Surfaces*—surfaces with a deterministic pattern of usually high aspect ratio geometric features designed to give a specific function. Figure 1.1.14 shows a beam shaper optical surface with concentric steps. Some of the surfaces also have patterns with varying aspect ratios. Figure 1.1.15 shows the cross-section of a Fresnel lens, where individual outer groove from the lens center has slightly increasing aspect ratio. Since the aspect ratio is not constant, some grooves may fall outside the resolution limit of the single instrument setting, and would require multiple measurement settings.

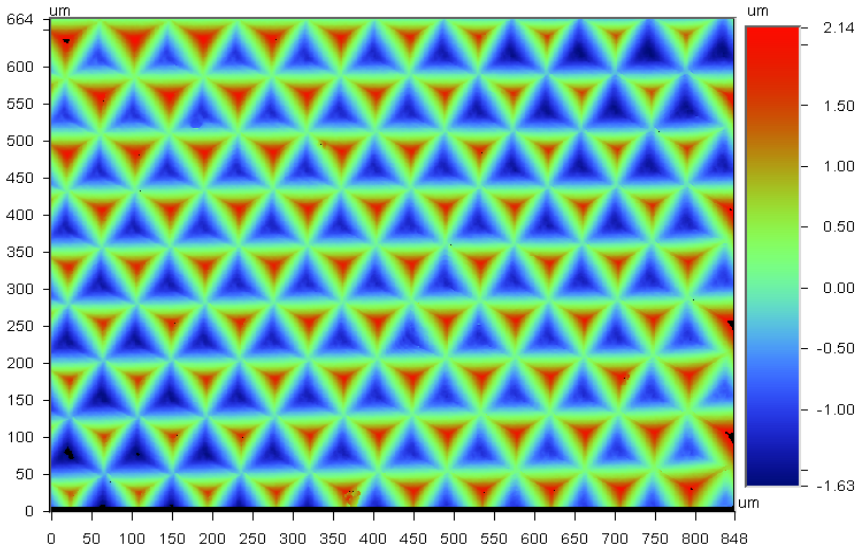

FIGURE 1.1.16: Three sided pyramid pattern mold.

- *Directional Surfaces*—surfaces with a deterministic pattern which exhibits specific directionality. Rough and fine honing is a two-step process that also results in this kind of surface. Figure 1.1.16 shows a three sided pyramid pattern of a micro mold surface. Pyramid pattern surfaces cannot be segmented using normal height based thresholding techniques and requires different parameter based segmentation approach. Three sided pattern is a unique pattern that cannot be segmented using a

single parameter based segmentation technique and requires multi-parameter based segmentation technique which will be explained in detail in the section 3.2.1.

- *Non-directional Surfaces*—surfaces with a deterministic pattern but without specific directionality. Textured rolling and etching result in this kind of surface. Figure 1.1.17 shows a non-directional surface of a diffuser optic.

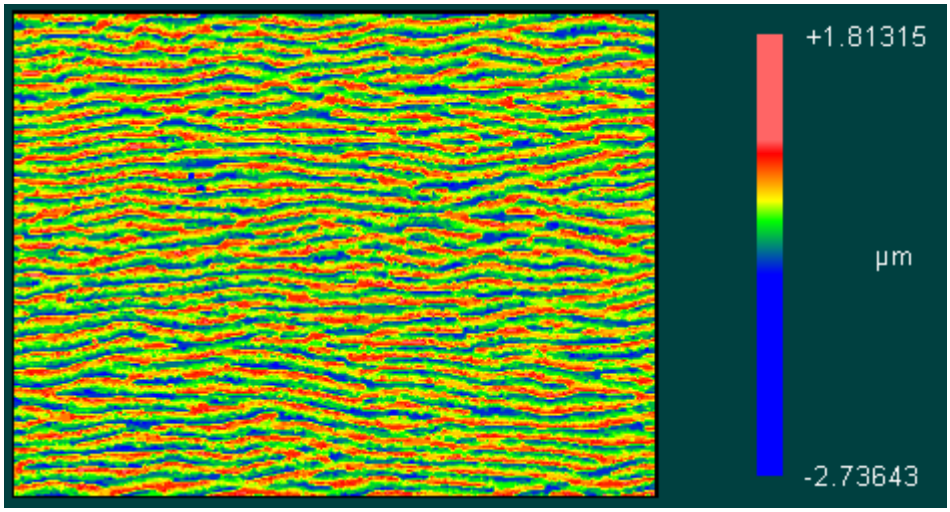

FIGURE 1.1.17: Non-directional structured surface of a diffuser optic.

Engineered multi-scale surfaces, both directional and non-directional, have been gaining use for development of functional surfaces, with specific functional intent at each scale. These high aspect ratio surfaces require development of new segmentation approaches. The varying aspect ratio surfaces need different resolution capabilities at different locations. This leads to multiple measurements using different resolutions, but the measurements are to be treated independently as the coordinate relationship between the measurements is not known.

The three technology trends discussed so far can be summarized as follows:

- Miniaturization has led to the development of components with micro-scale features which need to be characterized with respect to datum features separated by macro-

scale distances. This has resulted in a need to combine measurements obtained from multiple technologies.

- Convergence has resulted in the development of multi-scale surfaces and associated multi-scale models that were used to develop the functional intent of those surfaces. In order to characterize these multi-scale surfaces, measurement instruments have to be able to deliver consistent good resolution at varying scales.
- Development of multi-scale surfaces with high aspect ratios and varying aspect ratios, with specific functional performance intent at specific scales. Multi-scale characterization of these surfaces demand instruments with consistent resolution capabilities at varying scales.

For successful demonstration of a product or a manufacturing process, quantitative measurements traceable to an agreed upon metrology scale are required. Hence to convert these multi-disciplinary and multi-scale research efforts into successful business ventures, there is a significant need for relevant metrology tools that give the ability to measure in three dimensions over micro- to meso- scale areas. The basic measurement tasks are measurement of lateral and vertical distances between surfaces, geometry or form, texture, roughness and layer thickness.

In order to perform these measurement tasks, the measurement systems should be able to provide the following capabilities:

- *Multi-scale measurement capability:* The system or collection of systems should be able to cover the vertical and lateral ranges required to measure both the micro-scale features and the datum features which are macro-scale distance apart. The systems

should also be able to effectively measure and resolve features with varying aspect ratios.

- *Multi-scale surface characterization capability:* The systems should be able to correlate the measurements conducted across multiple scales and provide multi-scale data to be used for validating the multi-scale models and ensuring the functional performance of the measured surface.

Unfortunately, there is no single measurement system that can cover the entire gamut of the lateral measurement range without a significant drop in vertical range and resolution. Figure 1.1.18 illustrates how most technologies tend to overlap in their ability to measure lateral and vertical dimensions of products to cater to some limited range of product portfolio.

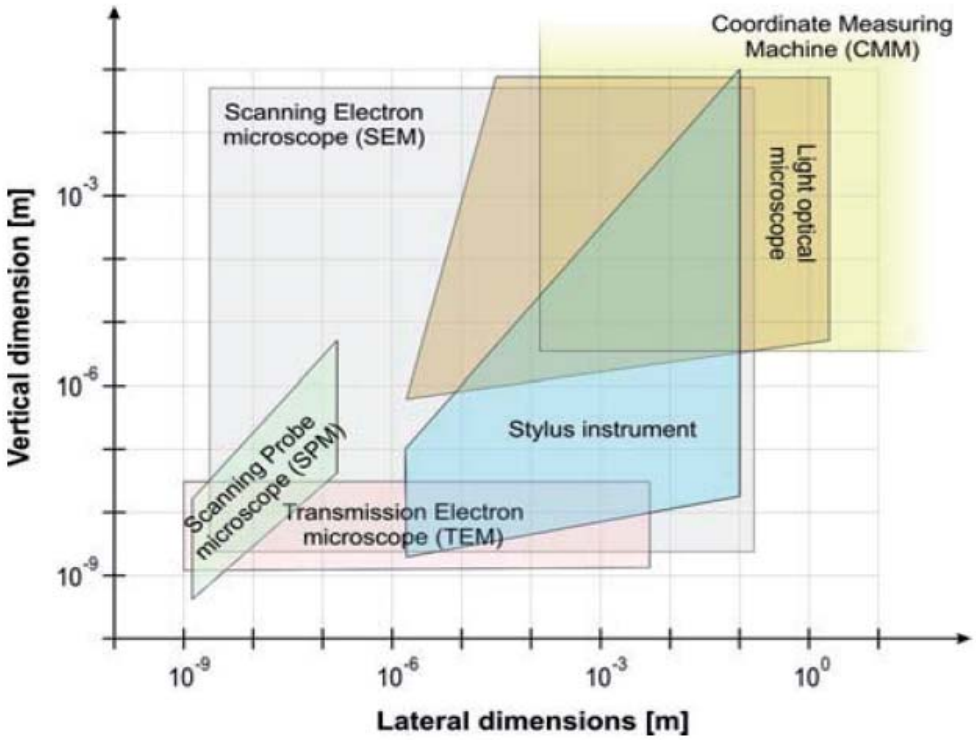

FIGURE 1.1.18: Measurement instruments capability [10].

To obtain all meaningful details of the surface at various required scales, one is left with only two options. The first option is to perform multiple measurements at the required highest resolution and then stitch those to cover the required lateral range. Stitching is prone to shape induced errors, as shown in figure 1.1.19. Figure shows the difference between measurements performed with and without reference flatness error (which will be discussed in detail in the second chapter) subtraction. Unless proper care is taken to ensure the optimum number of rows and columns involved in the stitch, these optical errors would induce shape errors.

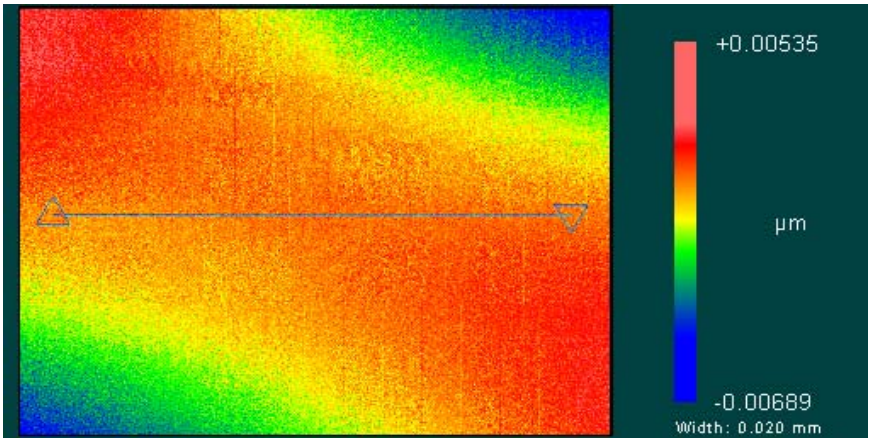

FIGURE 1.1.19: Stitching induced shape errors ("Potato chip effect").

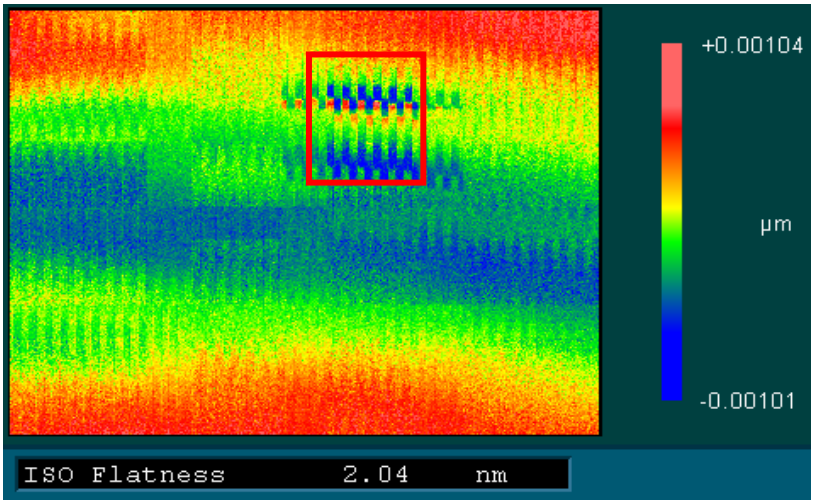

FIGURE 1.1.20: Difference between consecutive stitch measurements.

Some stitching methods might also result in lateral misalignment, as shown in figure 1.1.20. Figure shows the difference between two consecutive stitch measurements. The misalignment is shown within the red box. Hence stitching is not recommended.

The second option is to use a combination of instruments and technologies. Using this approach the focus has been on developing systems housing multiple technologies within a single frame. Several research efforts focused on the development of these multiple technology systems are briefly discussed in the next section. The potential gaps seen in those efforts towards addressing the need for multi-scale measurement and characterization are also discussed.

1.2. State-of-art: Current Metrology Research Efforts and Gaps

The metrology tools needed to perform multi-scale measurements and the related characterization needs could be categorized into the following:

- *Instrumentation* – true three-dimensional measurement systems for scales below 1-10 µm, including the comparison studies on their capabilities and development of multi-scale surface characterization tools.
- *Measurement standards* – standards for surface roughness, spacing, and coating standards, soft gauges for surface texture and similar software checks for other instrumentation and 3-D structures for calibrating micro- and nano-Coordinate Measuring Machines (CMM's), definition of metrological terms, symbols, procedure and globally accepted written standards.
- *Validation protocols* - identification of minimum requirements for the calibration of an instrument, criteria to determine the degree to which an instrument can be

calibrated reasonably, traceability and calibration procedures for nano-metrology tools.

Current research efforts are concentrated on instrumentation development with the recognition of the need for the development of data fusion tools and internationally accepted standards. Most of the efforts mainly fall under “bridge-type” systems, where the relationship between individual systems is previously known, calibrated and considered to be fairly stable. Hansen et al [10] describe integrated systems, called micro-CMMs and nano-CMMs which combine CMM for large scale positioning and an accurate AFM for micro- and nano-metrology, that were developed by academic institutions in US and EU and their later commercial counterparts. The instrumentation development efforts are described in detail in the following section.

1.2.1. Instrumentation Development

The previous section highlighted the need for multi-scale measurement and characterization and the general lack of single technology tools to effectively characterize those surfaces. This section discusses the instrumentation development efforts that are specifically oriented towards addressing that gap. The instrumentation development efforts can be categorized as (a) *Integrated sensors approach, (b) Cascaded sensors approach, (c) Scaled topometry approach, and (d) Multi-mode single instrument approach*

1.2.1.1. Integrated Sensors Approach

The integrated sensors approach is the first logical step and has been largely commercialized. In this approach, multiple technologies are attached to a common metrology frame. Many multi-sensor CMMs routinely combine touch trigger probes,

vision probes and laser point triangulation or line scanning probes, as shown in the schematic diagram in figure 1.2.1. Multiple probes are used to collectively obtain data clouds about the measured surface and then combined using data cloud manipulation software. The sensor selection is mainly based on the capabilities and limitations of individual probes towards measuring that particular feature. There are some systems that also provide probing options that are not purely for dimensional metrology purposes, like the MicroGlider ® by FRT GmbH [46], which provides a chromatic sensor, film thickness sensor, a camera and an AFM.

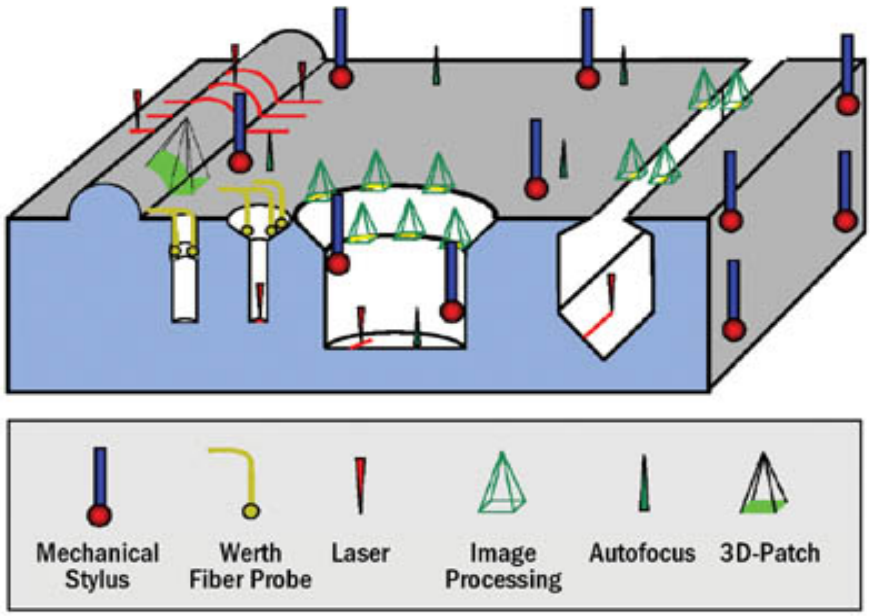

FIGURE 1.2.1: A Typical multi-sensor measurement approach in a CMM based dimensional metrology application [47].

1.2.1.2. Cascaded Sensors Approach

The cascaded sensors approach is the next evolutionary step from integrated sensors approach, where multiple sensors with different resolutions are used towards a common criterion of reduced measurement time with better uncertainty. Topfer et al [48]

proposed a cascaded system approach, as shown in figure 1.2.2, where each level has sensors that have a higher resolution by at least by a factor of 10 from the sensors from the next level. Lower level sensor's data is used to fine tune the location and measurement method (inspection planning/strategy) deployed on the next level of sensors. They highlight the fact that there are not many publications on dimensional metrology in the micro- and nano-range with several sensors and in particular, none on data fusion based on data from different sensors.

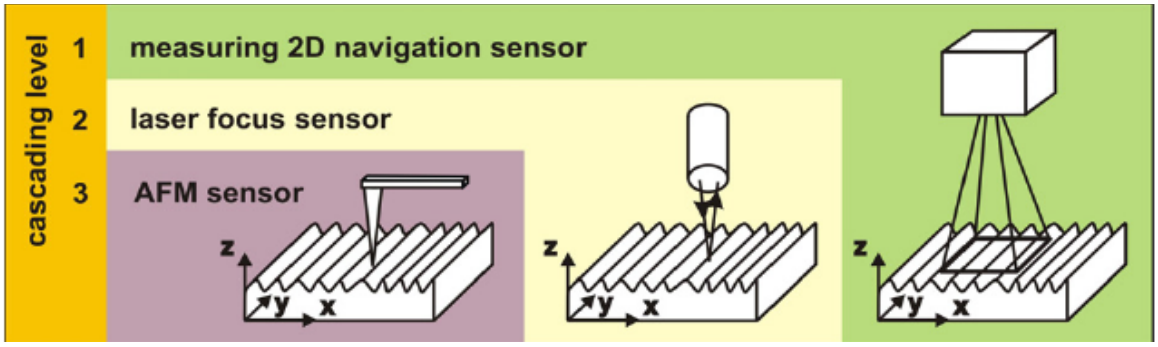

FIGURE 1.2.2: Cascaded system approach by Topfer et al [48].

1.2.1.3. Scaled Topometry Approach

The scaled topometry approach is similar to the cascaded systems approach for micro-scale metrology, but for extended surfaces [49, 50]. The concept of scaled topometry (shown in figure 1.2.3) consists of a systematic combination of various optical measurement techniques with overlapping ranges of resolution. These systems rely on building all technologies into one single frame, with known relation between coordinate systems referenced by those instruments. Parts are placed inside the measurement volume once and all the instruments are used in a logical sequence to obtain a surface map. Data obtained using multiple resolutions are merged using wavelet analysis based

data fusion techniques. But once the part is removed from the setup, any additional measurements cannot be correlated to the previous measurement dataset with precision.

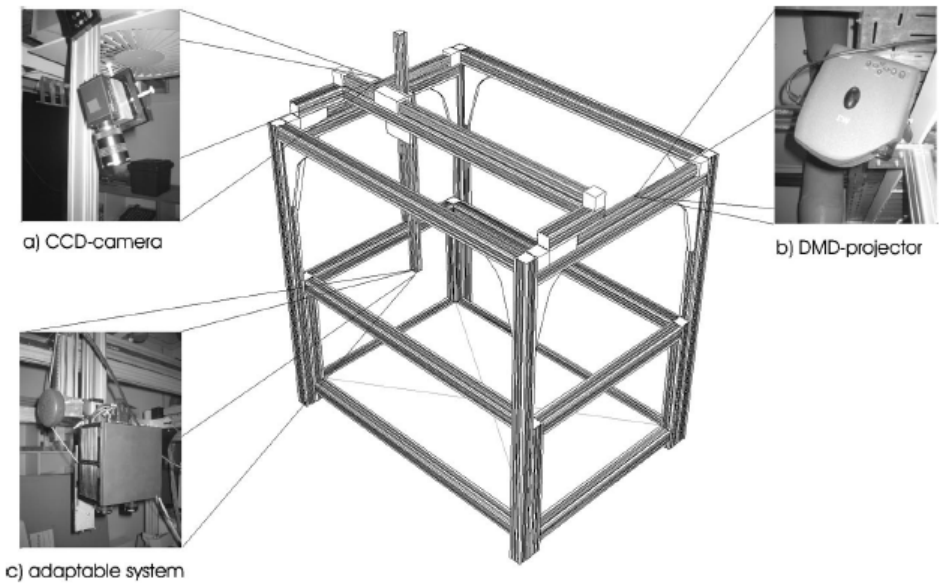

FIGURE 1.2.3: Setup using the concept of scaled topometry [50].

1.2.1.4. Multi-mode, Single-instrument Approach

The multi-mode, single-instrument approach provides the option of multiple technologies mostly on a rotary turret, using a known reference / origin and single metrology loop and multiple detection systems. There has been a steady increase in the number of commercially available hybrid systems utilizing this approach. Sensofar® by Solarius [51] (offers Phase Shifting Interferometry (PSI), Vertical Scanning Interferometry (VSI) and Confocal Microscopy modes on a rotary turret), NewView7300® by Zygo Corp. [52] (offers various software modes High 2G, High, Low), NT9000® by Bruker AXS[53] (Offers PSI, VSI and HD VSI), Alpha 500® by WITec GmbH [54] (offers Confocal Raman Microscopy, Atomic Force Microscopy and

Scanning Near-field Optical Microscopy probes as options on a rotary turret, shown in figure 1.2.4) fall under this category.

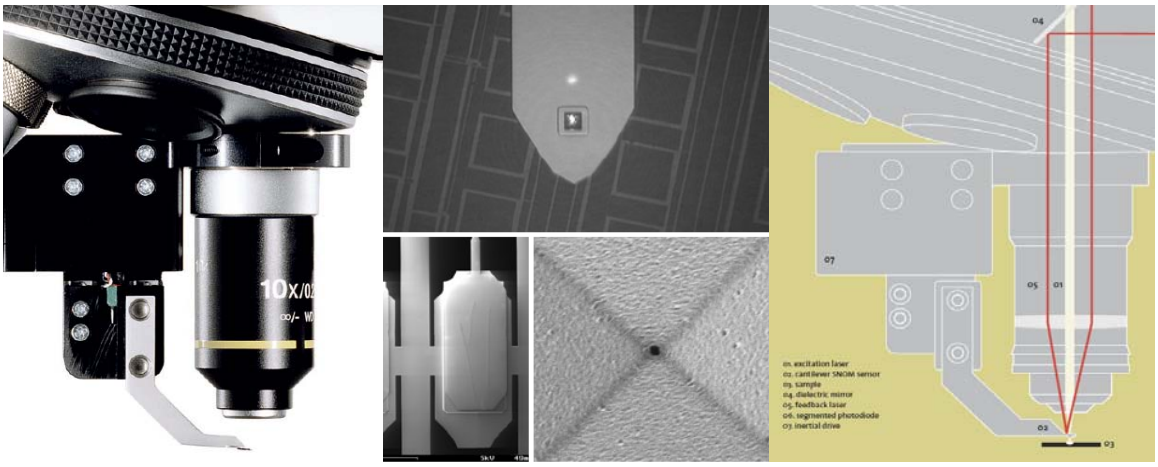

FIGURE 1.2.4: Combined CRM, AFM and SNOM probe by WITec GmbH [54].

The instrumentation development efforts have a strong focus on hardware based combination of different sensors. Under industrial settings, it becomes cumbersome to figure out all possible technologies and to cascade those into multiple systems, not to mention the cost burden involved with setting up the bridge type system with the selected technologies. The stability of the relationship between the individual coordinate systems needs further long term study. The overlapping systems pose a limitation on the positioning accuracy of the stages, requiring the stages of an individual measurement system to be capable to meet positioning requirement of its successive system.

The sensors communicate with each other, but data is not necessarily merged together. These systems enable the user to obtain different surface maps using various technologies, but user doesn't readily have the ability to combine all the obtained data into one single dataset. But for effectively characterizing the multi-scale surface, all the

datasets need to be aligned with respect to each other. It is not sufficient to just perform measurements are multiple scales, but also be capable of characterizing the entire multi-scale surface. Previously described systems are able to perform measurements at multiple scales but lack the much required multi-scale characterization capability. The multi-scale characterization gaps are further explained in the next section.

1.2.2. Multi-scale Characterization Gaps

Researchers and instrument manufacturers have developed instruments with the capability to perform measurements at multiple scales, but the ability to address the multi-scale characterization capability still has not been effectively resolved. By enabling measurements using different magnifications / sampling intervals, in the Amplitude-Wavelength domain, the effective utilizable space of the instrument is expanded, as shown in figure 1.2.5.

Consider the Fresnel micro lens array shown in figure 1.2.6, where the individual features have varying aspect ratios. The central features on individual lens are resolved much better compared to the region shown inside the black circled area, under the selected measurement condition – 10X objective with a 0.5X magnification tube and 100 µm scan length on NV6300 system. The features are better resolved at a higher magnification using the same 10X objective but with a 2.0X magnification tube, as shown in figure 1.2.7.

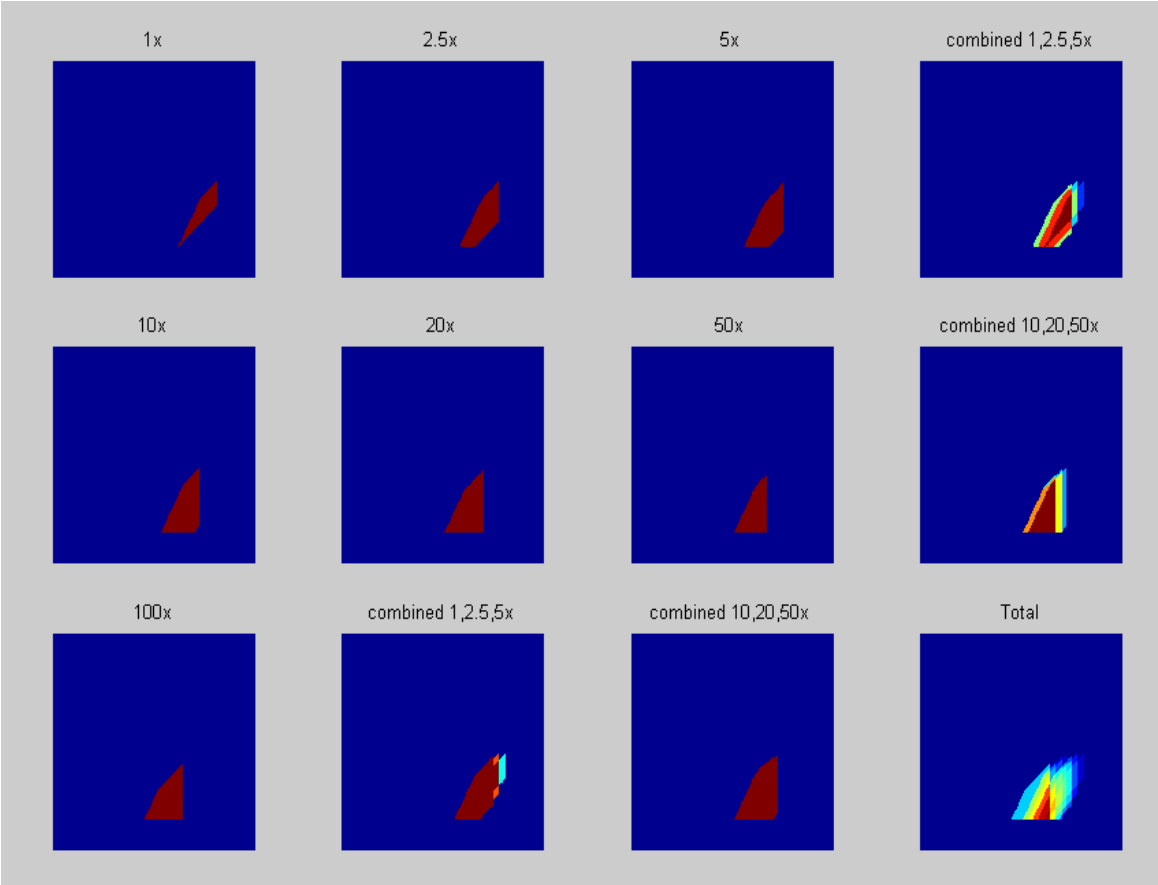

FIGURE 1.2.5: AW map of individual magnifications in NV6300 system [2].

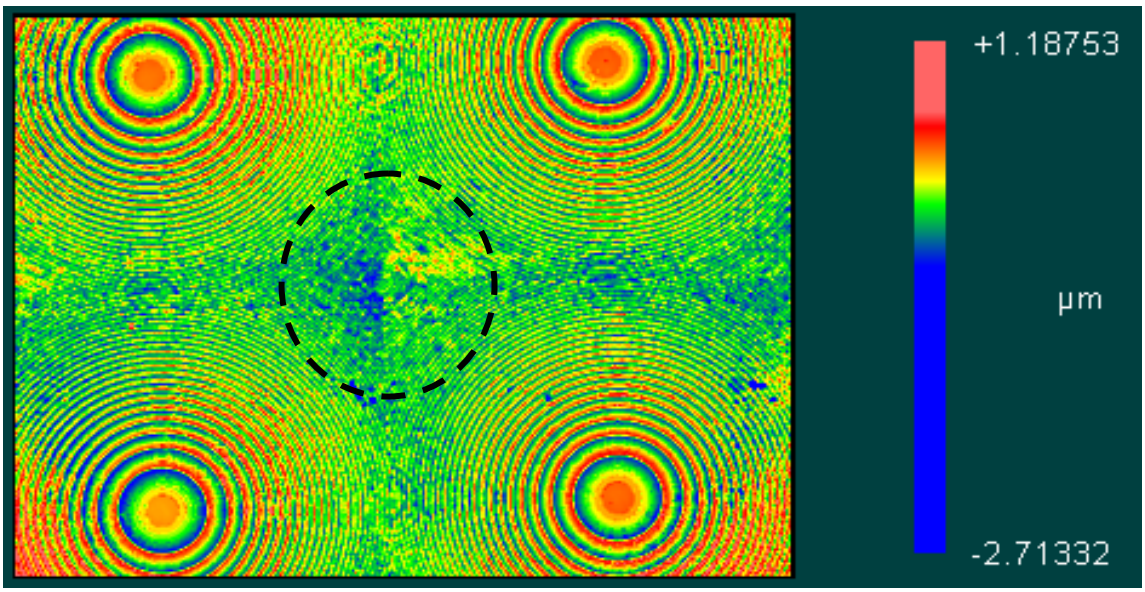

FIGURE 1.2.6: Fresnel micro lens array at 5X magnification.

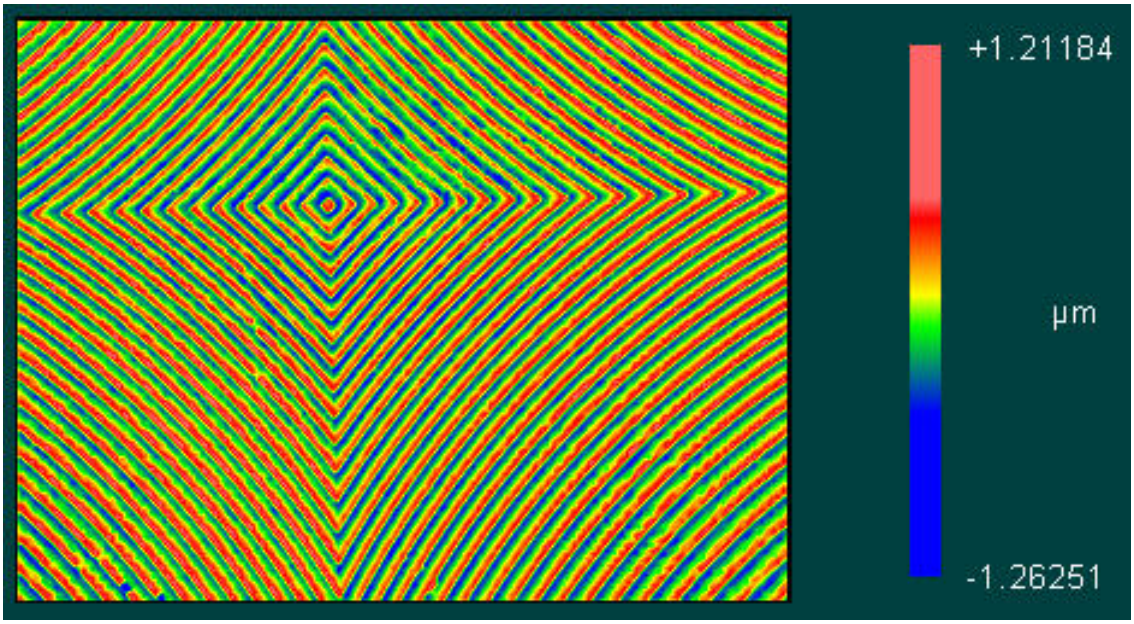

FIGURE 1.2.7: Fresnel micro lens array at 20X magnification.

With these two magnifications, the features are effectively resolved, but the two datasets are independent. In order to correlate both data and characterize the entire surface, the coordinate relationship between the data needs to be established. Data cloud manipulation software packages [55] are available to handle datasets obtained from macro-scale 3D measurement systems, but have not been widely used with micro-scale surface measurement systems. From figures 1.2.6 and 1.2.7, the potential advantage of combining multiple magnification datasets is evident – better capability for characterizing varying aspect ratios. This example illustrates the first multi-scale characterization gap, which could be addressed by development of strategies for fusion of data obtained from same instrument but with different magnifications / sampling intervals. This would result in better preservation of resolution at different ranges and increased confidence on data.

Light setting and other available software options could be used to obtain more data using the same magnification. A typical example is data obtained on a spherical surface (feature on a hard disk drive suspension shown in figure 1.1.4) from using a Coherence Scanning Interferometry (CSI) system (NT8000 from Bruker AXS at 10X magnification and 20% light setting) is shown in figure 1.2.8.

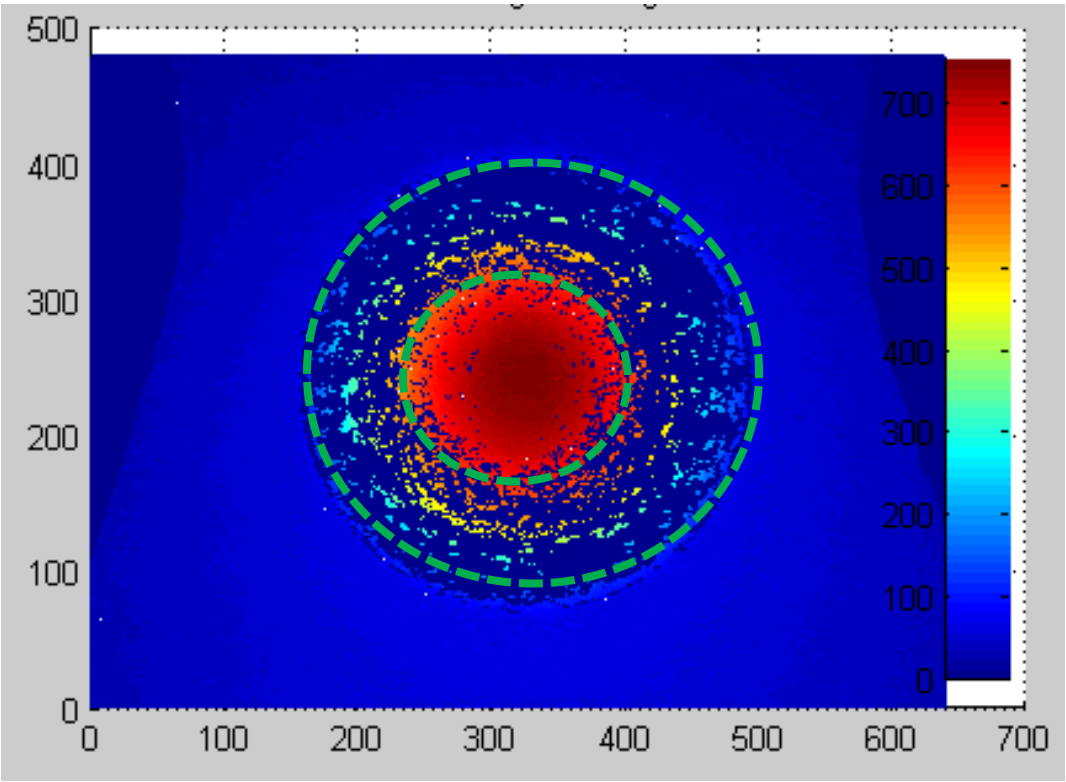

FIGURE 1.2.8: 3D surface plot of the spherical surface at 25% light setting.

There is significant data drop out at the regions with high slopes (area within two dashed green circles shown in figure 1.2.8) which are normally attributed to numerical aperture limitations of the objective. This data drop out impacts the capability of the sphere fitting algorithms. In order to reduce the data drop out, the light levels could be increased. With the change in light setting from 20% to 35%, side slope regions can also be measured, but this results in significant saturation on all other areas, as shown in

figure 1.2.9 (indicated by dark blue regions). There is no built-in option available in the system that could merge these two data. This example illustrates the second need for the development of fusion strategies involving datasets obtained from same instrument but with different settings.

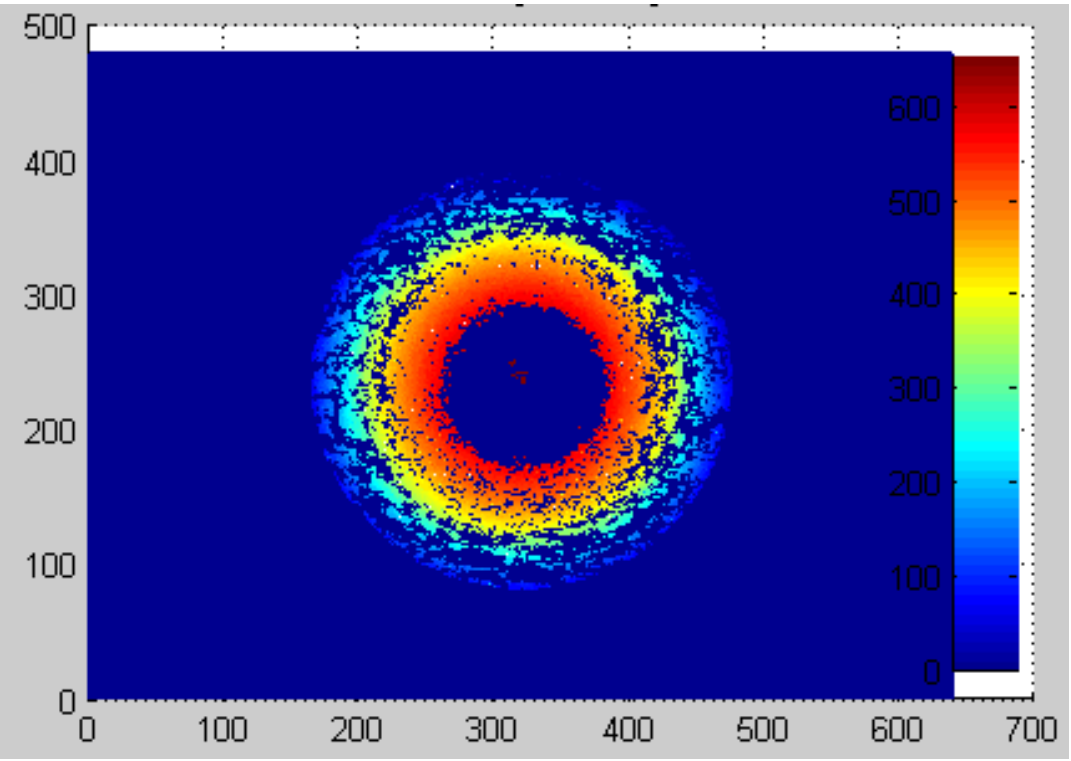

FIGURE 1.2.9: 3D surface plot of the spherical surface at 35% light setting.

If the CSI system is also used for measuring the datums, the individual measurements have to be measured at the same magnification and stitching is the only available option which is time consuming. The hole and slot can be measured using a vision system (Pinnacle systems from VIEW Micro-Metrology [56] with 2.5X and 10X magnifications) with good resolution. A better option would be to measure the datums at a suitable magnification in a vision system, measure the 3D features using CSI systems at a suitable magnification and then merge those datasets together. This situation demands

development of fusion strategies dealing with datasets obtained from different systems but with similar sampling intervals. This example illustrates a clear third need for development of software based data fusion tools in the surface metrology domain and also for the possible union 2D and 3D datasets for performing dimensional measurements and surface characterization on single dataset.

Data fusion strategies capable of handling these three scenarios would enable minimization of measurement time while preserving or maximizing data fidelity. The effective approach towards multi-scale measurement and characterization would be to use the individual measurement tools and finding a method to relate the individual coordinate systems and use an offline virtual tool to unify, manipulate, segment, merge and retrieve data. This approach would enable cost effective characterization of surfaces without sacrificing the fidelity of data. Data fusion has also been used in surface metrology domain, but mainly in the perspective of image fusion based on focus criteria, which is explained in the next section.

1.3. Data Fusion

Data fusion is used at different levels of complexity from a simple overlay to stereo vision where two images obtained from cameras fixed at two viewpoints are used to triangulate and calculate a 3D image. Data obtained from two technologies could be overlaid on top of each other without any further processing, assuming there are minimal transformational errors between the two datasets, as shown in figure 1.3.1.

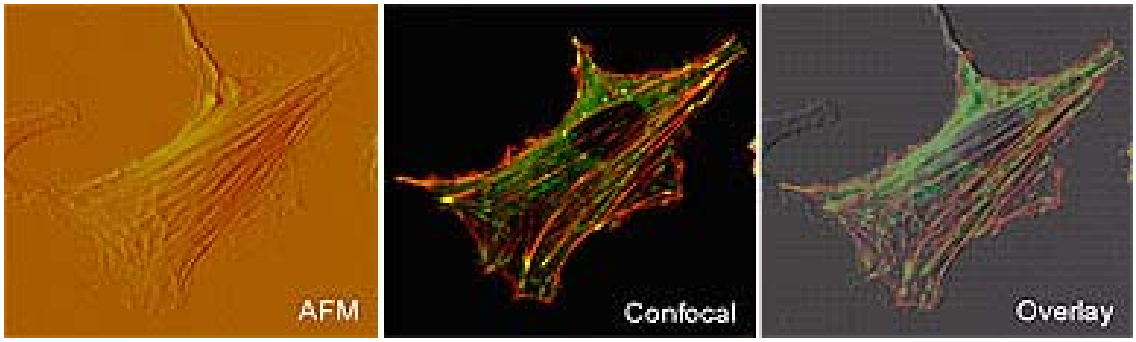

FIGURE 1.3.1: Image overlay of AFM and Confocal images [57].

Depth-from-focus and focus variation based methods rely on merging data obtained from images taken at different z height intervals, and then finding the maximum contrast points at each image to create 3D image [58] with all points at virtually infinite focus. The main gap seen in this approach is that this cannot be utilized to merge two data datasets which already exhibit the infinite focus condition. This approach also assumes that the data are pre-registered and are of same magnification. Hence, it does not permit data fusion of multiple resolutions or magnifications.

Shaw and Weckenmann [59] have demonstrated the possibility of fusion of data obtained from two different sensors for effective optical characterization in the dimensional metrology domain. They proposed segmentation of data into shape primitives and based on the capability of each sensor, selected primitives from individual data is merged together to generate the final data. In the surface metrology domain, shape primitives based segmentation and instrument capability based fusion is not effective due to lack of primitive shapes in surface measurements. Focus based fusion strategies cannot be used as every data point in the data sets under consideration has to be treated as essentially at optimal focus. Hence, there is a need to explore different fusion

strategies pertaining to surface metrology domain, where individual pixel level data fusion can be performed based on selected criteria.

Wavelet and fractal analysis has been successfully used for data segmentation and fusion purposes in other macro level fields [60], and are being explored as possible solutions for the micro- and nano-level data fusion, as shown in figure 1.3.2. This approach still utilizes focus variation between images, hence cannot be used for data containing multiple resolutions or magnifications.

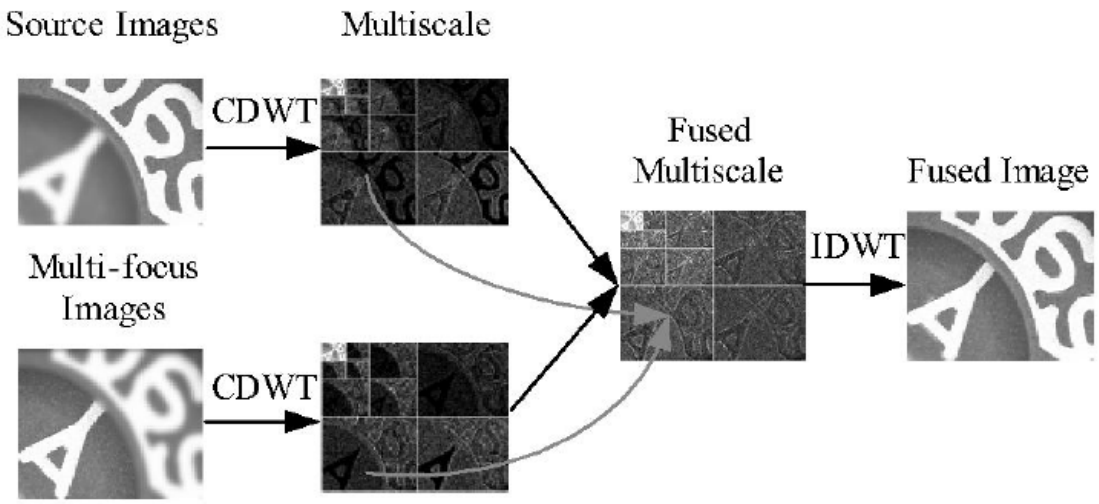

FIGURE 1.3.2: Data fusion using complex values wavelet transformation [61].

Single-scale overlay is not feasible when both the data are not accurately registered. Hence, either single-scale or multi-scale data fusion is the preferred option. Shape primitive based single-scale fusion has been successfully demonstrated in dimensional metrology domain but cannot be effectively used in surface metrology domain as surface data lack shape primitives. Also, if both the data were obtained using same instrument, then primitive shape selection criteria gets complicated. Focus based multi-scale fusion methods are also ineffective as all data points in both datasets are

under optimal focus conditions. Therefore, multi-scale data fusion methods that are not based on focus need to be explored. A detailed description of individual steps of generic multi-scale data fusion will be briefly explained in the next section.

1.4. Multi-scale Data Fusion

Joint Directors of Laboratories [62] defines data fusion as a “multi-level, multi-faceted process handling the automatic detection, association, correlation, estimation and combination of data and information from several sources”. Ranchin and Wald [63] proposed the ARSIS concept (in French “Amelioration de la resolution spatiale par injection de structures” meaning ‘improvement of the spatial resolution by structure injection’) as a framework for fusion of multi-modal images specifically for satellite imagery [64] and then generalized it for fusion of images with different spatial and spectral resolutions. A generic frame work for Multi-Scale Data Fusion (MSDF) (based on [65]) is shown in figure 1.4.1. The individual steps are discussed in detail along the options available under each basic step.

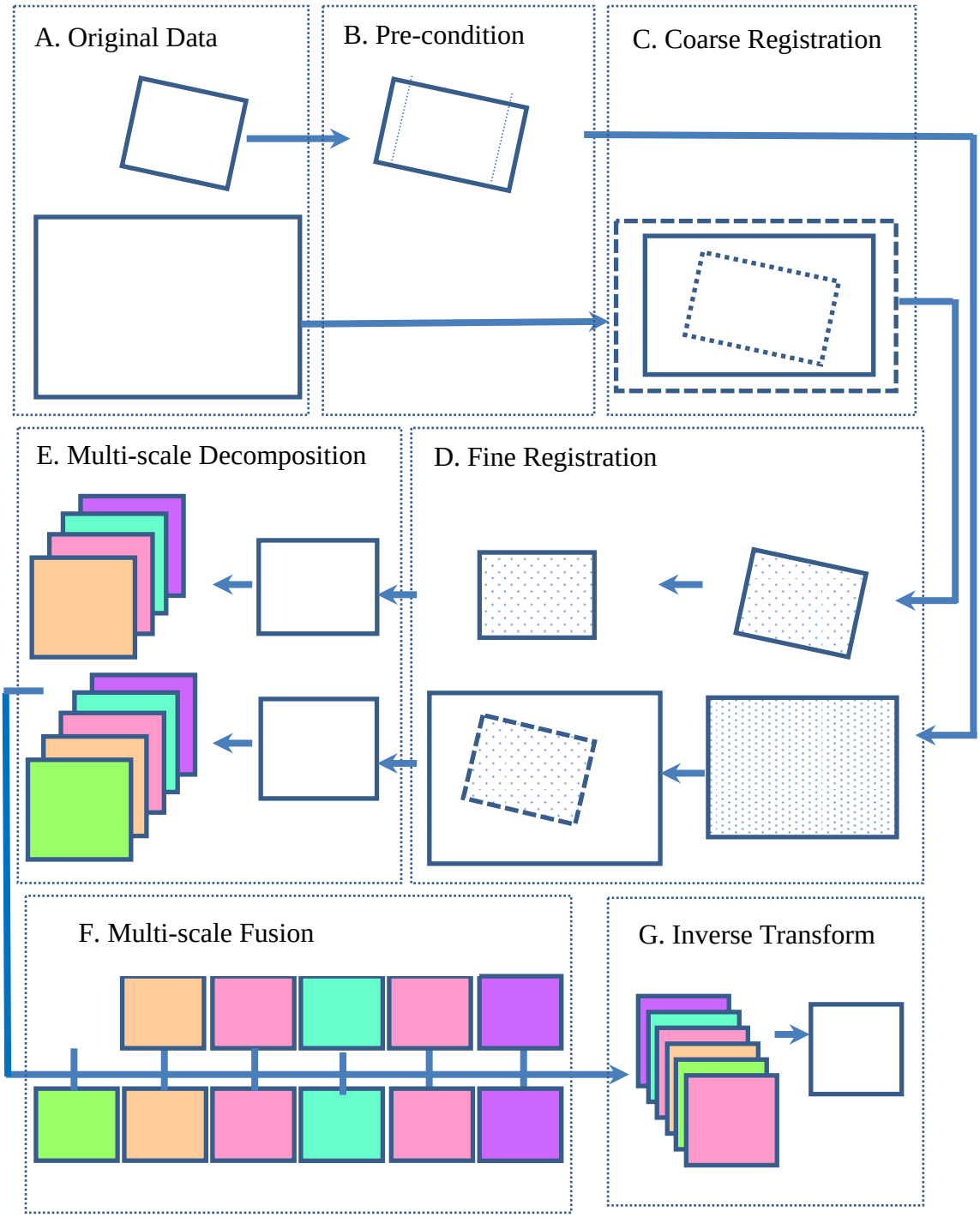

FIGURE 1.4.1: Schematic of generic multi-scale data fusion (A) Original Data (B) Pre-condition (outlier removal, plane removal, resample and resize) (C) Coarse registration (D) Fine registration after control point detection (E) Multi scale decomposition on selected same size area from both data (F) Multi scale Fusion (G) Inverse Transform on fused sub-datasets to obtain fused data.

1.4.1. Pre-conditioning

The data sets need pre-conditioning to ensure that multi-scale decomposition would be effective. Outliers and missing data need to be removed and replaced with the data mean or zero. The dataset with the higher sampling interval is down sampled to match the dataset with the lower sampling interval. If the sampling intervals (spatial resolution) of the datasets under consideration do not have the ratio of power of two, then the decimation algorithm cannot be used effectively. Therefore, resampling has to be performed to ensure that the ratio of the sampling intervals is a power of two and also padded with zeros or mean value of data to make the array size a power of 2.

1.4.2. Coarse Registration

After the datasets have been pre-conditioned, the next step is to roughly align both datasets, which is called coarse registration. Coarse registration can be either done manually by locating unique fiducial markers and edges on both the images, or automated programs could be utilized. Sum of Absolute Differences (SAD) and Normalized Cross Correlation (NCC) could be used to find the approximate translation offsets between the two datasets.

1.4.3. Fine Registration

The datasets have to be precisely aligned before data fusion. Typically fine registration is performed by finding matching fiducial / control points [66] on both the datasets and then calculating a transformation matrix which would match the control points in both the datasets using least squares optimization. Edge detection [67, 68] is used to find contours on both datasets which could be used as control points. Different segmentation algorithms [69] could be used to find more uniform dispersion of control

points for effective alignment. Iterative Closest Point (ICP) algorithms [70] and its variants [71, 72] are widely used for alignment.

1.4.4. Multi-scale Decomposition

Multi-scale decomposition deals with representing the given signal at different resolutions depending on the scale at which it is analyzed. It was first explored for 2D signals [73, 74] and then for various image processing applications in medical data and image processing [75, 76] and image compression [77].

The multi-scale nature of surfaces and non-directional, non-repeating features posed an interesting challenge to the traditional Fourier based analysis methods. Fourier theory enables the decomposition of any signal into a series of sine and cosine functions, but it is not possible to have both frequency and time resolution at the same time, due to the Heisenberg's uncertainty principle. In order to overcome this disadvantage, Windowed Fourier transform and Short-term Fourier transform were developed, followed by Gabor transform [78] and discrete wavelet transform. Wavelets are compact zero-sum signals vanishing outside the finite interval, giving the benefit of effective localization in both time and frequency, enabling better characterization of multi-scale engineered surfaces. Rather than being restricted to a single wave type, wavelet transform opens the possibility of using any wavelet as the basis function. This enables wavelet transform to be versatile compared to traditional sine wave based Fourier transform. The simplest wavelet is a square-shaped 'Haar wavelet' [77] shown in figure 1.4.2. The real and imaginary components of a generic harmonic wavelet [79] is shown in figure 1.4.3 'a' and 'b'. Figure 1.4.4 illustrates how a given input signal could be decomposed using a Haar wavelet.

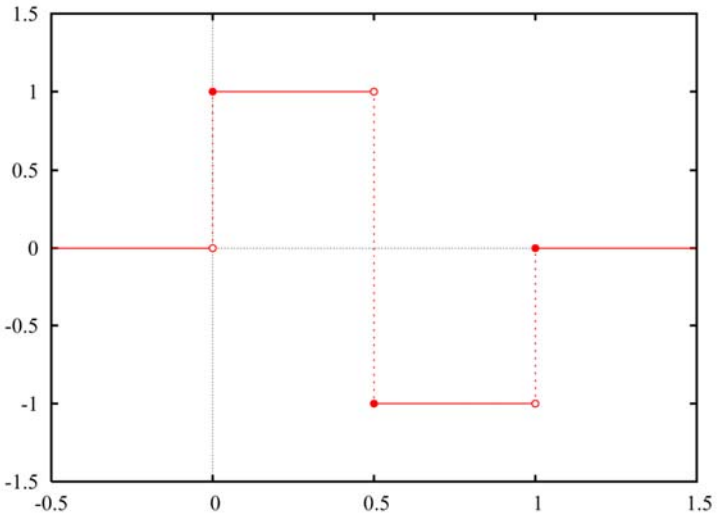

FIGURE 1.4.2: Haar wavelet.

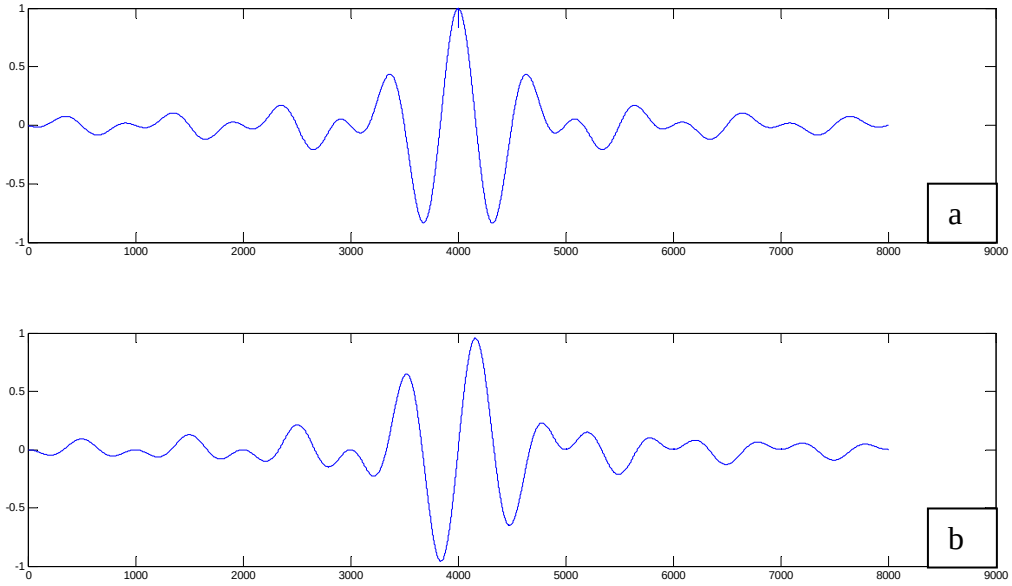

FIGURE 1.4.3: (a) Real and (b) Imaginary part of a generic harmonic wavelet [79].

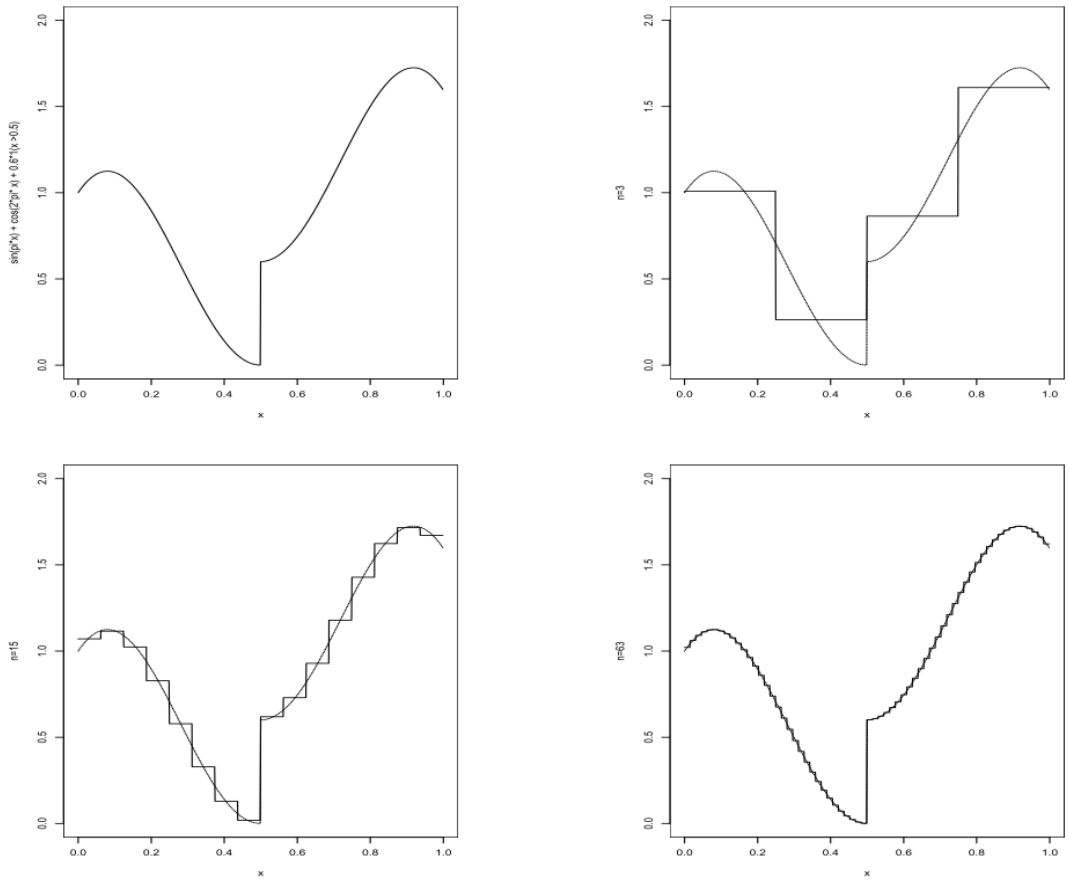

FIGURE 1.4.4: Decomposition of a signal using Haar wavelet [80].

Wavelets enable a signal to be decomposed to different scales without reduction in the resolution, unlike the traditional Fourier transform. Figure 1.4.5 shows the decomposition of a signal into seven scales. The localized noise in the input signal is effectively captured at the higher resolution scales and the sine wave is captured in the lowest resolution scale. This example demonstrates the capability of wavelet transform method to detect localized signal variations.

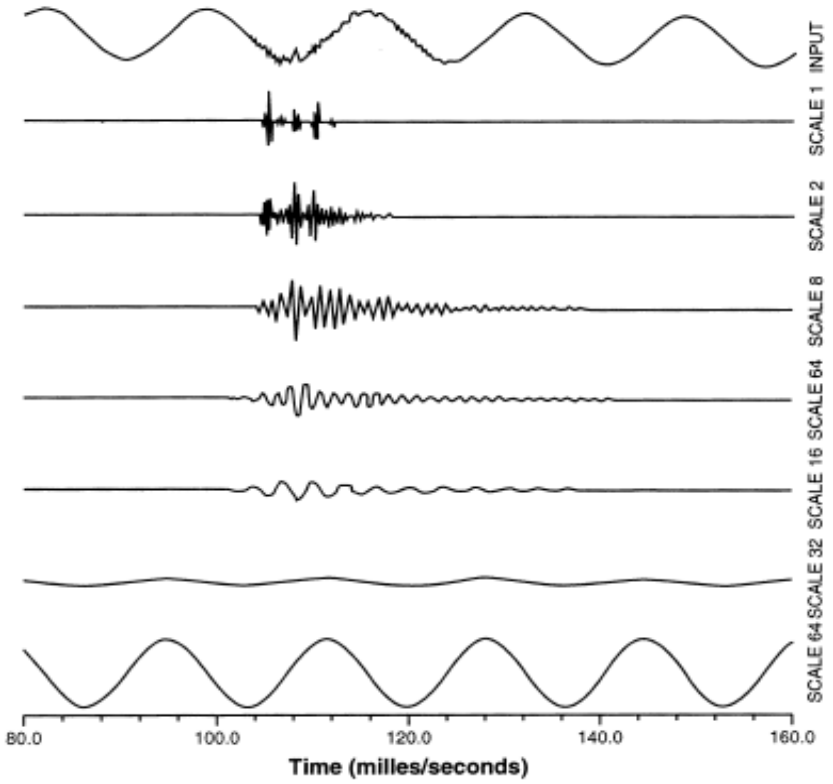

FIGURE 1.4.5: Decomposition of a signal into different scales [81].

Wavelet based multi-scale decomposition and representation of data has been successfully used in surface metrology domain for multi-scale analysis of engineered surfaces [82, 83]. Wavelet based multi-scale decomposition and fusion has been successfully demonstrated in medical image data fusion [84] and remote sensing [85].

A typical analogy used for multi-scale decomposition and representation of data is to compare the data to a pyramid [86], as shown in figure 1.4.6. Assuming that the bottom most plane is the data at its full resolution, each successive upper tier is an approximation of the tier directly below it.

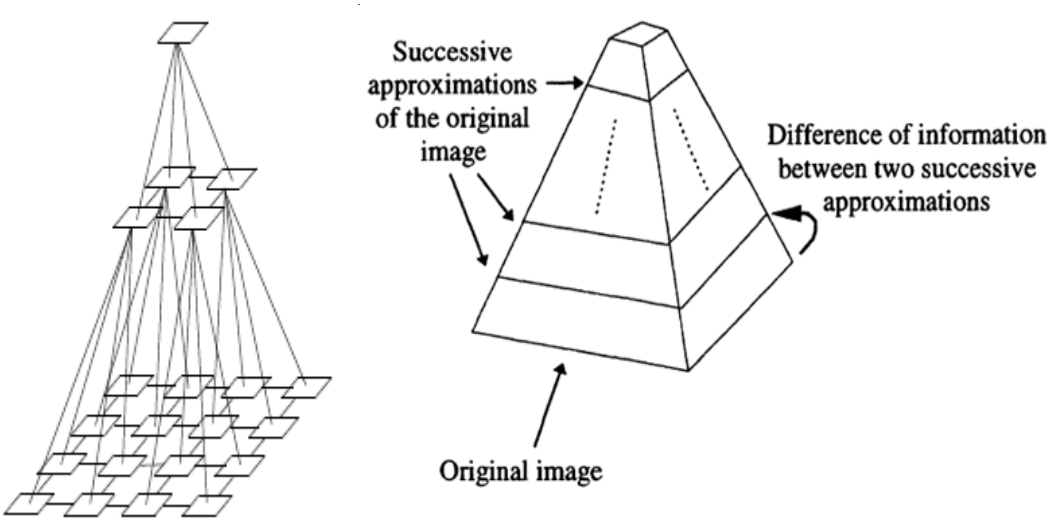

FIGURE 1.4.6: Pyramid model of data approximation [86].

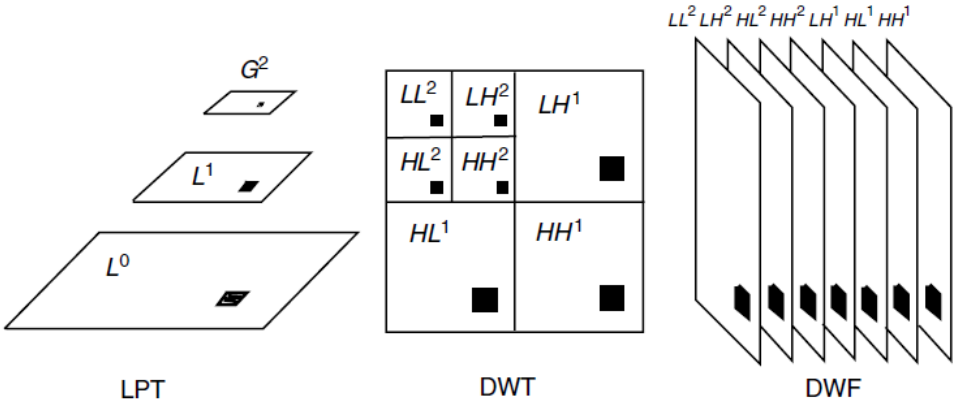

FIGURE 1.4.7: Three common multi scale decomposition methods – Laplacian Pyramid Transform (LPT), Discrete Wavelet Transform (DWT) and Discrete Wavelet Frame (DWF) [86].

The three common methods used for multi-scale decomposition methods are the Pyramid Transform (PT) or Generalized Laplacian Pyramid Transform (GLP) [87, 88], Discrete Wavelet Transform (DWT) or Mallat method [89] and Discrete Wavelet Frame (DWF) or À Trous method [90], as shown in figure 1.4.7. LPT method follows the typical pyramid system of reduction, resulting in an image half the size of its predecessor. DWT usually results in three images after every transform – horizontal, vertical and

diagonal (denoted by LH, HL and HH). DWF results in frames of the same size as the original data.

Human visual perception is very good at facial recognition even at very low resolutions, as demonstrated by the fact that vast majority of Americans being able to recognize the image shown in figure 1.4.8 as President Abraham Lincoln. Therefore, in order to compare the performance of DWT and DWF, an image 'Haritha' of a human face on a background filled with ripples is used (Image courtesy – Dr. Brian D. Boudreau).

FIGURE 1.4.8: Pixelated image of President Abraham Lincoln.

1.4.4.1. Discrete Wavelet Transform (DWT)

The Morlet-Grossmann definition [91] of the Continuous Wavelet Transform (CWT) for a 1-dimensional signal $f(x) \in L^2(R)$, the space of all square integrable functions, is given by:

$$W(a,b) = \frac{1}{\sqrt{a}} \int_{-\infty}^{\infty} f(x) \psi^*\left(\frac{x-b}{a}\right) dx \text{, where}$$

- $W(a,b)$ is the wavelet coefficient of the function $f(x)$
- $\psi(x)$ is the analyzing wavelet
- a (> 0) is the scale parameter
- b is the position parameter

CWT has three properties, linearity, covariance under translation and covariance under dilation. Covariance under dilation is very useful for analyzing multi scale surfaces enabling analysis at different scales without losing the resolution.

CSI and AFM make discrete point measurements requiring a discrete wavelet transform. In DWT, the dataset is repeatedly down sampled by dyadic reduction and then a convolution is applied using the corresponding scaled mother wavelet. For efficient transformation, the datasets are padded to a size of power of 2. Figure 1.4.9 a-d, shows the 4-level decomposition of image 'Haritha' using 'Coiflet 5' as the mother wavelet. At each level of decomposition, the size of the resulting image is half the size of the previous image.

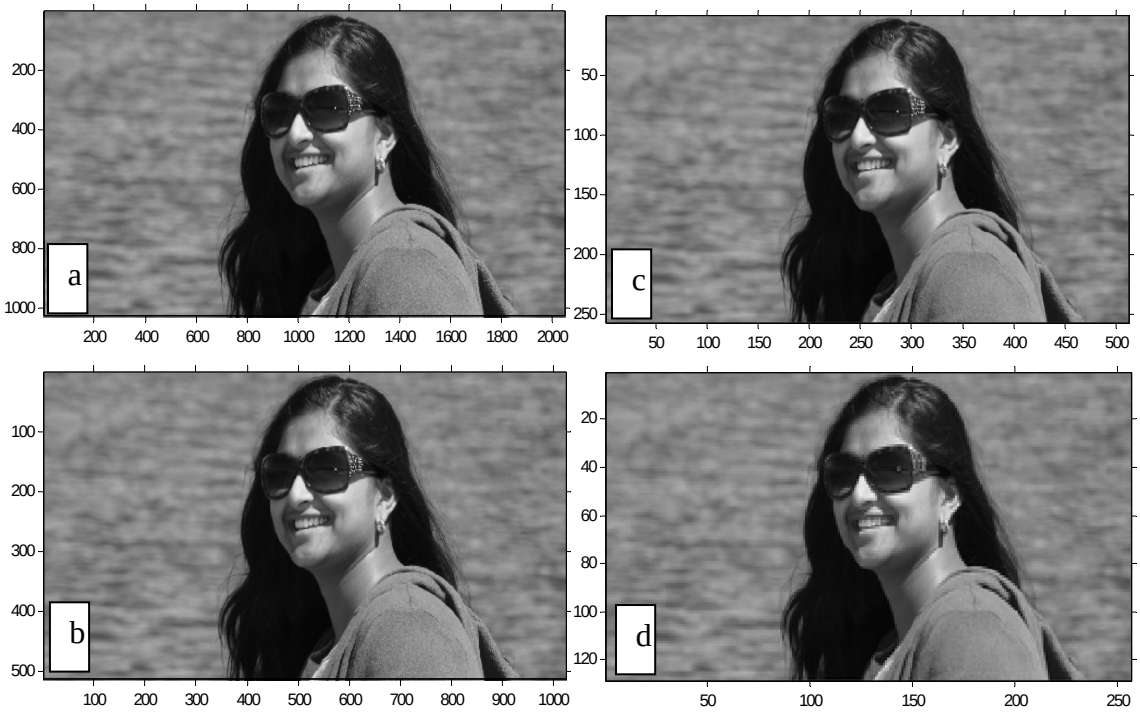

FIGURE 1.4.9: 4-level DWT decomposition of (a) Original image 'Haritha' at 1024 x 2048 size decomposed to (d) 128x 256 size using Coiflet 5 as mother wavelet.

1.4.4.2. Discrete Wavelet Frame (DWF)

DWT requires dyadic reduction at each level of decomposition and hence results in an image that is half the size of the previous level. In order to retain the same size, discrete wavelet frame method is preferred, where no decimation is performed. This method is also called à trous (with holes) method as instead of decimation, data is replaced with zeros. Figure 1.4.10 shows individual frames of image 'Haritha' after a 6 level decomposition using a B3 spline.

FIGURE 1.4.10: 6-level DWF based decomposition of image 'Haritha' using B3 spline as mother wavelet.

At each level of decomposition, a wavelet coefficient plane W_j is generated with the difference between successive decompositions C_j and C_{j-1}. In order to regenerate the

original data C_0, the last smoothed data C_n is added to the summation of all coefficient planes. Since DWF is non-decimating and is shift-invariant, it is generally preferred for image fusion. An n-Level multi-scale decomposition of both the datasets using DWF results in two sets of 'n' sub-datasets, which will be used for data fusion.

1.4.5. Data Fusion

Data fusion is carried out at individual scales. First the sub-datasets obtained from multi-scale decomposition are matched according to scale. For the sub-datasets at each scale, data fusion is performed at individual data point level by means of simple methods like choosing the maximum, minimum or mean of the two data points or weighted averaging methods can also be used. Since the useful features in the data are usually larger than one data point, single data point based maximum, minimum or mean approach are not recommended and instead, a kernel based weighted average is generally preferable [92].

1.4.6. Inverse Transform

Inverse transformation is performed on the fused datasets to obtain the fused final dataset.

The pre-requisites for using existing pixel level multi-scale data fusion strategies are:

- Images shall have different spatial and spectral resolutions,
- Images shall represent the same area,
- Images shall be accurately registered, and
- No major change shall have occurred on the area between the acquisition of those images

In surface metrology domain, the datasets may or may not have different spectral resolutions and may or may not represent the same area. For data sets which are of approximately same area but with different spatial resolutions, both the datasets are initially leveled to remove shape. But for measurements obtained using CSI at various magnifications, the area also correspondingly changes and shape removal may or may not be permitted depending upon the measurement intent. Optics induced shape errors are not similar at different magnifications. These challenges demand development of MSDF strategies suited for multi-scale surface characterization of engineered surfaces in general and non-planar surfaces in particular.

Accurate registration of datasets cannot be guaranteed because of orientation and placement errors along with measurement system's axis errors. Surface datasets also may not have easily locatable control points or markers to enable manual selection and alignment. For segmentation of structured engineered surfaces with non-planar patterns existing height based separation methods are not effective. Therefore, effective segmentation and edge detection algorithms have to be studied. For multi-scale decomposition in DWF domain, three different options could be used: (a) performing in 2D where the rows are executed first followed by columns using a 2D mother wavelet (b) performing in 3D where rows and columns are executed simultaneously using a 3D mother wavelet and (c) performing in hybrid 3D for patterned surfaces for better edge preservation. The pros and cons of these three methods for different kinds of surfaces need to be characterized. Various single-scale and multi-scale fusion metrics have been proposed in image fusion domain, but detailed analysis is needed to find the metrics that are effective for surface metrology domain. Performance of different data fusion

methods on multiple surface types (engineered directional and non-directional surfaces, unstructured and systematic surfaces) needs to be evaluated. The main steps involved with MSDF are coarse and fine registration, multi-scale decomposition and data fusion. For performing these individual steps, various options are available. Hence further study is needed to select optimal choice of tools to perform these steps.

Exploring multi-scale data fusion strategies suited for multi-scale surface characterization and selection of options for individual steps will be the focus of this research, which will be explained in detail in the next section.

1.5. Research Focus

The primary focus of this research is "to explore possible multi-scale data fusion strategies and options for surface metrology domain and to develop enabling software tools in order to obtain effective multi-scale surface characterization, maximizing fidelity while minimizing measurement cost and time".

Fusion strategies for surface datasets are treated in four different categories:

- *Single-scale, single-domain data*, where data sets obtained from the same instrument but with multiple light settings are considered.
- *Single-scale, multi-domain data*, where data sets obtained from different instruments but approximately same sampling interval are considered.
- *Multi-scale, single-domain data*, where data sets obtained from similar technology instruments but with different sampling intervals are considered.
- *Multi-scale, multi-domain data*, where data sets obtained from multiple technology instruments and different sampling intervals are considered.

Two main optical characterization tools that will be considered are the vision CMMs (for 2D characterization) and CSIs (for 3D characterization). Effective data fusion is possible when the input data sets have good signal-to-noise ratio and closely oriented with respect to each other. Hence, better understanding of possible error sources that would affect fusion performance is necessary and best practices / proper procedures have to be followed to ensure high fidelity data. Therefore, calibration, adjustment and error estimation methods that could be used for CSIs will be analyzed in detail.

Selected datasets will be subject to various additive and defocus noise, and translational and rotational misalignment in order to understand the impact of noise and misalignment on coarse and fine registration. Directional, non-directional and non-engineered surfaces will be used to study the performance of different transformation methods and select the optimal method suitable for handling different surfaces. Fusion metrics will be studied by comparing their performance on quantifying the similarity between multiple types of surface datasets and their noisy versions. Based on the selected fusion metrics, available data fusion methods will be evaluated and robust method with highest data fidelity will be selected. After selecting options suitable for handling wide varieties of surface types, possible solution of handling non-planar data sets will be explored.

CHAPTER 2: ADJUSTMENT PROCEDURES FOR A COHERENCE SCANNING INTERFEROMETER AND QUANTIFICATION OF ITS ERRORS

For effective Multi-Scale Data Fusion (MSDF) with high data fidelity, care should be taken to ensure that the individual data obtained at different magnifications are accurate. In order to better understand a system, calibration and adjustment protocols of the system and quantification of error sources is necessary. Therefore, standard calibration and adjustment procedures have to be followed to ensure the system is at optimal performance at all magnification settings. Since the research focus is on fusion of data obtained from Coherence Scanning Interferometers (CSIs) and Vision CMMs, special attention will be made towards adjustment and quantification of errors in CSI systems. NPL GPG No.108 and 116 [93, 94] describes best practices for sample preparation and instrument setup and also discusses possible error sources. The ISO 25178 [95] specification standards on areal surface topography measurements detail a series of tests that can be used to calibrate CSI systems and list the metrological characteristics of CSI systems. Giusca and Leach [96] document the basic calibration procedure for areal surface topography measuring instruments. These four documents form the basis for the calibration and adjustment procedures detailed in this chapter.

Various publications document possible error sources involved with CSIs, such as the uncertainty of calibration standard used, non-linearity of instrument in lateral and vertical axes, Abbe offset errors, sample alignment errors, thermal drift induced errors, cross talk between axes, evaluation method, piezo materials inherent errors like creep, hysteresis, non-linearity, drift and aging. There is a need for a comprehensive treatment, detailing the adjustment sequence and what error sources to be aware of depending upon the application. This chapter details the basic adjustment procedure for CSI that can be readily deployed and then goes over error sources, test methods to find their impacts on X, Y and Z measurements, and their possible impact on MSDF process. Most of the tests were conducted on NewView^{TM} 7300 3D optical profiler system by Zygo Corporation, but could be readily used for any CSI system.

Before discussing the calibration, adjustment procedures and error evaluation methods, a typical structure of CSI system is explained. With better understanding of the system's metrology structure, listing the possible error sources becomes easy.

2.1. Configuration of a Coherence Scanning Interferometer

The typical CSI is shown in figure 2.1.1. Typically a halogen or LED light source is used. Light is then expanded, homogenized and shaped using optical sub systems, aperture stop and field stop. The treated light is then directed to the non-polarizing beam splitter using a 45° mirror. The beam splitter directs the light into the interferometer objective, which is mounted on a multi position turret. Objective turret is mounted to a scanner, which is attached to the rigid frame. The reference mirror is housed inside the Mirau type objective (low magnifications do use Michelson type setup). The light is focused on to the surface to be measured. The reflected light then interferes with the

reference beam and creates an interference pattern. This pattern is magnified through the magnification/zoom tube setup, which can be mounted on a separate turret. The beam is focused into the detector, which can be a CCD or CMOS camera. CSI systems typically rely on the fidelity of the scanner for Z accuracy and repeatability. Some systems do provide an optional secondary system to provide feedback for the actual position of scanner. These secondary systems could be capacitance or interferometer based. This schematic shows a secondary interferometer system with a laser power source which travels the same path and gets reflected back from the reference mirror. A beam splitter could be used to direct the secondary laser into a secondary detector.

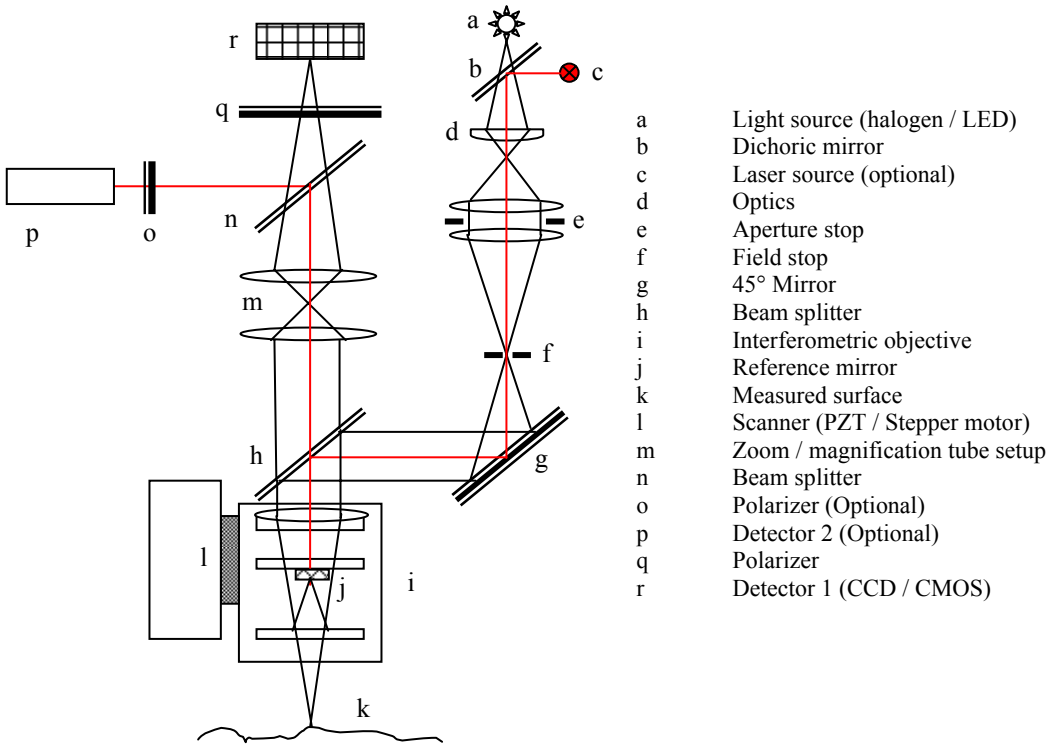

FIGURE 2.1.1: Schematic of a typical coherence scanning interferometer.

Some CSI instruments rely on the scanner for Z accuracy and therefore Z calibration is of prime importance for those systems. The other sources of error could be any hardware that lays on the beam path all the way from the light source to the detector and signal processing and transmission devices between detector to the computer, software algorithms that convert voltage signals to Z heights. The bandwidth of light source, aberrations in relaying and conditioning optics and mirrors, drift and non-linearity of scanner, stability of objective and magnification tube turrets, detector non-linearity, static and dynamic noises in the setup, external vibrations, overall frame stability are possible sources of errors, to name a few. The various calibration standards that would be used for performing the tests described in section 2.2, 2.3 and 2.4 are as described in the following section.

2.1.1. Calibration Standards

2.1.1.1. Silicon Carbide (SiC) Reference Flat Standard

This standard (shown in figure 2.1.2) provides sub-Angstrom level flat reference surface which could be used to map the reference mirror and relay optics form errors (The standard used was certified for RMS 0.37 Angstrom).

FIGURE 2.1.2: Silicon Carbide reference flat standard [97].

2.1.1.2. Step Height Standard

This NIST traceable standard (shown in figure 2.1.3) provides a 100 µm wide, 750 µm long stepped surface etched on quartz and coated with chromium for good reflectivity. At least three step heights are preferable to cover the Z range of interest. It is used for calibration of Z axis scanner of the system. The standards used were certified to 1.81 ± 0.011 µm, 24.23 ± 0.144 µm and 23.874 ± 0.144 µm. This standard also has a pitch pattern which is used for the test described in section 2.3.9.

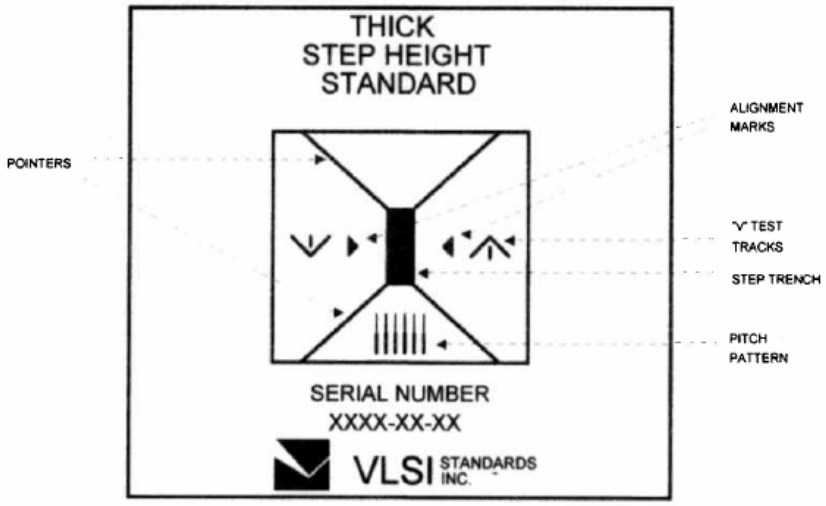

FIGURE 2.1.3: Step height standard [98].

2.1.1.3. Lateral Calibration Standard

This NIST traceable standard (shown in figure 2.1.4) provides patterned surfaces etched on silicon dioxide and coated with platinum. It enables the calculation of magnification of each objective to better precision, resulting in precise lateral measurements. This standard is also used for calculating turret relocation offsets when multiple magnifications are used, but any surface with a well-defined horizontal and vertical edge that could be used to align to a cross hair would suffice. The standard used

was certified for the following pitches 3 ± 0.018 µm, 10 ± 0.020 µm, 30 ± 0.18 µm, 100 ± 0.6 µm, 200 ± 1.3 µm and 500 ± 3.1 µm.

FIGURE 2.1.4: Lateral calibration standard [99].

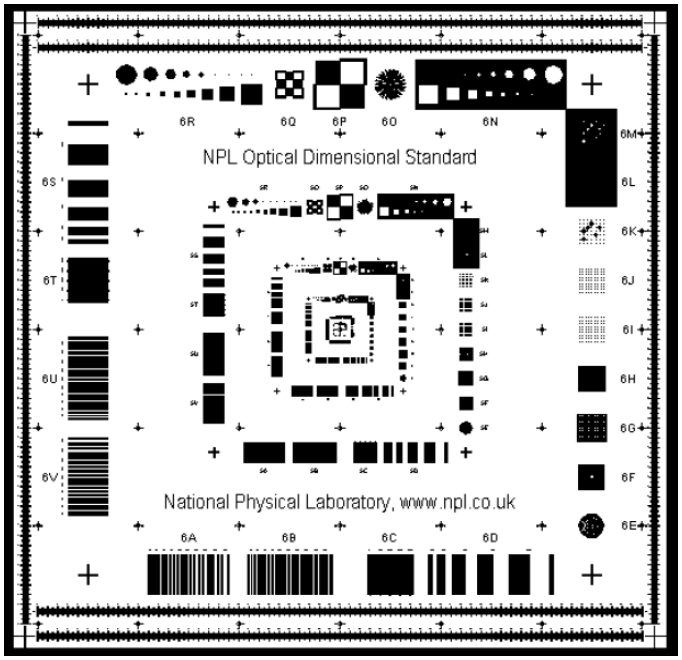

FIGURE 2.1.5: Patterns in optical dimensional standard [100].

2.1.1.4. Optical Dimensional Standard

This NPL traceable standard (shown in figure 2.1.5) is a 100 mm square chrome-on-quartz photo mask that is typically be used for calibration of vision systems. It contains 22 patterns (A through V) in a square ring format repeated six times (1 through 6) at different magnifications to form square concentric rings. Each specific pattern has a

unique alphanumeric code (ex. 6M means clear log-normal array pattern of the outer most ring. Concentric circle pattern 6E could be used to calculate turret offsets and for the test described in section 2.3.1 and 2.4.2, location 6M is used merely as a precision flat surface with good reflectance and any chrome-on-glass patterned surface could be used instead for that purpose. This standard could also be used for lateral calibration.

2.1.1.5. Surface Roughness Reference Standards

These NIST traceable surface roughness and spacing reference standards based on type C (Spacing measurement standards) and D (Roughness measurement standards) of ISO 5436 – 1:2000 [101] are available with different periodic profiles and random profiles (as shown in figure 2.1.6), and roughness values. Depending on the typical product spectrum, it is recommended to select these artifacts to cover the entire vertical range needed. Different profiles are preferable for performing the test described in section 2.3.4, so a selection of sinusoidal, square and random surface roughness reference standards could be used.

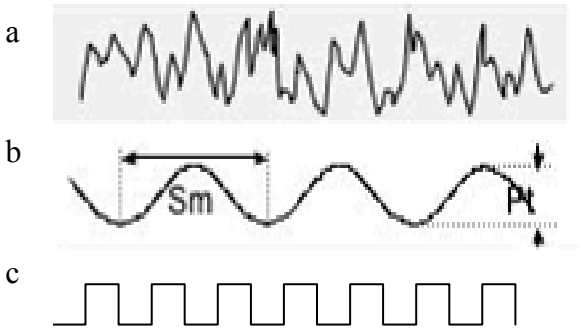

FIGURE 2.1.6: Cross sectional profiles of (a) random surface (b) sinusoidal surface and (c) square wave surface [102].

2.2. Basic Adjustment Steps

2.2.1. Vibration Level

Vibrations generally impact the measurements by convolving actual data and their impact can be seen as ripples or ripples of missing data under high vibration levels, as shown in figure 2.2.1.

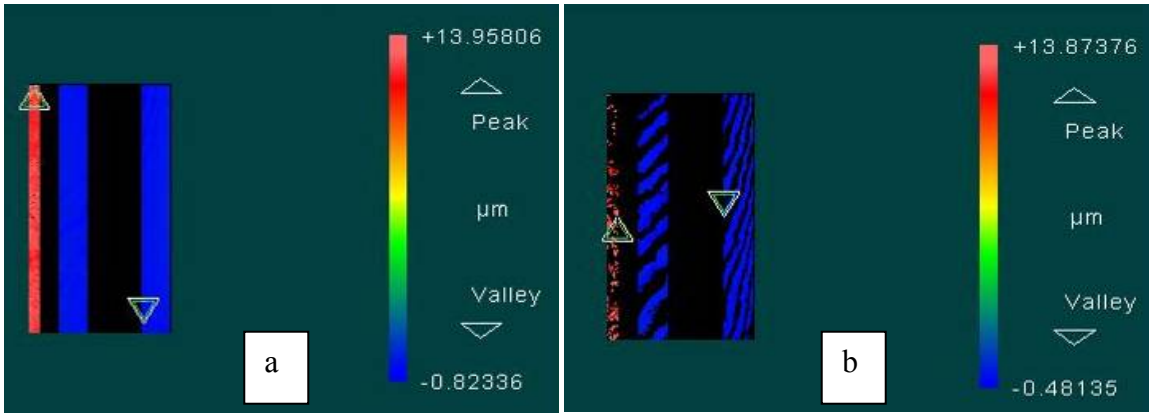

FIGURE 2.2.1: (a) Measurements taken under ideal environment (b) under high vibration levels, seen as ripples of missing data.

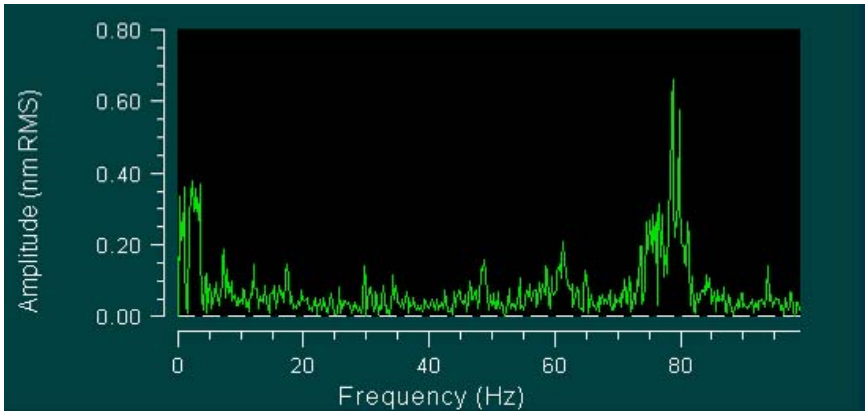

FIGURE 2.2.2: Amplitude Vs. Frequency plot of a vibration on a stable system.

The impact of vibrations partially depends on the algorithm used [103]. Missing data impact the performance of DWT and other interpolation algorithms that might be

used during the fusion process. Ripples impact the performance of kernel based weighted average data fusion methods.

Assuming that only one algorithm is used for a chosen system, the vibration levels have to be tested to ensure it is within the vibration level requirements. The systems vibration limitations are based on scanning speed and the capability of the vibration isolation table. Typically the RMS noise is expected to be below 5 nm. Figure 2.2.2 shows Amplitude –Frequency plot for a system under low vibration levels.

The instrument was placed at three locations, each location susceptible to different vibration levels due to active vibrations from near by systems. Step height on the step height standard was measured 25 times, along with the vibration levels measured using a spindle error analyzer [104]. Figure 2.2.3 shows the linear relationship between measured amplitudes (peak-to-peak) and the repeatability of step height measured.

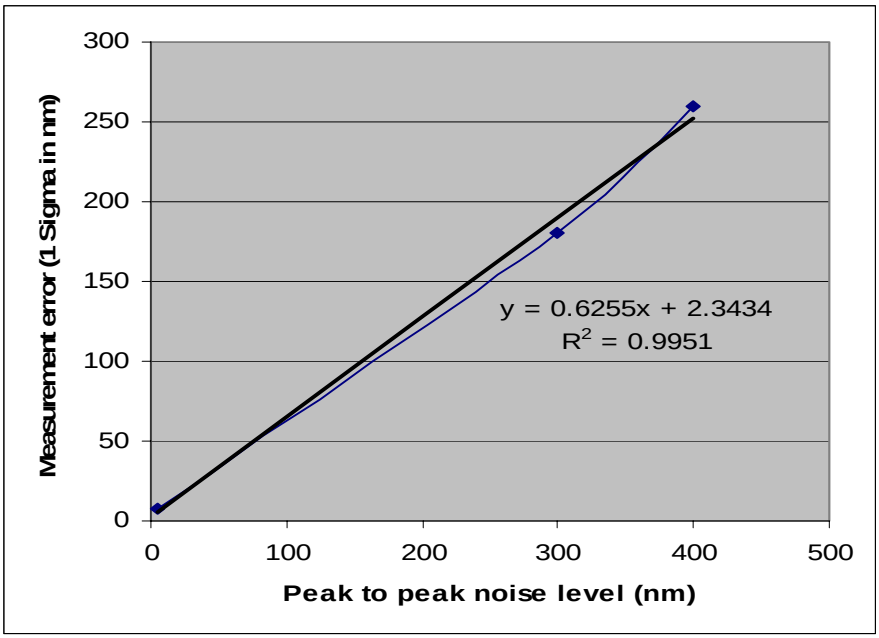

FIGURE 2.2.3: Relation between vibration levels and measurement error.

2.2.2. Z Calibration

The main purpose of the instrument is to make accurate Z measurements, so the calibration of that axis is critical (Some systems use secondary laser source to monitor the actual Z movement, so those systems do not need Z calibration). Care should be taken to select the scan lengths that will be commonly used and the corresponding step height standard. The step height standard should be aligned such that only one fringe occurs on the selected surface area. Masks have to be applied to avoid the edge effects [105]. If possible, objective with the highest numerical aperture (NA) with robust design (some high numerical aperture objectives are tunable, which is not preferred for this step) and the most commonly used scan length are to be used. The central point on the bi-directional scan is to be set such that it is at a nominal center height between the two heights of the step height standard that is being measured. Plane removal is done with respect to the bottom surface. For this test, bottom surface was considered as a reference surface and the top surface as test surface). The masked regions and the run results for a 24 μm step height standard are shown in figure 2.2.4. The standard deviation is taken as the step height measurement repeatability.

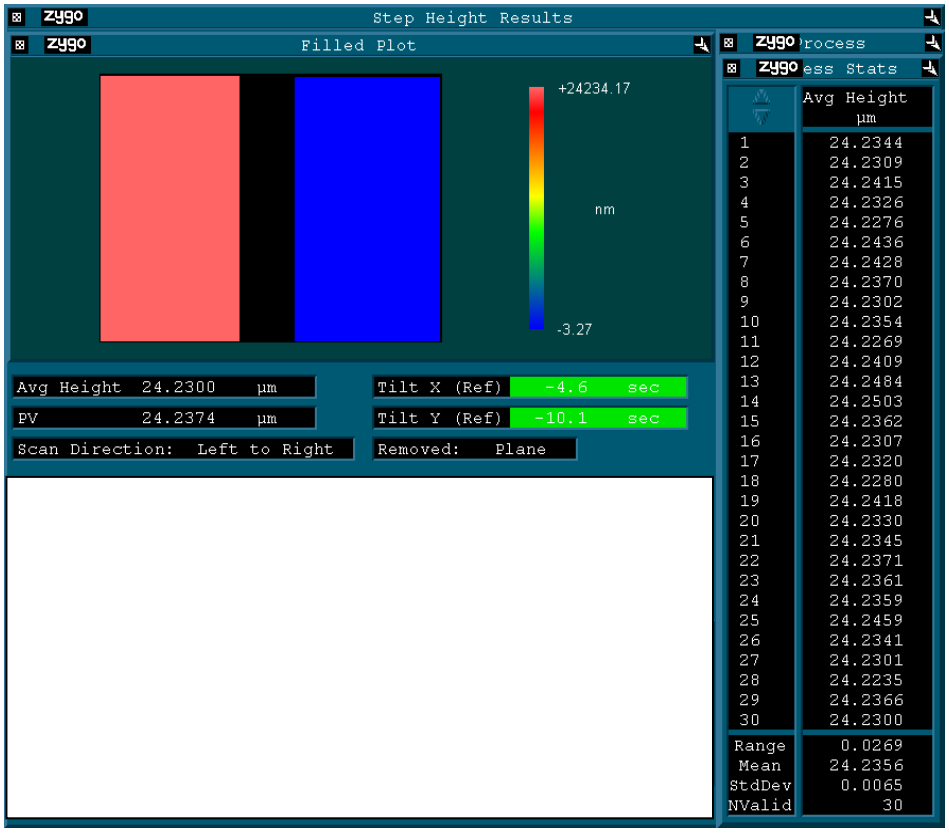

FIGURE 2.2.4: Screen shot of results on 30 measurements taken on 24.23 µm step height standard.

2.2.3. Lateral Calibration

Lateral calibration is to be performed to find the actual magnification of individual objectives along with the possible zoom tube configurations and to convert the pixel spacing into absolute units of measurement. Place the lateral calibration standard at the approximate center of the stage and select the required section of the lateral calibration standard for the objectives to be calibrated. Null the fringes and set the scan location to the optimum focus for individual objective and zoom tube configurations. Some instruments have a built in lateral calibration application which is shown in figure 2.2.5, but the procedure could be easily performed using available edge detection

algorithms in any generic image processing software after converting the datasets into binary images.

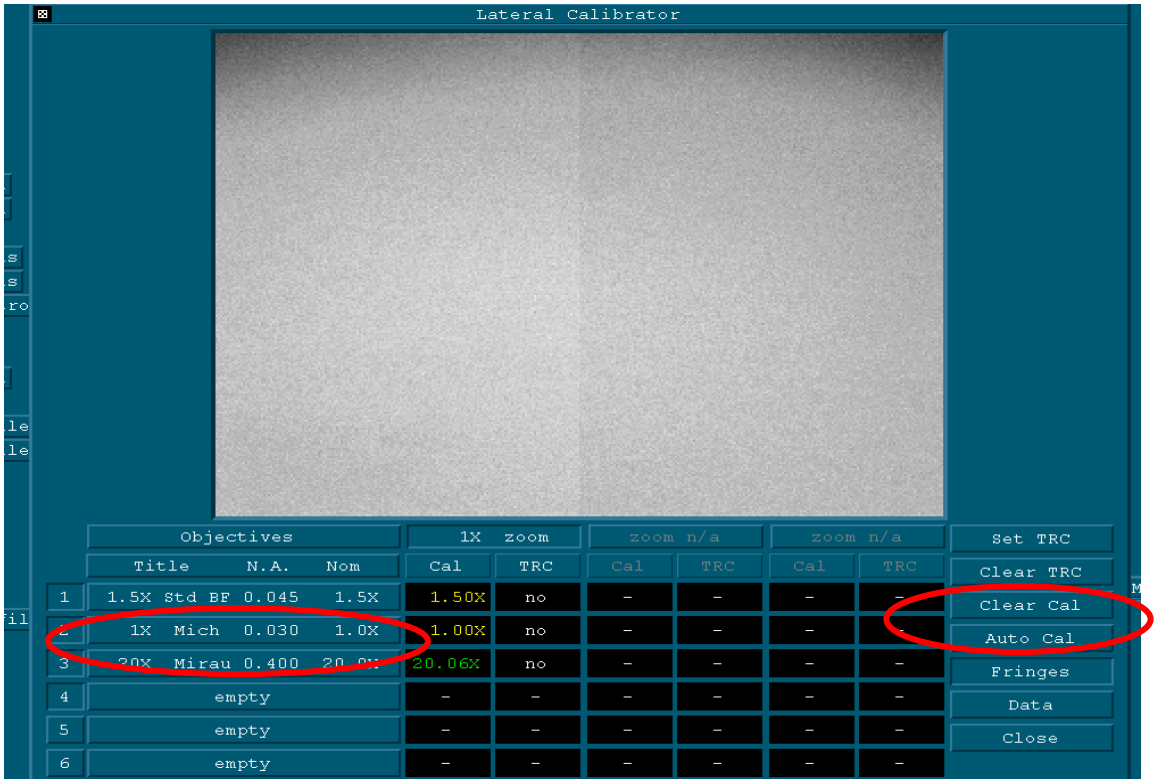

FIGURE 2.2.5: Lateral Calibrator Window.

2.2.4. High Magnification Objective Optimization

Most 50X and above magnifications have the flexibility of tuning to reduce the errors induced to the changes in the optical relay [106] due to external influences. Optimum setting of these magnifications will ensure that both the surface and the fringe come to focus at the same time. One suggested guideline is to fine tune the objective by twisting the objective housing until the surface roughness measured is the maximum, but it is not valid for the entire surface roughness regime. Figure 2.2.6 shows the Pa surface roughness values obtained on 5 different samples (L01 and L15 were selected with a surface roughness range of 25 - 50 nm, M09 and M10 within 50 - 100 nm, and H05 100 -

150 nm). The objective was optimized using an Aluminum-Titanium-Carbon (ALTIC) surface until the obtained surface roughness was ~5 nm. First set of measurements were taken at optimal focus, the second set of measurements were taken at a defocus condition and then the third set of measurement was taken after refocusing the objective. It can be seen that even though the objective was set to optimal focus when the obtained surface roughness was maximal on the ALTIC surface, the measured roughness values on the selected surfaces decreased.

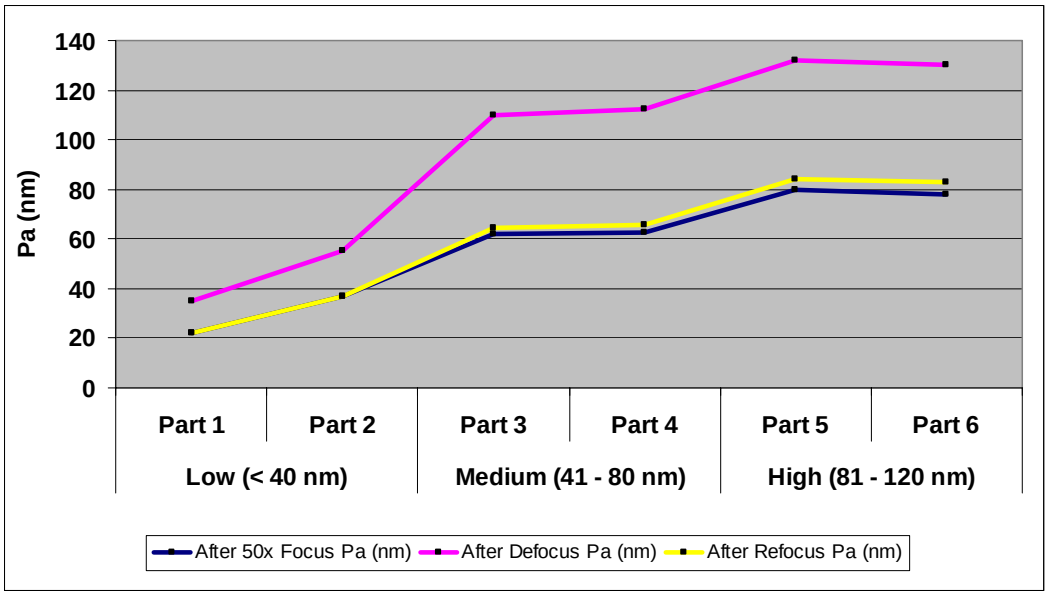

FIGURE 2.2.6: Effect of focus on roughness for selected samples with varying roughness values.

Therefore, it is recommended to track the surface roughness values along with the rotation interval and then reset to either the local minima or maxima. Optimization of high magnification objectives is critical because in most data fusion process, the high frequency portion of the high magnification data is to be fused with the low frequency portion of the low magnification data. When high magnification objective is not at optimal condition, defocus effects alter the instrument transfer function, there by affecting the fidelity of the data obtained using different objectives.

2.2.5. Turret Reference Coordinates

In order to correct for angular and spatial offsets between different magnification configurations, the turret reference coordinates need to be set up, ensuring that the sample surface is centered and in focus. By presetting the turret reference coordinates, the dependence on coarse registration algorithm is reduced. Also, this test enables the estimation of expected translational and angular misalignment due to rotary turrets. The offsets are calculated with respect to the most commonly used magnification configuration, and therefore this process is initiated with that magnification configuration. (Before starting this process, it is preferable to warm up the objective and zoom tube turrets by rotating them for a couple of rotations). One edge of a square pattern in the lateral calibration standard is taken and one corner is positioned such that it aligns with the intersection point of the cross hairs and the two edges align with the cross hairs placed in the field of view. For each magnification configuration, the fringes are nulled to the top surface of the square and then realigned to match the cross hairs, as shown in figure 2.2.7. The X, Y offsets and θ, Φ offsets from the commonly used magnification configuration are noted.

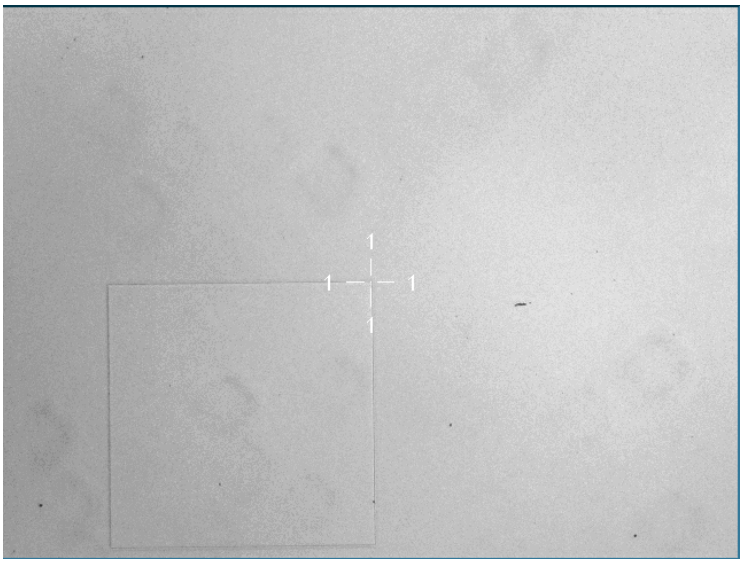

FIGURE 2.2.7: Image of one corner of Lateral calibration standard used for finding offset between different magnifications.

2.2.6. Reference Mirror Flatness Test

In order to reduce the errors induced by variations on the reference mirror and optical relay systems alignment and aberrations [107, 108], a temporal average of the reference mirror surface measurement could be subtracted from individual measurements. This reference mirror measurement has to be performed on each magnification configuration. A SiC optical flat standard free of surface defects and dents is aligned such that the fringes are nulled. Then multiple measurements are taken separated by correlation length and then averaged to obtain the map of the reference flatness mirror for that magnification configuration, as shown in figure 2.2.8. The reference mirror measurement is used to reduce the error induced in the shape of the measurand. Since the datasets will be obtained using two different magnifications, if fusion is performed on raw data without this error correction, it will result in erroneous fusion of the low frequency portion of the data.

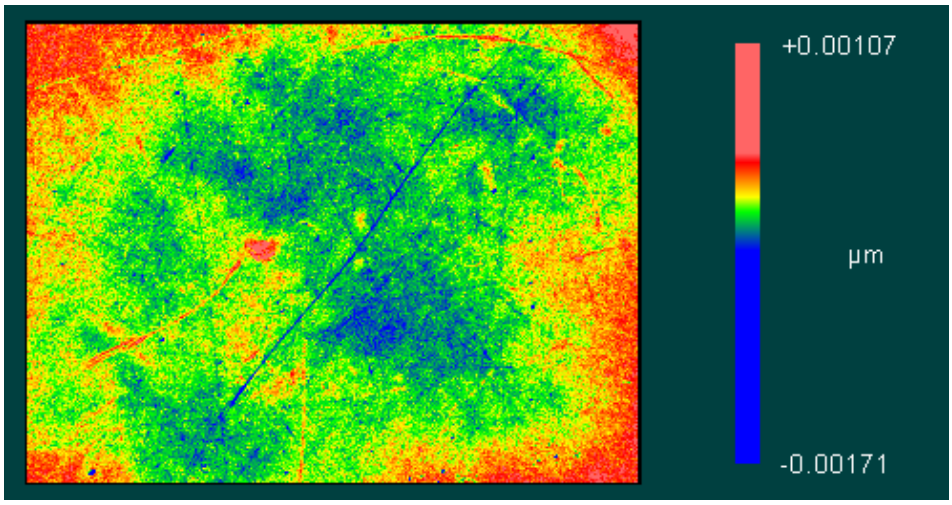

FIGURE 2.2.8: Reference mirror surface error map for a chosen magnification (objective and zoom tube combination).

Calibration of X, Y and Z axes and optimization of focus for high magnification objectives forms the basic operations needed to ensure data fidelity across magnifications. Reference mirror flatness test enables to quantify relay optics errors and account for those while measuring smooth and flat surfaces. Turret reference coordinates test enables to reduce the translational and rotational offset between different magnification settings. System vibration level testing quantifies the system baseline capability. After calibration of individual axes, the next step is to quantify errors. The systematic errors could be quantified and used to adjust the measurements. The next section discusses the error sources impacting mainly the Z axis, followed by another section detailing the error sources impacting X and Y axes.

2.3. Z-axis Based Errors

2.3.1. Repeatability (Regular and Auto Focus)

Repeatability of the system establishes the baseline capability of the system and in turn, the uncertainty of the data fusion process. In order to quantify the repeatability of the system under regular measurement conditions and while using 'auto focus' option, optical dimensional standard at location 6M is used (any optical standard with chrome plated circle pattern could be used instead). Thirty measurements are taken in a sequence with 'auto focus' option turned on and next set of thirty measurements are taken with 'auto focus' option turned off. All chrome coated surfaces are masked, as shown in figure 2.3.1 (regions filled with golden yellow color are considered and area inside of circles are not considered for further analysis) and no plane removal is done. If plane removal is chosen, then the results will mainly show the system's dynamic noise and not the z axis repeatability. Average different between successive measurements will show the z offset between measurements, therefore surface roughness parameter Sa is calculated on the difference between two successive measurements, as shown in figure 2.3.2. The obtained Sa values are shown in figure 2.3.3.

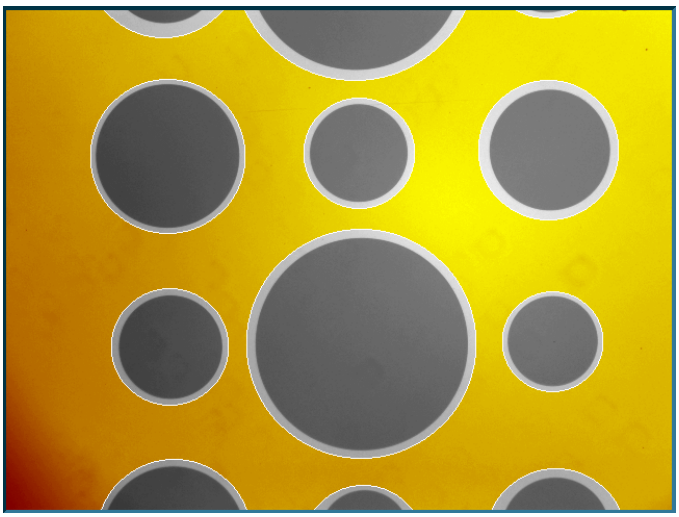

FIGURE 2.3.1: Image obtained on 6M location in NPL optical dimensional standard, regions masked for further analysis.

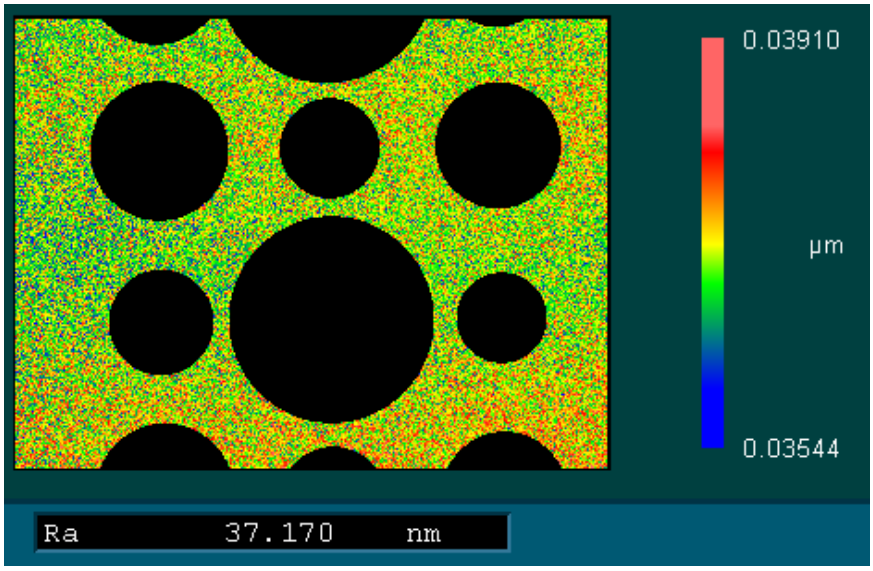

FIGURE 2.3.2: Map of difference between successive measurements.

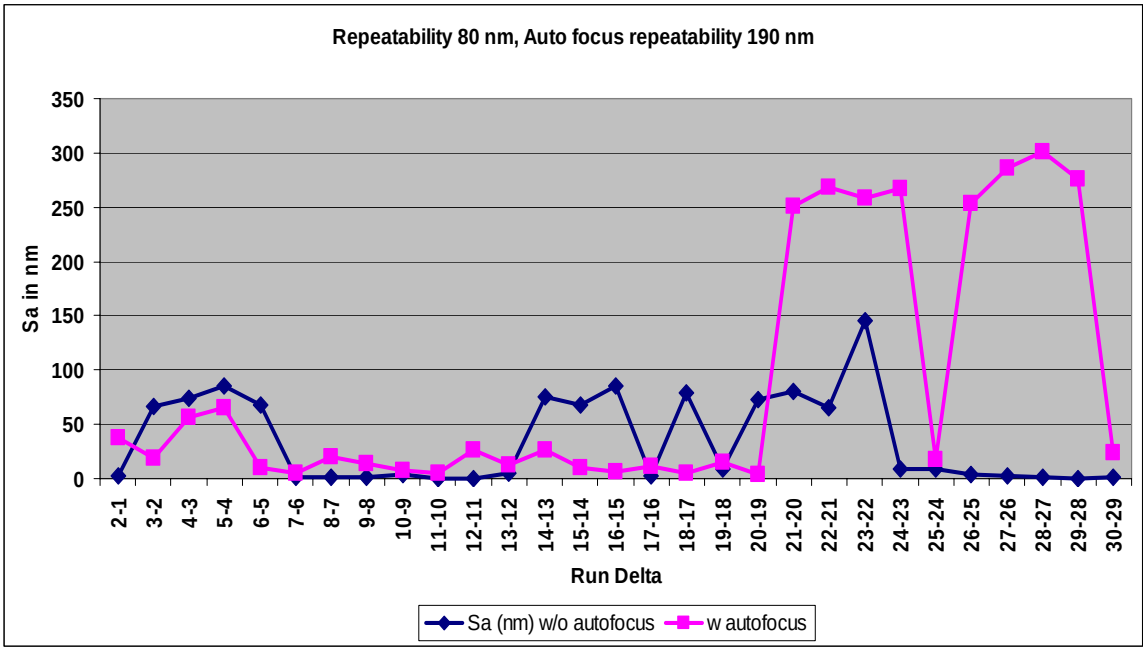

FIGURE 2.3.3: Deviations in height between successive measurements.

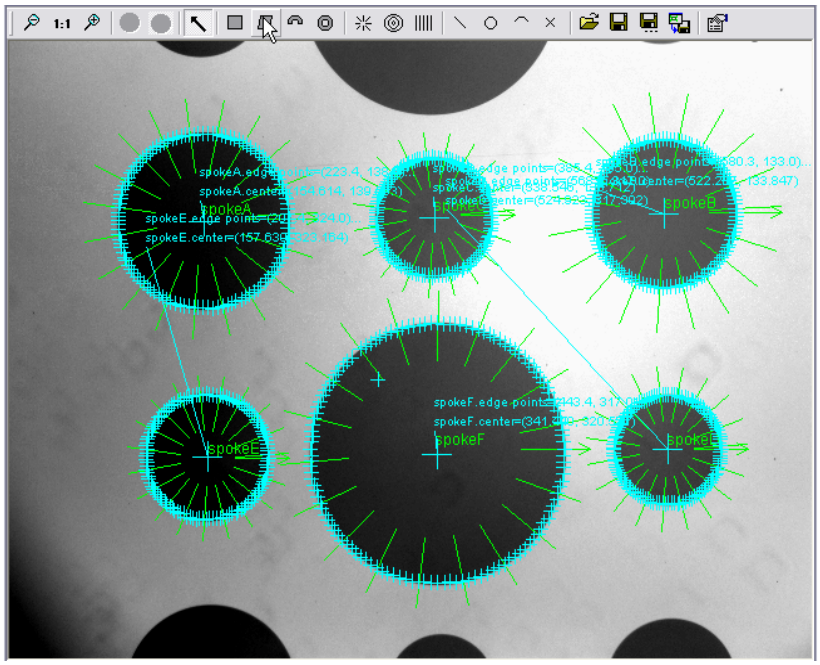

FIGURE 2.3.4: Circles analyzed using Sherlock ® [109] software for diameters and center coordinates.

The sum of average and one standard deviation of 29 difference measurements is taken as the Z stage repeatability [95]. Sum of squares method is used to calculate the impact of auto focus measurements. In order to calculate the impact on dimensional measurement, the 50 datasets (25 without 'autofocus' and 25 with 'autofocus') were converted to image format and six different circles within the field-of-view (as shown in figure 2.3.4) were analyzed for diameter and center coordinates, as shown in figure 2.3.5.

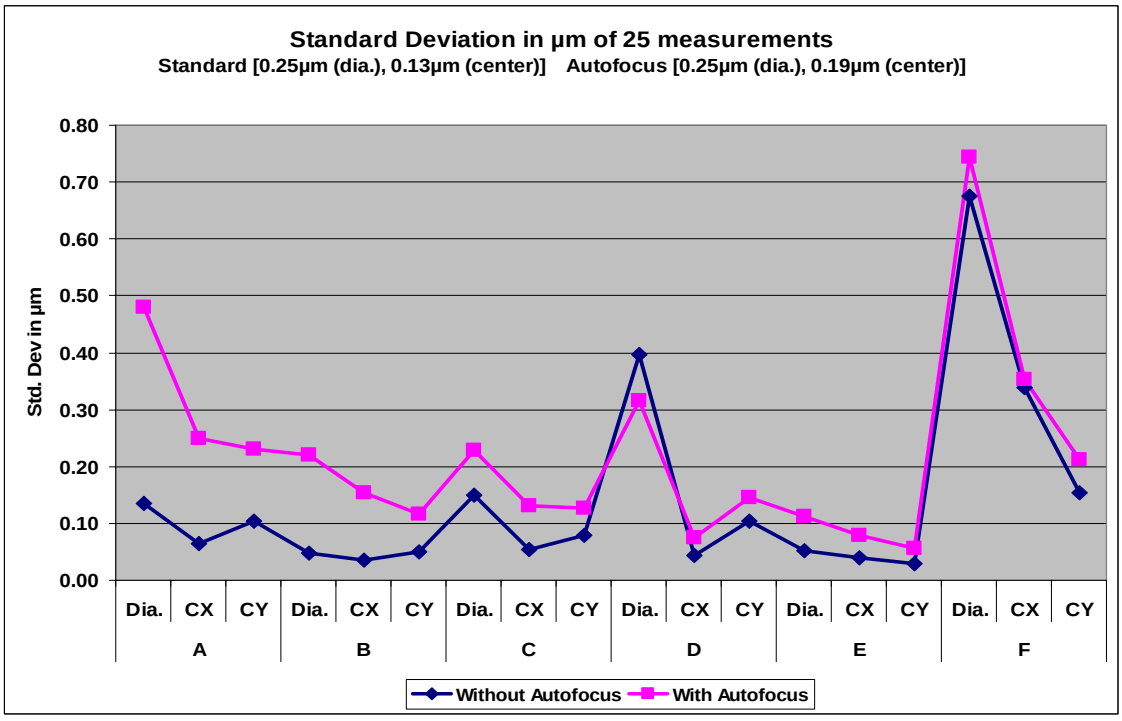

FIGURE 2.3.5: Standard deviations of circle diameters and centers for 25 measurements.

The root sum of squares of standard deviations of six circles from first set (25 datasets measured without 'autofocus' option) of measurements is taken as standard repeatability (σ_S) and then corresponding value (σ_T) is calculated for second set of measurements (25 datasets with 'autofocus' option). Impact of autofocus on repeatability (σ_{AF}) is given by $\sigma_{AF} = \sqrt{\sigma_T^2 - \sigma_S^2}$

It should be noted that the repeatability depends on various factors like scan length, surface reflectivity and roughness etc. So, care should be taken to ensure that appropriate surface samples are used to conduct this test. Figure 2.3.6 shows the difference between successive measurements of optical dimensional standard. In the figure, it can be noticed that the variations are significantly different on chrome (background) and non-chrome (circular areas) surfaces. This demonstrates the fact that the uncertainty involved with data fusion pertaining to surfaces with non-uniform optical properties will also be non-uniform.

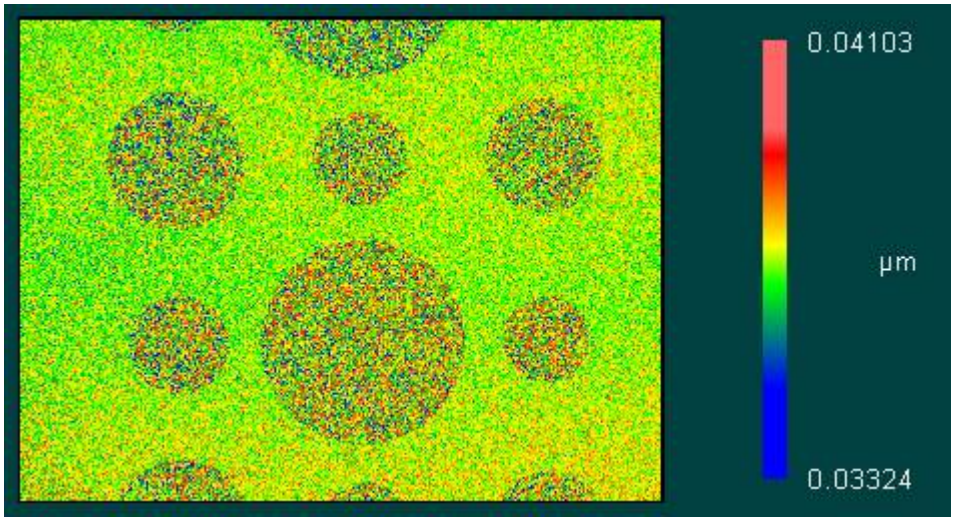

FIGURE 2.3.6: Plot showing the difference between successive measurements on chrome surface with non-chrome circular areas.

2.3.2. Scan Length

Some CSI systems use Piezoelectric Transducer (PZT) based scanner and for each scan length, a specific ramp file (a ramp file is the map of the non-linearity of the PZT) could be used. Z calibration is generally performed using one specific scan length, so other scan lengths have to be characterized. Z scaling error between the standard scan length to different available scan lengths, for different magnifications needs to be

established. An average of five measurements is taken for on three different step height standards (1.816, 23.847 and 49.094 μm) using different scan lengths (5, 10, 20, 40, 65, 100 and 150 μm) and magnifications (2.5X, 10X and 50X objectives with 0.5X, 1.0X and 2.0X zoom tubes). For each magnification, 100 μm scan length is taken as the standard and the scaling ratios are calculated, as shown in Table 2.3.1.

TABLE 2.3.1: Scan length based z scaling errors for chosen magnifications (objective and zoom tube combinations).

	Scan Length	Obj 2.5x			Obj 10x			Obj. 50x
		Zoom 0.5x	Zoom 1.0x	Zoom 2.0x	Zoom 0.5x	Zoom 1.0x	Zoom 2.0x	Zoom 0.5x
Step Ht 1.816μm	5	1.811	1.813	1.809	1.813	1.816	1.815	1.816
	10	1.813	1.812	1.810	1.814	1.816	1.815	1.817
	20	1.813	1.813	1.812	1.814	1.816	1.814	1.815
	40	1.811	1.811	1.810	1.814	1.815	1.814	1.815
	65	1.810	1.810	1.807	1.813	1.814	1.814	1.815
	100	1.809	1.809	1.807	1.812	1.813	1.813	1.813
	150	1.810	1.809	1.806	1.811	1.811	1.811	1.812
Step Ht 23.847μm	5	-	-	-	-	-	-	-
	10	-	-	-	-	-	-	-
	20	-	-	-	-	-	-	-
	40	-	-	-	-	-	-	-
	65	23.925	23.922	23.937	23.926	23.929	23.927	23.925
	100	23.915	23.905	23.922	23.915	23.915	23.913	23.914
	150	23.907	23.895	23.917	23.907	23.904	23.902	23.904
Step Ht 49.094μm	5	-	-	-	-	-	-	-
	10	-	-	-	-	-	-	-
	20	-	-	-	-	-	-	-
	40	-	-	-	-	-	-	-
	65	-	-	-	-	-	-	-
	100	49.006	49.007	48.989	48.977	48.967	48.966	48.897
	150	48.995	48.998	48.975	48.963	48.953	48.952	48.886
Ratio wrt 100μm scan	5	1.0011	1.0021	1.0011	1.0006	1.0015	1.0014	1.0014
	10	1.0019	1.0013	1.0014	1.0010	1.0018	1.0012	1.0019
	20	1.0022	1.0021	1.0025	1.0009	1.0019	1.0008	1.0011
	40	1.0012	1.0008	1.0015	1.0009	1.0010	1.0006	1.0012
	65	1.0005	1.0006	1.0004	1.0005	1.0007	1.0005	1.0008
	100	1.0000	1.0000	1.0000	1.0000	1.0000	1.0000	1.0000
	150	1.0000	0.9996	0.9996	0.9995	0.9995	0.9994	0.9996

2.3.3. NA Correction Factor

After the Z calibration factor is calculated for the chosen objective, correction factors [110-113] for other objectives have to be calculated. These correction factors are needed to ensure that there is high correlation between data obtained using multiple objectives, which is very crucial to ensure the fidelity of data fusion process. A chosen step height (49.094 μm) is aligned; scan location and masks are set according to best

practices detailed for Z calibration. Step height is measured using different magnification (2.5X, 10X and 50X objectives along with 0.5X, 1.0X and 2.0X zoom tubes) and average of 20 measurements is taken and then the correction factor (ratio between the calculated heights to the height measured using magnification used for Z calibration) with respect to 10X magnification (10X objective and 1.0X zoom tube) is calculated accordingly, as shown in Table 2.3.2.

TABLE 2.3.2: NA Correction factor for chosen magnifications with respect to 10X objective and 1X zoom.

	Average Step Height in µm					
	Obj. 2.5x		Obj. 10x			Obj. 50x
Run No.	Zoom 1x	Zoom 2x	Zoom 0.5x	Zoom 1x	Zoom 2x	Zoom 0.5x
1	48.9593	48.9593	48.9624	48.9601	48.9602	48.9618
2	48.9649	48.9608	48.9635	48.9546	48.9600	48.9621
3	48.9643	48.9639	48.9612	48.9541	48.9673	48.9626
4	48.9639	48.9620	48.9667	48.9529	48.9569	48.9710
5	48.9591	48.9614	48.9639	48.9528	48.9641	48.9693
6	48.9596	48.9643	48.9634	48.9587	48.9612	48.9667
7	48.9637	48.9652	48.9627	48.9537	48.9642	48.9611
8	48.9617	48.9669	48.9630	48.9565	48.9630	48.9660
9	48.9560	48.9578	48.9658	48.9532	48.9667	48.9684
10	48.9589	48.9578	48.9714	48.9522	48.9623	48.9646
11	48.9598	48.9653	48.9653	48.9590	48.9625	48.9635
12	48.9577	48.9571	48.9662	48.9581	48.9618	48.9618
13	48.9668	48.9617	48.9614	48.9569	48.9614	48.9666
14	48.9621	48.9685	48.9620	48.9552	48.9582	48.9593
15	48.9587	48.9693	48.9673	48.9536	48.9632	48.9648
16	48.9590	48.9670	48.9666	48.9532	48.9633	48.9686
17	48.9662	48.9649	48.9664	48.9549	48.9634	48.9654
18	48.9627	48.9620	48.9687	48.9566	48.9646	48.9604
19	48.9634	48.9648	48.9659	48.9512	48.9608	48.9638
20	48.9617	48.9691	48.9645	48.9597	48.9676	48.9655
average	48.9615	48.9635	48.9649	48.9554	48.9626	48.9647
std. dev	0.0030	0.0038	0.0026	0.0027	0.0028	0.0032
NAC	1.0001	1.0002	1.0002	1.0000	1.0001	1.0002

2.3.4. Algorithms

Different algorithms [114-117] accommodate different levels of vibrations, and phase skewing effects. Therefore, there is a need to evaluate different algorithm options available on the system. Various disceprencies have been documented between

measurements taken on same surface using multiple technologies [118, 119]. Tests have also shown that the differences between technologies do not produce a similar effect for different surface roughness ranges [120]. Hence it is generally not recommended to fuse data obtained using different algorithms. In situations where this is unavoidable, it is recommended to use this test to establish the expected error. To quantify the impact of algorithms, random surface roughness reference specimen standards (30, 100 and 150 nm Ra specimens), sinusoidal shaped periodic profile reference specimen standards (60 and 100 nm wavelength spacing) and square wave shaped pitch standard (40 nm step height) were measured using three different algorithm modes (High2G, High, Normal and Low are the four available options on NV6300® system by Zygo Corp. For this test, only High2G, High and Normal were used). Figure 2.3.7 shows the difference in profile plots obtained on the square wave standard using three different modes. Mode 3 shows significant edge transition errors. .Figure 2.3.8 shows profile plots of random surface roughness specimen with 150 nm Ra, measured under three different modes. Figure 2.3.9 shows the measured Ra values of three random surface roughness specimens (30, 100 and 150 nm). From the graph, it can be seen that the there is no consistent bias measured Ra values between different algorithm modes. Figure 2.3.10 shows the difference between three modes on all the standards used. Average of these deviations is taken as the impact of surface roughness on algorithm.

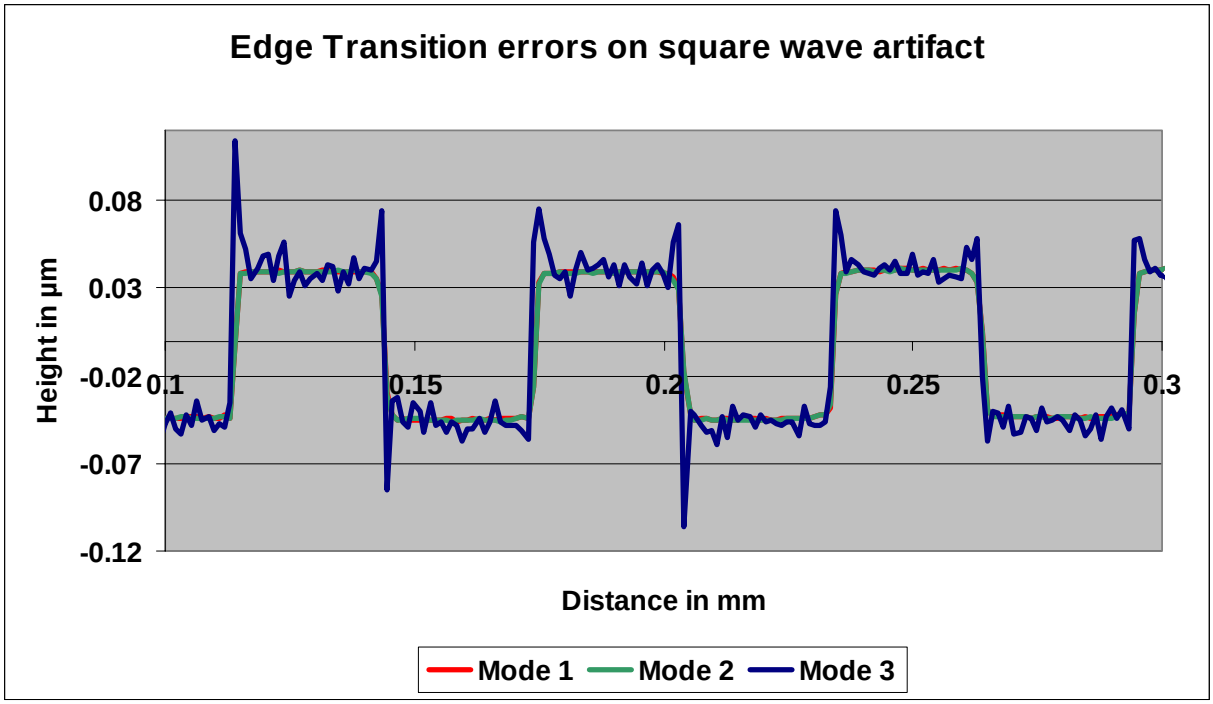

FIGURE 2.3.7: Surface profiles obtained on square wave standard using different algorithm settings.

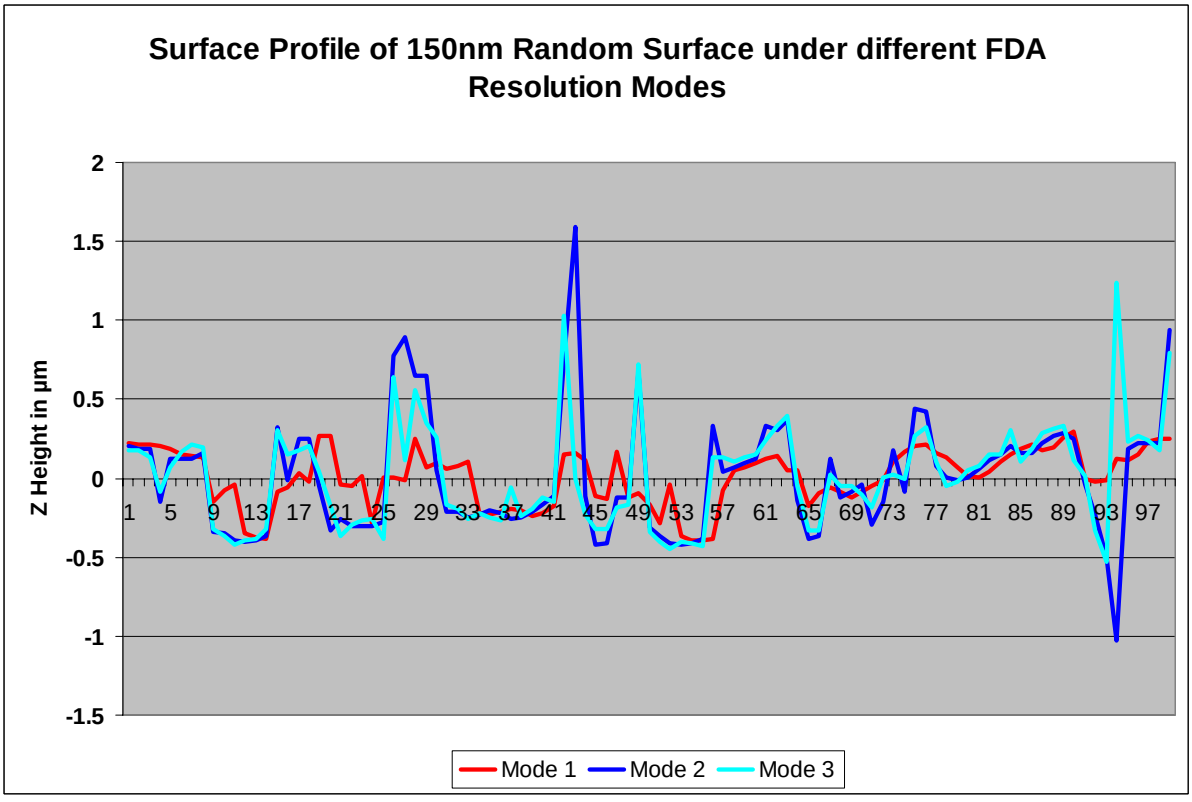

FIGURE 2.3.8: Surface profiles obtained on 150 nm random surface standard using different algorithm settings.

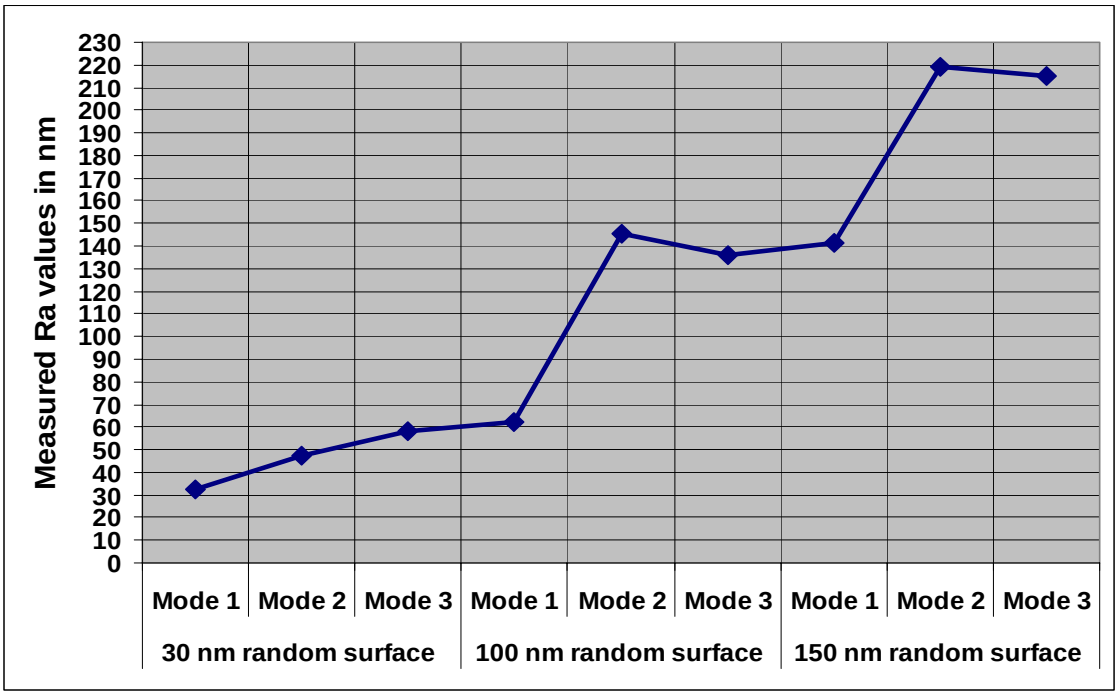

FIGURE 2.3.9: Measured Ra values on different random surface standards using different algorithm modes.

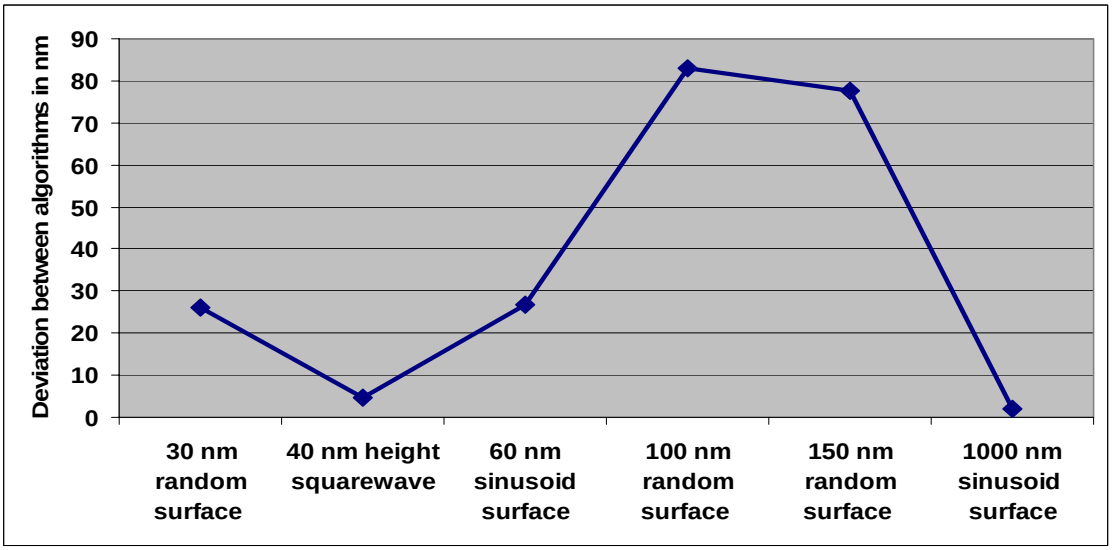

FIGURE 2.3.10: Deviations in Ra values on different random profile surface standards using different algorithm modes.

2.3.5. Noise

In order to calculate the instrument's noise level, SiC optical flat standard is measured 26 times using the preferred objective and zoom tube combination along with the preferred scan length. This test is to be performed after ensuring proper alignment / optimum null cavity and optimal focus. It is also recommended that a least squares plane be removed from the data. Differences between successive data sets are calculated and for those difference of datasets, ISO flatness, tilt along *X* and *Y* axis are calculated, as shown in table 2.3.3. ISO flatness is the envelope containing the data points, therefore could be treated as the maximum difference between successive measurements. Peak-to-Valley (PV) value also could be used, but PV would provide vertical difference whereas ISO flatness would provide orthogonal distance from the least squares plane fitted to the surface, thereby compensating for the tilt. This methodology enables separation of angular variations from the vertical noise. The average of these 25 ISO flatness and tilt values are taken as the error contribution due to a combination of system static noise, dynamic noise and environmental noise.

TABLE 2.3.3: ISO Flatness and tilt variation between successive scans on SiC standard.

Run Delta	ISO Flatness (nm)	Tilt X (°)	Tilt Y (°)
2-1	4.9650	0.0000	0.0000
3-2	5.0670	-0.0001	0.0000
4-3	6.6150	0.0000	0.0000
5-4	6.8290	0.0000	0.0000
6-5	6.4690	0.0000	0.0000
7-6	4.9700	0.0000	0.0000
8-7	5.0620	0.0000	0.0000
9-8	5.4460	0.0001	0.0000
10-9	4.4510	0.0000	0.0000
11-10	6.6840	0.0000	0.0000
12-11	3.8630	0.0000	0.0000
13-12	4.3430	0.0000	0.0000
14-13	5.1160	0.0001	0.0000
15-14	5.9300	0.0000	0.0000
16-15	5.4250	0.0000	0.0000
17-16	4.7220	0.0000	0.0000
18-17	5.0210	0.0001	0.0000
19-18	5.6500	0.0001	0.0000
20-19	5.5170	0.0000	0.0000
21-20	5.9240	0.0001	0.0000
22-21	5.1920	0.0000	0.0000
23-22	5.2050	0.0001	0.0000
24-23	4.3150	0.0000	0.0000
25-24	5.5530	0.0000	0.0000
26-25	5.0520	0.0000	0.0000
26-1	7.8880	0.0012	-0.0005
Average	**5.3354**	0.0000	0.0000

2.3.6. Z Non-linearity

Z calibration coefficient does not account for non-linearity in the Z stage's scanner [121-125]. In order to calculate the Z non-linearity, a SiC optical flat standard is placed at an inclination such that the measured Z heights would cover the entire scan length. The high contrast fringe is focused at the center of the field of view for the first set of ten measurements (multiple measurements are taken to reduce the impact due to dynamic noise and vibration induced errors) and then the Z stage is moved by one fringe up for the second set of ten measurements and one fringe down for the third set of ten measurements. The test is repeated with the standard rotated by 90°. The standard is tiled in the opposite direction and the next set of measurements is taken followed by

another set of measurements after the standard is rotated by 90°. The differences between the three measurements are calculated (as shown in figure 2.3.11) and then an average of those two datasets is calculated. The average of eight PV values is taken as the contribution of the Z scanner's non-linearity towards measurement uncertainty.

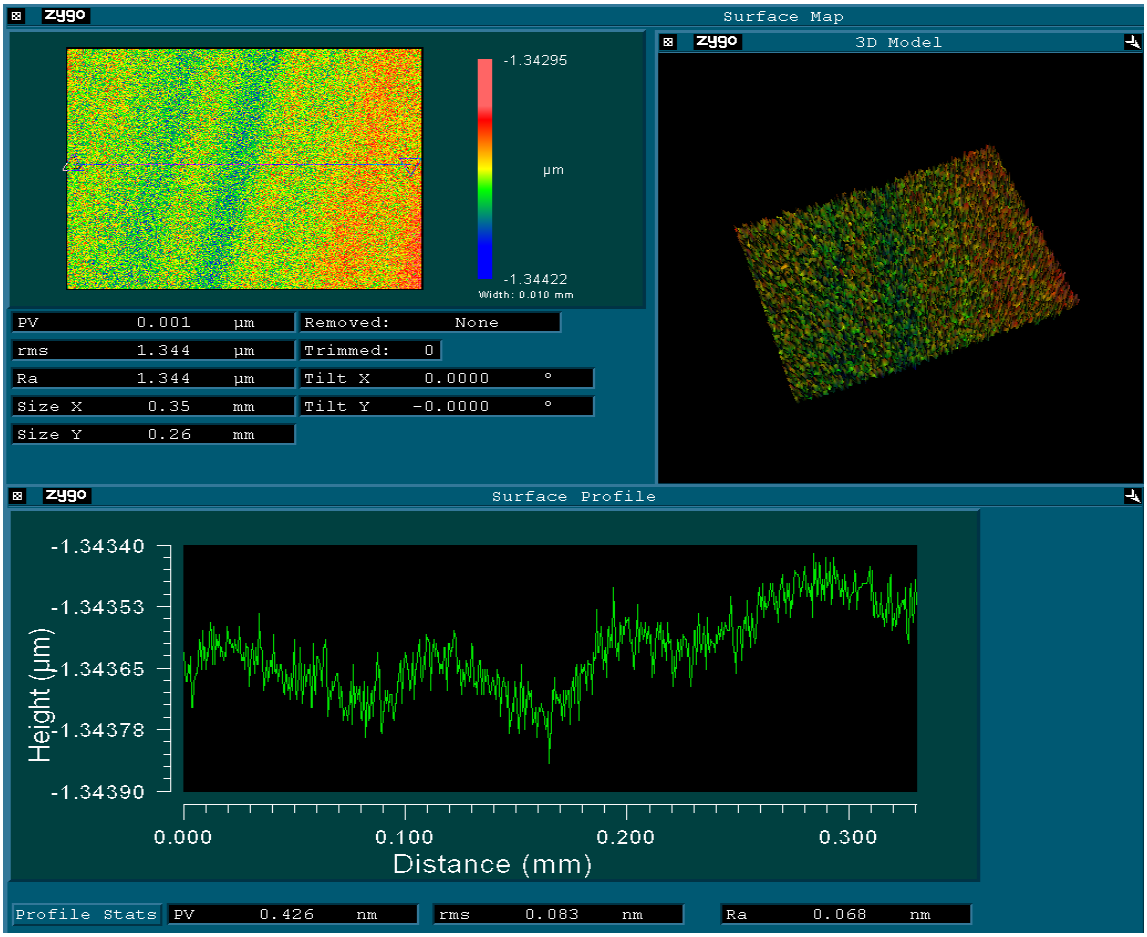

FIGURE 2.3.11: Difference between two measurements taken at different Z heights.

2.3.7. Focus Errors

When the surface is not under optimal focus condition [126, 127], errors are induced in the shape of the measured surface. So, it is recommended to ensure that best practices are used while obtaining multiple magnification measurements. Turret

reference coordinate system setup reduces the impact but does not eliminate the need for this error. The impact partially depends on the surface roughness, surface lateral and vertical heights. 1.8 µm step height standard is positioned such that only the bottom surface of the standard in the field of view. First measurement is taken with the surface at optimal focus (as shown in figure 2.3.12a) and then second measurement is taken at a Z offset of +25 µm. The difference between both measurements is shown in figure 2.3.12b. ISO flatness of the difference is taken as the contribution of out-of-focus towards measurement uncertainty for nominally flat surfaces.

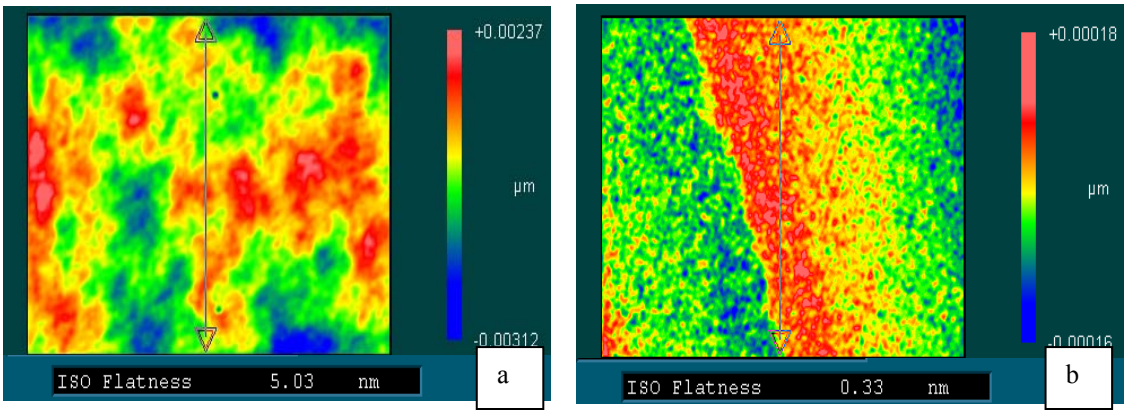

FIGURE 2.3.12: (a) Surface map of bottom surface of 1.8 µm step height standard at optimal focus (b) Height differences from (a) when measured at 25 µm Z offset.

The standard is then repositioned such that both the top and bottom surfaces can be measured. First measurement is taken after top surface is focused and fringes are nulled on that surface. Plane removal is performed using top surface as the reference surface. Second measurement is taken at approximately 20 µm above this point and third measurement is taken at approximately 20 µm the focus point. The difference between these three surfaces is shown in figure 2.3.13.

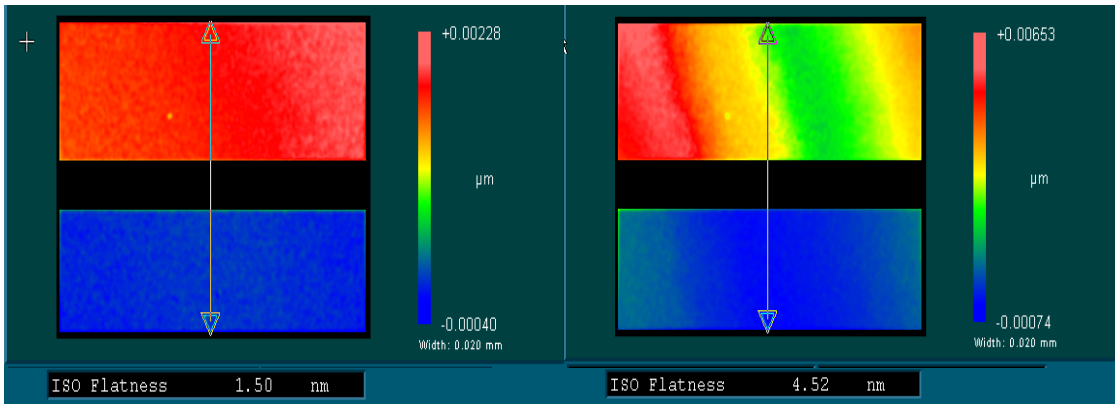

FIGURE 2.3.13: Step height differences on 1.8 µm step height standard, due to measurements taken at different focus heights.

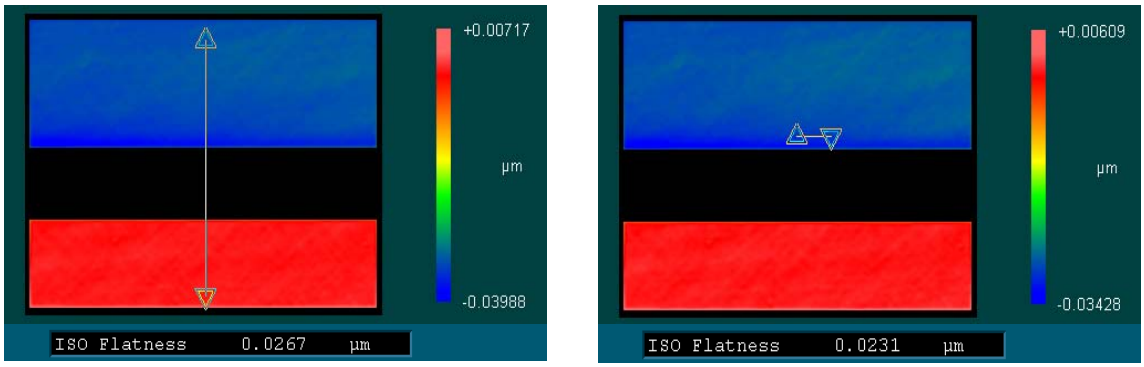

FIGURE 2.3.14: Step height differences on 49.09 µm step height standard, due to measurements taken at different focus heights.

Since plane removal was performed on all three datasets using the top surface as the reference, it is expected that on the difference measurements, one surface would be nominally zero, but due to errors induced because of out-of-focus condition, both top and bottom surfaces are not at the nominal location. The same process is repeated on 49.09 µm step height standard and the results are shown in figure 2.3.14. Average of ISO flatness calculated from these difference datasets is taken as the contribution of out-of-focus conditions for stepped surfaces.

2.3.8. Dissimilar Materials

Unaccounted phase changes [128, 129] occur if dissimilar material surfaces are measured together. If the same kind of surface configuration is routinely measured, then the sample surface could be sputter coated with one uniform metal coating and then measured. Figure 2.3.15 shows a sample surface with two copper pads above a layer of dielectric. The step height between the copper layer and dielectric layer of five samples are measured under normal conditions and after sputter coating. The difference between the heights obtained before and after coating is taken as the error induced due to measurement of materials with dissimilar optical properties, as shown in table 2.3.4.

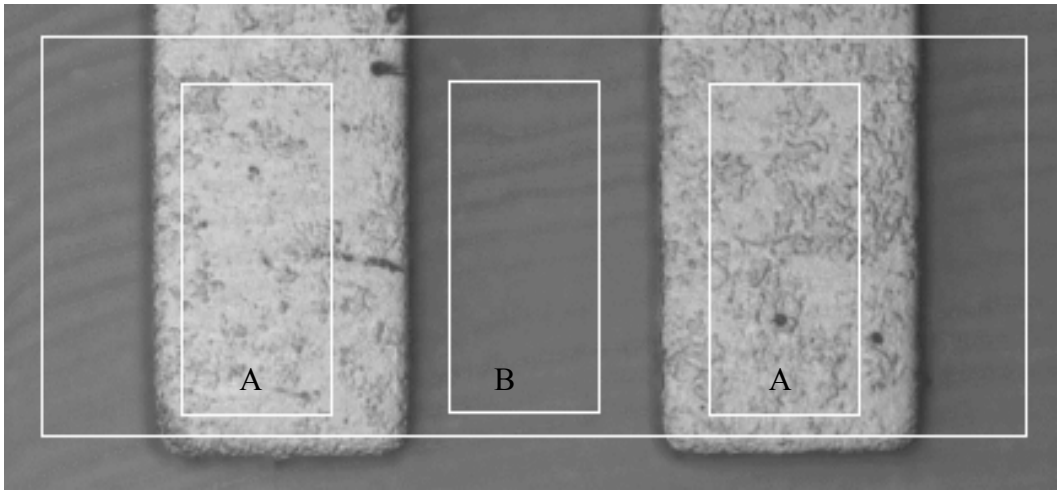

FIGURE 2.3.15: Sample surface showing two copper reference surfaces (A) with respect to which dielectric surface (B) is measured.

TABLE 2.3.4: Step height differences measured on five samples before and after sputter coating.

Sample No.	Step Height in µm		
	Before Coating	After Coating	Delta
1	12.3062	12.3021	0.0041
2	12.3067	12.3017	0.0050
3	12.3063	12.3021	0.0042
4	12.3067	12.3012	0.0055
5	12.3068	12.3025	0.0043
	Average		0.0046

2.3.9. Environmental Changes

It is good practice to obtain multiple magnification measurements within least time interval between measurements. But for some experiments, like those involved with wear studies, long delay between measurements is inevitable. For these kinds of datasets, impact of environmental changes needs to be factored in. In order to account for errors induced due to environmental changes like temperature, humidity and pressure, instead of trying to find individual contributions, an all-inclusive approach is taken. The 24.23 µm step height standard is used for this test, but instead of the regular location, the pitch pattern location is used. Step height of the top surface is measured with respect to bottom surface on either side (as shown in figure 2.3.16a) and width is calculated on the image generated by converting height values to normalized intensity values (as shown in figure 2.3.16b).

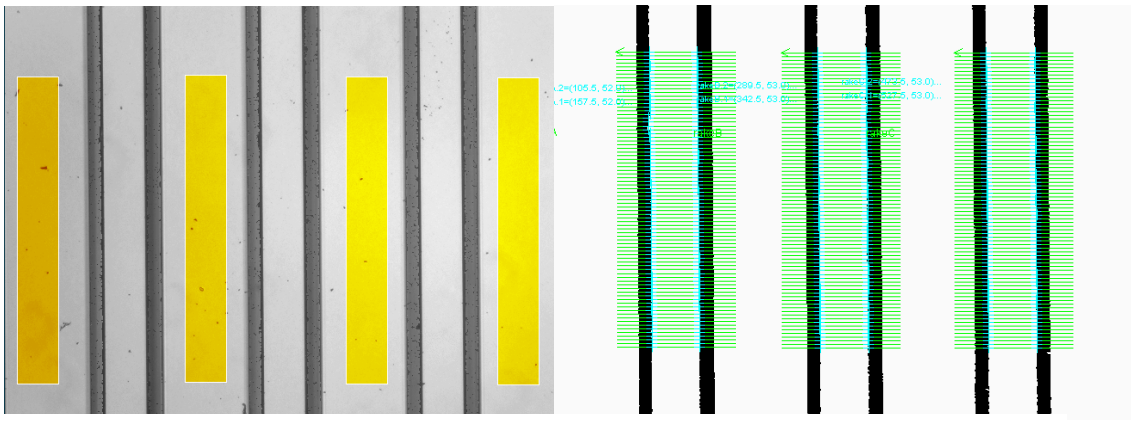

FIGURE 2.3.16: (a) Reference masks on the pitch pattern location (b) Width measurement.

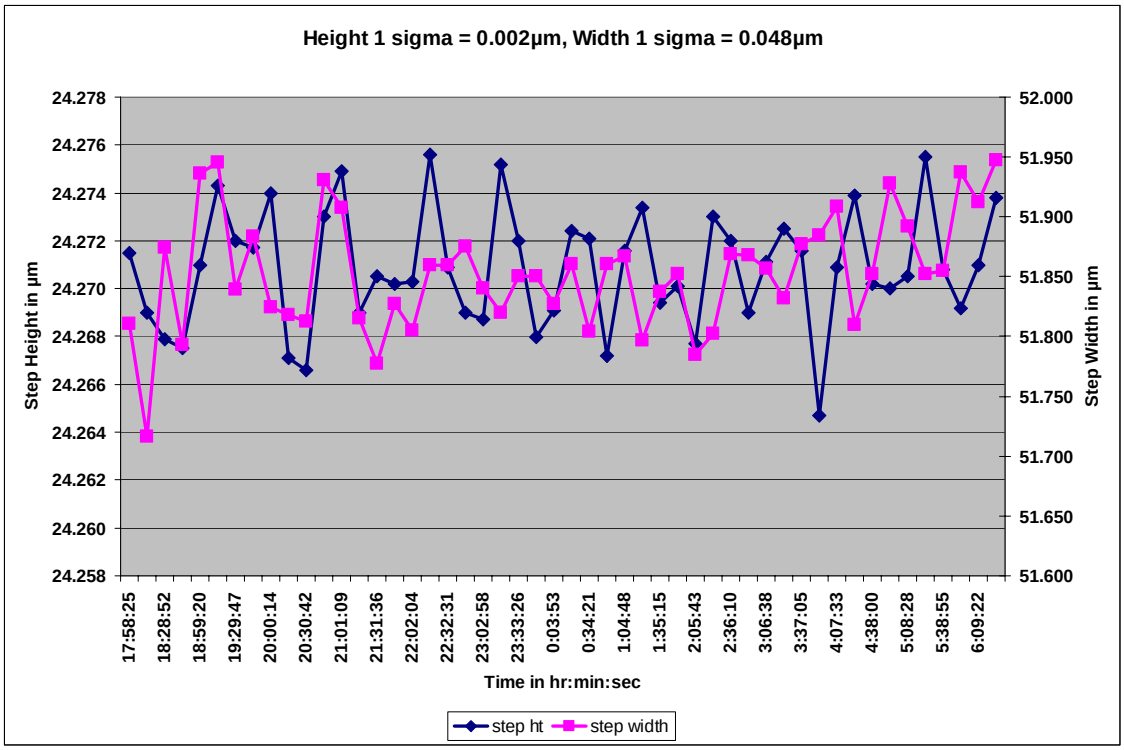

FIGURE 2.3.17: Long term stability impact on height and width measurements.

Step height and width are measured for 24 hours with 15 minute time interval between each measurement with no change in magnification configuration, as shown in figure 2.3.17. The variation in width measurement is taken as the impact on dimensional measurement. The variation in height measurement is taken as the impact on Z height measurement.

2.3.10. Stitching Errors

Non-symmetric matrix type stitching could result in 'potato-chip' effect – distortion in the shape (shape can be distorted with a saddle minimum or maximum at the center), as shown in figure 2.3.18. When the system error map (obtained from the reference mirror flatness test detailed in section 2.2.6) was not subtracted from individual measurements, approximately 40 m radius of curvature was induced. Hence, when fusion is to be performed on stitched datasets, it is highly recommended to subtract system error map data to reduce errors that will be induced into the overall shape of the measured surface. Figure 2.3.19 shows the difference between two stitched datasets – one with system error map subtraction and one without. In order to account for stitching based errors, a square wave standard is stitched using 4x4 array with 25% overlap (shown in figure 2.3.20a). 26 measurements are taken and ISO flatness is calculated on the difference between consecutive measurements, as shown in figure 2.3.20b.

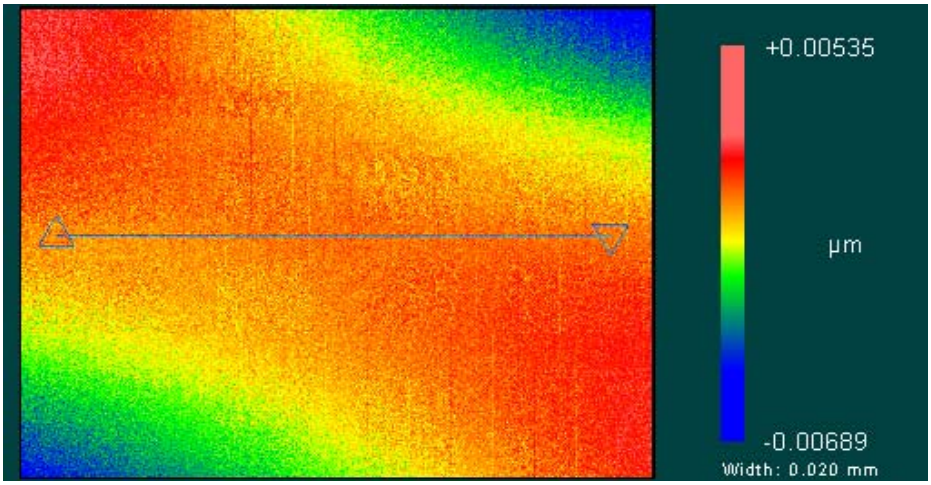

FIGURE 2.3.18: Stitching induced shape errors ("Potato chip effect").

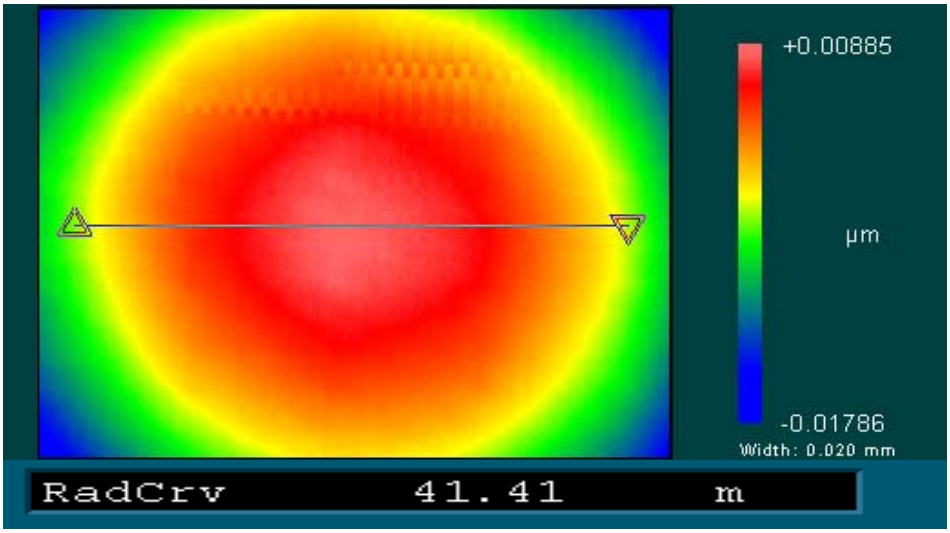

FIGURE 2.3.19: Spherical shape induced when stitched without subtraction of system error map.

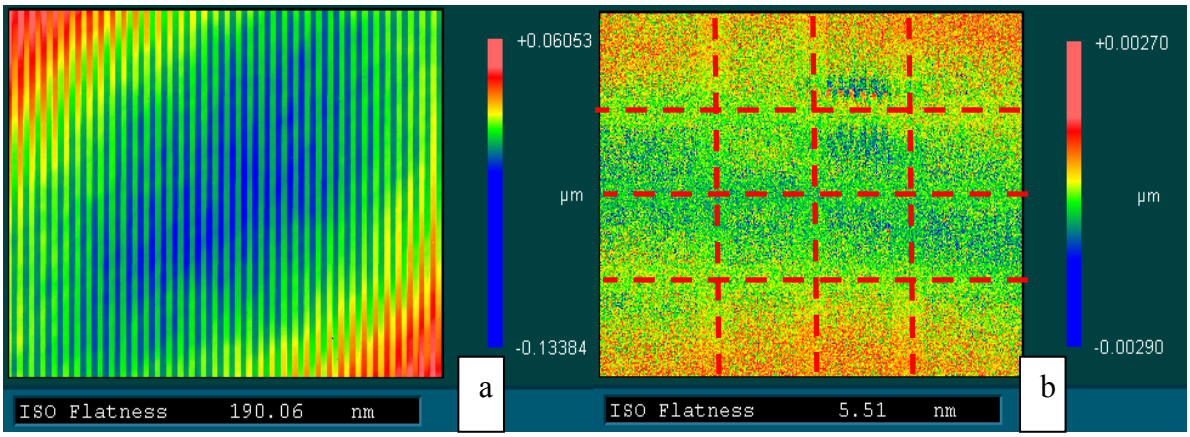

FIGURE 2.3.20: (a) Stitched surface of square wave standard (b) Difference between consecutive measurements.

It can be seen from figure 2.3.20b that the noise levels are less on the overlap regions, but there is significant edge effect on the area pertaining to the 3rd column and 1st row. Figure 2.3.21 shows the same difference plot after 5x5 kernel low pass filter and the affected area is shown inside red box. The difference between 25 successive measurements is shown in figure 2.3.22.

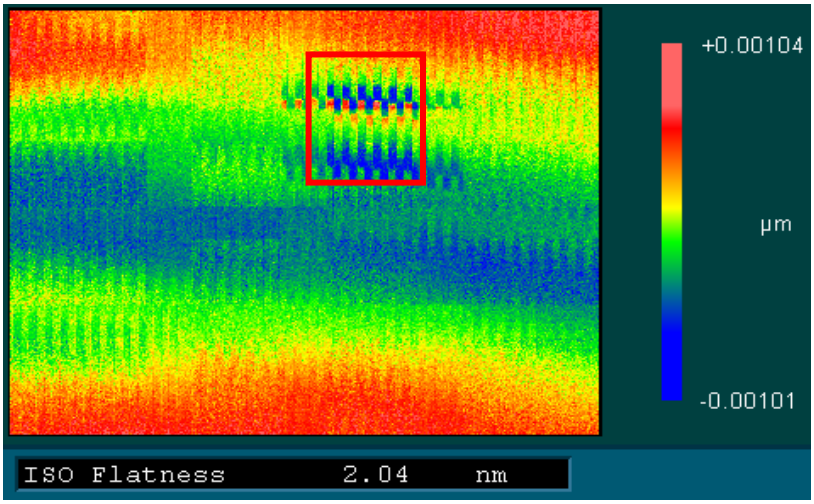

FIGURE 2.3.21: Difference between consecutive measurements after low pass filter.

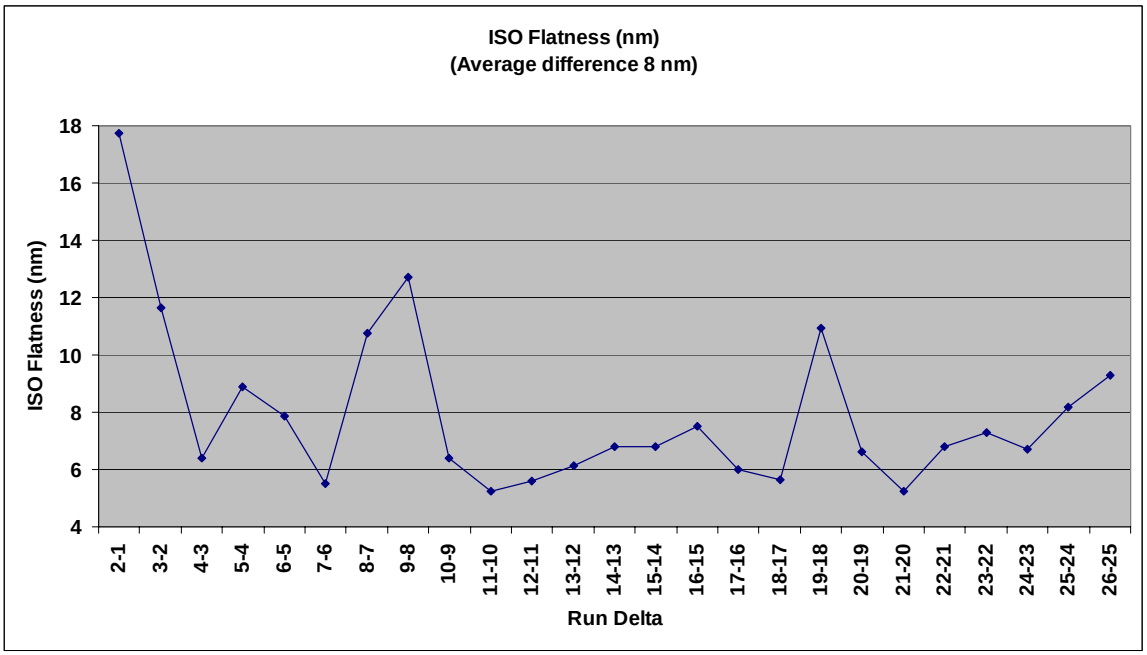

FIGURE 2.3.22: ISO Flatness of difference between consecutive measurements.

2.4. X,Y-axis Based Errors

2.4.1. Objective and Turret Repositioning Errors

In the case of automated measurements involving multiple magnifications, it is hard to ensure that the focus is optimal between magnification changes. Turret reference

coordinates can change by as much as 4 µm spatially and by several arc seconds along tip and tilt, due to turret's rotary positioning error. This variation would result in first order X, Y errors (impacting dimensional measurement) and Z errors of the second order (tip/tilt change would lead to focus change, which in turn impacts Z measurements). Concentric circles pattern 6E of optical dimensional standard is measured 30 times, with the magnification configuration changed between each measurement, by moving to a different magnification setting and then moving back to the required magnification. The average standard deviation of change in lateral coordinates for the center of the measured fiducial is taken as the nominal expected error in lateral variation due to repositioning error, as shown in table 2.4.1.

TABLE 2.4.1: Objective turret and zoom tube turret relocation errors.

	Zoom Tube Offset in µm				Objective + Zoom Tube Offset in µm			
	Nominal		Std. Deviation		Nominal		Std. Deviation	
Zoom Tube	X	Y	X	Y	X	Y	X	Y
1.0x	-34.781	0.386	0.038	0.035	-37.354	0.410	3.847	0.185
1.5x	-36.712	2.806	0.038	0.055	-34.386	2.633	3.506	0.105

2.4.2. XY Stage Non-linearity

While using the system for multiple field of view measurements either using single magnification configuration or multiple magnification configurations, apart from the objective and turret repositioning errors, stage non-linearity also impacts the dimensional measurements. Various self-calibration methods [130-132] have been proposed to calculate the stage non-linearity and out-of-plane errors. For testing stage non-linearity, a certified grid plate is placed on the stage and is allowed to stabilize for at least 8 hours. Then the grid locations shown in figure 2.4.1 are measured in the directional sequence 1-12. The center of each grid (shown in figure 2.4.2) is measured

for couple of runs until the stage has sufficiently warmed up (in this case 6 runs, as shown in figure 2.4.3) and then the difference in center positions of each grid is taken. The average value of those differences is taken as stage non-linearity error.

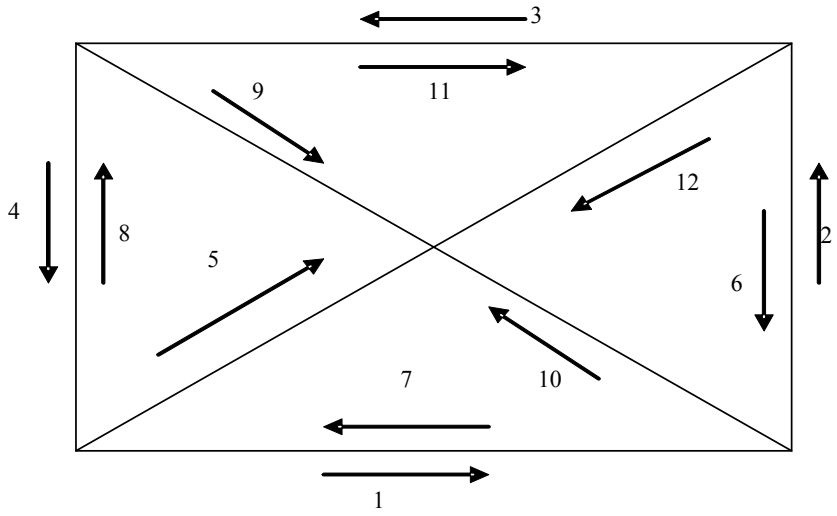

FIGURE 2.4.1: Stage travel map for measuring grid plate, to quantify stage non-linearity.

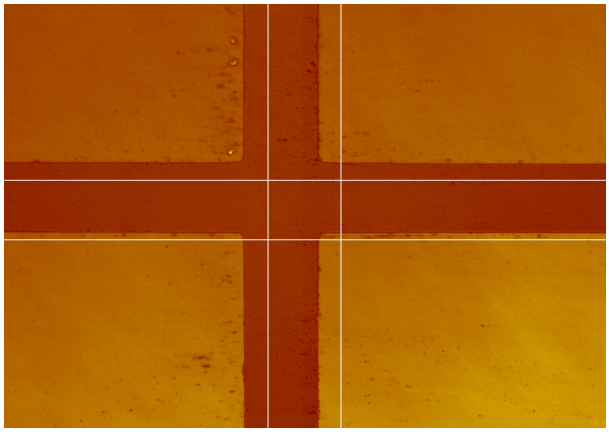

FIGURE 2.4.2: Grid plate measurement, showing variation between target and actual locations.

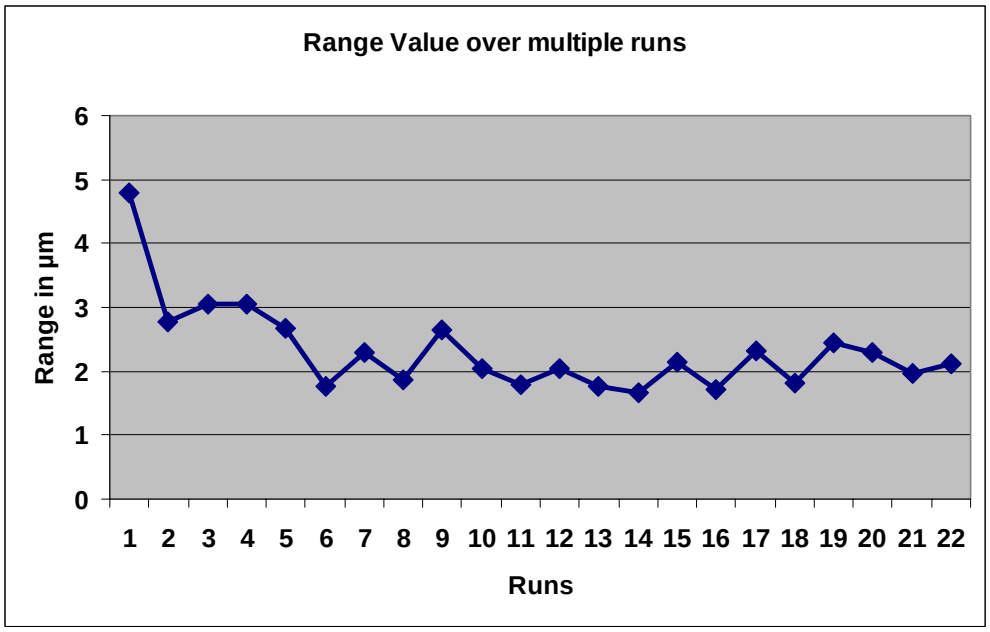

FIGURE 2.4.3: Grid plate location measured differences, showing initial stage warm-up and stabilization.

2.4.3. Camera Non-linear Warping Error

This error is generally assumed to be negligible for surface roughness analysis. But for precise dimensional measurement requirements, it is necessary to quantify this error. A lateral calibration standard could be used for calculating non-linear warping errors [133-135] of the combination of camera and all optics between the sample surface and the camera. The 3D map of lateral calibration standard and the background surface variation is shown in figure 2.4.4. The variation of the calculated centers from the certified nominal is taken as the errors induced on dimensional measurement due to image warping. The schematic is shown in figure 2.4.5. In order to account for measurement specific (diameter, width etc.) errors, the object of interest can be placed within 80% inner area of the field of view at multiple locations. Using sufficient sampling points to calculate the measurand, the standard deviation of the measurand is taken as the impact of non-linear warping induced by camera and optics.

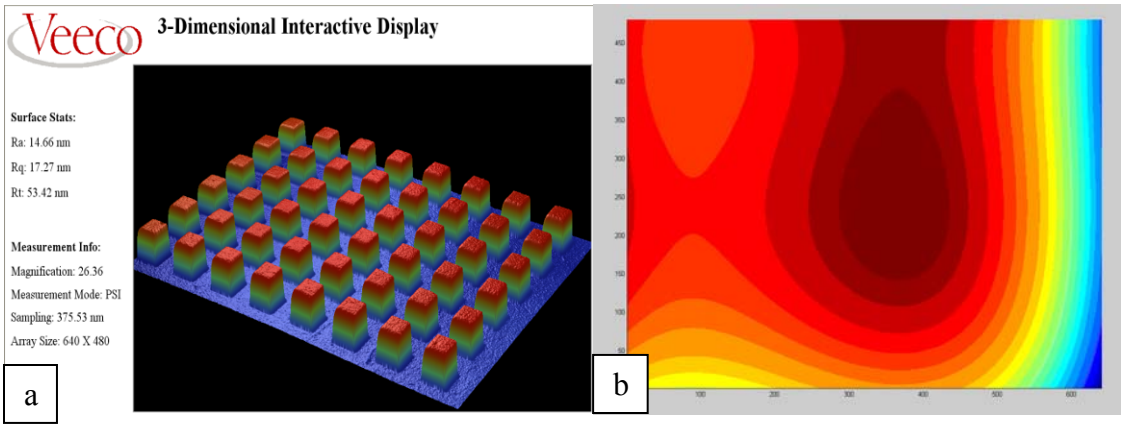

FIGURE 2.4.4: (a) 3D map of Lateral calibration standard (b) Background surface variation.

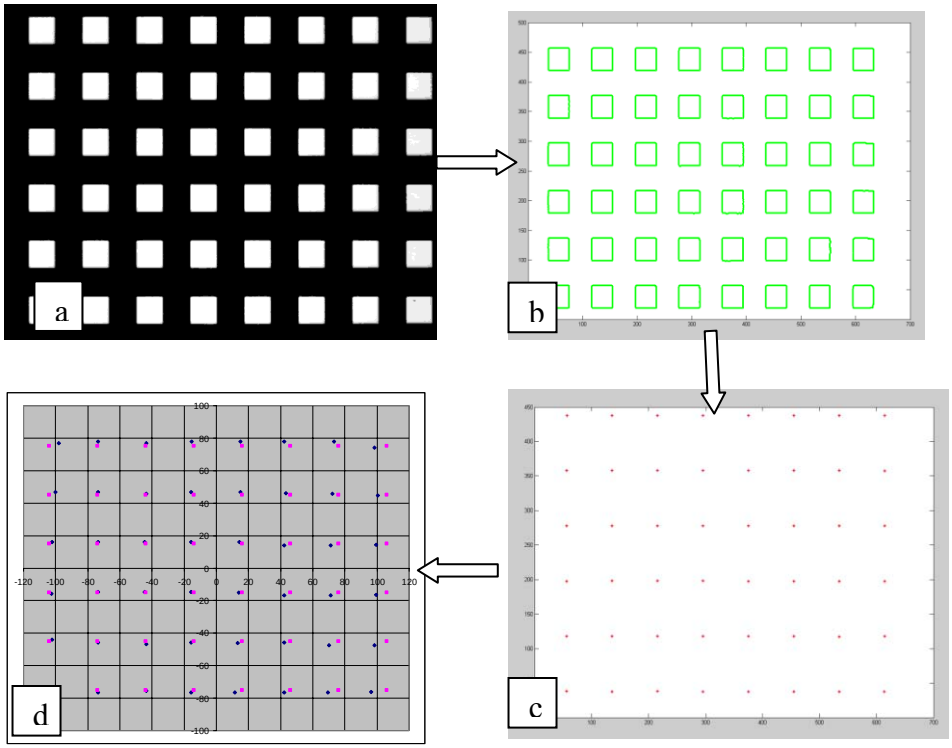

FIGURE 2.4.5: Schematic showing the camera non-linear warping error (a) Image of raw data (b) after edge detection (c) centroid of squares (d) location errors.

2.5. Summary

The best practices for calibrating and adjusting a CSI system were described, along with the standards (and associated uncertainties) that could be used to perform the calibration and other tests. Several test methods to evaluate the impact of those error sources on measurements along three axes were discussed. The error sources that would be potential requirements for the data fusion process, like the rotary turret repositioning errors and surface fitting residuals were discussed. Table 2.5.1 summarizes the error sources along with their impact on X, Y and Z axis measurements and comments on when those error sources need to be considered.

The above mentioned error sources and methods are not all-inclusive and doesn't account for system settings change due to changes in the nominal wavelength and bandwidth of the light source, light intensity change, PZT drift, aperture settings etc. For Z height calibration, it is preferable to use at least three step heights – first one at minimum step height just above correlation length, second one at maximum step height that is just below the maximum scan length possible and third one at the approximate mean. The average of three z calibration coefficients [136, 137] is taken as the over-all z calibration coefficient. While measuring engineered patterned surfaces, different measurement technologies and magnification have individual spatial and vertical resolution limits [138-140], therefore individual magnification should be tested for this.

TABLE 2.5.1: Summary of CSI error sources and their possible impacts.

Sl. No	Error Source	Symbol	1 Sigma in µm		Comments
			Z	XY	
1	Standard step ht repeatability	RHT	0.0065	0.0800	Basic system capability in measuring heights
2	Z stage repeatability	RZ	0.0800	0.1300	Impacts non-referenced surface measurements
3	Autofocus repeatability	AFR	0.1900	0.1900	Impacts panel/wafer level measurements with built-in autofocus routines
4	Focus (High Mag)	FMG	0.0050		Shows up as stable system-to-system bias
5	Reference Mirror + Optical Relay	RMOR	0.0001		Impacts stitching
6	Scan Length	SL	1.0020x		Impacts all z measurements taken using scan lengths other than what was used for calibration
7	Numerical Aperture Correction	NAC	1.0002x		Impacts all z measurements taken using objectives other than what was used for calibration
8	Algorithm	ALG	0.0400		Impacts all z measurements taken algorithm settings other than what was used for calibration
9	Dynamic Noise	DN	0.0050		
10	Z stage non-linearity	ZNL	0.0004		Impacts shape/form measurement
11	Scan Location	SSL	0.0250		Impacts all z measurements in combination with (2)
12	Dissimilar Materials	DM	0.0050		Impacts z measurements while measuring optically dissimilar materials
13	Environmental Impacts	E	0.0020	0.0500	Impacts Gage repeatability and reproducibility and long term stability
14	Camera Non-linear warping	NLWC		0.0400	Impacts within field-of-view dimensional measurements
14	objective turret repositioning error	OTRE		3.8000	Impacts dimensional measurements involving multiple magnifications
15	zoom turret repositioning error	ZTRE		0.0400	Impacts dimensional measurements involving multiple magnifications
16	XY stage repositioning error	XY		2.0000	Impacts dimensional measurements involving multiple field-of-views
17	Surface fitting residual	SF	0.2500		Impacts surface roughness parameter measurements on non-planar surfaces
18	Stitching error	S	0.0008	0.7700	Impacts dimensional measurements involving multiple field-of-views

It was shown that around 4 μm of misalignment is expected between measurements taken using multiple magnifications on the same system and stage positioning accuracy was 2 μm. This gives the potential misalignment between data sets obtained using different magnifications as, $2 \times \sqrt{2^2 + 4^2} = 9\,\mu\text{m}$. The coarse and fine registration algorithms should be able to handle this 9 μm misalignment and align the datasets to within one pixel.

In order to ensure effective data fusion, systematic errors due to NA correction and scan length have to be accounted for and compensated at individual measurements. Having established the capability of the measurement system and the expected misalignment, the next step is to evaluate whether the coarse and fine registration steps can handle the possible misalignment between measurements. It was also shown that vibration based, defocus based random noise can be present on the data. Performance of coarse and fine registration methods on data sets under the influence of additive noise and defocus noise needs to be evaluated. The performance of coarse and fine registration methods to account for the noise levels and possible misalignment will be evaluated in the next chapter.

CHAPTER 3: COARSE AND FINE REGISTRATION

In order to establish confidence in the Multi-Scale Data Fusion (MSDF) process, evaluation of the performance of individual steps and algorithms is very important. Li et al [141] stress the significance proper choice of individual process steps on the fusion performance and the lack of comprehensive analysis and comparison of different schemes. They recommend evaluation of different fusion algorithms not only on the fused data based performance criteria, but also the computation complexity and processing time requirement. Therefore, in this chapter, simulation studies that are performed to evaluate the performance of coarse and fine registration will be explained in detail.

The first major step in the MSDF process is coarse registration. In the second chapter, it was demonstrated that the rotary turret relocation errors could be around 9 µm. It was also shown that defocus and Numerical Aperture (NA) based errors could affect the measurements. In order to understand the impact of translation and rotational misalignment between datasets on coarse and fine registration, a simulation study is performed. The objective is to study the impact of noise and blurring of datasets on coarse registration.

Traditionally, noise is induced at single-scale. In this section, a new methodology for generating multi-scale noise is proposed and used to compare the performance of coarse registration. This simulation based study is used to establish the limitations of coarse registration, which directly impacts the performance of fine registration.

Within Discrete Wavelet Frame (DWF) transformation domain, there are three different approaches that could be used for multi-scale decomposition of data. The performance characteristics of these three approaches will be studied in detail, along with possible applications of those approaches for other characterization needs.

Fine registration is the most critical step in MSDF. Data fusion cannot be effective, if the datasets are not aligned to within one pixel accuracy. The impact of three DWF methods, two edge detection methods, and noise on fine registration will be studied in detail.

3.1. Coarse Registration

Coarse registration is usually performed either by manually selecting fiducial markers in both the datasets or by automated methods like Sum of Absolute Differences (*SAD*) and Normalized Cross Correlation (*NCC*). *SAD* will be minimum at the position where similarity between both the data is maximum and *NCC* will be maximum at the position where similarity between both the data is maximum. *SAD* of two datasets $I_c(x,y)$ of length $M \times N$ and $I_\gamma(x,y)$ of length $P \times Q$ is calculated by

$$SAD(x,y) = \sum_{i=0}^{P-1}\sum_{j=0}^{Q-1}\left|I_C(x+i,y+j) - I_r(i,j)\right|, \begin{matrix} x = 0,1,2,\ldots,M-1 \\ y = 0,1,2,\ldots,N-1 \end{matrix}$$

NCC is given by

$$NCC(x,y) = \sum_{i=0}^{N-1}\sum_{j=0}^{M-1} \frac{I_c(x+i,y+j)I_r(i,j)}{\sqrt{\sum_{i=0}^{N-1}\sum_{j=0}^{M-1} I^2{}_c(x+i,y+j)}\sqrt{\sum_{i=0}^{N-1}\sum_{j=0}^{M-1} I^2{}_r(i,j)}}$$

Raol [142] summarizes a performance evaluation of NCC and SAD under three noise levels as follows:

- In the absence of noise, both NCC and SAD are equally accurate
- In the presence of 'Salt & Pepper' noise, SAD is more accurate compared to NCC
- In the presence of 'Gaussian' noise, NCC proved to be more accurate compared to SAD.

Based on this recommendation, NCC was chosen as preferred method for coarse registration for this study. Consider the datasets obtained from a honed surface at 5X and 20X magnifications (shown in figure 3.1.1 a and b) measured on a NV7300 CSI system. Both the datasets are pre-conditioned by removing outliers and filling missing data points with mean of the dataset.

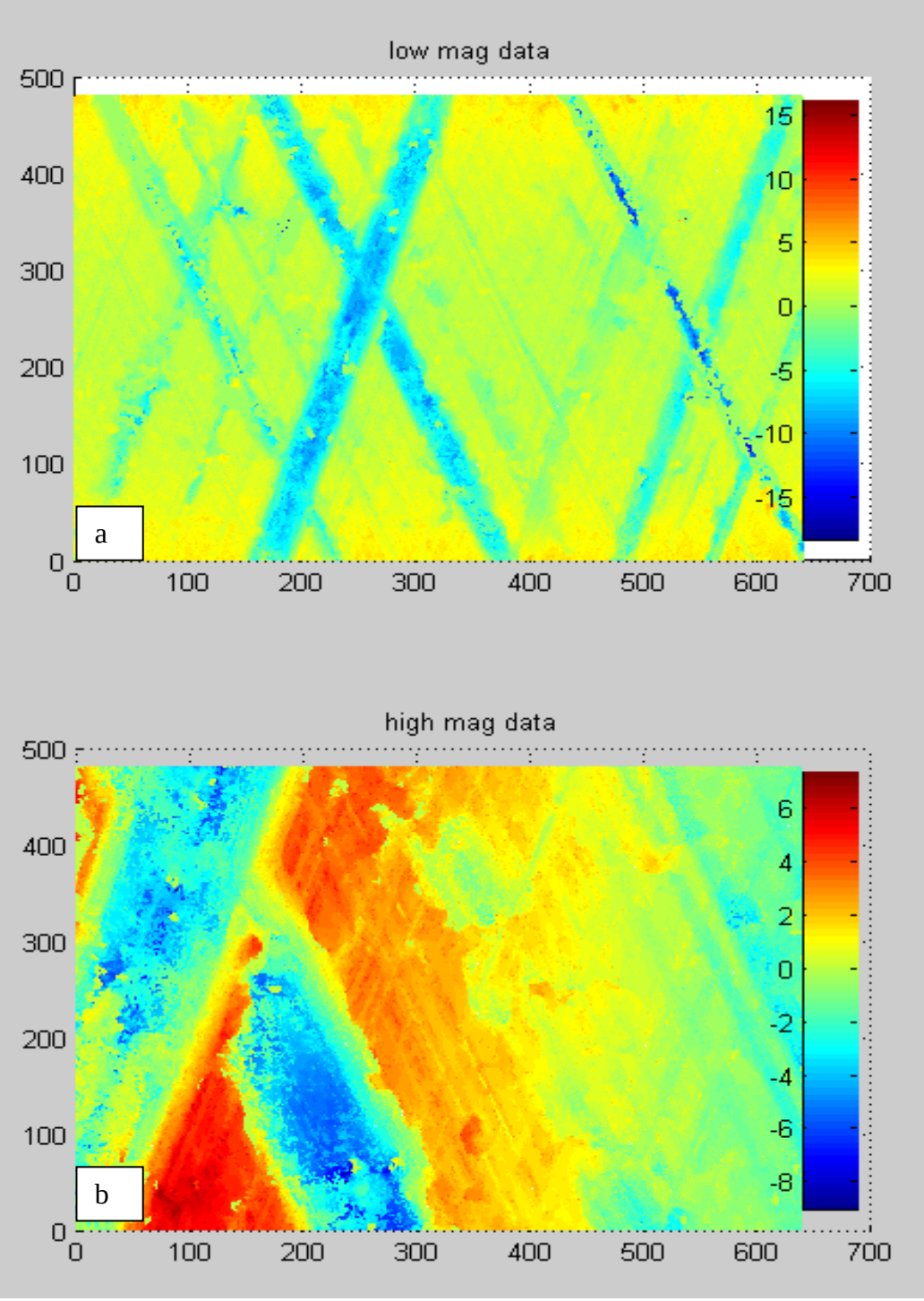

FIGURE 3.1.1: Honed surface at (a) 5X and (b) 20X optical magnification.

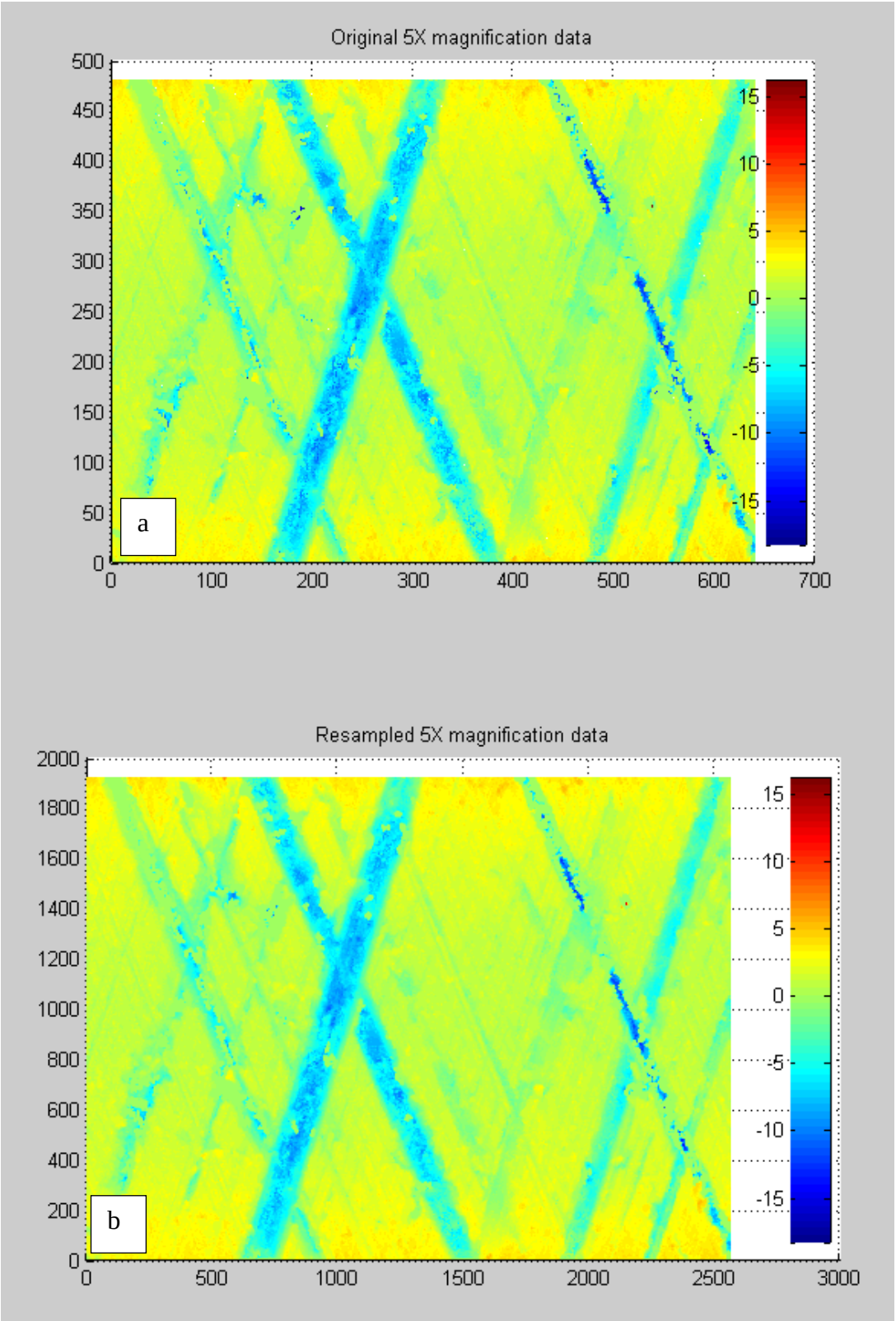

FIGURE 3.1.2: (a) 5X magnification data of honed surface (b) Resampled version to match 20X magnification data's sampling interval.

The 5X data is resampled to match the 20X data, as shown in figure 3.1.2 a and b. The resampled 5X data (shown in figure 3.1.2b) and the 20X data (shown in figure 3.1.1 b) are used to calculate NCC, as shown in figure 3.1.3. The identified peak location is within the circle inset shown in figure 3.1.3.

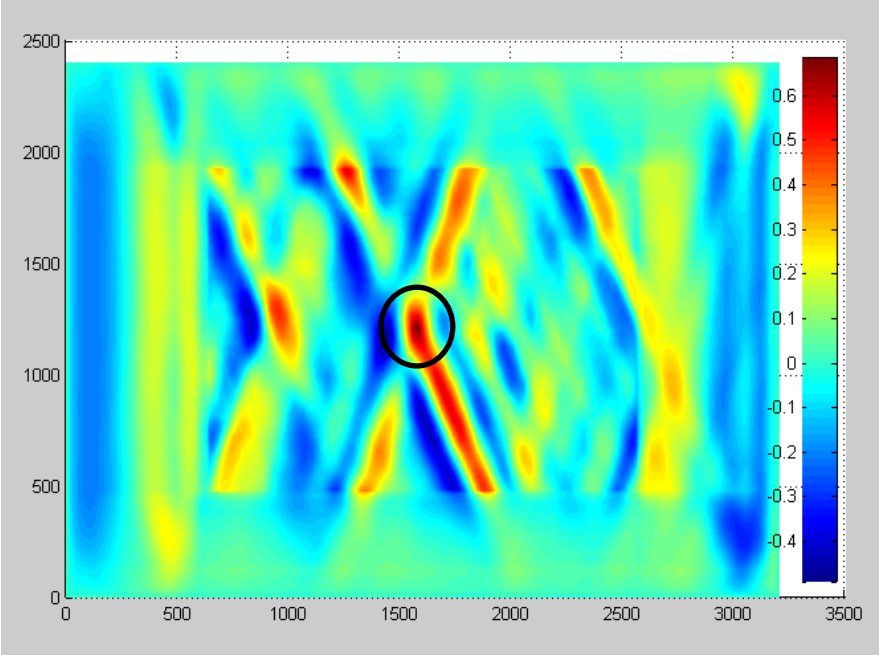

FIGURE 3.1.3: 3D mesh of NCC for 20X magnification data on 5X magnification data.

After finding the approximate location of the dataset with higher sampling interval (D_{High}) inside the dataset with lower sampling interval (D_{Low}), a new dataset ($D_{LowClip,}$ shown in figure 3.1.4) is generated by trimming D_{Low} to the size of D_{High}.

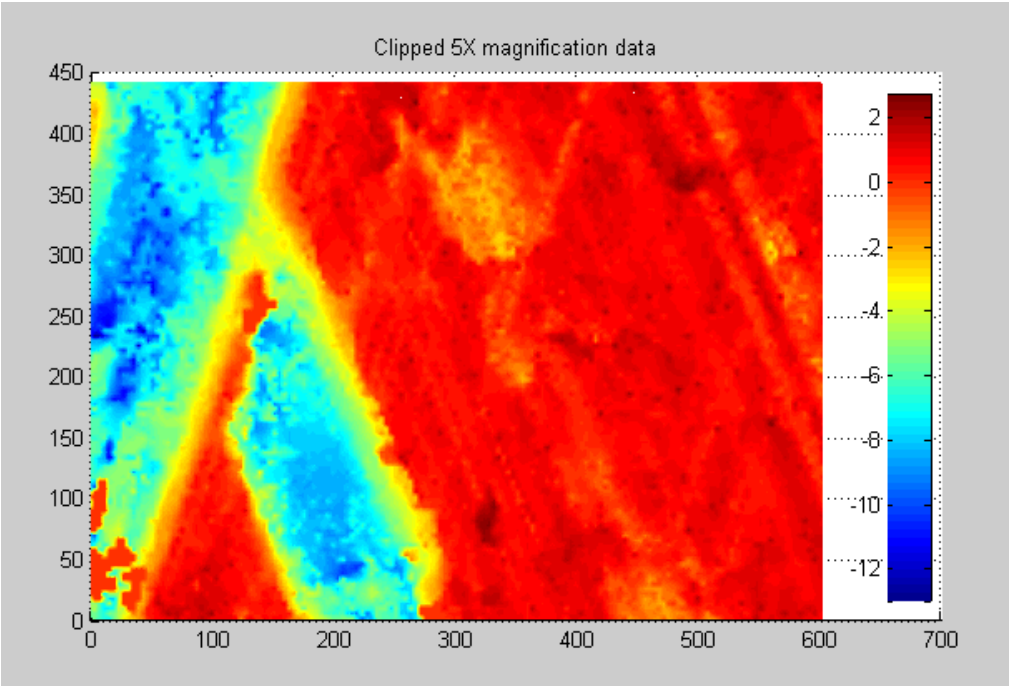

FIGURE 3.1.4: Clipped 5X magnification data.

3.1.1. Impact of Noise and Misalignment on Coarse Registration

In order to characterize the impact of noise and angular misalignment between two datasets on coarse registration, a study was performed on 12 different datasets, shown in figure 3.1.5.

Each datasets was treated with 10 noise conditions - Gaussian noise with three variance levels (0.005, 0.01 and 0.015), and Speckle noise with three variance levels (0.02, 0.04 and 0.06), Salt & Pepper noise with three noise density levels (0.025, 0.05, and 0.075), and Poisson noise. Instead of adding noise at single level, it is added at multiple scales, based on the schematic shown in figure 3.1.6.

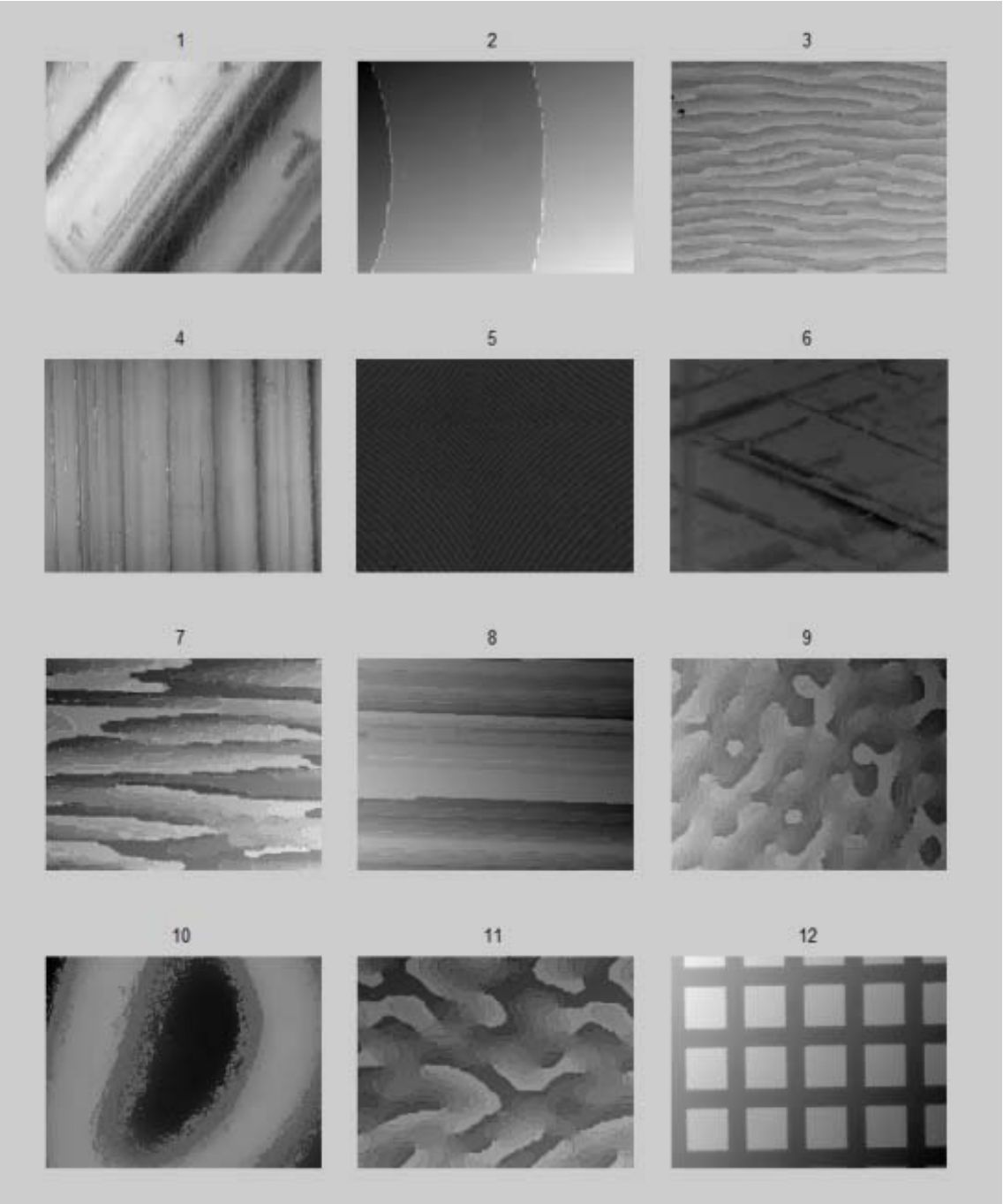

FIGURE 3.1.5: Sample datasets chosen for the comparison study (1) Lapped surface (2) beam shaper optical surface (3) Dipole diffuser optical surface (4) Turned surface (5) Fresnel lens surface (6) Honed surface (7),(8) and (9) Pattern generator surfaces (10) Formed surface (11) Spot array generator (12) Square grid array surface.

A set of six noise maps are generated for the individual noise type and a six-level DWF is performed with B3 spline using 3D Hybrid method. A sub image from each noise map is taken to generate a new multi-scale noise map. Figure 3.1.7a shows the original image and 3.1.7b-k shows the images obtained after addition of multi-scale noise.

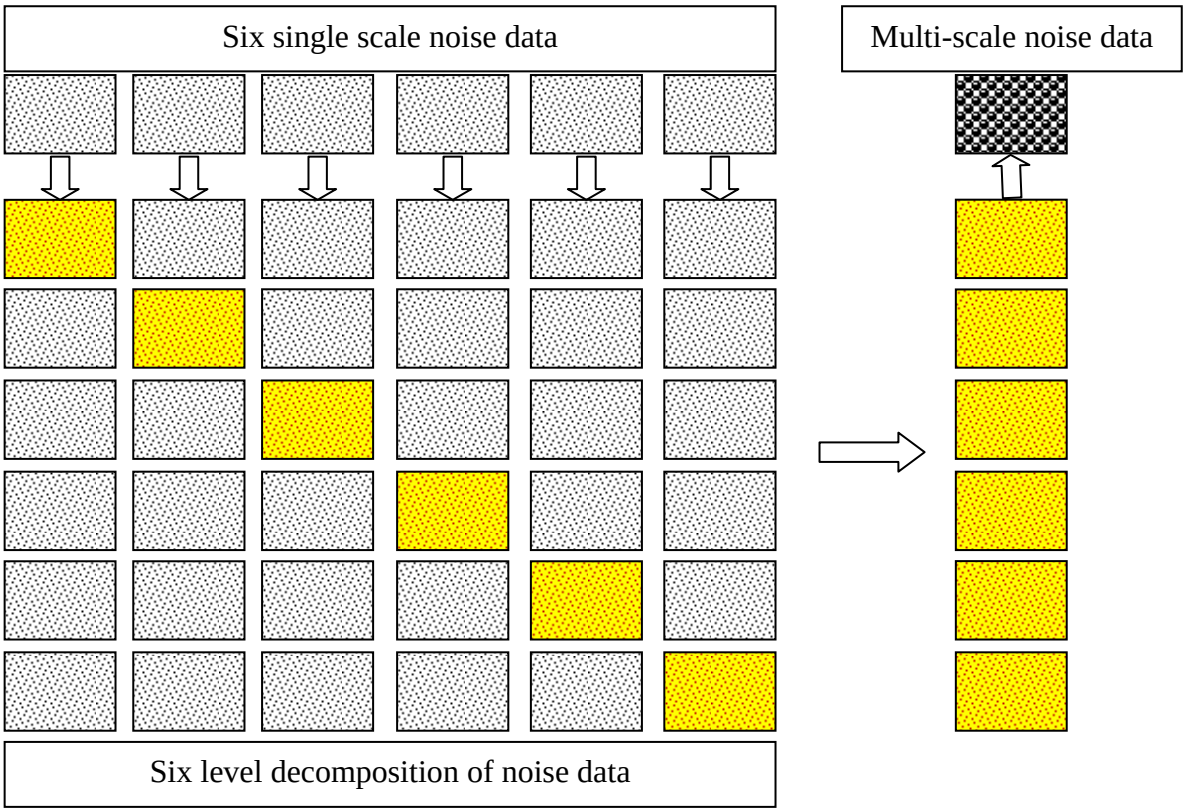

FIGURE 3.1.6: Schematic showing the method of generation of multi scale noise.

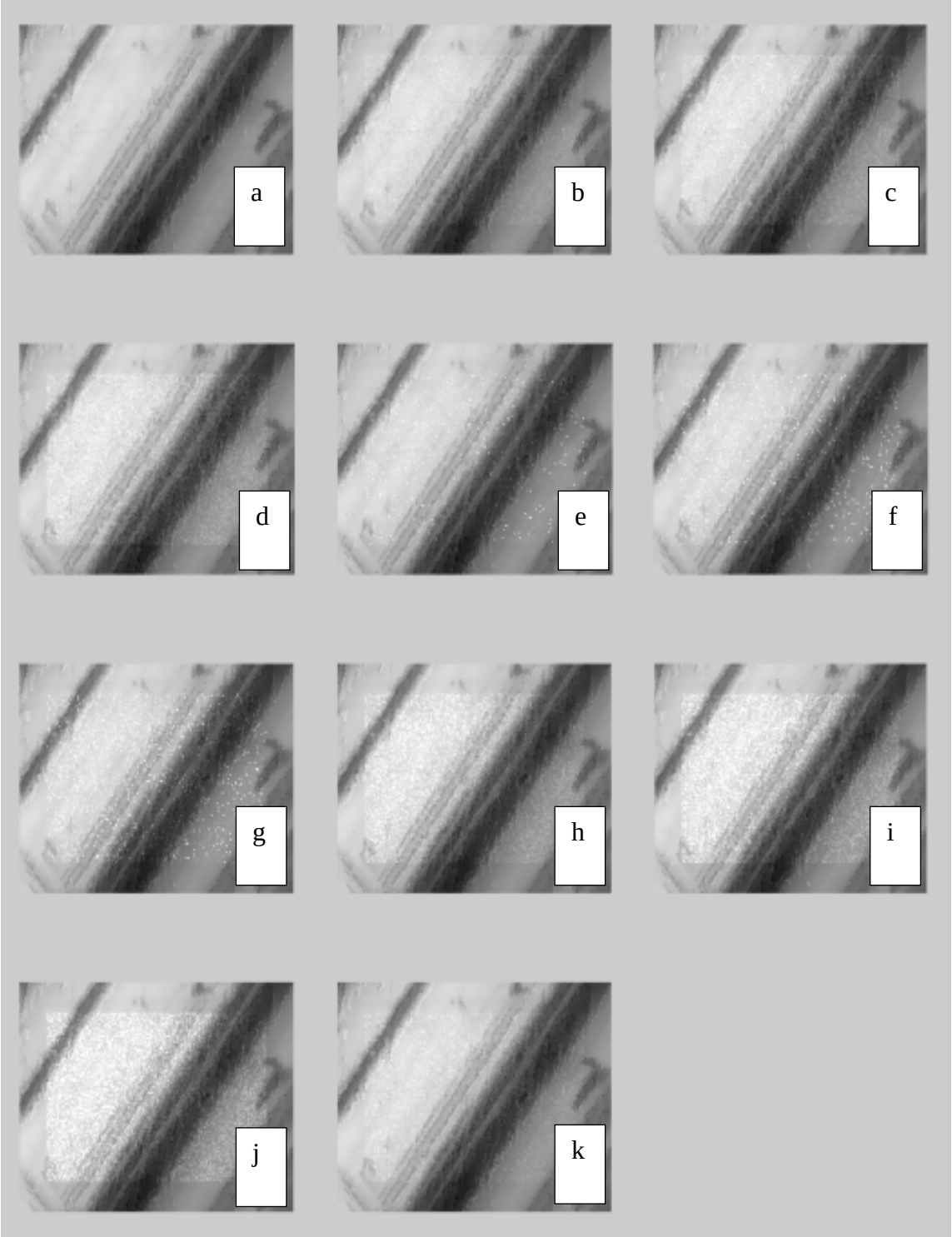

FIGURE 3.1.7: (a) Original Image (b)-(d) Image obtained after addition of multi-scale Gaussian noise (e)-(g) Images obtained after addition of multi-scale salt and pepper noise (h)-(j) Images after addition of multi-scale speckle noise (k) Image after addition of Poisson noise.

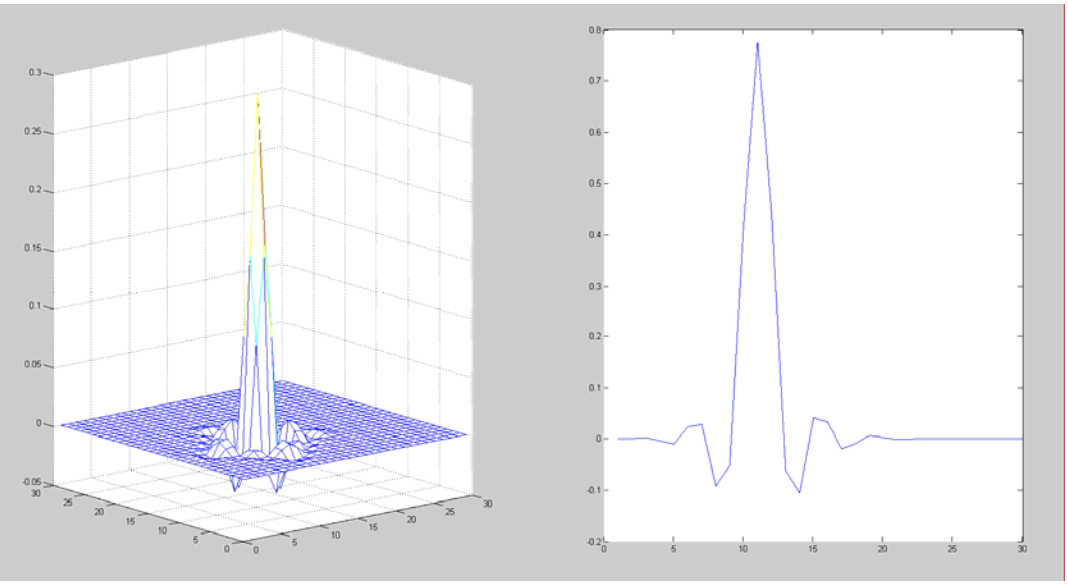

FIGURE 3.1.8: 3D and 2D representation of the Coiflet wavelet used as point spread function.

Convolution was performed using a Coiflet wavelet (shown in figure 3.1.8) to simulate blurring of data due to NA and lateral resolution based errors. Each noisy image obtained is then rotated from -1° to +1° in increments of 0.25° and NCC is used to find the approximate location in the original image that best correlates to the rotated version of the noisy sub image. The calculated location values for 12 datasets are as shown in figure 3.1.9. It can be seen that dataset no.5 (Fresnel lens) showed a huge impact of angular misalignment, shown by red circles. Figure 3.1.10 shows the calculated location values with respect to the noise type. From the figure it can be seen that there is no difference in pattern with respect to noise type. Based on this it is concluded that the type of noise has negligible impact on the coarse registration.

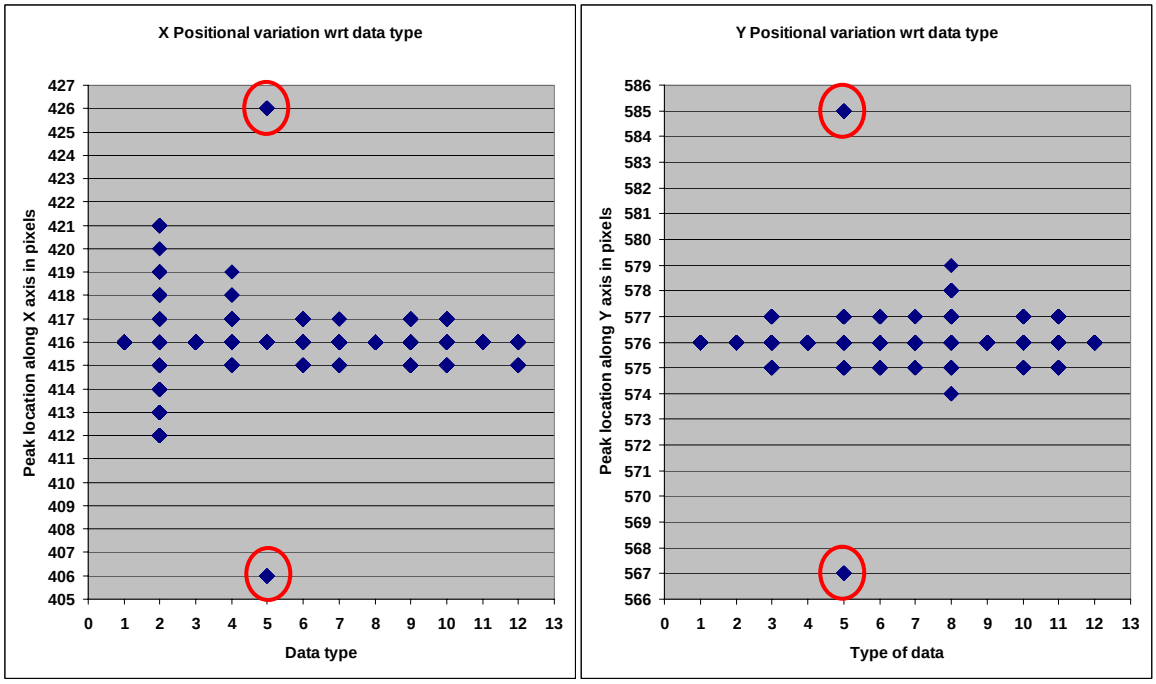

FIGURE 3.1.9: Calculated X and Y location for 12 datasets with different noise levels and angular misalignment.

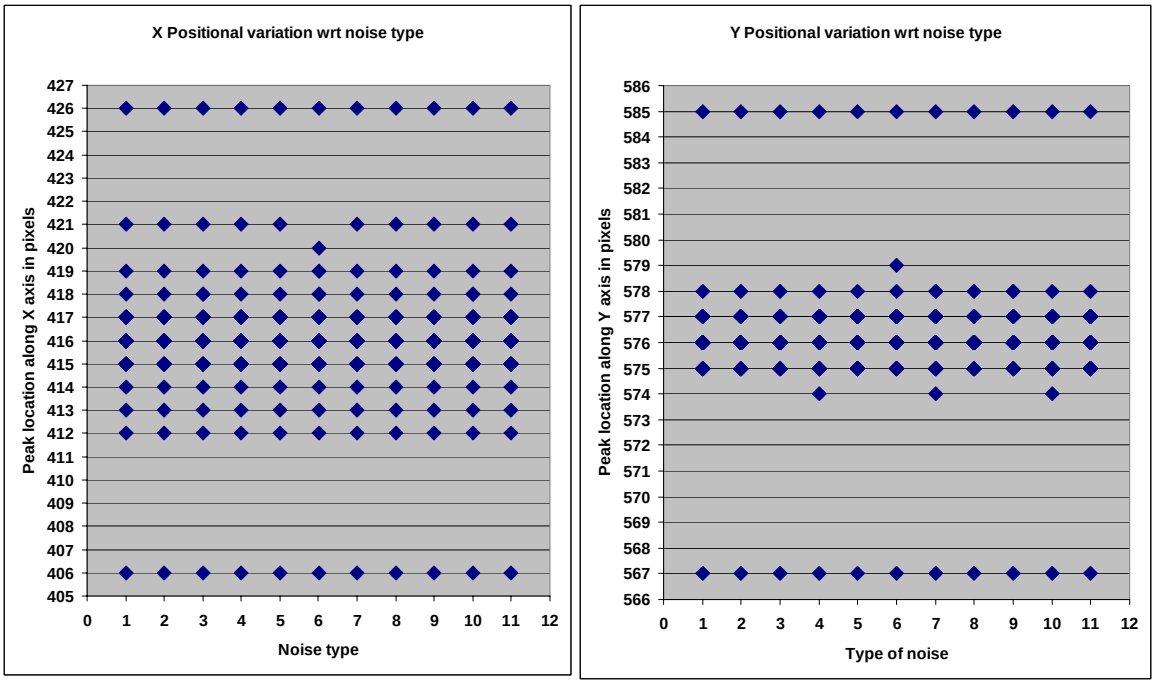

FIGURE 3.1.10: Calculated X and Y location with respect to noise type.

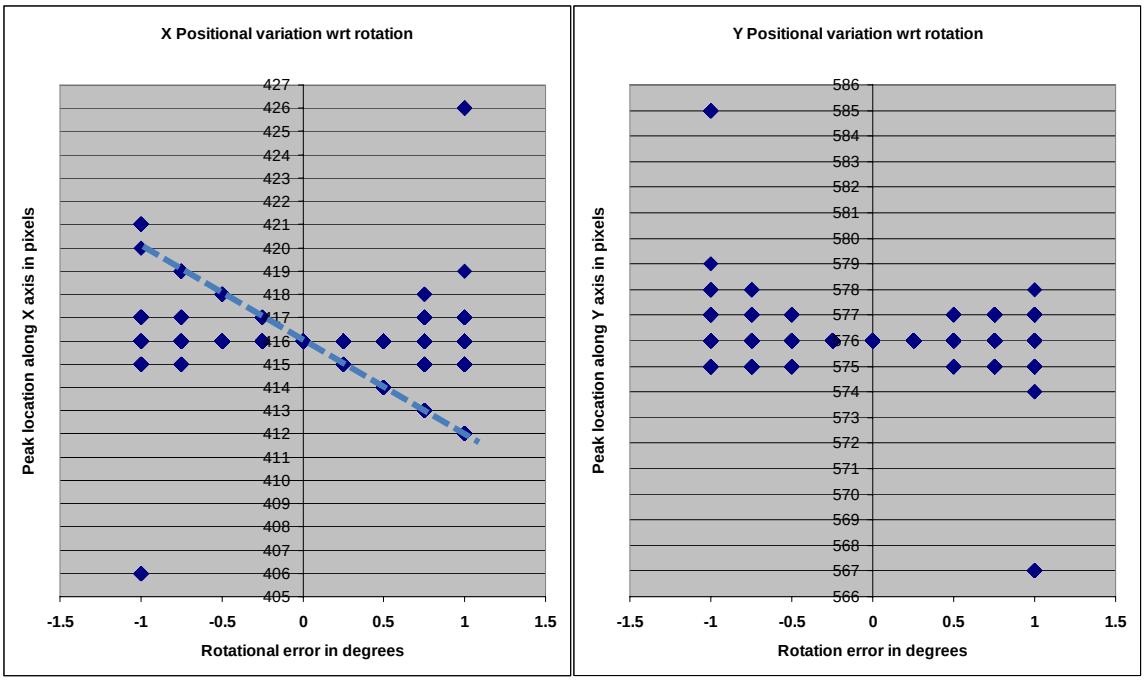

FIGURE 3.1.11: Calculated X and Y location with respect to angular misalignment.

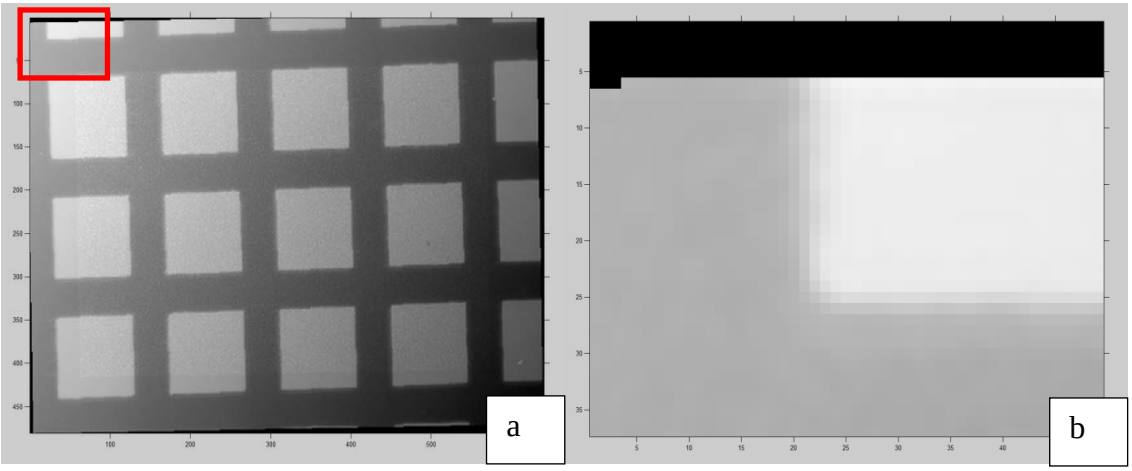

FIGURE 3.1.12: (a) Noisy image rotated by 1° (b) Zoomed in view of area shown inside red box in (a) to show the 5 pixel offset.

Figure 3.1.11 shows the calculated location values with respect to the angular misalignment. From the figure, it can be seen that the coarse alignment performance is strongly dependent on the angular misalignment, and as much as 4 pixel misalignment can be expected for a 1° angular misalignment. Figure 3.1.12a shows the noisy image obtained after 1° rotation. The area within the red box is shown in figure 3.1.12b. It can be seen that the starting point has shifted by five pixels. Hence, the 4 pixel misalignment obtained using coarse registration is considered within the limits of actual angular rotation that was induced.

After coarse registration, the next step in MSDF is to perform fine registration. Fine registration is accomplished by two sub-steps, called segmentation and transformation. First the datasets under consideration are segmented to identify areas of interest which could be used as control points for transformation. Defects, cracks, and edges could be used as control points. Edge detection tools are very effective in finding these control points. Alternate approach would be to identify a uniform spread of control points across the entire surface that was measured. This approach is comparable to 'Watershed' based edge detection approach, hence was not considered for further evaluation.

3.2. Fine Registration

The datasets $D_{LowClip}$,(shown in figure 3.1.4) and D_{High} (shown in figure 3.1.1b) have to be precisely aligned before data fusion. Typically fine registration is performed by finding matching fiducial / control points on both the datasets and then calculating a transformation matrix which would match the control points in both the datasets using least squares optimization, represented by B=T x A, where A and B are the two matrices

containing the *x, y, z* coordinates of the control points from both the datasets. T is the transformation matrix given by,

$$\begin{bmatrix} \cos\beta\cos\gamma & \cos\alpha\sin\gamma+\sin\alpha\sin\beta\cos\gamma & \sin\alpha\sin\gamma-\cos\alpha\sin\beta\cos\gamma & t_x \\ -\cos\beta\sin\gamma & \cos\alpha\cos\gamma-\sin\alpha\sin\beta\sin\gamma & \sin\alpha\cos\gamma+\cos\alpha\sin\beta\sin\gamma & t_y \\ \sin\beta & -\sin\alpha\cos\beta & \cos\alpha\cos\beta & t_z \\ 0 & 0 & 0 & 1 \end{bmatrix}$$

where, t_x, t_y, t_z are the translational offsets along *x, y* and *z* axis, α, β, γ are the angles of rotation with respect to the *x, y* and *z* axis. The Iterative Closest Point (ICP) algorithm is efficient and robust under two conditions:

- The closest local minimum for the integration of the datasets is equivalent to the global one. This means that the two datasets should not be separated too far from each other to guarantee the merging into the right areas.
- Low and high resolutions do not differ much from each other, i.e., there are enough data points in the areas of the low resolution data set into which the high resolution local data set should be integrated, to direct the merging to a high-precision registration.

Figure 3.2.1 shows the data points used for fine registration – green data points obtained from 20X magnification data and blue data points from 5X magnification data. Magenta data points were obtained after realignment using ICP finite difference [143] method.

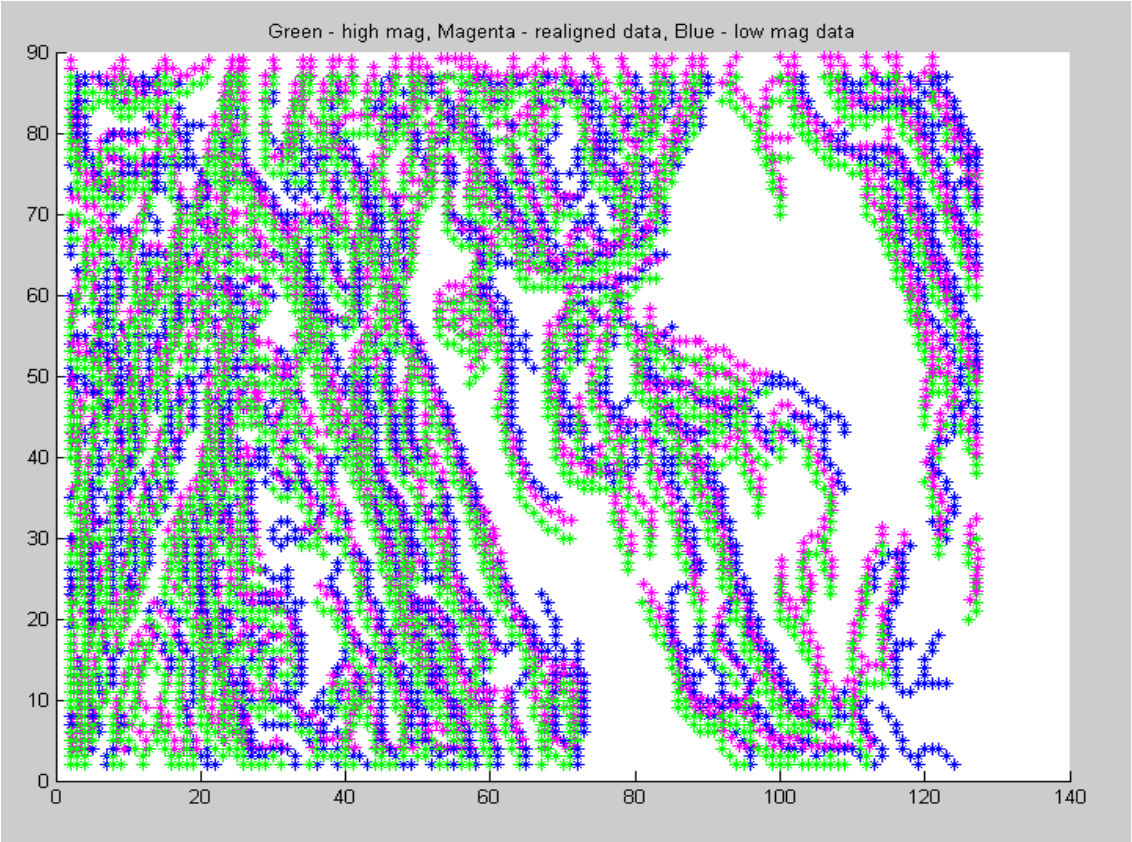

FIGURE 3.2.1: Green data points obtained from 20X magnification data, blue data points obtained from 5X magnification data and magenta data points are the realigned location of green data points.

After finding the transformation matrix using ICP algorithm, D_{High} is rotated with respect to all three axes for α, β, γ accordingly and translated along Z axis by t_z to match $D_{LowClip}$. After each rotation, resampling using bilinear interpolation method is performed to preserve the shape of the data. After fine registration, D_{Low} is trimmed to generate $D_{LowClipNew}$ to exactly match the size of $D_{High,}$ by using the translation offsets t_x, t_y obtained from the transformation matrix. $D_{LowClipNew}$ is then up sampled using linear interpolation techniques to match the sampling interval of D_{High}, to generate $D_{LowClipNewRes}$.as shown in figure 3.2.2.

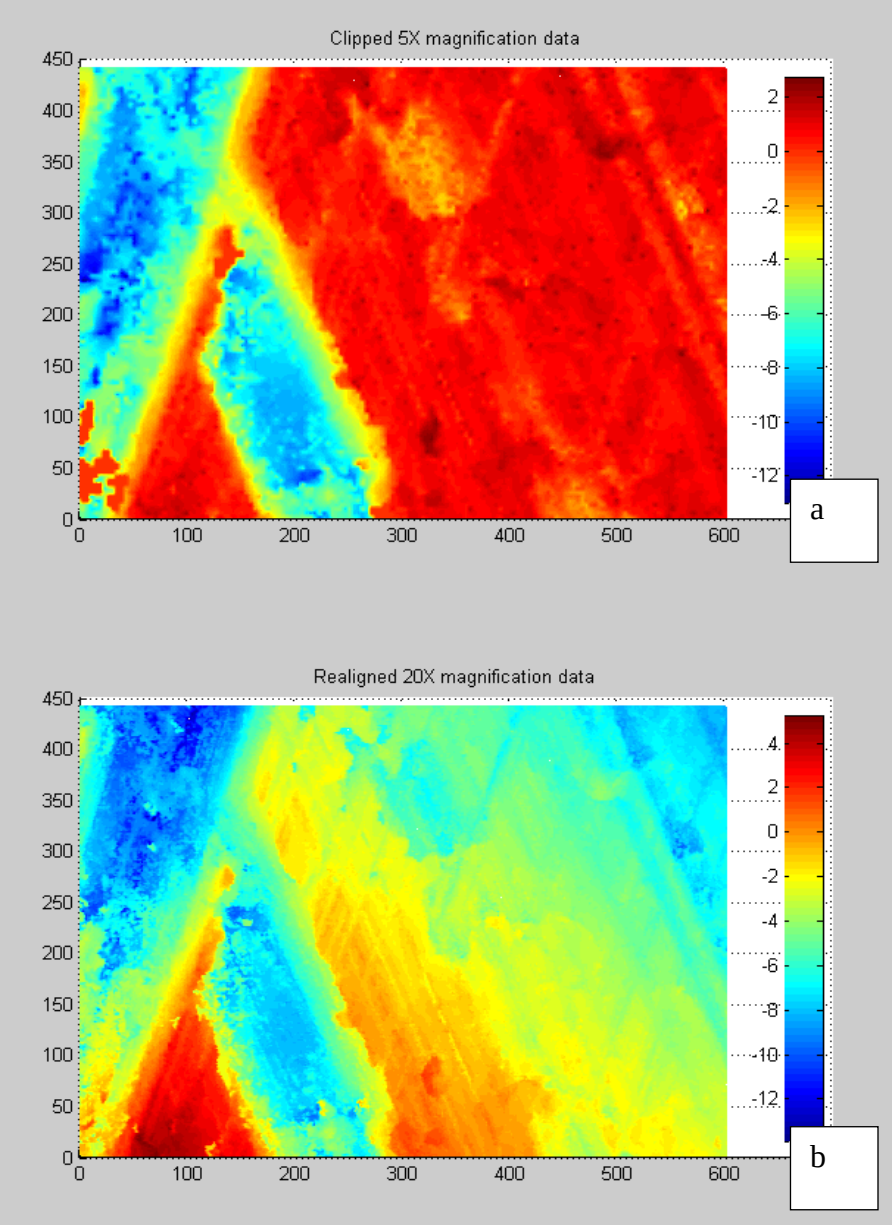

FIGURE 3.2.2: (a) Clipped 5X magnification data (b) Realigned 20X magnification data.

Effective data segmentation is crucial for determination of control points which will be used for fine registration. Segmentation is also a critical process for characterization of engineered surfaces. Mathia et al [144] discuss the need for an

automated method to segment the structured surfaces into regions of interest. Hence, different segmentation techniques will be explored in detail.

3.2.1. Segmentation Approaches for Engineered Surfaces

For patterned surfaces with stepped planar surfaces, such as Fresnel micro-lens arrays, existing height based separation or segmentation of surfaces [145] and edge detection in image analysis domain can be readily used. Verma and Raja [146] have developed a MATLAB® based software system to automatically locate features on the surface and dimensionally characterize them. Once the segmentation is performed, features are extracted and primary objects are identified and then dimensions are calculated. Kong et al [147] have presented an image processing approach to the characterization of optical microstructures, mainly on the spatial height based data separation approach.

For surfaces with different textured areas, single parameter based clustering and segmentation could also be effective. Senin et al [148] proposed a clustering based segmentation approach. They have successfully applied the already developed methods in image analysis domain to segmentation of 3D surface data, under the premise that 3D surface data could also be treated similar to gray scale image data. They also mention that the only other image analysis based method deployed in surface topography domain – watershed based segmentation [149], which is being included in the new ISO standard [150] for areal surface texture characterization. Clustering based on one parameter, albeit on any transform domain is the main suggestion of the authors. When suggesting the use of multiple parameters, they took the weighted average approach to find one metric which is a weighted average of selected parameters. They conclude that multi-parameter

method is not significantly better than one parameter method. Three facetted pyramid, shown in figure 3.2.3, is a unique surface model which cannot be segmented using single parameter and needs multiple parameter based segmentation.

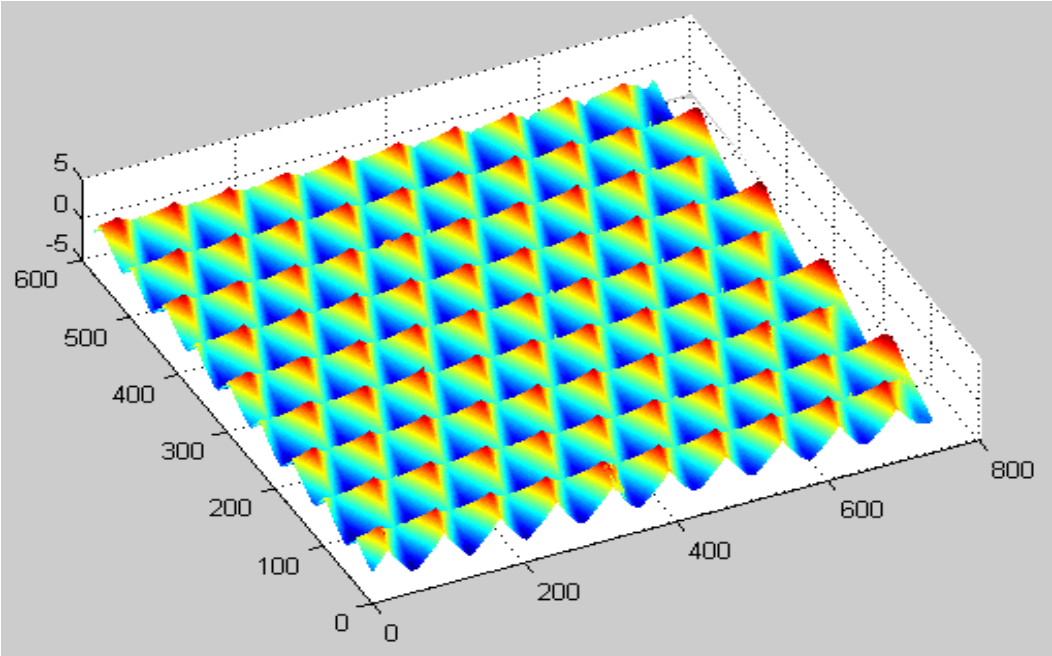

FIGURE 3.2.3: Three faceted pyramid patterned surface.

Using Hough Transform [151] and Radon Transform [152] to identify specific patterns on engineered surfaces has already been documented. The peaks on data obtained using either of the transforms are used to generate an image of interest, which could be further processed using standard image morphological analysis tools. The proposed approach takes a next step from the single parameter based segmentation approach and proposes the use of multiple parameters for segmentation. The concept is very much in use in the image analysis domain [153], where the image is converted to any other domain and two different parameters are analyzed in a two- dimensional histogram [154] to find individual clusters. The clusters can be identified and separated using regular thresholding [155] algorithms and corresponding indices are used to

separate the height data into multiple segments. The conceptual schematic is shown in figure 3.2.4.

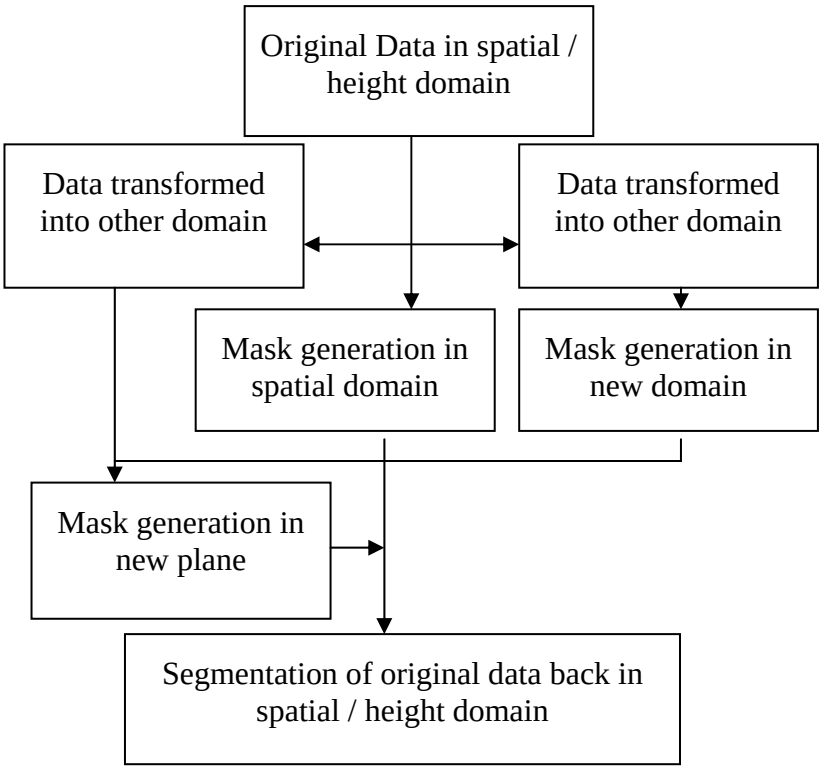

FIGURE 3.2.4: Schematic showing the multi-parameter based segmentation approach.

3.2.2. Multiple Domain Based Segmentation

In order to find edges, a 4-level DWF [156] transform with B3 spline as mother wavelet is performed and the obtained wavelet planes are shown in figure 3.2.5. A region of W1 plane is shown in figure 3.2.6b along with the raw data in 3.2.6a. Comparing figures 3.2.6 a and b, it can be visually seen that the W1 plane is able to show the edges better and even the individual tool path is clearly visible. It is also seen that the top and bottom edges are not similar, which is a characteristic limitation of the micro size ball

milling process. Planes W1 or W2 could be used to find the edges as shown in figure 3.2.7.

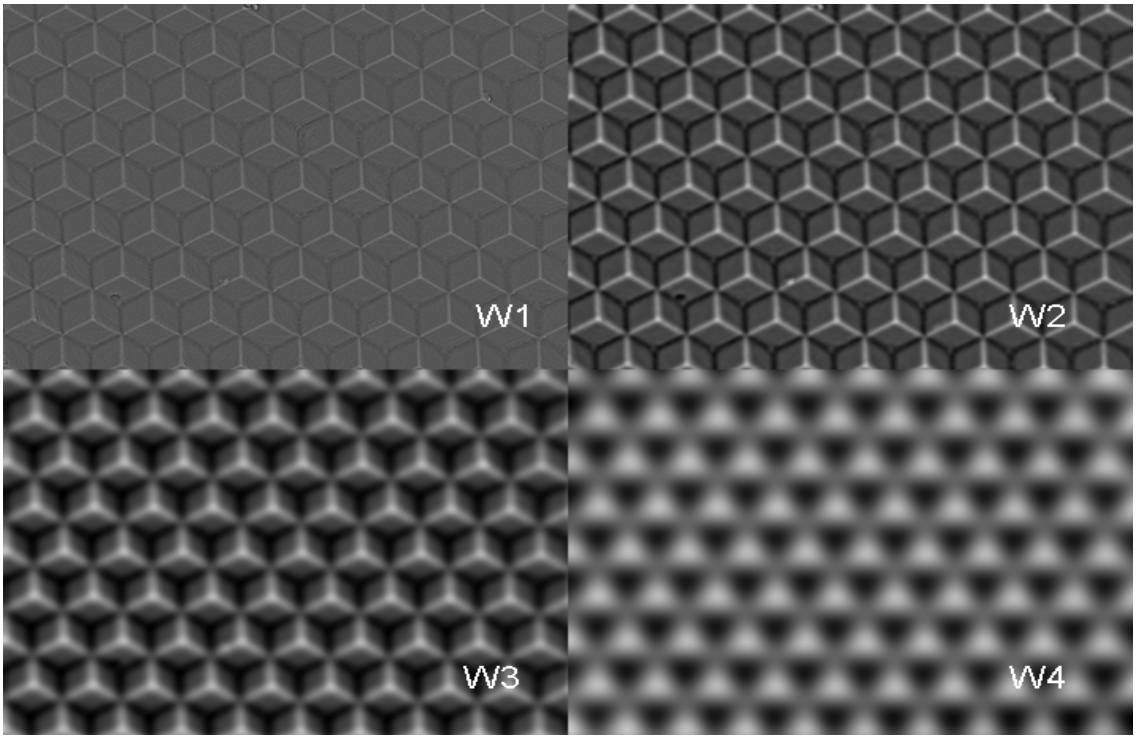

FIGURE 3.2.5: Images obtained by DWF Transform.

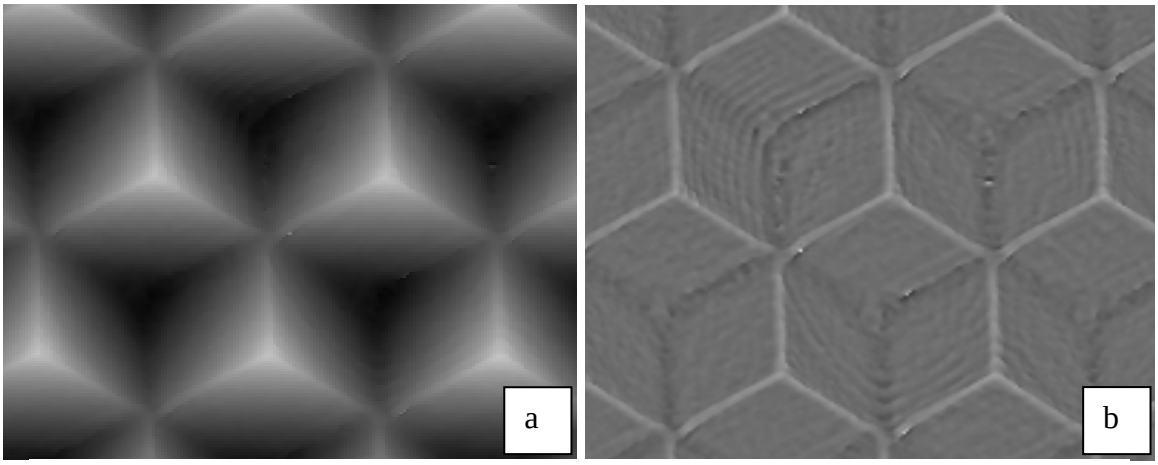

FIGURE 3.2.6: (a) Raw data (b) W1 plane obtained by DWF Transform.

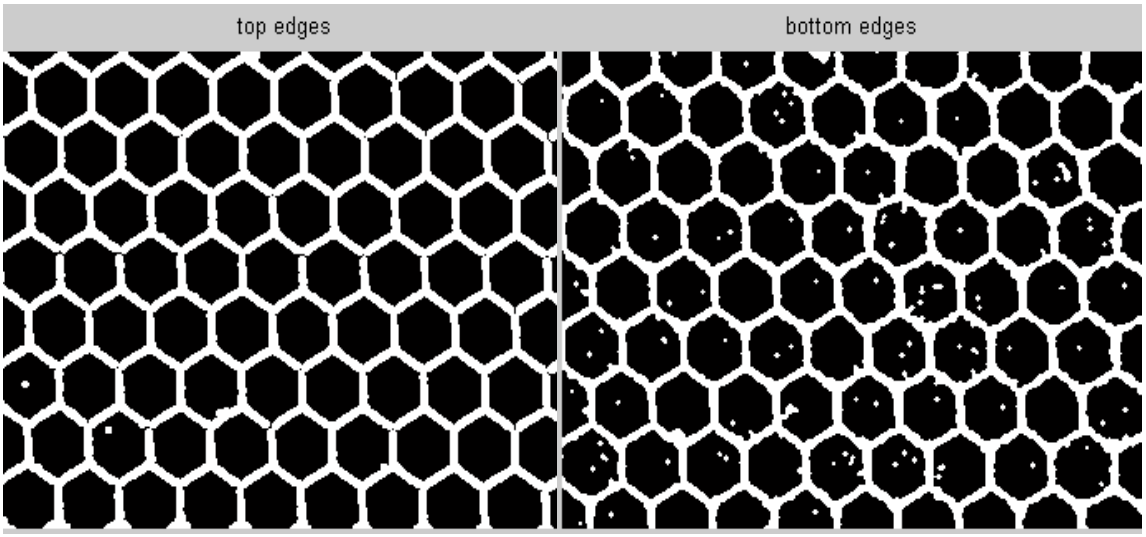

FIGURE 3.2.7: Edge detected on W1 Image obtained by DWP Transform.

Since the top and bottom edges are different in edge crispiness, each one needs slightly different morphological filtering approaches. The edges obtained (shown in figure 3.2.7) could be combined to generate a binary mask to segment the individual facets as shown in figure 3.2.8.

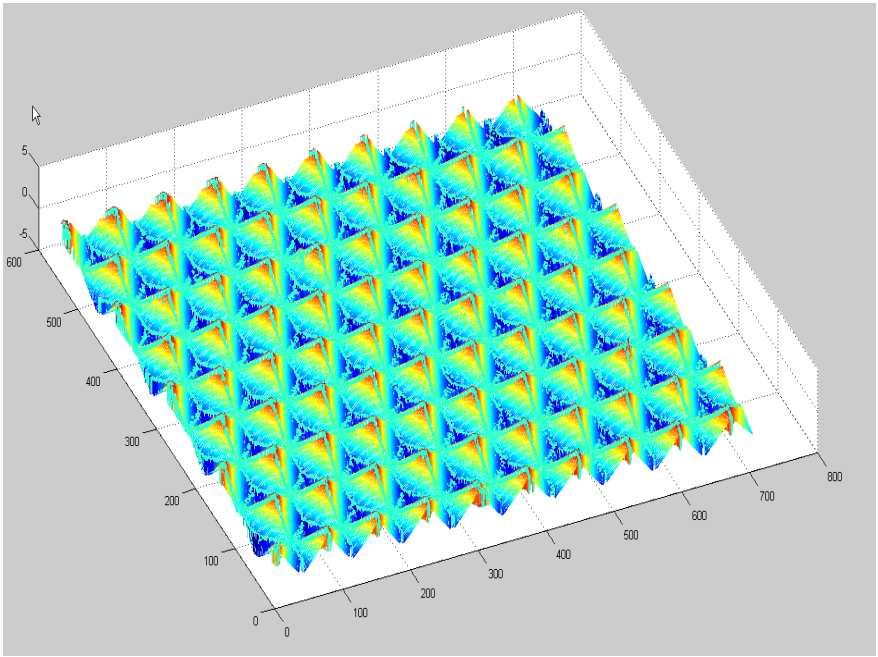

FIGURE 3.2.8: Segmented dataset obtained by applying the binary mask to original data.

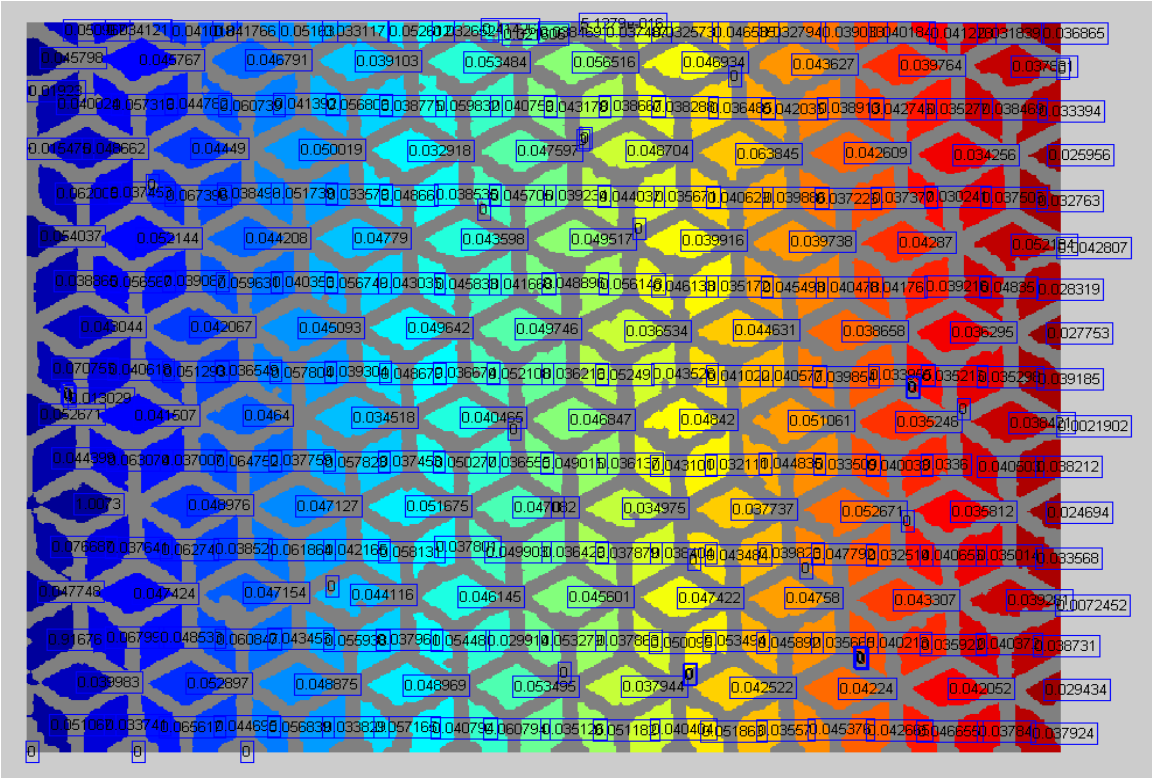

FIGURE 3.2.9: Surface roughness values of individual segments.

The segments are identified, labeled and surface roughness parameter ‘Sa’ is calculated, as shown in figure 3.2.9. The edges obtained from figure 3.2.5 could also be used analyze individual edge variations using Radon transform as shown in figure 3.2.10. The radon transformed image (b) can be converted to a binary image (c) by generic threshold algorithms and then inverse transformed to obtain (d). The variations in the lines correlate to the actual variation of the edges.

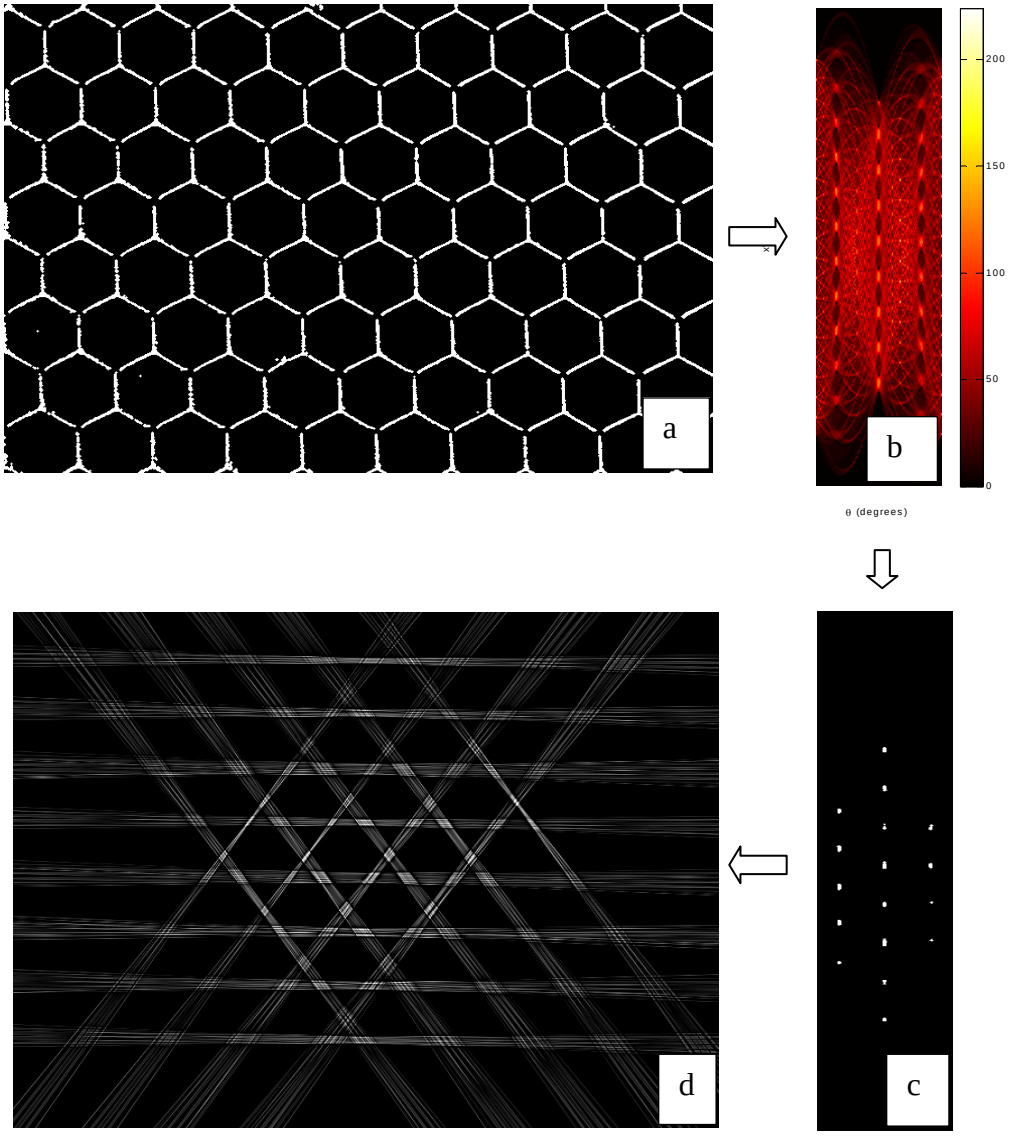

FIGURE 3.2.10: Using Radon Transform for calculating edge variation in pattern.

The same method could also be used for effectively characterizing the cross-hatch angle of honed surfaces. Single-scale analysis of a honed surface is shown in figure 3.2.11b. Multi-scale analysis of the same surface is shown in figure 3.2.11c. Comparing figures b and c, it can be seen that the multi-scale analysis yields better results.

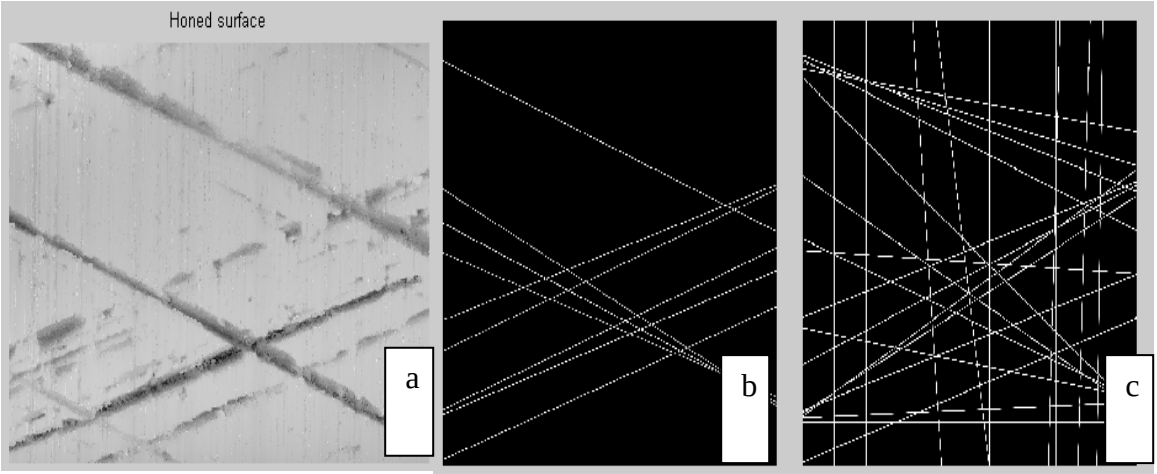

FIGURE 3.2.11: (a) Surface after honing process (b) Result from single-scale analysis (c) Result from multi-scale analysis (B3 spline and 2D DWF).

3.2.3. Multiple Parameter Based Segmentation

The alternate method is to perform multiple parameters based masking. For this, the x and y gradients of the height data are calculated and a 2D histogram (with 200 x 200 bins) of the slopes is generated as shown in figure 3.2.12. Generic peak picking algorithms [157] could be used to identify the number of peaks in the histogram and used to separate the cluster data close to these three peaks. Sub-images a – c in figure 3.2.13, show the segmented individual facets and figure 3.2.13d shows the combined image color coded to show the three facets of the pattern. Once the three facet data is grouped, each facet can be separated, segmented and labeled, as shown in figure 3.2.14.

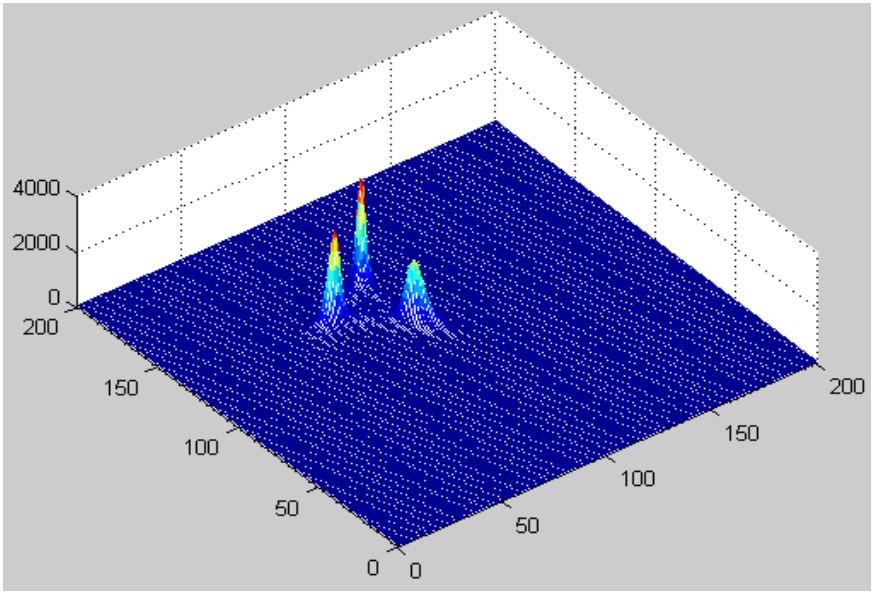

FIGURE 3.2.12: 2D histogram plot of slopes.

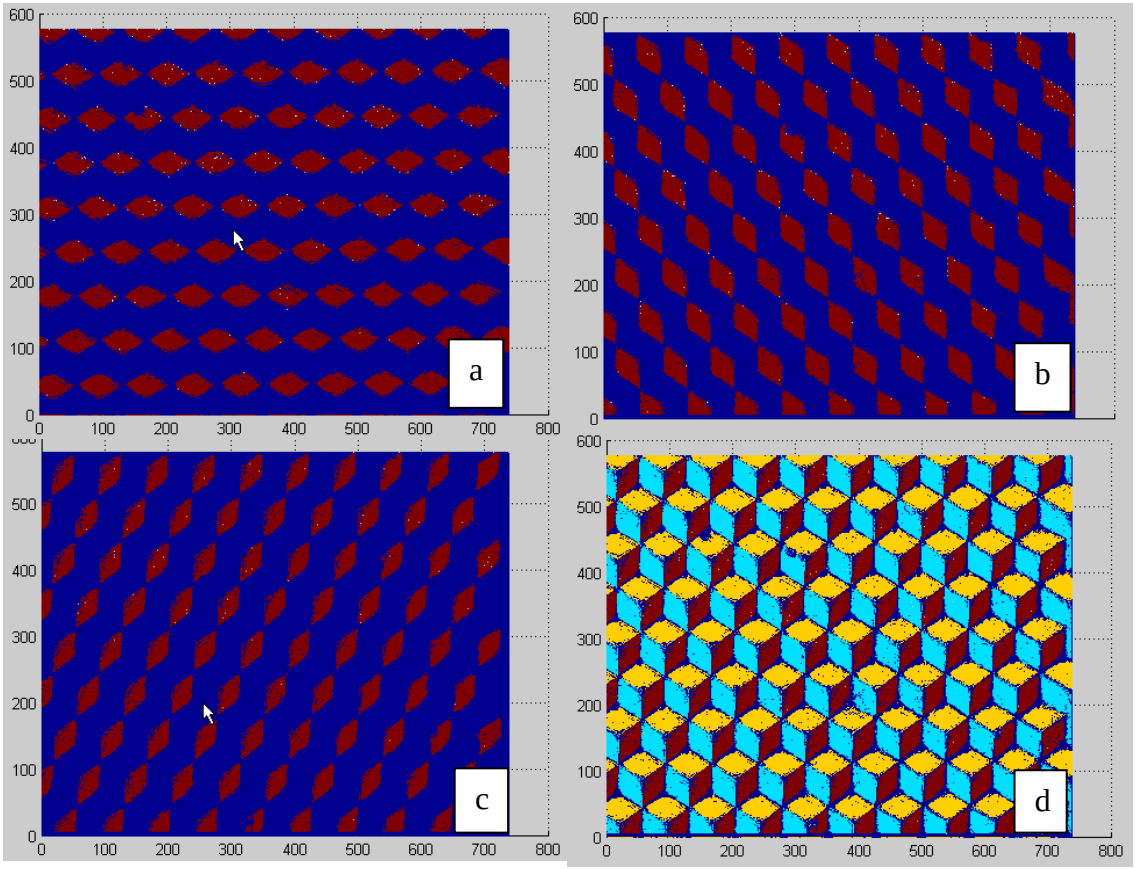

FIGURE 3.2.13: (a-c) Three individual facets (d) all three facets shown together.

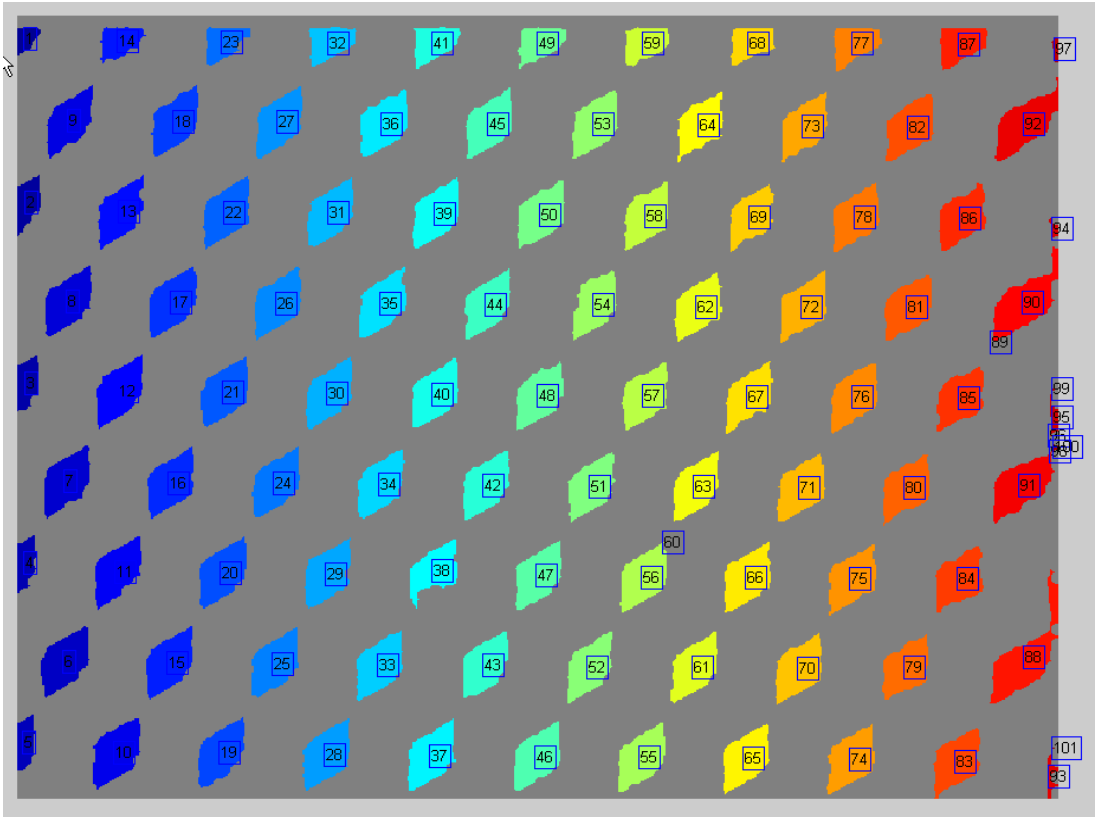

FIGURE 3.2.14: Labeled segments of selected facet of the pyramid pattern.

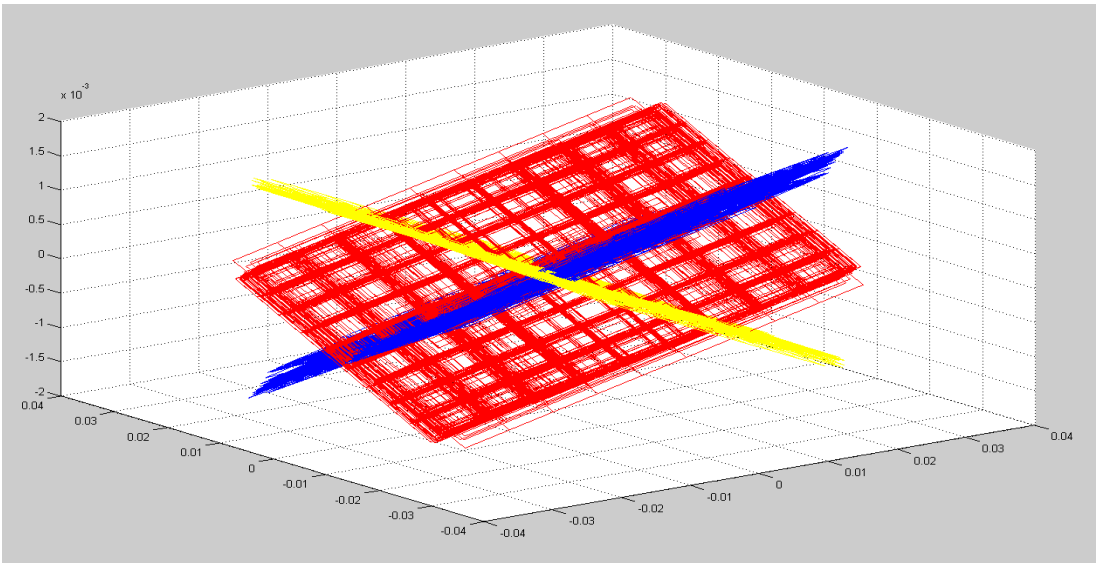

FIGURE 3.2.15: Color coded least squares plane of all facets of the pyramid pattern.

The least squares planes fit on the individual facets are shown in figure 3.2.15, with three facets represented in separate colors. Table 3.2.1 shows the average and standard deviation of angle made by individual facets with respect to the horizontal plane.

Table 3.2.1: Average and standard deviations of calculated normals for facets.

Facets		Angle (Degrees)	
		Average	Std. dev.
1	**Red**	2.693	0.130
2	**Yellow**	2.641	0.211
3	**Blue**	3.088	0.178

Benefits of using multi-scale analysis were briefly mentioned while explaining different segmentation approaches. Segmentation on multi-scale decomposed data is very effective for multi-scale defect characterization. Multi-scale decomposition or transformation could be performed using three different methods, yielding different sub-sets of data. The effectiveness of segmentation directly depends on the obtained sub-sets. Therefore, these three methods will be discussed in detail in the following section.

3.2.4. Transformation Methods for Engineered Surfaces

Only DWF method was considered for this study, because of their non-decimation and shift invariance advantages. Within DWF method, three transformation methods that were considered for this study are described as follows:

- *2D DWF method:* DWT is usually performed in two-steps, with row operations followed by column operations. The same approach could also be used for DWF method. For example, a 2D B3 spline could be used as mother wavelet, and row and columns could be transformed in stages.
- *3D DWF method:* The second methods would be to create a 3D B3 spline and perform row and column transformations simultaneously. The 3D B3 spline is given by,

$$\begin{bmatrix} \frac{1}{256} & \frac{1}{64} & \frac{3}{128} & \frac{1}{64} & \frac{1}{256} \\ \frac{1}{64} & \frac{1}{16} & \frac{3}{32} & \frac{1}{16} & \frac{1}{64} \\ \frac{3}{128} & \frac{3}{32} & \frac{9}{64} & \frac{3}{32} & \frac{3}{128} \\ \frac{1}{64} & \frac{1}{16} & \frac{3}{32} & \frac{1}{16} & \frac{1}{64} \\ \frac{1}{256} & \frac{1}{64} & \frac{3}{128} & \frac{1}{64} & \frac{1}{256} \end{bmatrix}$$

- *3D Hybrid DWF method*: The third method is a hybrid method where the value pertaining to 3D approach is calculated and then the mean value of that calculated value and the actual data point is taken. This method is similar to hybrid median filter used in image processing domain, as an edge preserving method. For structured surfaces with high aspect ratios and sudden height transitions, this method would be able to better preserve the edges at different scales.

The impact of using these methods on the data fusion was studied using two samples – one containing an array of square grids and another a square wave spacing specimen standard. A six-level DWF transformation was performed on the square grid array data using B3 spline. All three methods yield the original data upon inverse transformation, as shown in figure 3.2.16.

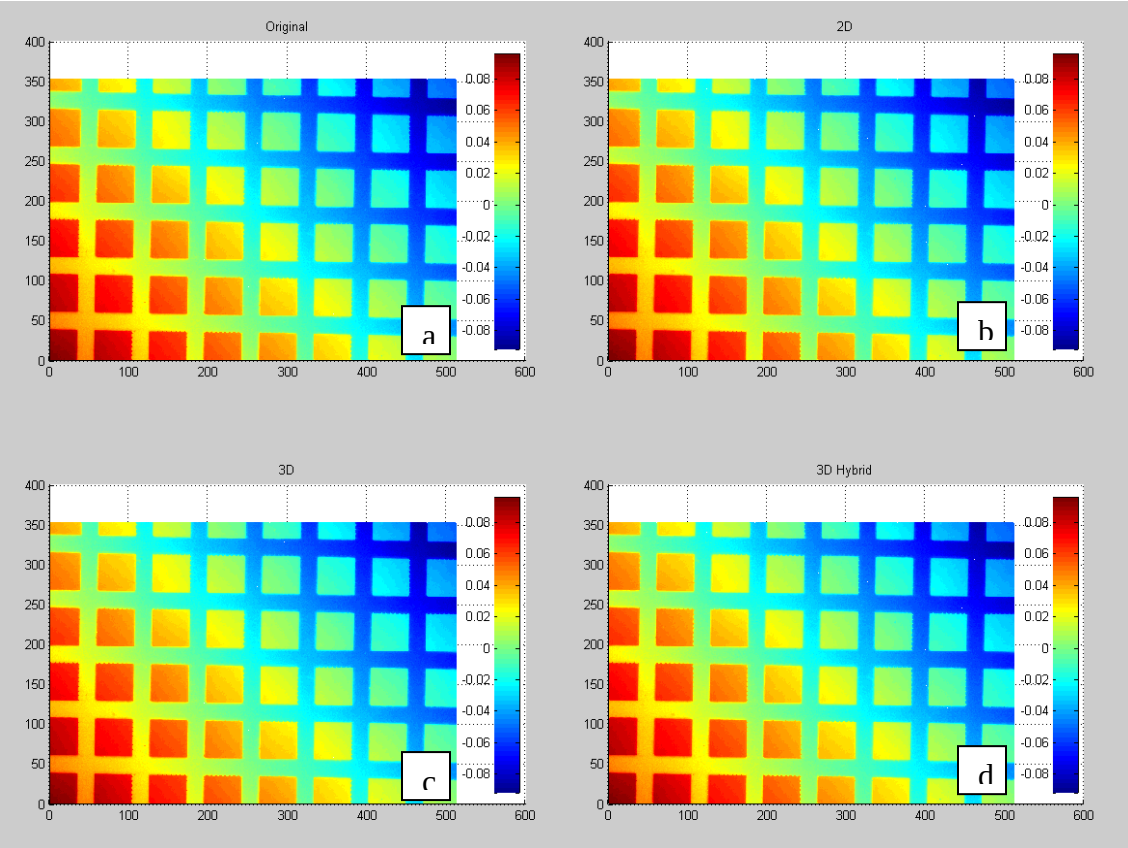

FIGURE 3.2.16: (a) Original data , (b-d) Data obtained after inverse transformation of 6 sub sets obtained of 2D, 3D and 3D Hybrid methods respectively.

The sub sets obtained using 2D, 3D and 3D Hybrid method are shown in figures 3.2.17, 3.2.18 and 3.2.19 respectively. It can be seen that even though the three methods yield the original data back after inverse transformation, the individual sub set data are different when individual sub sets are compared between the three methods. This would result in different fused data when fusion is performed using weighted average methods.

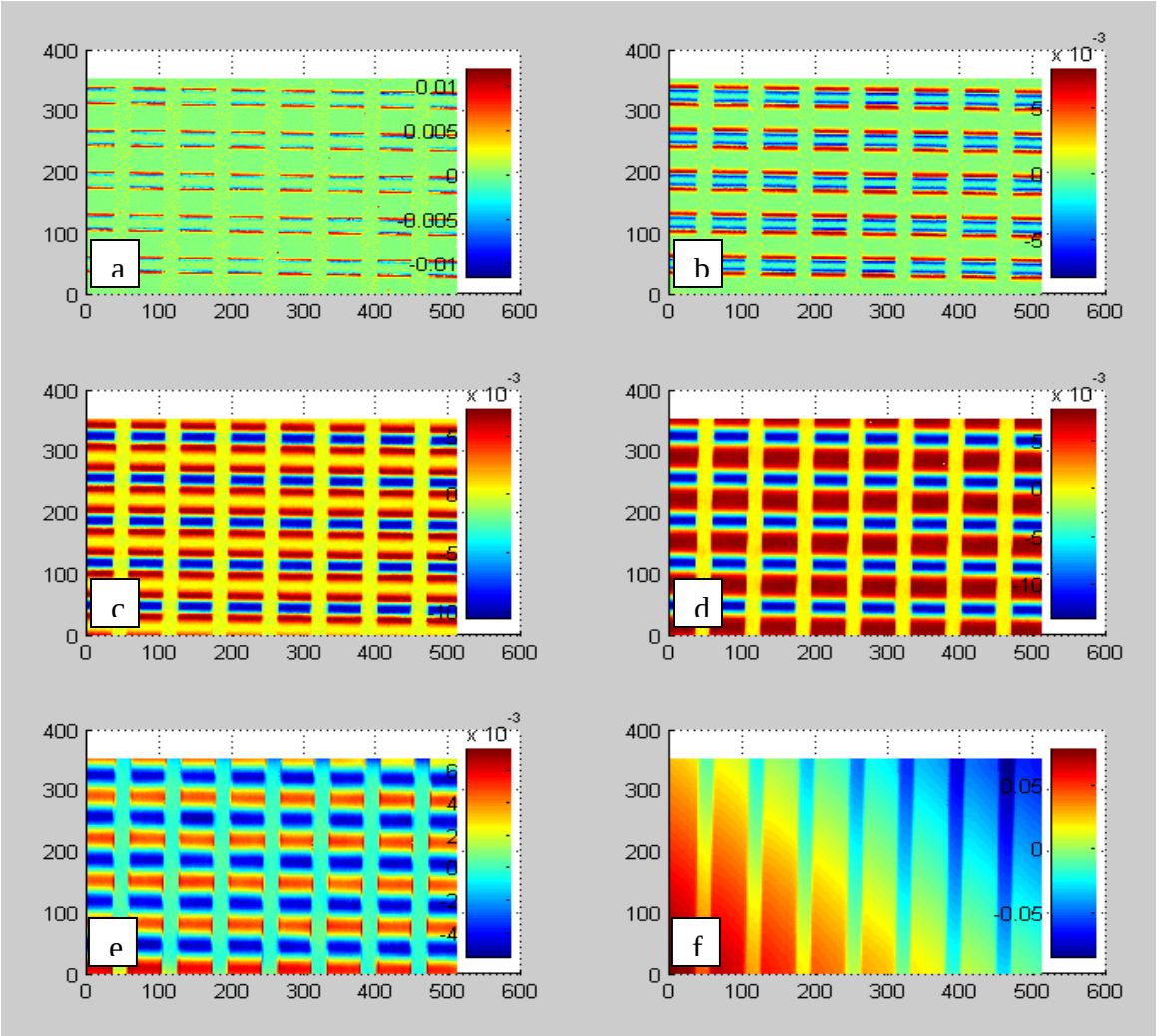

FIGURE 3.2.17: Square grid array sub datasets obtained using 2D method.

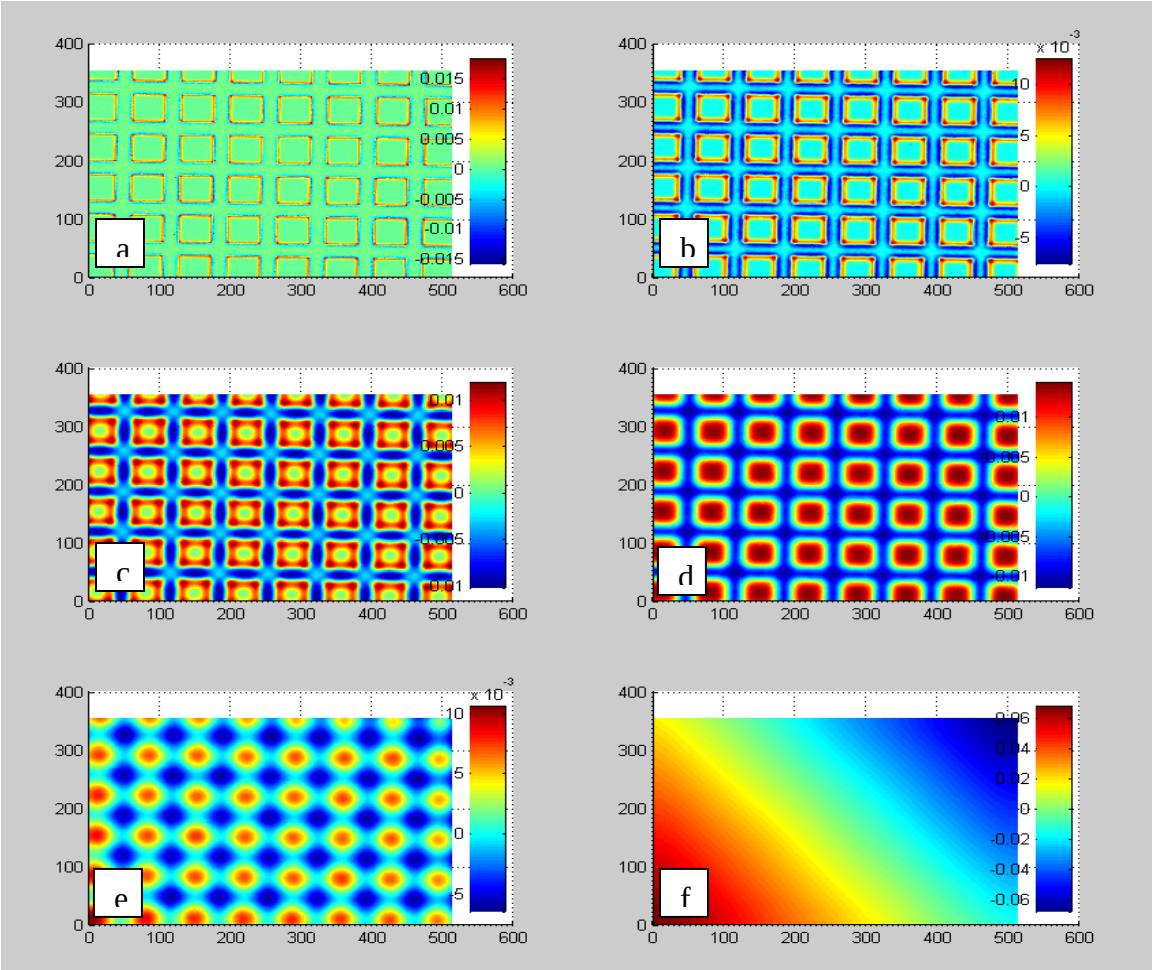

FIGURE 3.2.18: Square grid array sub datasets obtained using 3D method.

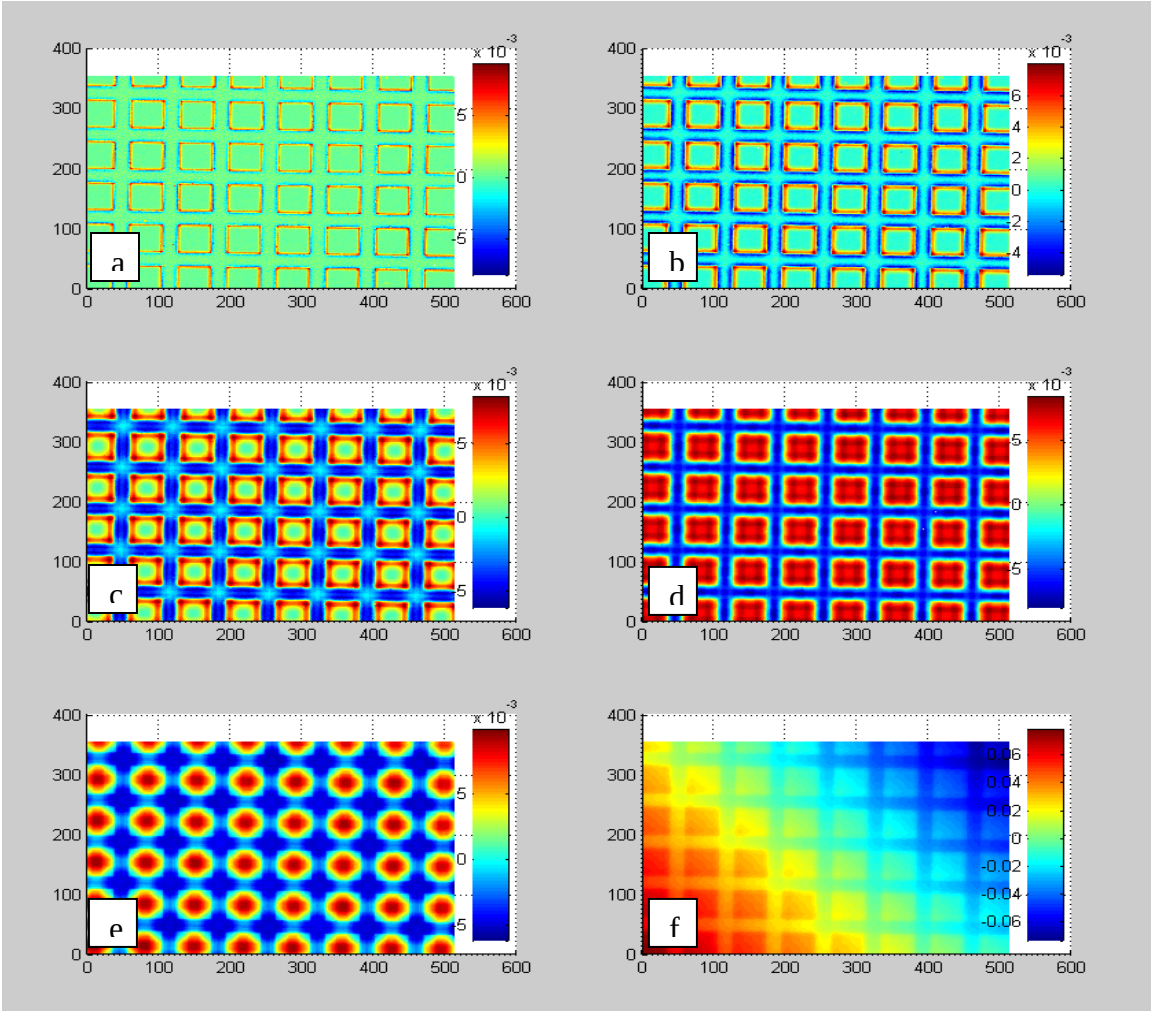

FIGURE 3.2.19: Square grid array sub datasets obtained using 3D Hybrid method.

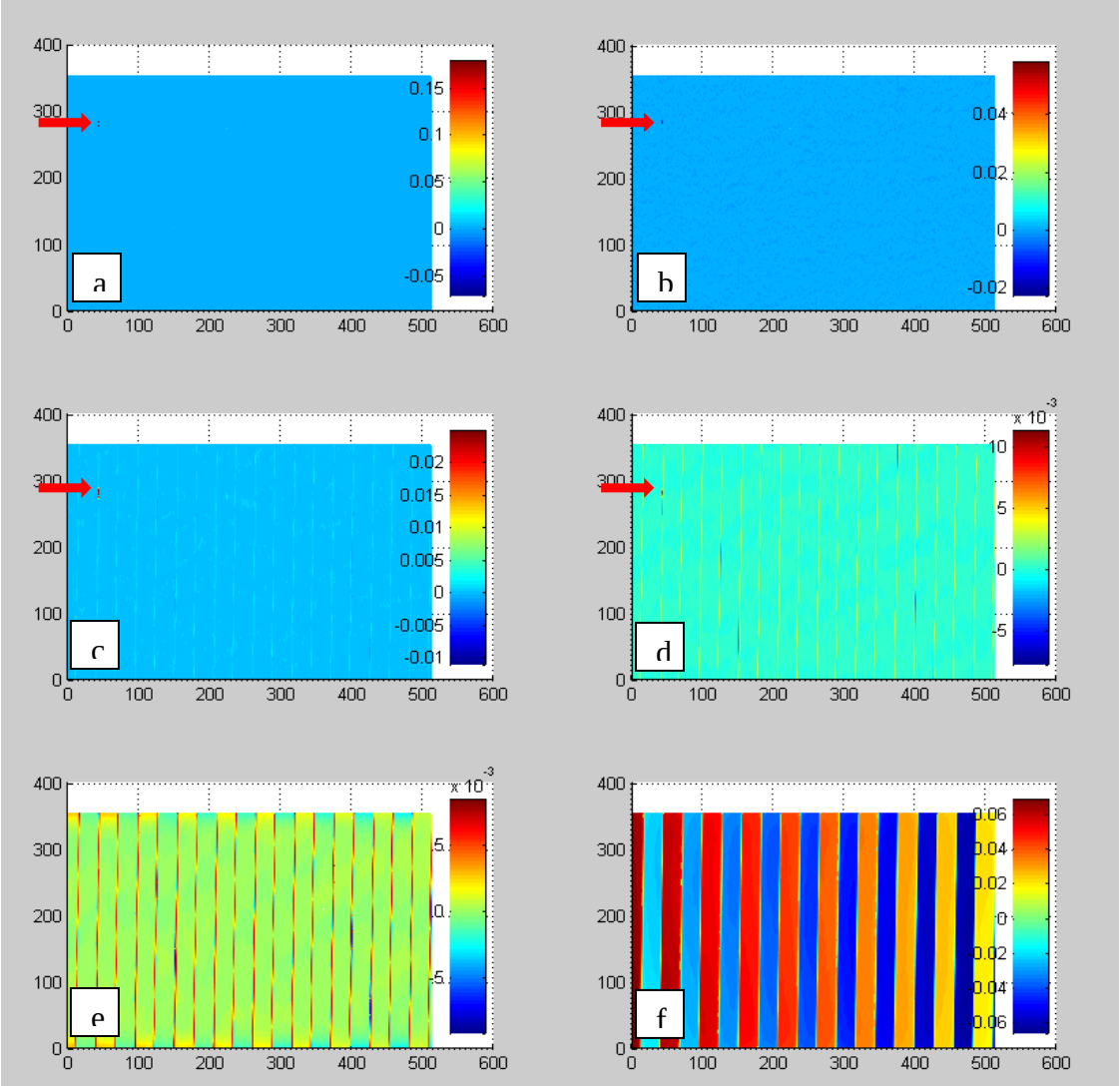

FIGURE 3.2.20: Square wave spacing specimen sub datasets obtained using 2D method.

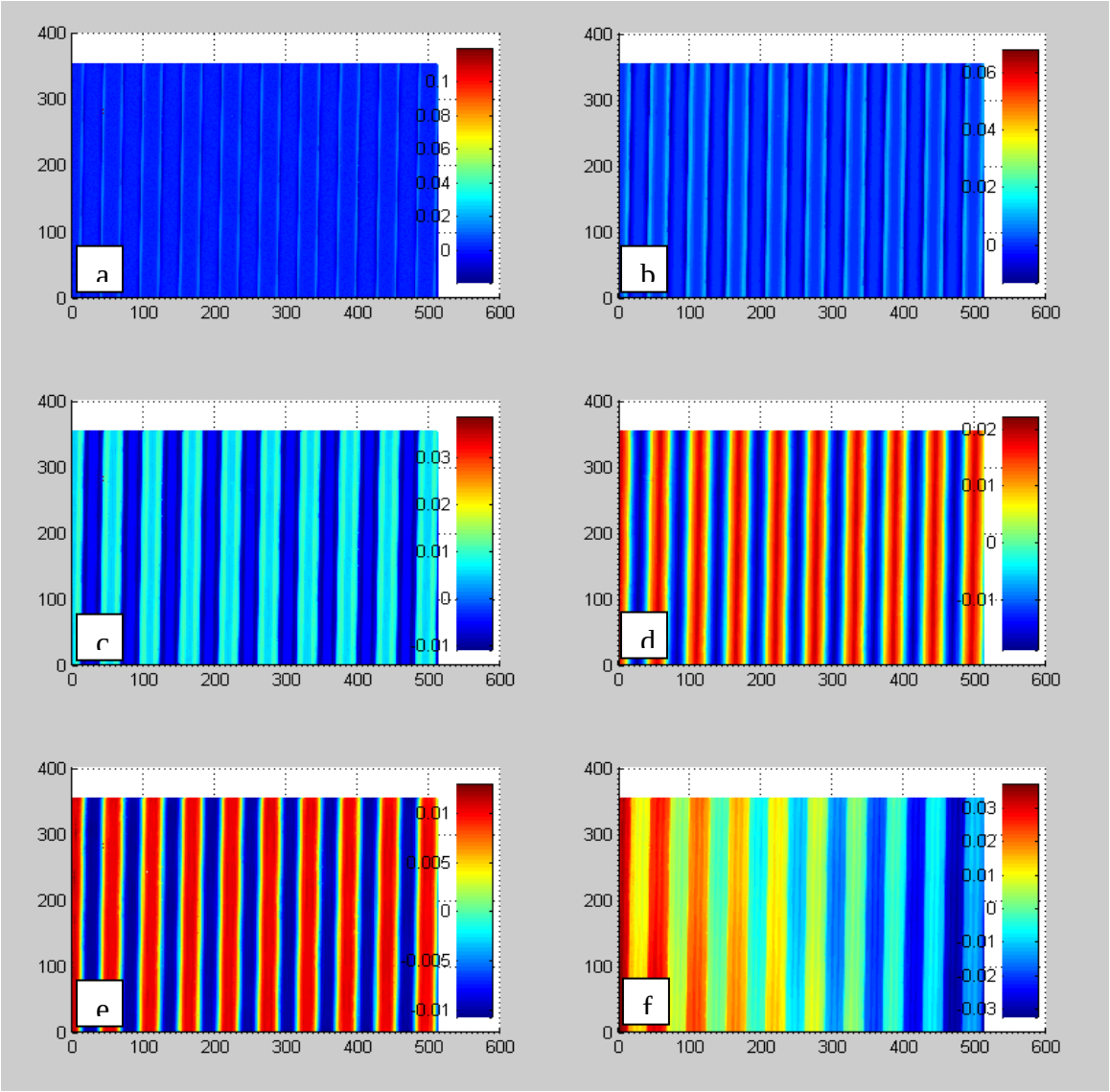

FIGURE 3.2.21: Square wave spacing specimen sub datasets obtained using 3D method.

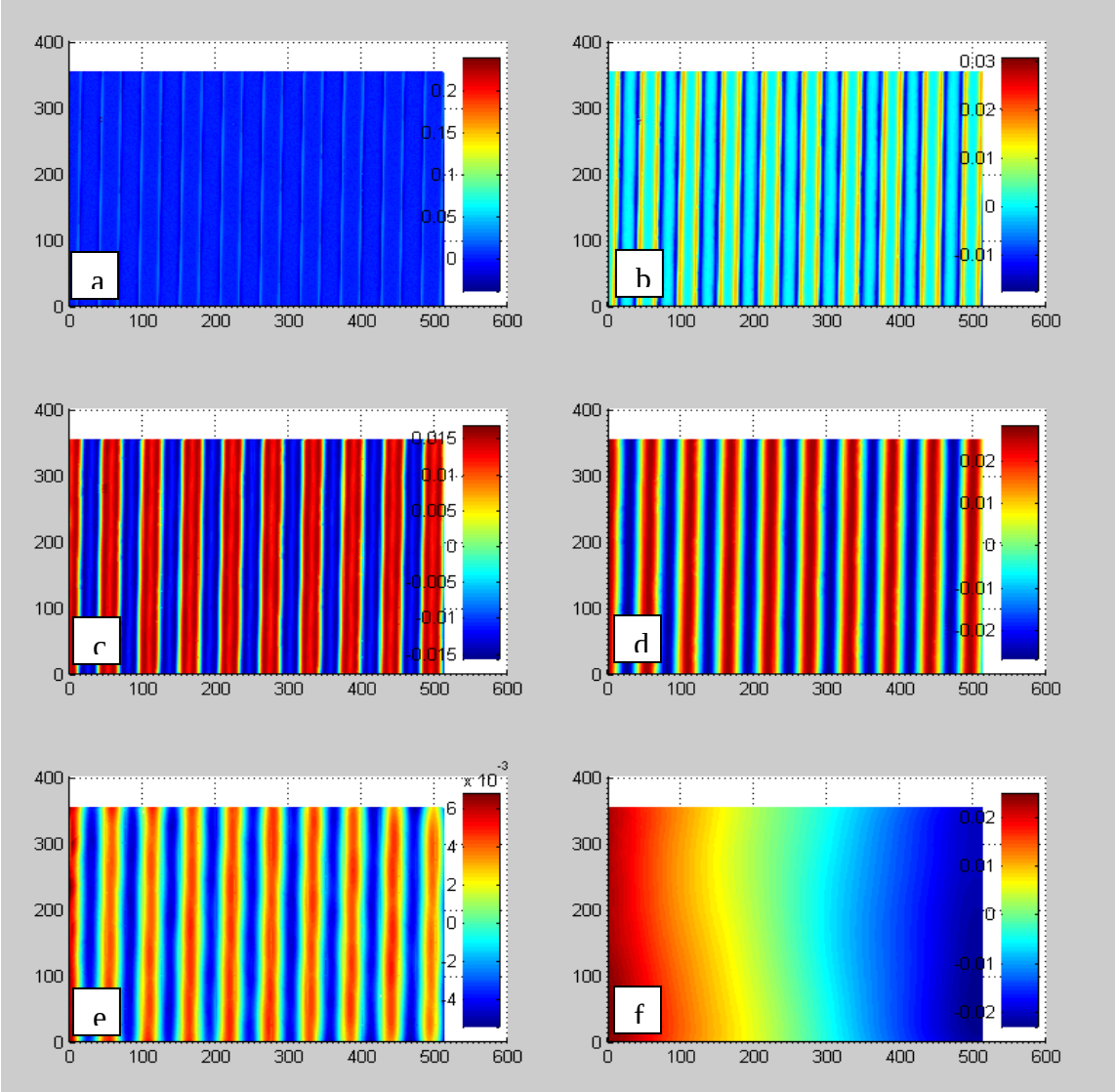

FIGURE 3.2.22: Square wave spacing specimen sub datasets obtained using 3D Hybrid method.

The sub-sets obtained on square wave spacing specimen standard are shown in figures 3.2.20, 3.2.21 and 3.2.22 respectively. From figure 3.2.20, it can be seen that this method could be of potential use for defect characterization (pointed out by four red arrows), as the other two methods do not show this defect effectively. Since the 2D method results in sub-sets which show column wise features more pronounced, this method is not preferred for fusion. Therefore, only 3D and 3D Hybrid methods will be considered for fusion needs, but all three will be considered for fine registration purposes.

The salient differences between three DWF methods were described using two patterned surface samples. It was shown that 2D method was very effective for defect characterization. Since the sub sets obtained using 2D method showed pronounced features along one axis only, it was removed from further study for consideration for data fusion step. All three approaches were able to reproduce the original surface, but individual sub sets were characteristically different. Hence would result in different performance levels for same type of edge detection methods. The impact of transformation methods on edge detection is detailed in the following section.

3.2.5. Impact of Transformation Methods on Edge Detection

Three most commonly used edge detection methods -'Canny', 'Sobel', and 'Watershed', were chosen for this study. The edges obtained from these three methods are different from the perspective of number of points detected, spread etc, as shown in figure 3.2.23. Figure 3.2.23a shows the data obtained on a honed surface, which is converted to a gray scale image. Figure 3.2.23b shows the edges obtained using 'Canny' method performed at single scale. Figure 3.2.23c and d show results obtained using 'Sobel' and 'Watershed' methods respectively. It can be seen from figure 3.2.23d, that 'Watershed' method generates a higher magnitude of control points, which are distributed across the entire area. Even though the 'Watershed' method yields the highest density of data points, it may not be the efficient way as the excessive amount of data points result in increased computation time during alignment.

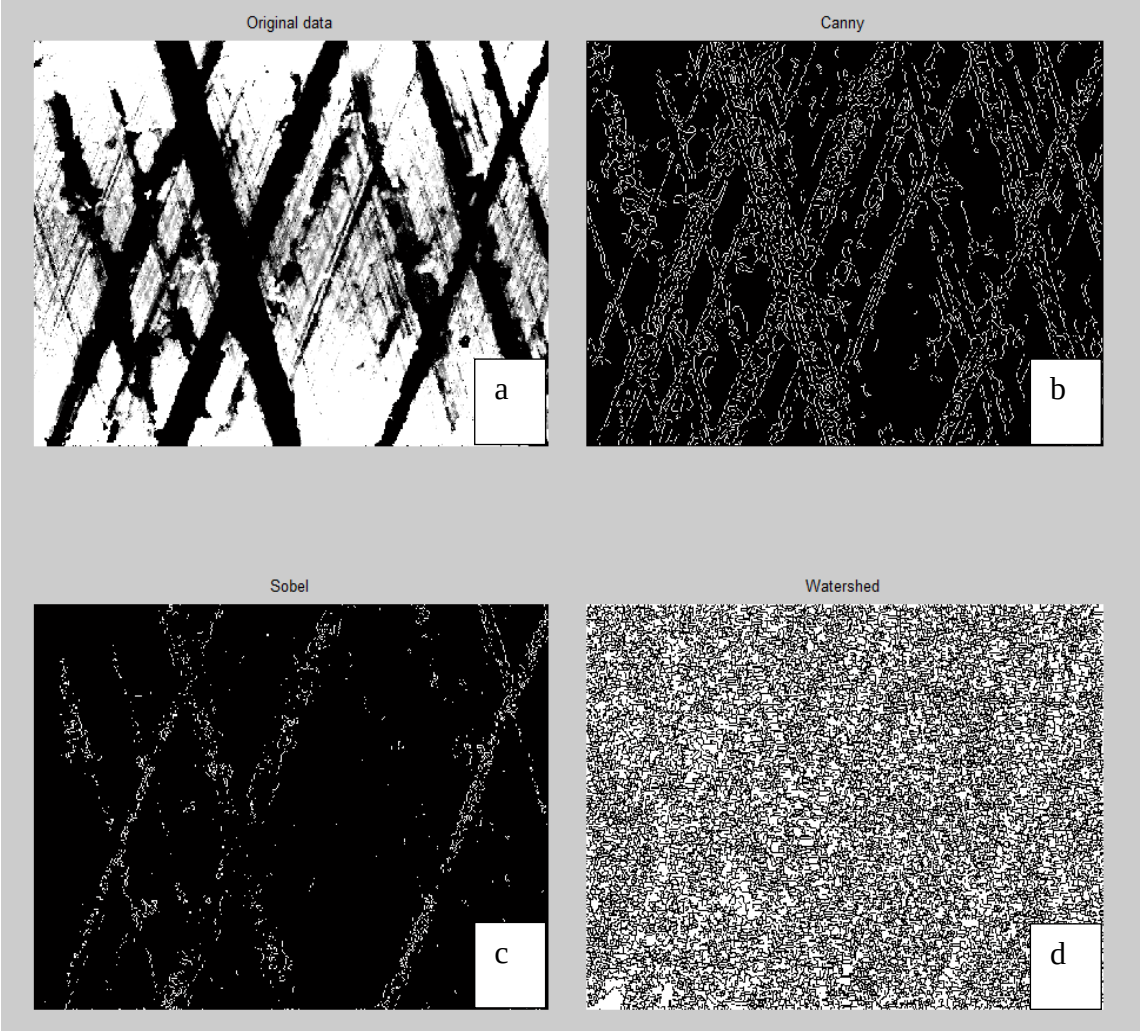

FIGURE 3.2.23: (a) Original Image (b) Edges detected using ‘Canny’ method (c) Edges detected using ‘Sobel’ method (d) Edges detected using ‘Watershed’ method.

For this study, ‘Watershed’ edge detection method was only used on a single-scale, and four levels of decomposition was performed using three methods of decomposition (2D, 3D and 3D Hybrid) and individual sub-images were treated with two edge detection methods (‘Canny’ and ‘Sobel’). Detected edges were combined at increasing levels of decomposition as shown in figures 3.2.24 and 3.2.25. Comparing figures 3.2.23b with 3.2.24 a- d, it can be seen that edges obtained in DWF sub-images are comparatively higher compared to single-scale edge detection.

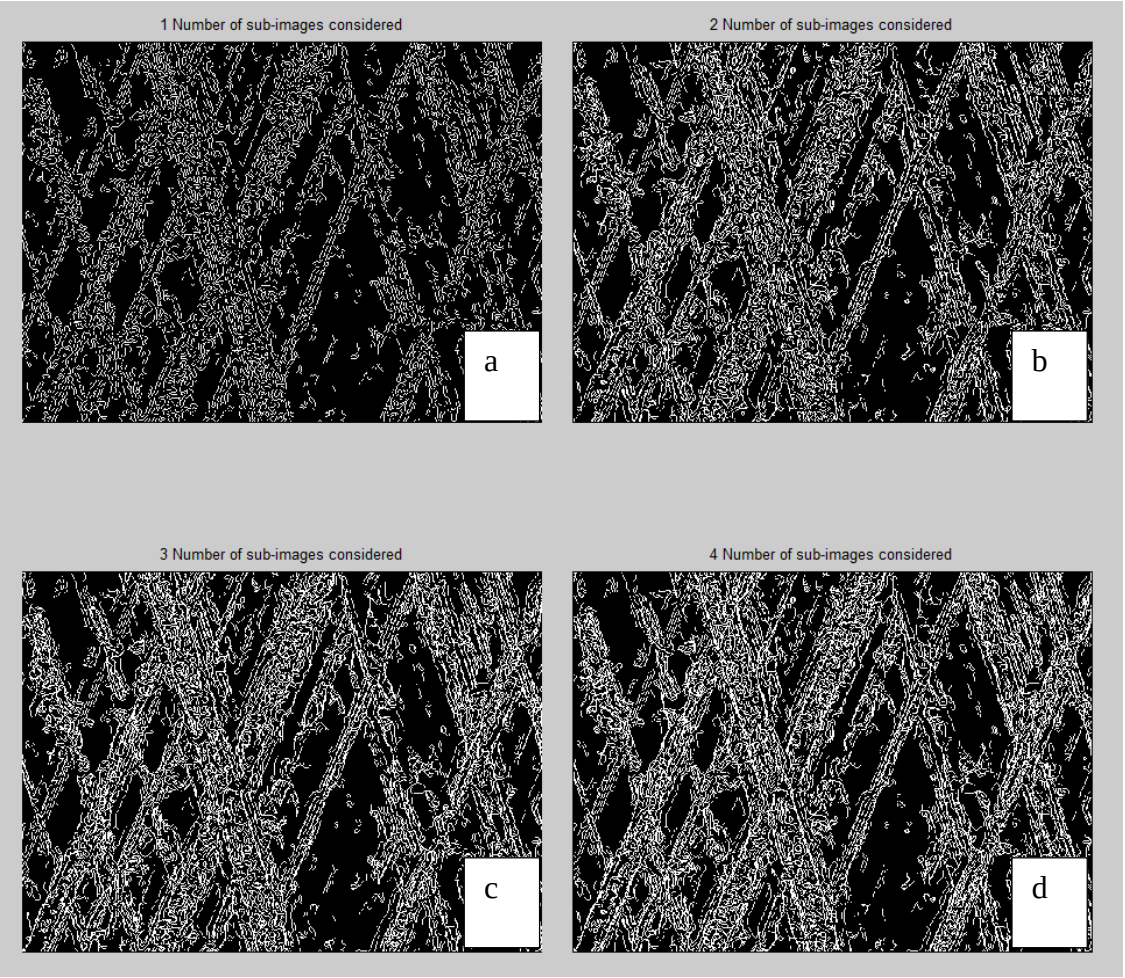

FIGURE 3.2.24: Edges detected using ‘Canny’ method on sub-images obtained using 4 level ‘3D’ DWT method (a) from first sub-image (b) from first two sub-images (c) from first three sub-images and (d)all four sub-images.

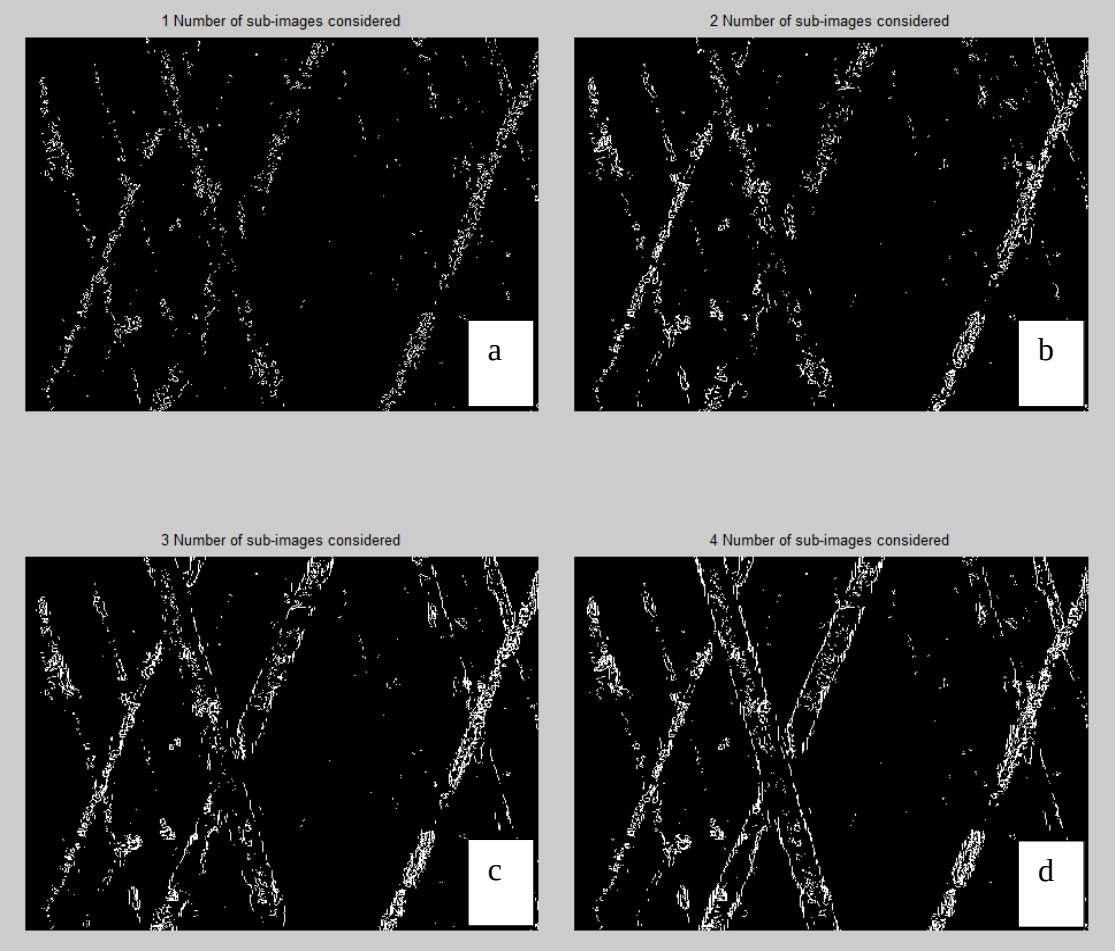

FIGURE 3.2.25: Edges detected using ‘Sobel’ method on sub-images obtained using 4 level ‘3D’ DWT method (a) from first sub-image (b) from first two sub-images (c) from first three sub-images and (d)all four sub-images.

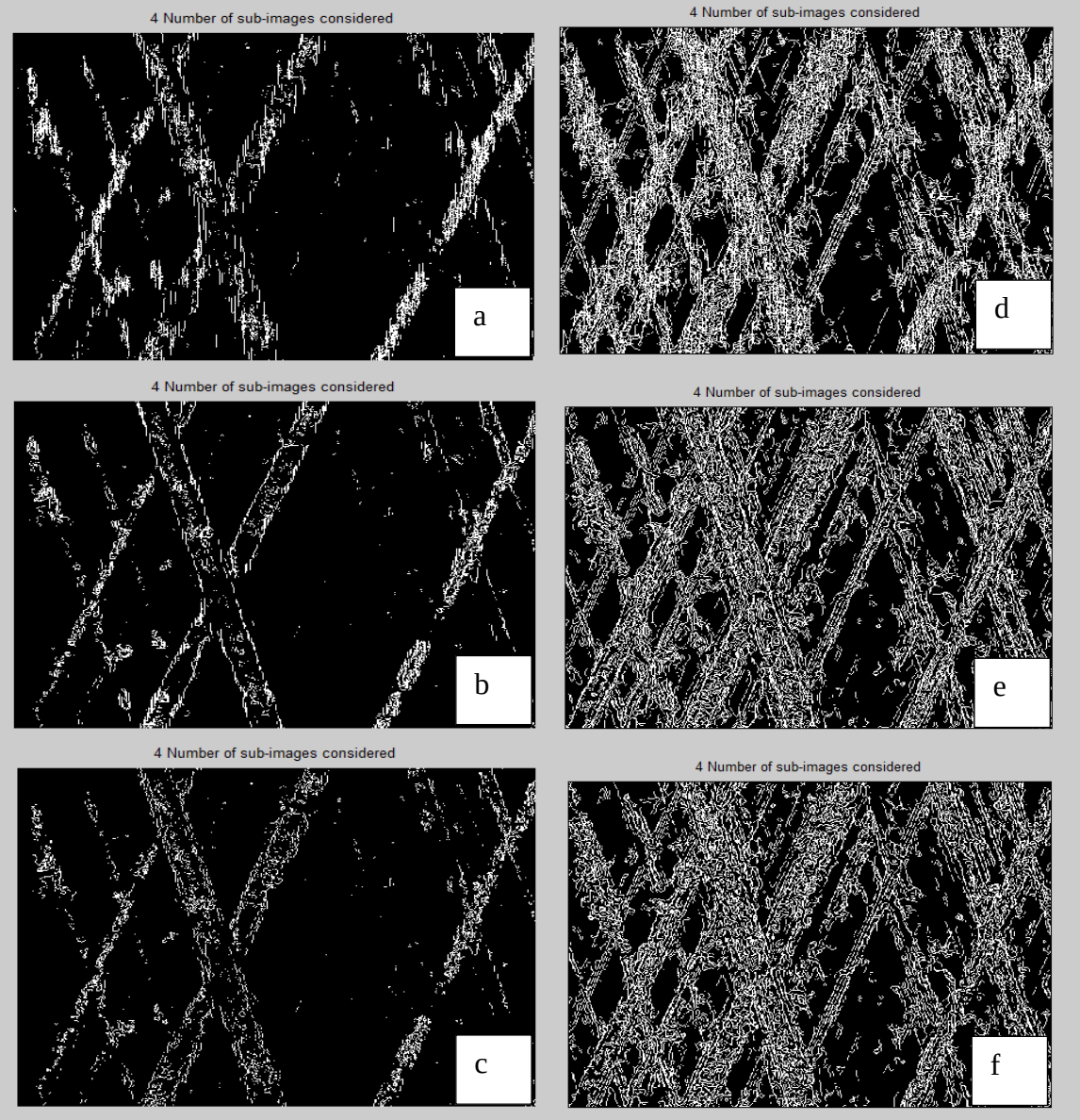

FIGURE 3.2.26: (a-c) Edges detected using 'Sobel' edge detection method on all sub-images obtained using (a) '2D' DWT (b) '3D' DWT (c) '3DH' DWT ; (d-f) Edges detected using 'Canny' edge detection method on all sub-images obtained using (d) '2D' DWT (e) '3D' DWT (f) '3DH' DWT.

Figure 3.2.26 compares edges obtained (when all four sub-images are used) from three DWF methods (2D, 3D and 3D Hybrid) and two edge detection methods ('Canny' and 'Sobel'). Comparing figures 'a' with 'd', 'b' with 'e', and 'c' with 'f', it can be seen that in general 'Canny' edge detection method performs better than 'Sobel' method.

Comparing figures ‘a’ with ‘b’ and ‘c’, and ‘d’ with ‘e’ and ‘f’, it can be seen that ‘2D’ method provides significantly noisy edges. Comparing figures ‘b’ with ‘c’ and ‘d’ with ‘e’, it can be seen that both ‘3D’ and ‘3DH’ method performs similar.

The benefits of using multi-scale decomposed images for edge detection and thereby calculating control points for transformation were discussed in detail. In order to select the transformation method, edge detection method for fine registration, a simulation study was performed, which will be explained in the following section.

3.2.6. Impact of Noise and Transformation Methods on Fine Registration

In order to characterize the impact of coarse registration, single scale and multi-scale edge detection methods and transformation methods, a study was performed on previously generated original and noisy versions of 12 datasets. First simulation run was performed as a best case scenario for axial and angular alignment, where the original image and the noisy version of the image were considered with no translation or rotational errors. Average translational error was computed from the results obtained from 10 noise types and is shown in figure 3.2.27a, along with the observed variations. The computation time on a HP computer (with Intel ® Core™ i5, 2.8 Ghz processor, 6 GB RAM and 64-bit operating system) is shown in figure 3.2.27b. From figure 3.2.27a, it can be seen that the single scale ‘Watershed’ edge detection performs significantly better compared to all other options and the next best performance is obtained from ‘Canny’ and ‘Sobel’ edge detection methods when ‘3D’ method of decomposition is used and edges obtained from at least 3 levels of sub images are considered.

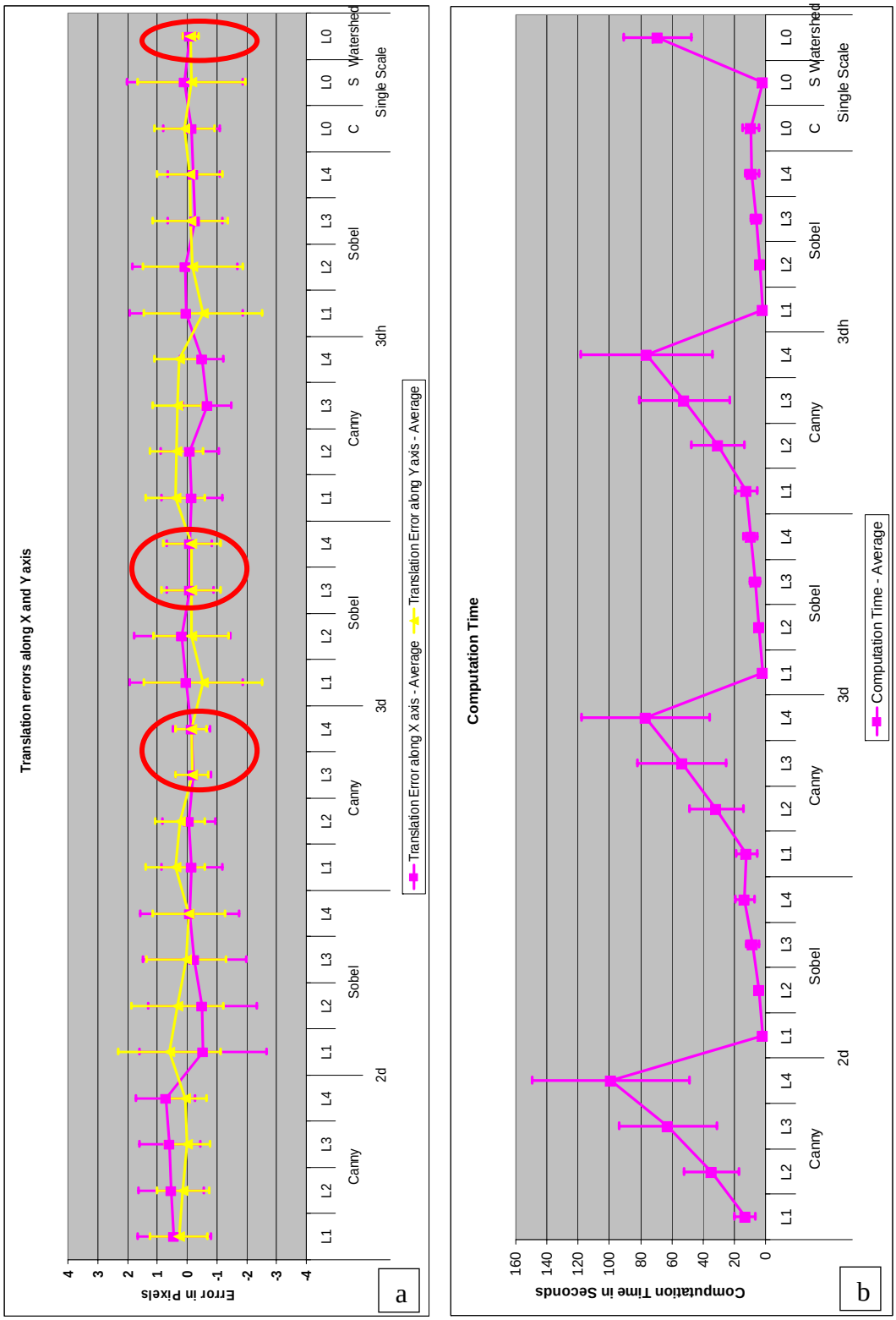

FIGURE 3.2.27: (a) Average and standard deviation of calculated translation values using different decomposition, edge detection options (b) Computation time for the different options, under zero translation and angular misalignment.

FIGURE 3.2.28: (a) Average and standard deviation of calculated translation values using different decomposition, edge detection options (b) Computation time for the different options, under 1 pixel translation and zero angular misalignment.

For the second run, the noisy image was shifted by one pixel along both axis and the results are shown in figure 3.2.28 a and b. For this scenario, single scale 'Watershed' option performed better followed by 'Canny' and 'Sobel' methods when '3D' method of decomposition was used and edges obtained from at least 3 levels of sub images are considered. 'Watershed' method yielded the translation offset values closest to one (which was the induced offset) and had the least variation.

For the third run, the noisy image was shifted by four pixels along both axis and rotated clockwise by 1°. The results are shown in figure 3.2.29 a and b. For this scenario too, single scale 'Watershed' option performed better followed by 'Canny' method when '3D Hybrid' method of decomposition was used and edges obtained from at least 3 levels of sub images are considered. 'Watershed' method yielded the translation offset values closest to four (which is the expected offset after 1° rotation) and has the least variation

For the fourth run, the noisy image was treated with a convolution filter and 1° rotation. The results are shown in figure 3.2.30 a and b. For this scenario, single scale 'Watershed' option performed significantly better followed by 'Canny' method when '3D Hybrid' method of decomposition was used and edges obtained from at least 3 levels of sub-images are considered.

The performance results for 'Watershed' edge detection method is summarized in the table 3.2.2. The performance results for 'Canny' edge detection method on sub images obtained using 3D Hybrid method when first three decomposition levels are considered are summarized in table 3.2.3 and table 3.2.4 summarizes the performance when all four levels are considered.

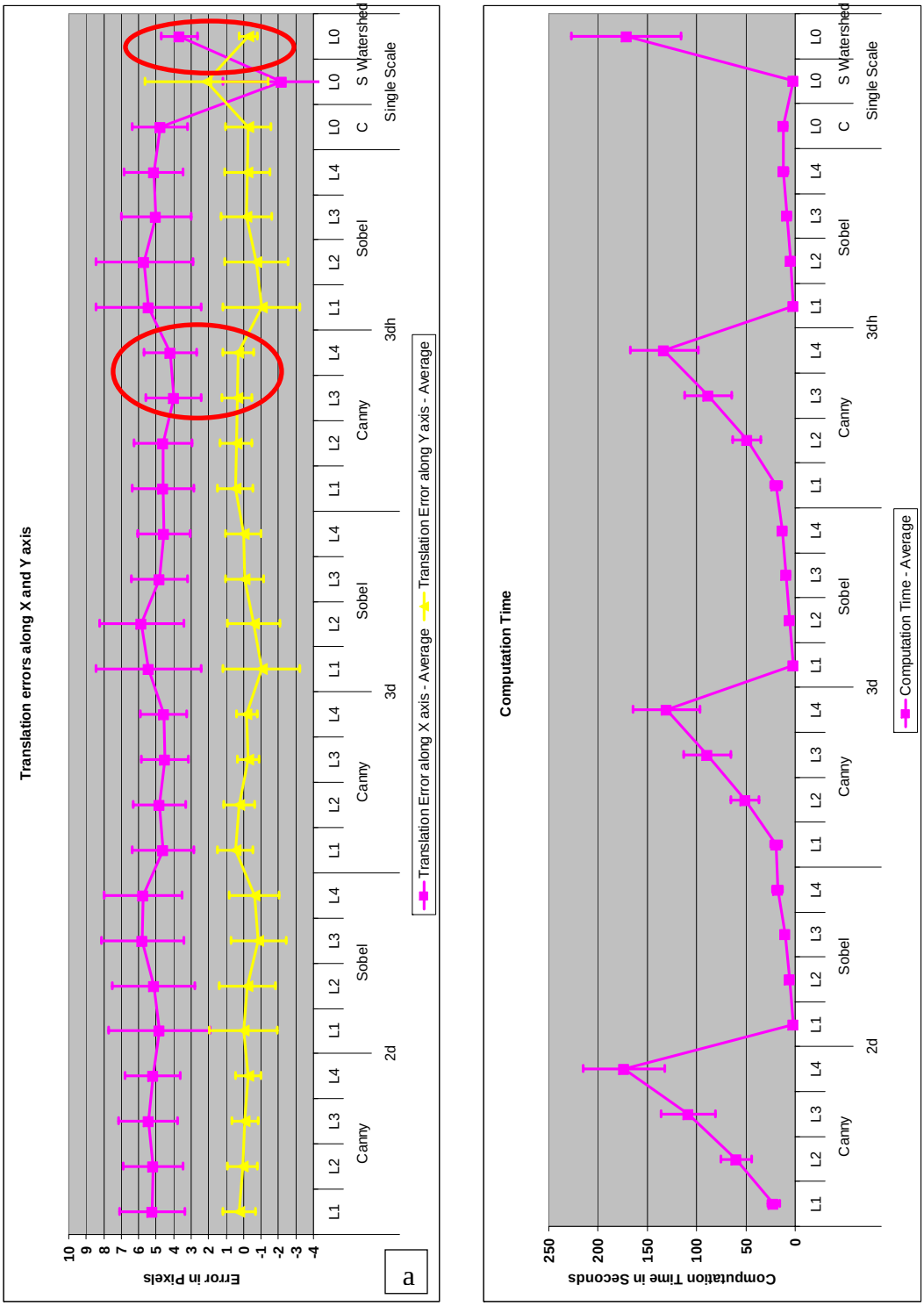

FIGURE 3.2.29: (a) Average and standard deviation of calculated translation values using different decomposition, edge detection options (b) Computation time for the different options, under 4 pixel translation and 1° angular misalignment.

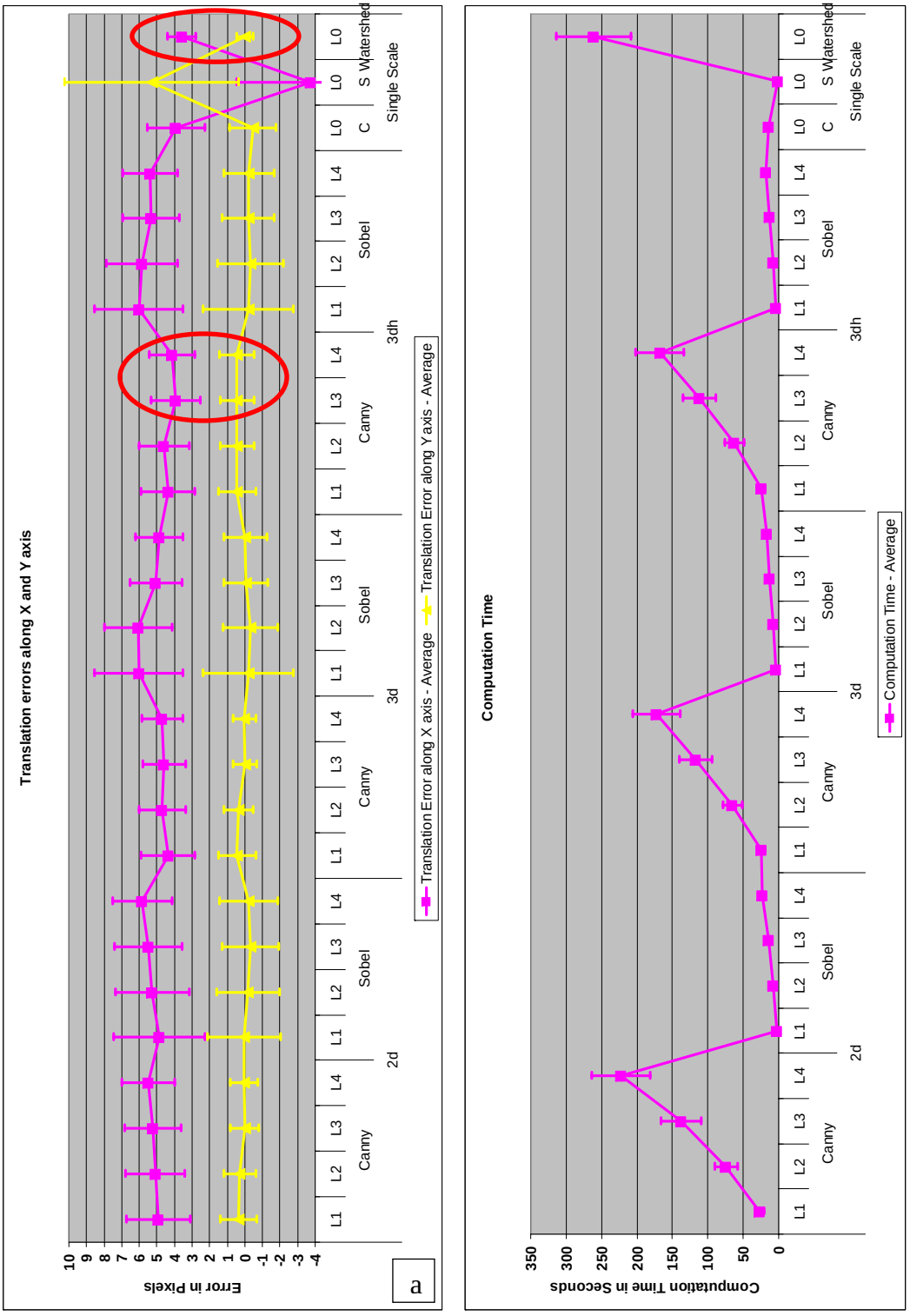

FIGURE 3.2.30: (a) Average and standard deviation of calculated translation values using different decomposition, edge detection options (b) Computation time for the different options, under convolution and 1° angular misalignment.

TABLE 3.2.2: Performance results of ‘Watershed’ edge detection method on single-scale images.

Watershed Edge Detection Method				
Sl.No	Test Type	Translation Error Std. Dev. (in pixels)		Avg. Computation Time (in Sec)
		X	Y	
1	With no misalignment	0.245	0.268	69
2	With 1 pixel misalignment	0.266	0.297	82
3	With 4 pixel misalignment	1.059	0.542	171
4	With 4 pixel misalignment and blurr	0.808	0.461	261

TABLE 3.2.3: Performance results of ‘Canny’ edge detection method on first three sub images obtained using a 4-level 3D Hybrid decomposition method.

Canny Edge Detection Method (3D Hybrid + L3)				
Sl.No	Test Type	Translation Error Std. Dev. (in pixels)		Avg. Computation Time (in Sec)
		X	Y	
1	With no misalignment	0.81	0.844	52
2	With 1 pixel misalignment	0.863	0.848	56
3	With 4 pixel misalignment	1.584	0.855	88
4	With 4 pixel misalignment and blurr	1.307	0.954	112

TABLE 3.2.4: Performance results of ‘Canny’ edge detection method on all sub images obtained using a 4-level 3D Hybrid decomposition method.

Canny Edge Detection Method (3D Hybrid + L4)				
Sl.No	Test Type	Translation Error Std. Dev. (in pixels)		Avg. Computation Time (in Sec)
		X	Y	
1	With no misalignment	0.727	0.834	76
2	With 1 pixel misalignment	0.809	0.871	82
3	With 4 pixel misalignment	1.505	0.879	132
4	With 4 pixel misalignment and blurr	1.307	0.969	167

Comparing the performance results summarized in tables 3.2.2, 3.2.3 and 3.2.4, it can be seen that even though single scale ‘Watershed’ edge detection method takes approximately twice the computation time of ‘Canny’ edge detection method (when at least three sub-images are considered), it is able to align the datasets within one pixel accuracy. Therefore, single scale ‘Watershed’ edge detection is selected as the preferred method for obtaining the control points for fine registration.

3.3. Summary

Coarse registration using Normalized Cross Correlation (NCC) was explained and a simulation study was performed to understand the impact of noise and defocus on coarse registration. It was shown that type of noise had negligible impact on coarse registration. Then segmentation and transformation used for fine registration was discussed. Multiple domains based and multiple parameter based segmentation was described. The potential advantages of multi-scale decomposition based edge detection and feature detection for effective characterization and defect analysis on engineered surfaces was explored. The impact of three different transformation methods on edge detection was explained.

A simulation study was conducted to find the impact of noise and transformation methods on fine registration. Based on this study, single scale ‘Watershed’ method was chosen as the preferred edge detection method. Among multi-scale methods, it was demonstrated that the performance is highly dependent on the type of surface. ‘Canny’ was chosen as the preferred method when ‘3D’ or ‘3D Hybrid’ method of decomposition is used and at least 3 levels of sub-images are considered.

After careful analysis of coarse registration capabilities, transformation methods, edge detection methods and fine registration, the next step is to evaluate the fusion methods and fusion metrics. Various single-scale and multi-scale fusion metrics have been proposed for image quality analysis purposes. These fusion metrics performance in fusion of data pertaining to surface metrology domain needs to be explored. Different weighted average based fusion schemes have been developed in order to generate fused data that would represent both the datasets, compared to scenario when either one is individually used. The capability of these fusion methods for different types of surface data needs to be compared in order to select the robust method that could handle most types of data and yield high synergy of data under consideration.

CHAPTER 4: FUSION STRATEGIES AND METRICS

In the previous chapter, the impact of translational and angular misalignment, and noise on coarse registration was analyzed. Three transformation methods and their impact on edge detection were discussed. Then the impact of noise and transformation methods on fine registration was analyzed. Based on simulation studies, 'Watershed' was chosen for single-scale based edge detection.

After coarse and fine registration, the next major step in Multi-Scale Data Fusion (MSDF) is data fusion. Data fusion can be performed at pixel level using simple methods like using the maximum, minimum or average value of the datasets. For example, when maxima based data fusion is performed, the following rule is used $F(i,j) = \text{Max}\,[A(i, j), B(i, j)]$, where $F(i, j)$ is a pixel in the fused data and $A(i, j)$, $B(i, j)$ are the corresponding pixels in both data. Apart from these methods, weighted averages could also be used. In order to evaluate the performance of different fusion methods, fusion metrics are used. Since there are multiple fusion metrics, performance evaluation and selection of the fusion metrics is critical. Therefore, various single-scale and multi-scale fusion metrics will be studied for their performance and then the selected fusion metrics will be used as performance metrics to study the selected fusion methods.

4.1. Fusion Metrics

4.1.1. Single-scale Based Performance Metrics

These metrics are mostly useful for characterizing single-scale data fusion methods, but can also be used for multi-scale data fusion methods for their simplicity. The most commonly used metrics are as below

- *Root Mean Square Error (RMSE) :* $RMSE = \sqrt{\frac{1}{NM}\sum_{i=1}^{N}\sum_{j=1}^{M}\left|R(i,j)-F(i,j)\right|^2}$,

  where *R* denotes reference data, *F* denotes fused data, *(i, j)* a given data point and *N x M* is the size of the data. *RMSE* increases with the increase in deviation between *R* and *F*. The method which results in least *RMSE* value is preferable.

- *Peak Signal to Noise Ratio (PSNR)*

  $PSNR = 10\log_{10}\left(\frac{L^2}{\frac{1}{NM}\sum_{i=1}^{N}\sum_{j=1}^{M}\left|R(i,j)-F(i,j)\right|^2}\right)$, where *L* is the number of gray levels in the image, after the data is converted to a normalized gray scale image d based on the heights in the data. *PSNR* will be infinity when *R* and *F* are exactly same. The data fusion process that yields the highest *PSNR* value is desirable.

- *Mutual Information (MI)*

  $MI = \sum_{i_1=1}^{L}\sum_{i_2=1}^{L} h_{R,F}(i_1,i_2)\log_2\frac{h_{R,F}(i_1,i_2)}{h_R(i_1)h_F(i_2)}$, where $h_{R,F}$ denotes the normalized joint gray level histogram images *R* and *F*, obtained by converting the datasets into gray scale images and h_R, h_F are the normalized marginal histograms of the two images.

- *Universal Quality Index (UQI)[158]*

  $UQI = \frac{4\sigma_{xy}\overline{x}\overline{y}}{(\sigma_x{}^2 + \sigma_y{}^2)[(\bar{x})^2 + (\bar{y})^2]}$, where *x* and *y* denotes the reference and test images obtained by converting the datasets into gray scale images and

  $$\bar{x} = \frac{1}{N}\sum_{i=1}^{N} x_i \quad \bar{y} = \frac{1}{N}\sum_{i=1}^{N} y_i$$

  $$\sigma^2{}_x = \frac{1}{N-1}\sum_{i=1}^{N}(x_i - \bar{x})^2$$

  $$\sigma^2{}_y = \frac{1}{N-1}\sum_{i=1}^{N}(y_i - \bar{y})^2$$

  $$\sigma_{xy} = \frac{1}{N-1}\sum_{i=1}^{N}(x_i - \bar{x})(y_i - \bar{y})$$

  UQI calculates the amount of salient information that has been effectively transferred from image *x* to image *y*. The possible values for *UQI* range from -1 to 1 and the best value 1 would be achieved images x and y are exact.

- *Overall Cross Entropy (CE)* : $CE(X,Y;F) = \frac{CE(X;F) + CE(Y;F)}{2}$, where

  $CE(X;F) = \sum_{i=0}^{L} h_X(i)\log_2 \frac{h_X(i)}{h_F(i)}$ and *X, Y* are the source images and *F* is the fused image, obtained by converting the datasets into gray scale images

4.1.2. Multi-scale Based Performance Metrics

These metrics are based on single-scale metrics but have been adapted for multi-scale data. Many of single-scale performance metrics could be directly applied to the individual scale images. The process would in a series of results corresponding to the

level of decomposition performed. These results could be averaged or weighted averaged to calculate the final result.

- *Multi Scale Root Mean Square Error (MS-RMSE)*

$MSRSME = \frac{1}{n}\sum_{j=1}^{n} RMSE_j$, where, $RMSE_j$ is the root mean square error value calculated on individual scale image j after n-level decomposition of original and fused images.

- *Multi Scale Structural Similarity Index (MS-SSIM)* [159, 160]

$$MS-SSIM(X,Y) = \left[l_M(X,Y)\right]^{\alpha M} \cdot \prod_{j=1}^{M}\left[c_j(X,Y)\right]^{\beta_j}\left[s_j(X,Y)\right]^{\gamma_j}$$

where, one of the original datasets X and the fused dataset Y are taken and both are decomposed to M levels. $l_M(X,Y)$ is the luminance comparison factor, which is computed only at the largest scale M and $c(X,Y)$ and $s(X,Y)$ are the contrast and structural similarity comparison factors computed at all scales.

$$l(X,Y) = \frac{2\mu_x\mu_y + C_1}{\mu_x^2 + \mu_y^2 + C_1}$$

$$c(X,Y) = \frac{2\sigma_x\sigma_y + C_2}{\sigma_x^2 + \sigma_y^2 + C_2}$$

$$s(X,Y) = \frac{\sigma_{xy} + C_3}{\sigma_x\sigma_y + C_3}$$

where μ_x, σ_x and σ_{xy} are mean of X, standard deviation of X and covariance of X and Y respectively and C_1, C_2 and C_3 are small constants given by $C1 = (K_1L)^2$, $C_2 = (K_2L)^2$ and $C_3 = C_2/2$, where L is the dynamic range of the gray scales (255), $K_1 << 1$ and $K_2 << 1$. α, β, γ are parameters chosen according to the importance of three factors – luminance,

contrast and structural similarity. When $\alpha = \beta = \gamma = 1$, and $C_1 = C_2 = 0$, the structural similarity index results in universal image quality index.

Instead of calculating an average value for *RMSE* and *SSIM* from all the sub datasets, the individual values are treated independently for the proposed analysis.

4.1.3. Evaluation of Performance Metrics

In order to characterize the performance of individual metrics, previously used set of 12 datasets and 11 noisy versions of those datasets were evaluated using single-scale based metrics (RMSE, PSNR, CE, MI, UQI and SSIM) and multi-scale based metrics (MS-SSIM and MS-RMSE). With the known levels of noise that was added to the data, the expected quality level should closely track the noise levels demonstrating a specific trend, as shown in figure 4.1.1.

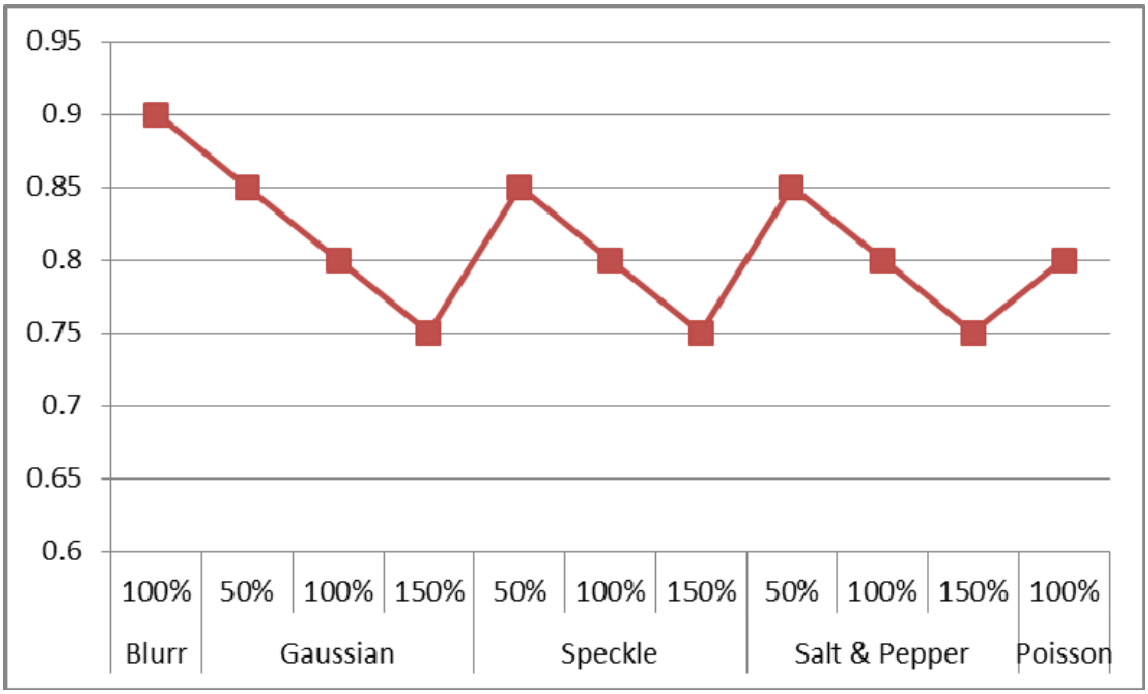

FIGURE 4.1.1: Expected quality metric to correspond to the levels of additive noise.

RMSE results (shown in figure 4.1.2) show that it is able to differentiate between noise levels within each data type, but there is no correlation between data types, as the metric doesn't follow the expected trend shown in figure 4.1.1. PSNR (shown in figure 4.1.3), and CE (shown in figure 5.1.3) perform similarly.

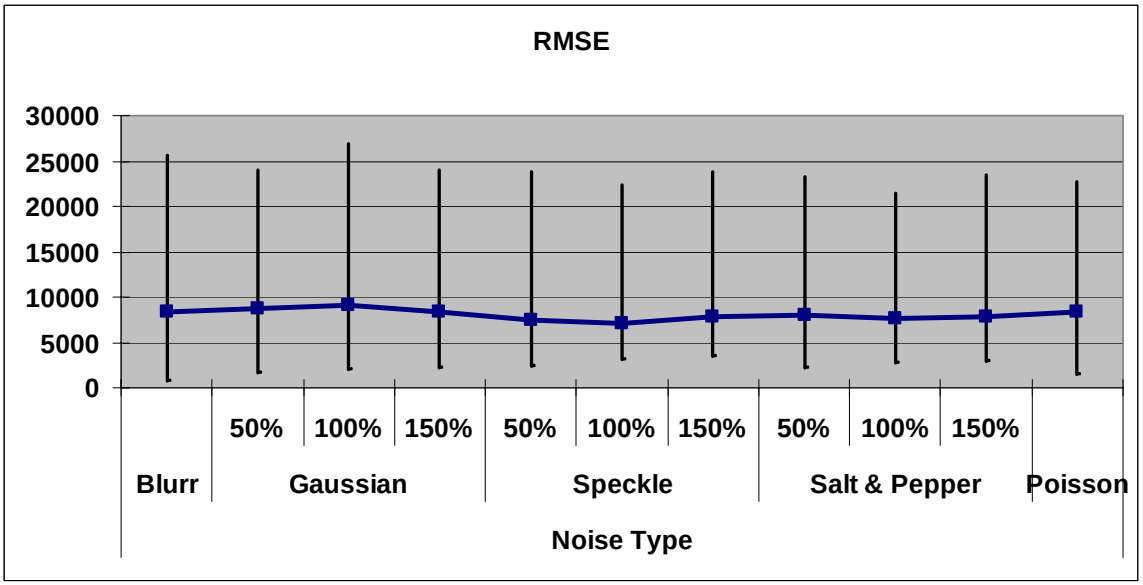

FIGURE 4.1.2: Root Mean Square Error (RMSE) values obtained on 12 datasets with 11 noise levels.

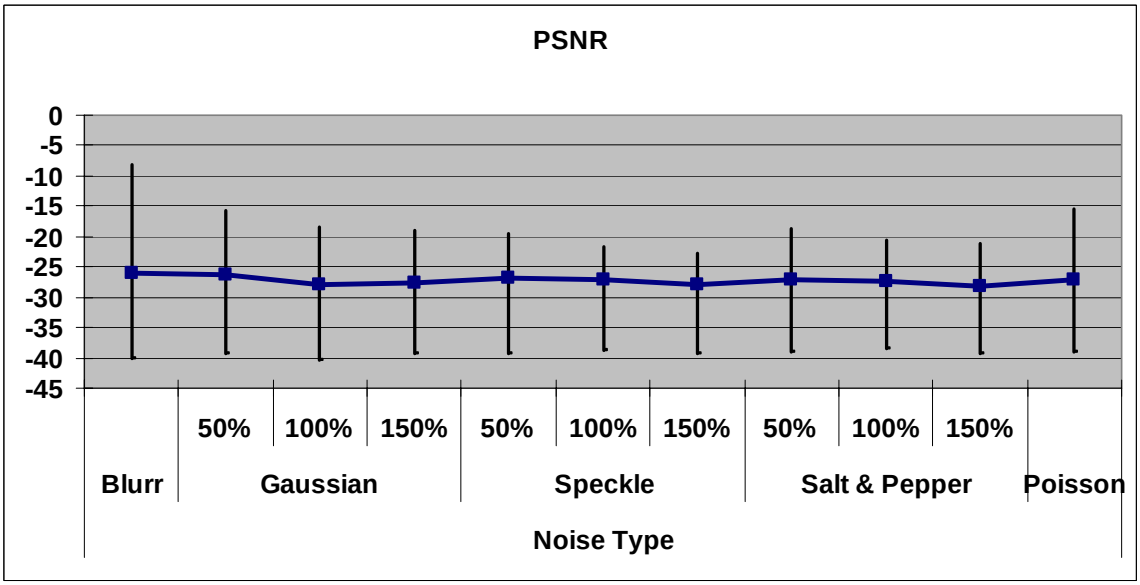

FIGURE 4.1.3: Picture Signal to Noise Ratio (PSNR) values obtained on 12 datasets with 11 noise levels.

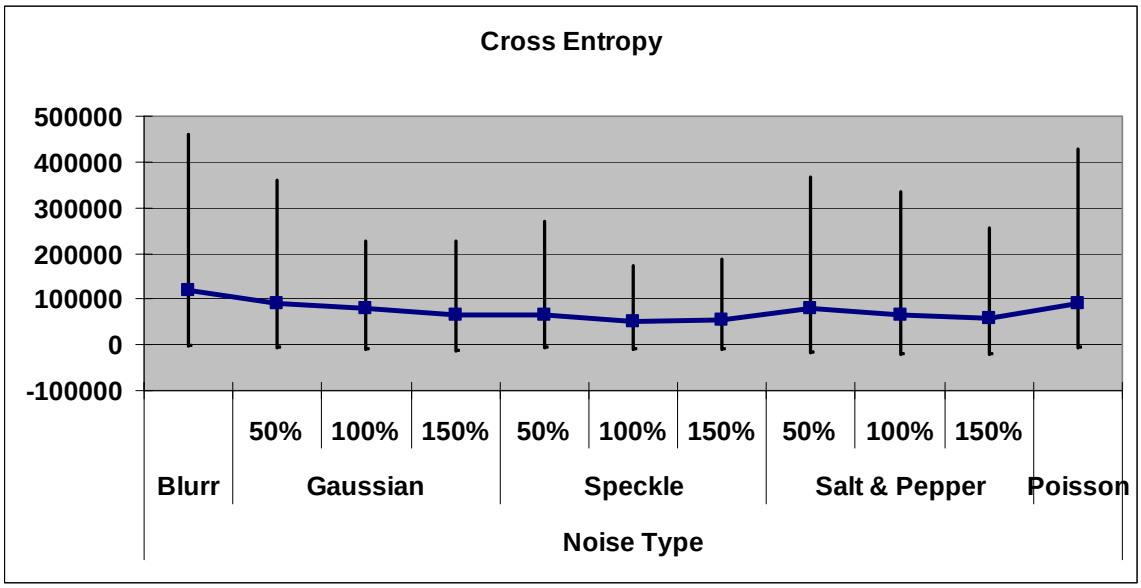

FIGURE 4.1.4: Cross Entropy (CE) values obtained on 12 datasets with 11 noise levels.

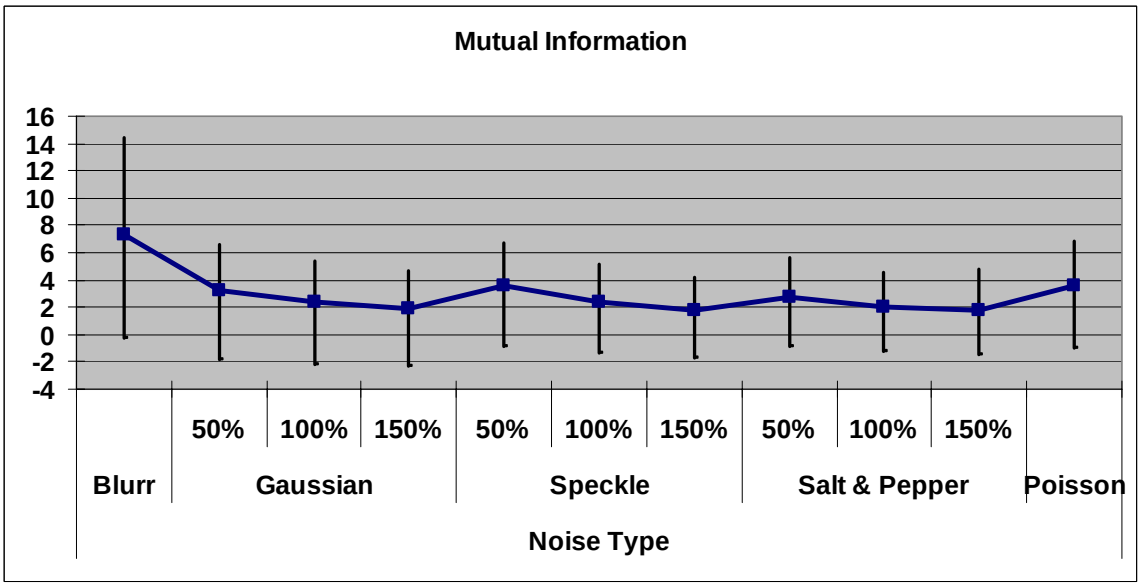

FIGURE 4.1.5: Mutual Information (MI) values obtained on 12 datasets with 11 noise levels.

MI (shown in figure 4.1.5), UQI (shown in figure 4.1.6), and SSIM (shown in figure 4.1.7) are able to differentiate between noise levels as well as show a stable correlation on all data types, similar to the expectation shown in figure 4.1.1. Based on

the performance in this study, MI, UQI, and SSIM were chosen as preferred metrics for single-scale based performance metrics.

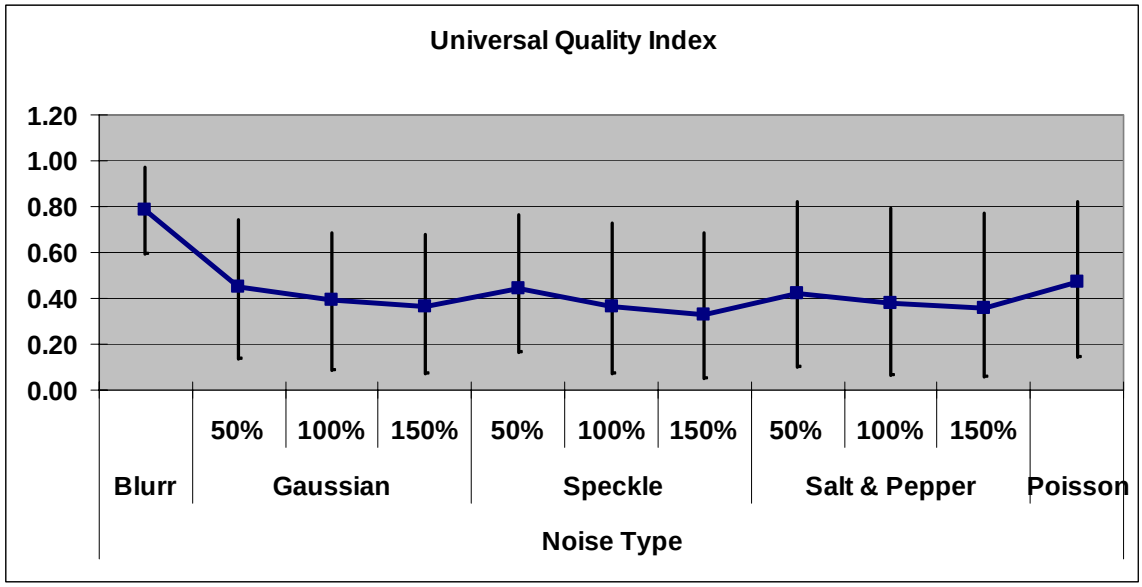

FIGURE 4.1.6: Universal Quality Index (UQI) values obtained on 12 datasets with 11 noise levels.

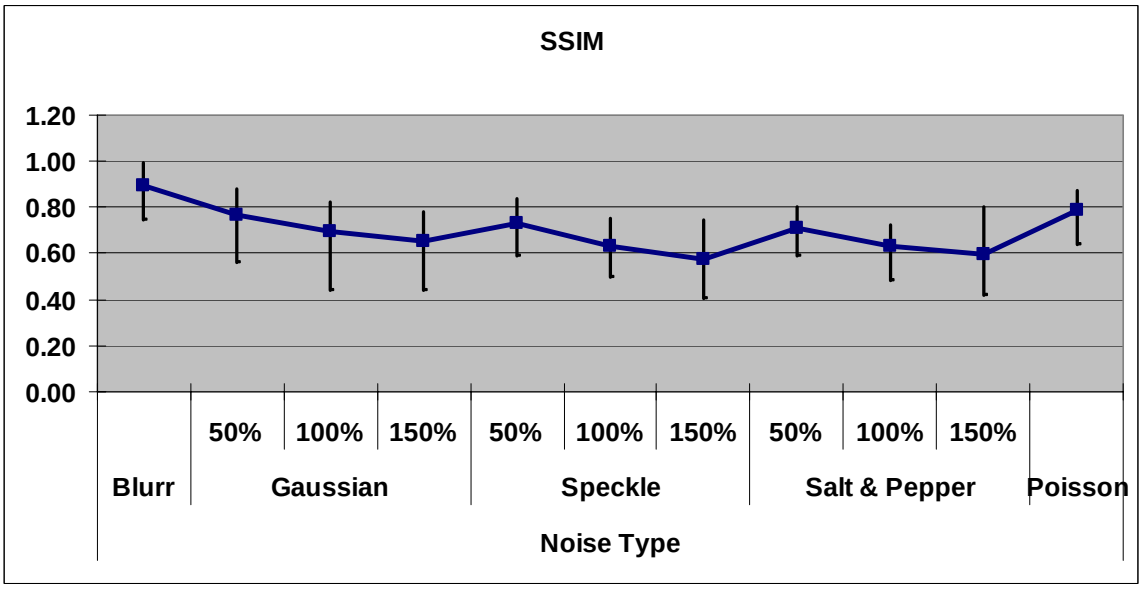

FIGURE 4.1.7: Structural Similarity Index (SSIM) values obtained on 12 datasets with 11 noise levels.

Figure 4.1.8 shows the MI values obtained on individual data sets. It can also be seen from figure 4.1.8 that MI is able to show that 'Data no.5' behaves differently compared to other data.

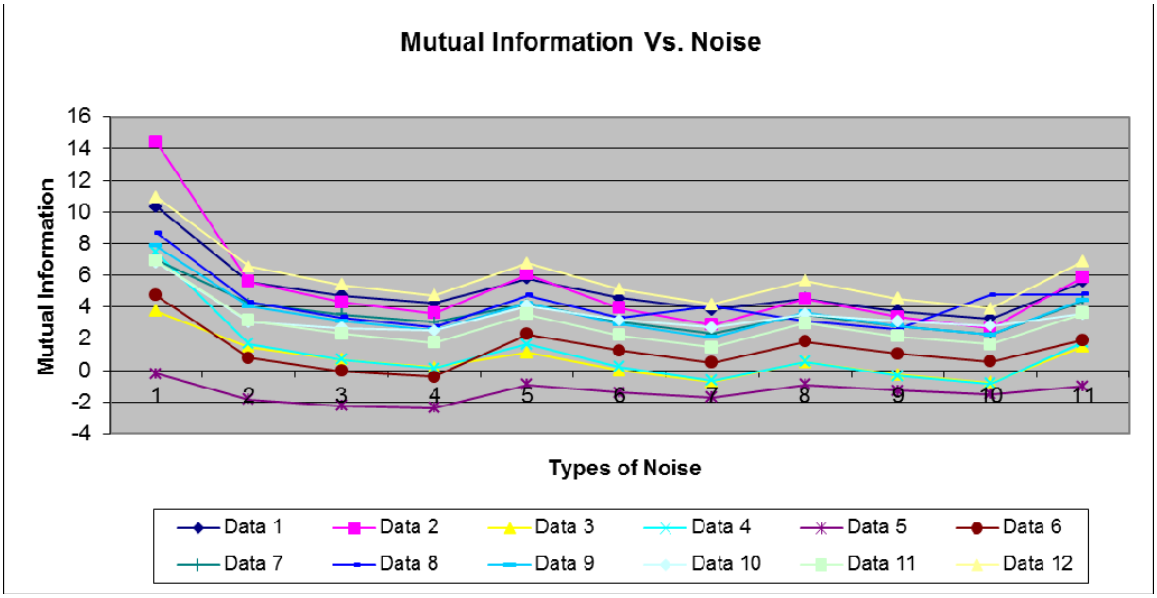

FIGURE 4.1.8: Individual Mutual Information (MI) values obtained on 12 datasets with 11 noise levels.

For multi-scale based metrics performance study, the images were transformed into six sub-images using 6-level DWF using '3D' method. Instead of calculating an average of six individual sub-image based values, the values were treated independently.

Figure 4.1.9 and 4.1.10 show the calculated SSIM values for first three and last three sub-images respectively. From figure 4.1.9, it can be seen that the major noise impacts are in the first level of sub-image and as the level progresses, there is gradually lesser impact of noise.

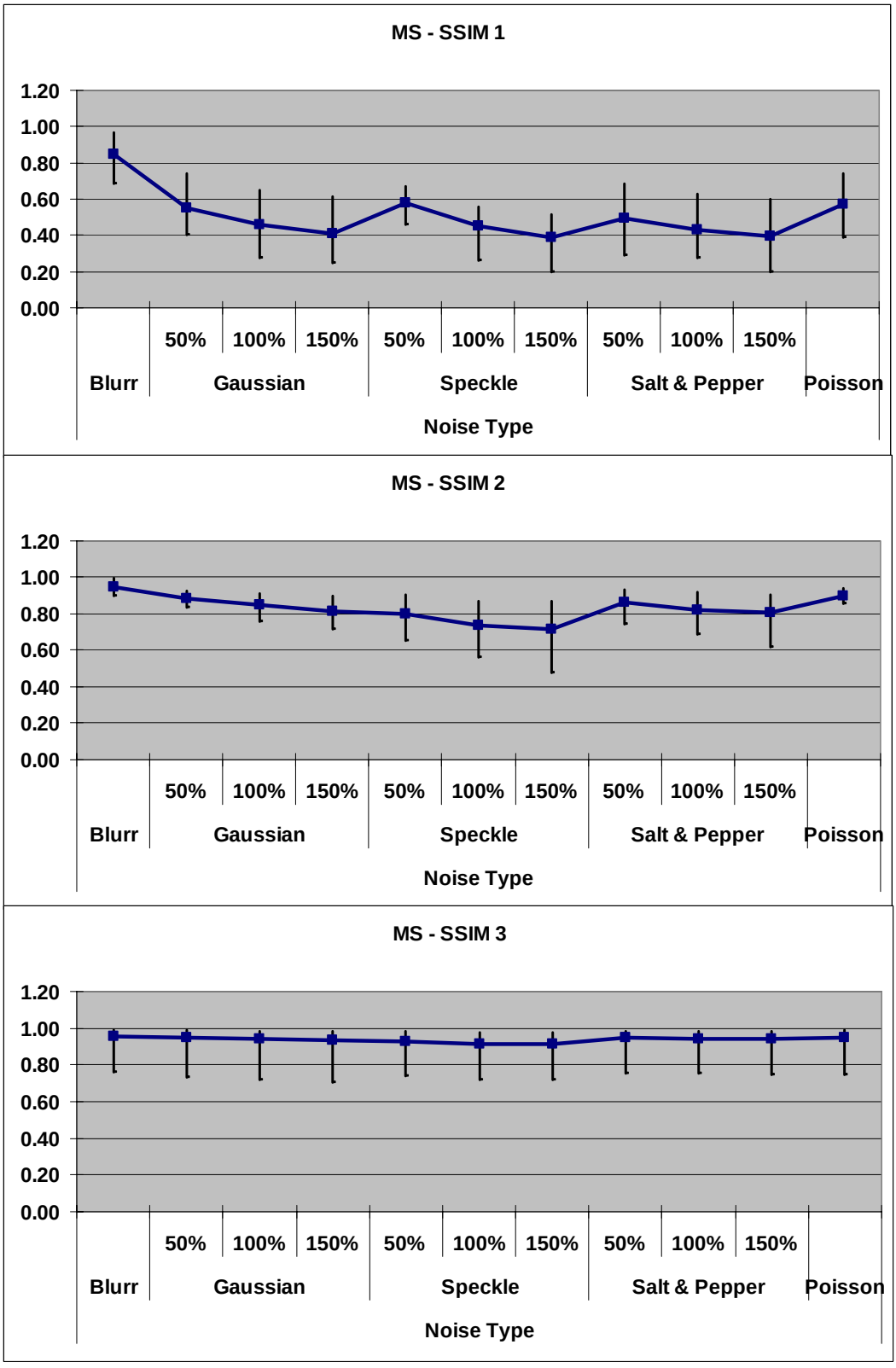

FIGURE 4.1.9: Structural Similarity Index (SSIM) values obtained on 12 datasets with 11 noise levels, for first three levels.

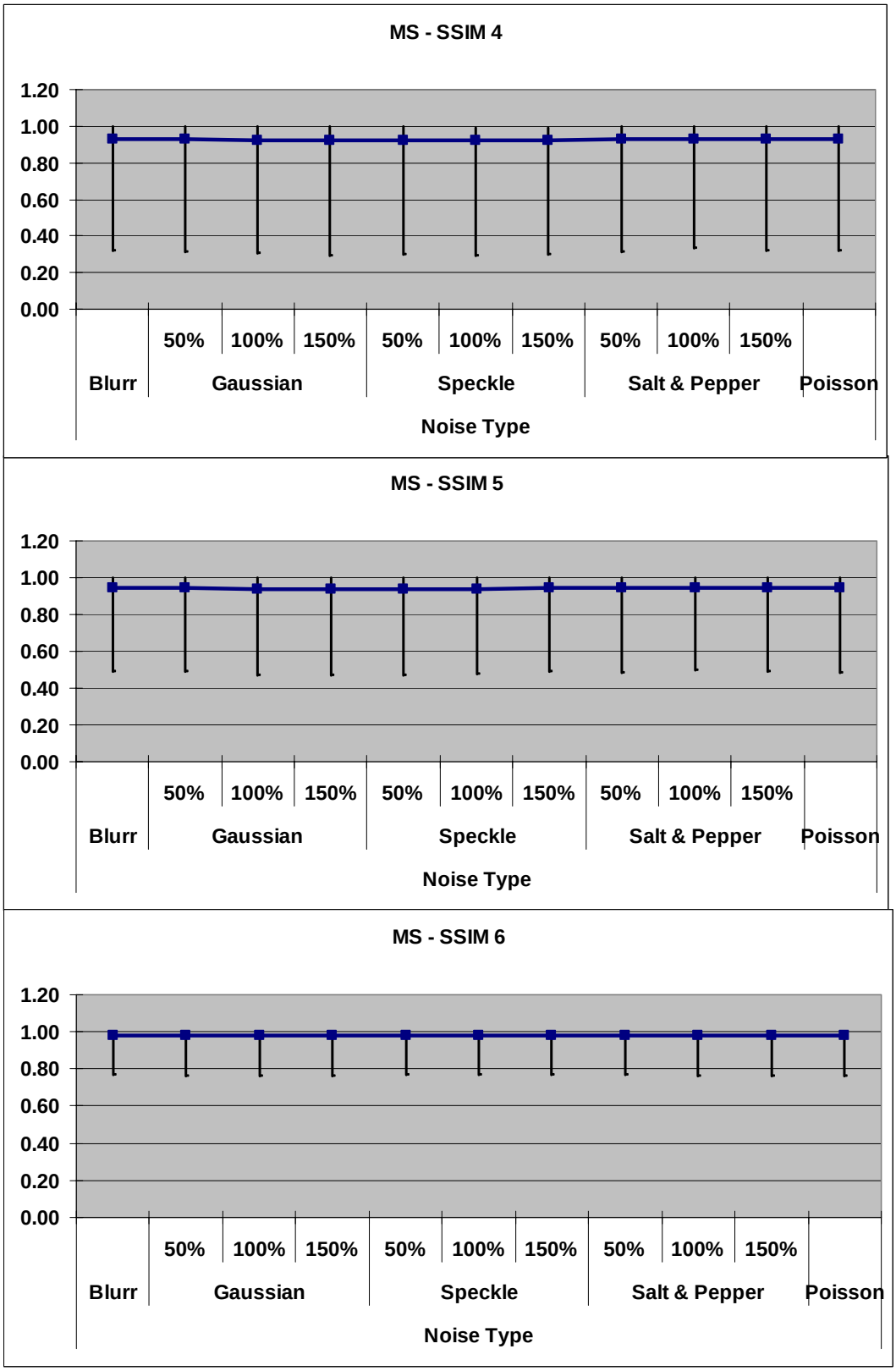

FIGURE 4.1.10: Structural Similarity Index (SSIM) values obtained on 12 datasets with 11 noise levels, for last three levels.

Even though MI was able to differentiate the impact of noise on 'Data no.5' similar to MS-SSIM, the potential drawback to this metric is that it doesn't provide a baseline to evaluate like UQI, SSIM and MS-SSIM, which are set to have a maximum value of 1.

Having selected the single-scale and multi-scale performance metrics, the next step is to evaluate different fusion methods. The easier options would be to either select the maximum value or mean value between the two datasets. Since the objective is to merge significant details from both the data, weighted averages are more suitable. Therefore, activity based weighted averages will be considered in detail in the next section.

4.2. Weighted Averaging Methods

Weighted averaging can be performed based on individual data point or based on a window / kernel or based on a combination of wavelet coefficients and window.

4.2.1. *Regional Energy Based (RE)*

This method [161] uses window based activity level measurement called regional energy and then a match degree is computed. Based on a preset threshold value, the match degree is the used to calculate weighted averages. After n level of decomposition, two sub images *A(i, j)* and *B(i, j)* are taken and region energies *VA(i, j)* and *VB(i, j)* are calculated.

$$VA(i,j) = \frac{1}{MN}\sum_{m=-l}^{l}\sum_{n=-v}^{v}(A(i+m, j+n))^2 ,$$

where *M, N* are the values of local region (3 x 3, 5 x 5 etc.)

$$VB(i,j) = \frac{1}{MN}\sum_{m=-l}^{l}\sum_{n=-v}^{v}(B(i+m, j+n))^2$$

The match degree *M (i, j)* is then computed using the formula

$$M(i,j) = \frac{\frac{2}{MN}\sum_{m=-l}^{l}\sum_{n=-v}^{v} A(i+m, j+n)B(i+m, j+n)}{VA(i,j)+VB(i,j)},$$

where

$$l = \frac{M-1}{2}, v = \frac{N-1}{2}$$

The fusion rule is given (for a selected threshold of T (T > 0.5)) by,

If *M (i, j)* < *T*, then $F(i,j) = \begin{cases} A(i,j) & VA(i,j) \geq VB(i,j) \\ B(i,j) & VA(i,j) < VB(i,j) \end{cases}$

If *M (i, j)* ≥ *T*, then $F(i,j) = \begin{cases} \alpha \times A(i,j) + (1-\alpha) \times B(i,j) & VA(i,j) \geq VB(i,j) \\ (1-\alpha) \times A(i,j) + \alpha \times B(i,j) & VA(i,j) < VB(i,j) \end{cases}$,

where $\alpha = \frac{1}{2} + \frac{1}{2}\left[\frac{1-M(i,j)}{1-T}\right]$

4.2.2. Regional Edge Intensity Based (REI)

This method [162] also uses a window based activity level measurement called edge intensity, which is used to calculate corresponding weightage factors. After n level of decomposition, if *f (i, j)* refers to the data point in a sub image and *R (m, n)* a *m* x *n* window. Then the edge intensity of *R(m, n)* is defined by

$$E_{R(m,n)} = \sum_{i=1}^{n}\sum_{j=1}^{m}\left|\frac{(f(i,j)-\overline{m}}{m \times n - 1}\right|,$$

where $\overline{m} = \sum_{i=1}^{n}\sum_{j=1}^{m}\frac{f(i,j)}{m \times n}$

The weights are calculated using the formula

$$W_{A(i,j)} = \frac{E_{A_{R(i,j)}}}{(E_{A_{R(i,j)}} + E_{B_{R(i,j)}})}$$

$$W_{B(i,j)} = \frac{E_{B_{R(i,j)}}}{(E_{A_{R(i,j)}} + E_{B_{R(i,j)}})}$$

The new pixel value is obtained by

$$f(i,j) = W_{A(i,j)} \times A(i,j) + W_{B(i,j)} \times B(i,j)$$

4.2.3. Combination of Wavelet Coefficients and Local Gradients (WGC):

This method [163] uses a combination of two activity level measurements to calculate the weightage factors. Let $W^A{}_{j,k}\ (m,n)$ and $W^B{}_{j,k}\ (m,n)$ stand for wavelet coefficients of source image *A* and source image *B*, j is the decomposed resolution level and *k-0,1,2,3* are the four frequency bands. The local gradient of wavelet coefficient $W_{j,k}(m,n)$ is defined as below

$$Gradient(W_{j,k}(m,n)) = \max\left\{\left|K_p \times W_{j,k}(m,n)\right|, p = 1-4\right\},$$

where K_p are the four directional gradient operators. *p=1* is the convolution kernel for 135 degree directions, *p=2* for the 90 degree, *p=3* for 0 degree and *p=4* for 45 degree, as shown in figure 4.2.1.

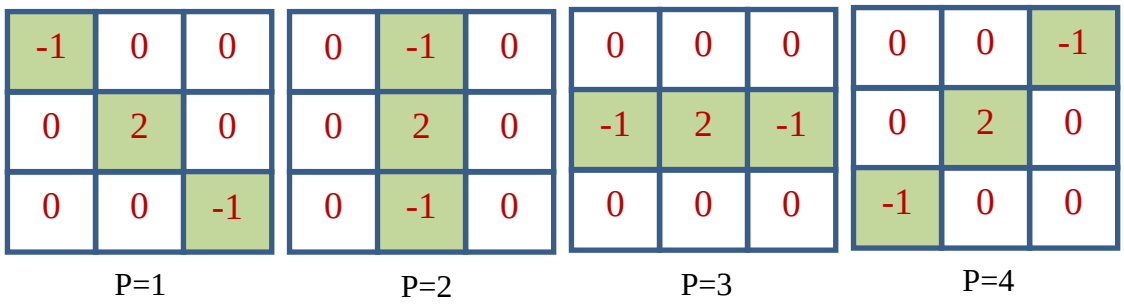

FIGURE 4.2.1: Four directional convolution kernels.

The proposed image activity level measurement combines the wavelet coefficient at the sampling point *(m, n)* and its local wavelet coefficient gradient feature together.

$$A(W_{j,k}(m,n)) = Gradient(W_{j,k}(m,n)) \times \left| W_{j,k}(m,n) \right|,$$

where $A\ (W_{j,k}(m,n))$ reflects the activity level information of the wavelet coefficient $W_{j,k}(m,n)$. The image fusion scheme is given by,

$$W^{out}{}_{j,k}(m,n) = \begin{cases} W^{A}{}_{j,k}(m,n) & A(W^{A}{}_{j,k}(m,n)) > A(W^{B}{}_{j,k}(m,n)) \\ W^{B}{}_{j,k}(m,n) & A(W^{A}{}_{j,k}(m,n)) \le A(W^{B}{}_{j,k}(m,n)) \end{cases}$$

Three activity based weighted average data fusion methods (RE, REI and WGC) were described. In order to evaluate the three methods and select the optimal method for surface metrology domain, a study was conducted, which will be explained in detail in the following sections. Before describing the performance study, the data fusion process step is explained in detail in the next section

4.3. Data Fusion

For data fusion, the previously matched and registered locations from both magnification datasets are decomposed into six sub-images using DWF method. Figure 4.3.1 and 4.3.2 show the six sub-images obtained on a honed surface at 5X and 20X magnification respectively, that were previously registered using coarse and fine registration steps.

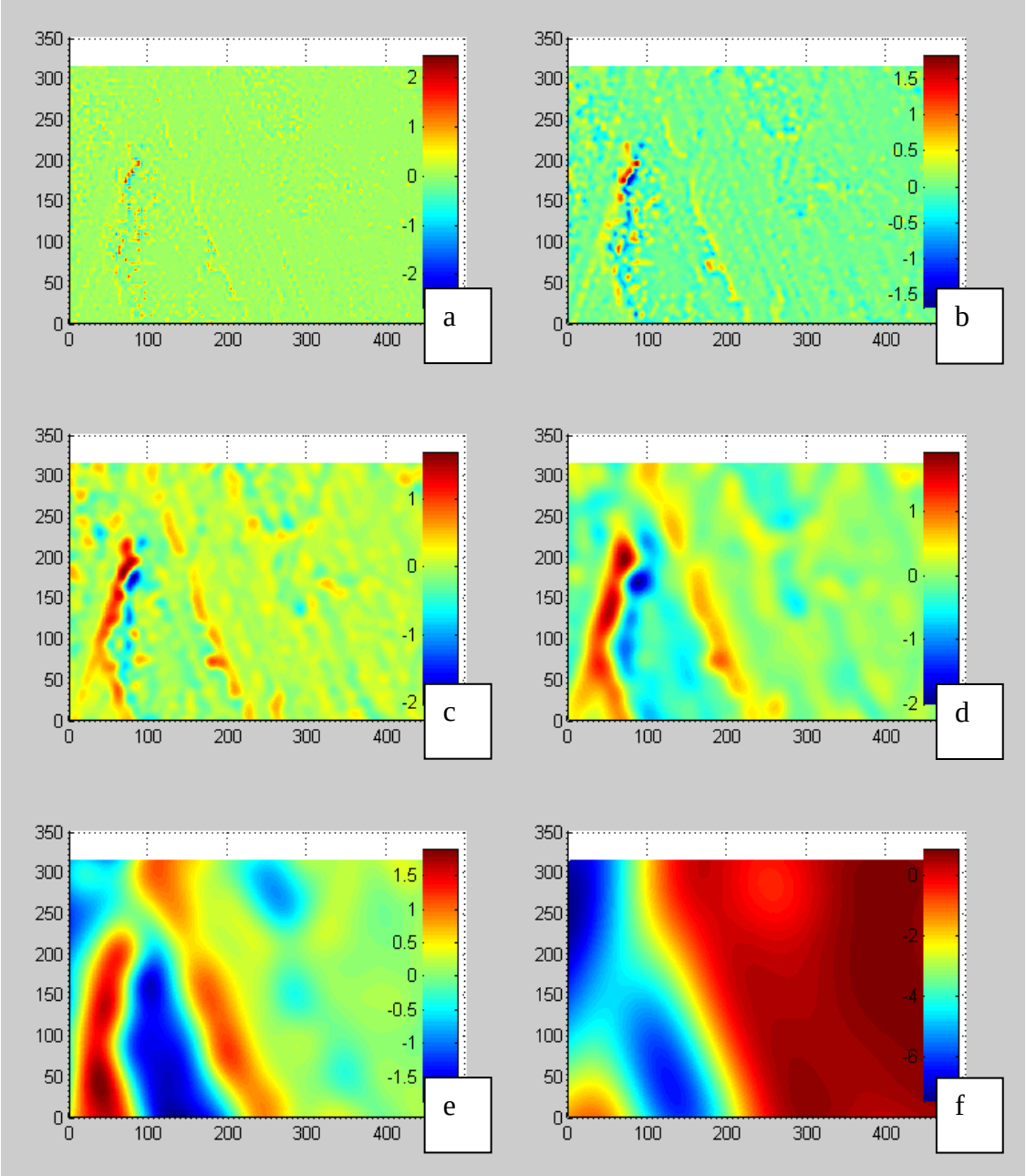

FIGURE 4.3.1: Six wavelet planes (a-f) obtained from 5X magnification measurement on honed surface.

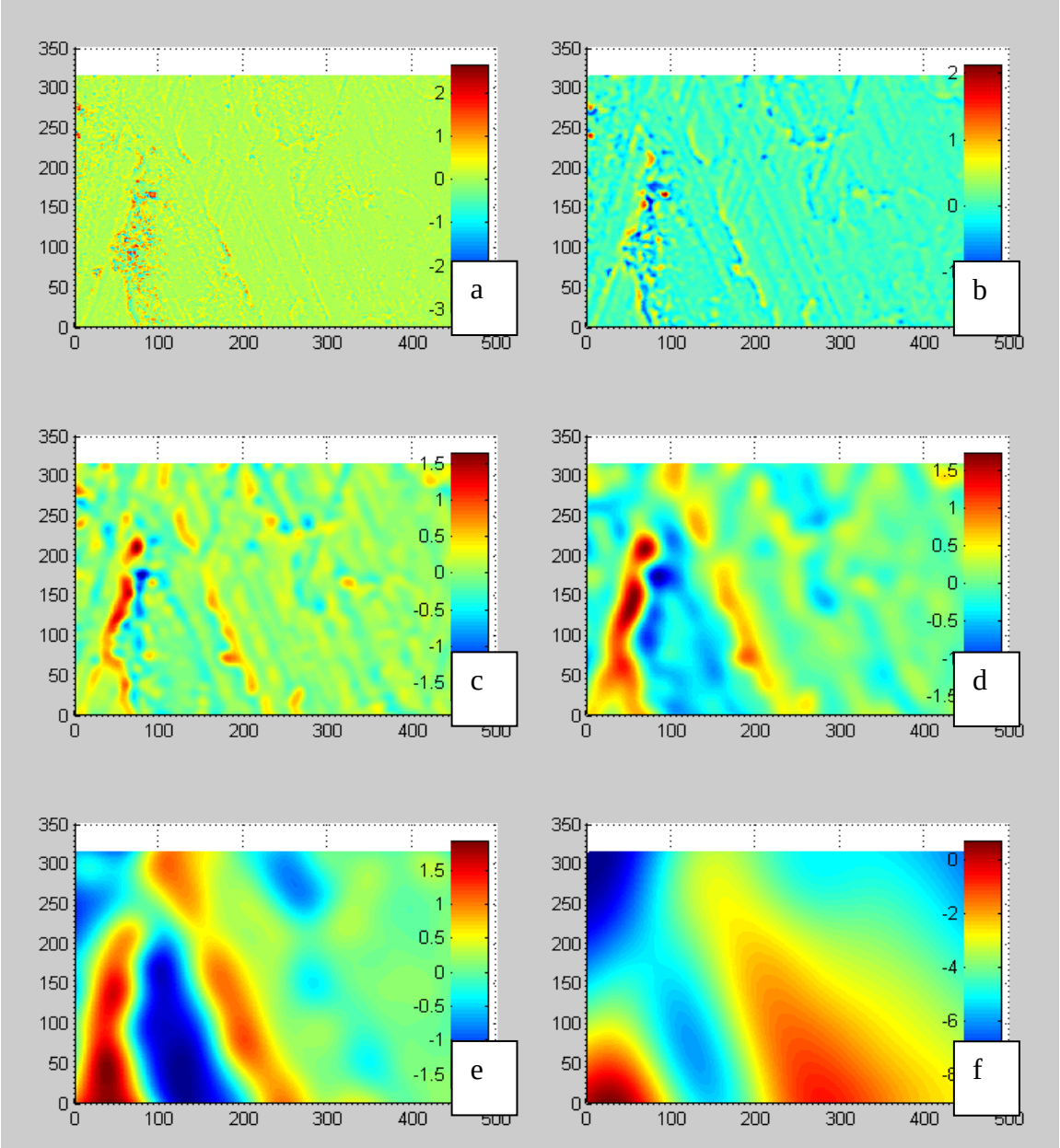

FIGURE 4.3.2: Six wavelet planes obtained from 20X magnification measurement on honed surface.

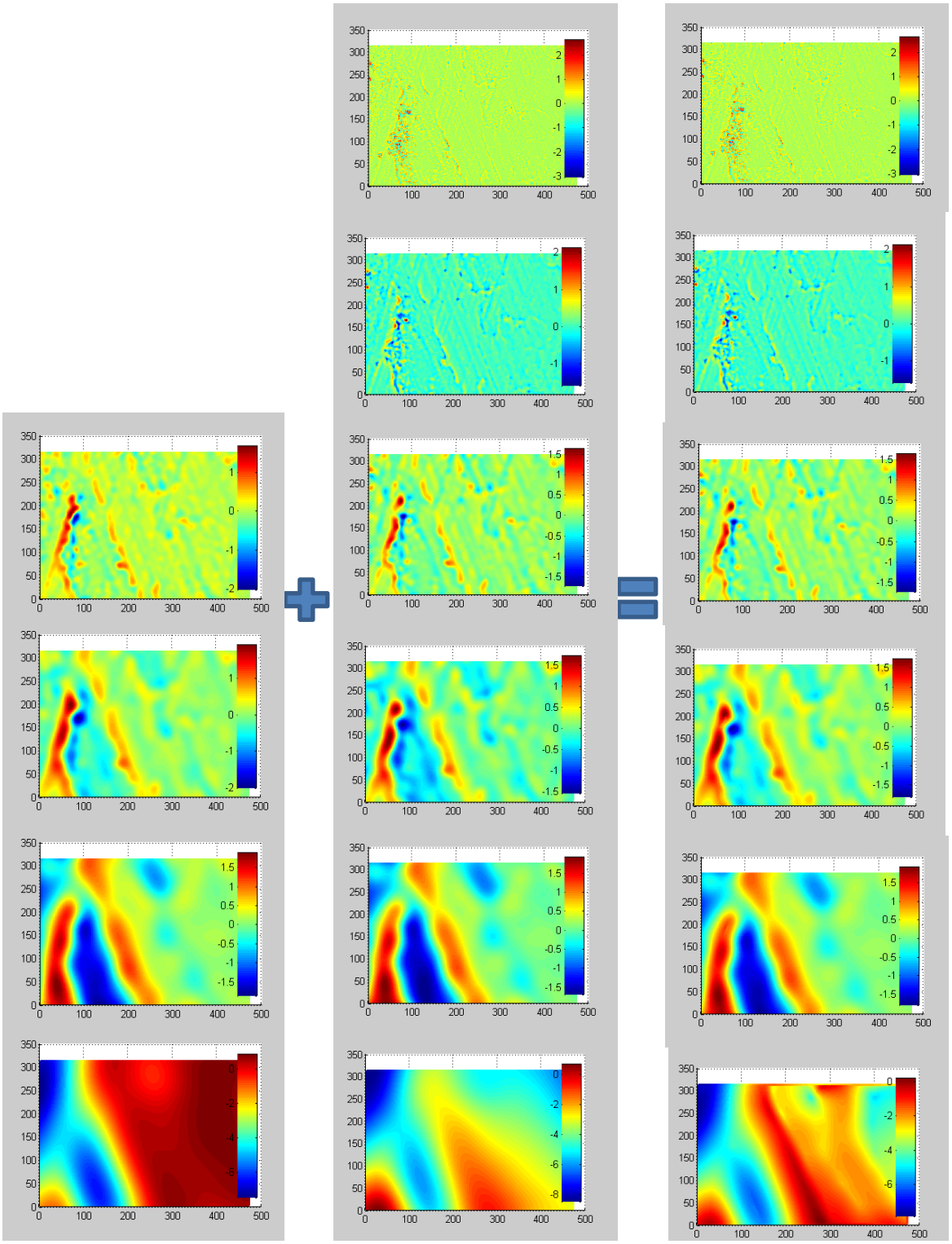

FIGURE 4.3.3: Two set of six wavelet planes fused to obtain new set of six wavelet planes.

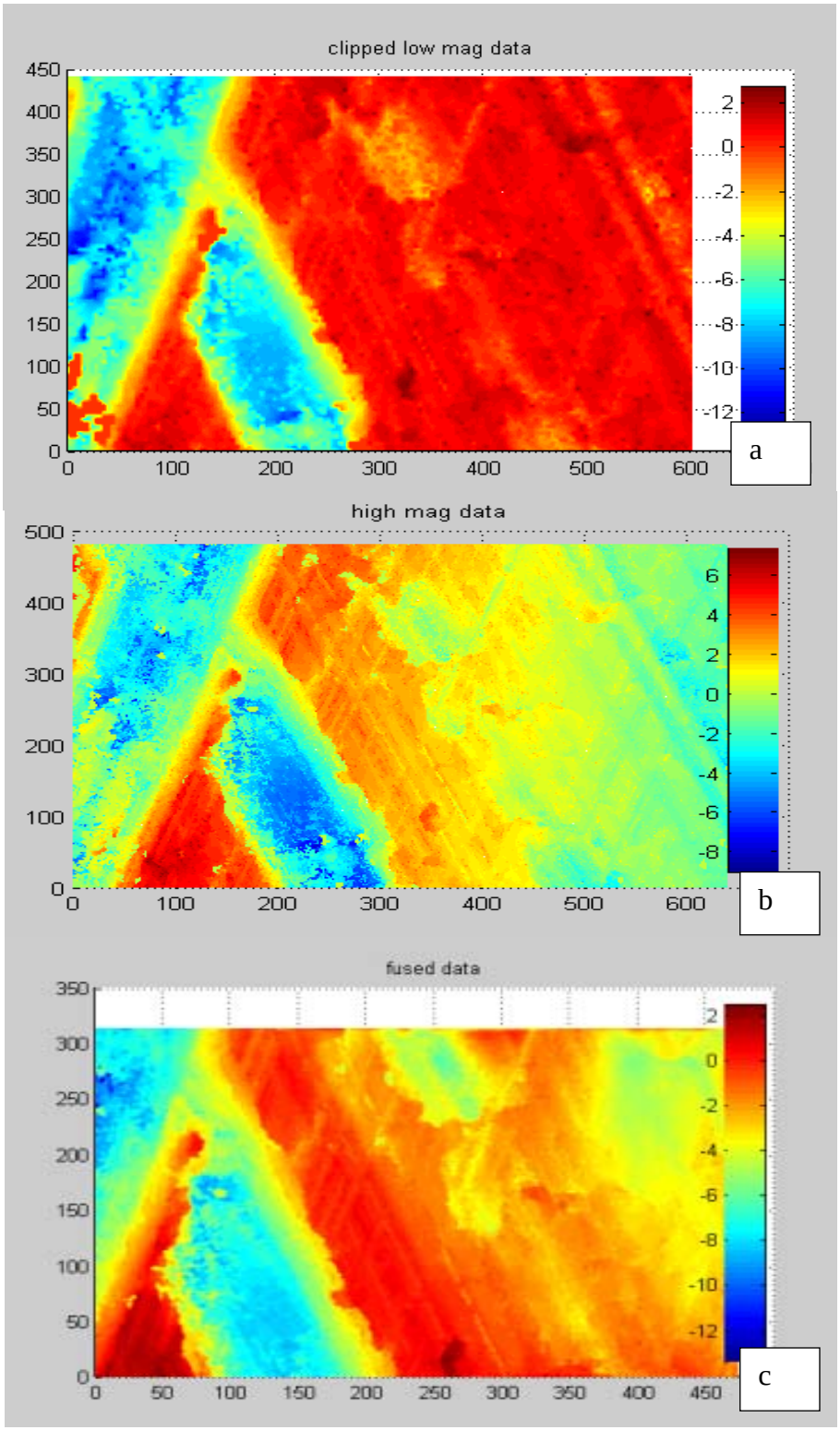

FIGURE 4.3.4: (a) 5X magnification data (b) 20X magnification data (c) Fused data on honed surface.

The individual sub-images at each level of decomposition are then fused using selected weighted average methods to obtain a new set of six sub-images, as shown in figure 4.3.3. The 5X magnification data is shown in figure 4.3.4a and 20X magnification data is shown in figure 4.3.4b. The six fused wavelet planes are inverse transformed to obtain the fused data, as shown in figure 4.3.4c.

In order to evaluate the three weighted average based data fusion methods (RE, REI and WGC) and select the optimal method for surface metrology domain, a study was conducted, which will be explained in detail in the next section.

4.4. Performance Evaluation of Transformation and Fusion Methods

In order to evaluate the performance of two transformation methods (3D and 3D Hybrid), and three fusion methods (RE,REI and WGC), 12 sets of data - 4 sets each of directional structured surface (shown in figure 4.4.1) , non-directional structured surface (shown in figure 4.4.2) and systematic non-engineered surface (shown in figure 4.4.3), were fused using a 6-level DWF transformation, coarse registration was performed using NCC, ‘Watershed’ edge detection on single scale was used and the obtained control points were used for fine registration using ICP finite difference method.

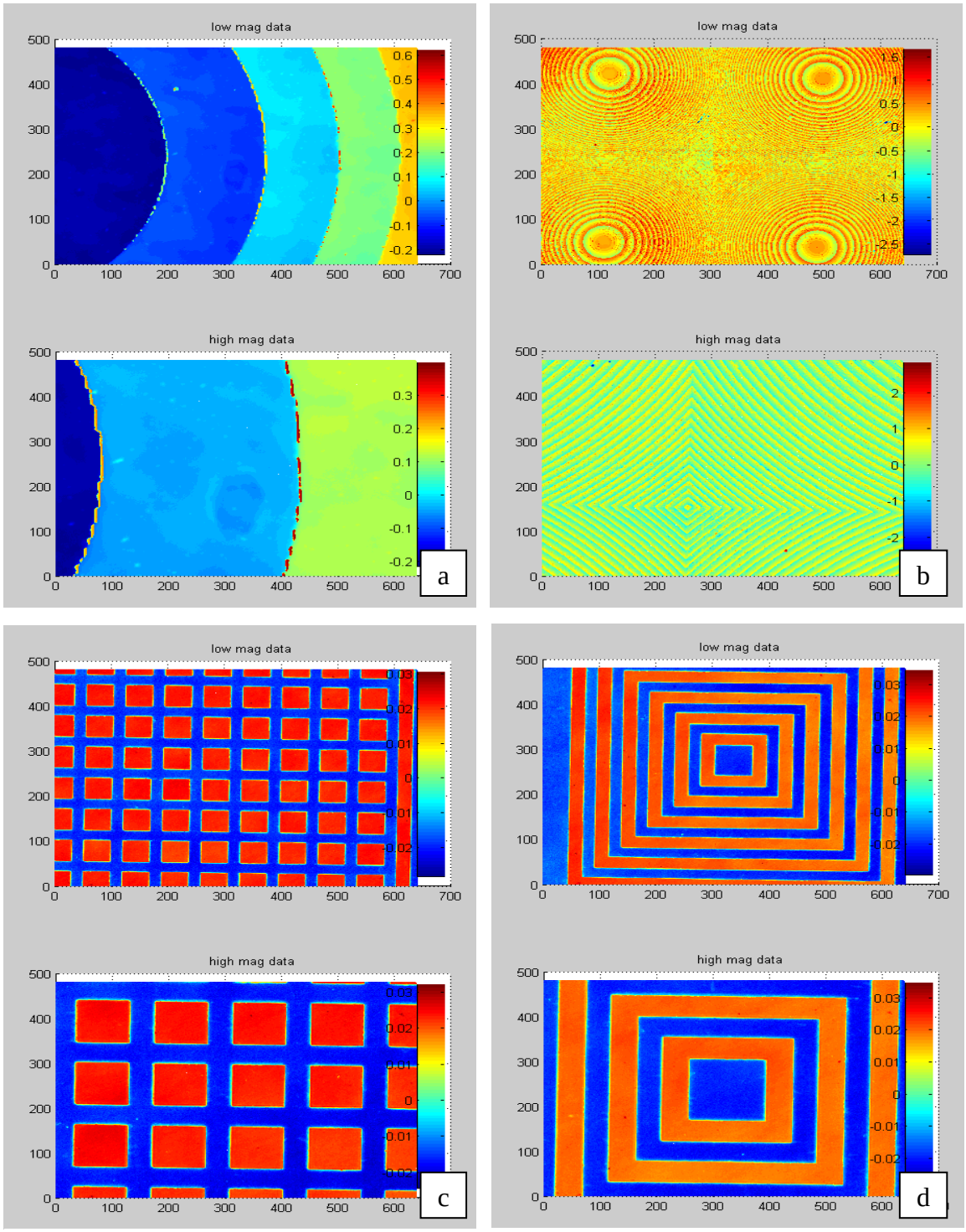

FIGURE 4.4.1: Four structured directional surfaces considered (a) Beam shaper optical surface at 50X and 100X optical magnification (b) Fresnel micro-lens array at 5X and 20X optical magnification (c) Square grid pattern surface at 10X and 20X optical magnification (d) Concentric square pattern surface at 10X and 20X optical magnification.

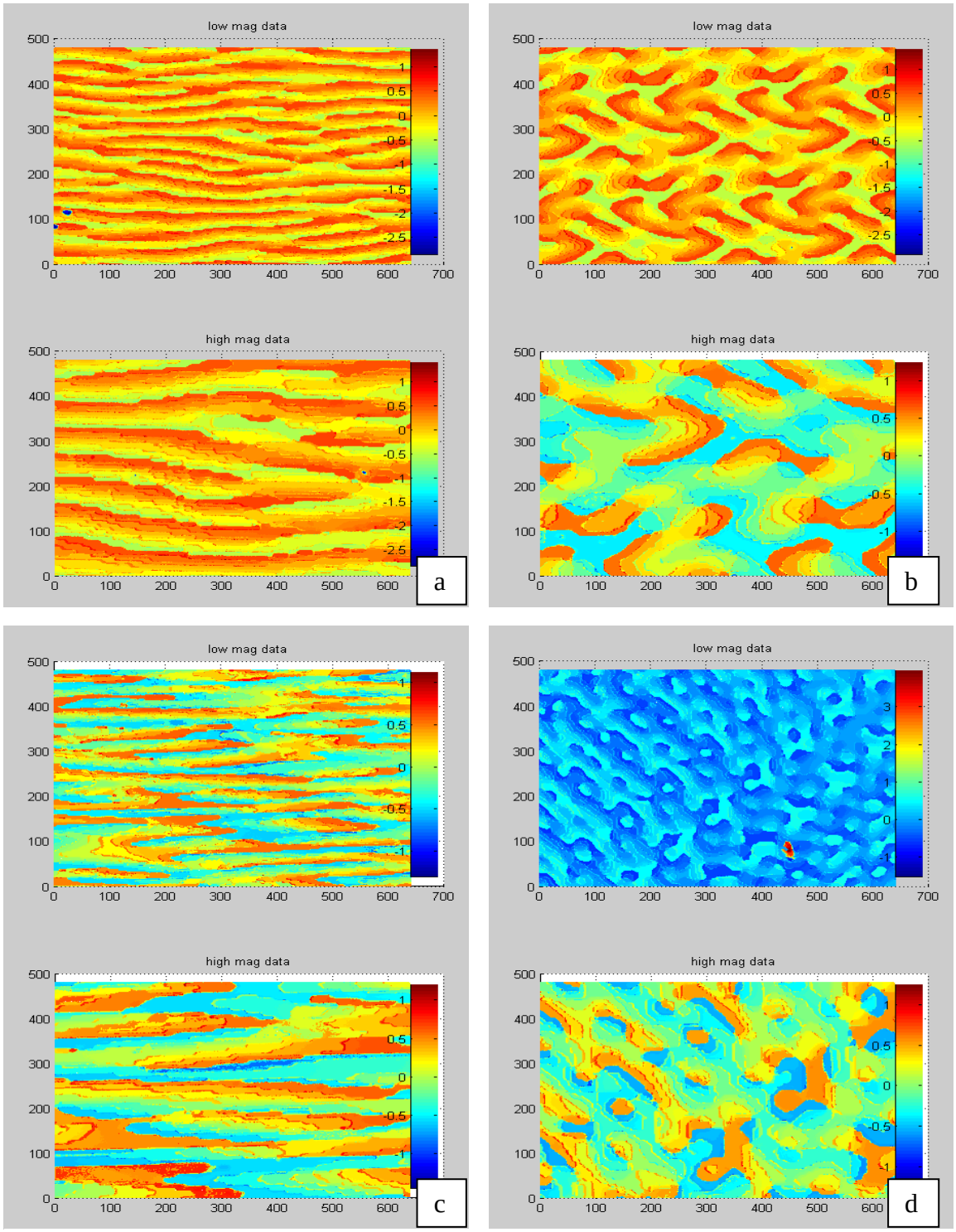

FIGURE 4.4.2: Four structured non-directional surfaces considered (a) Dipole diffuser optical surface at 50X and 100X optical magnification (b) Spot array generator optical surface at 50X and 10X optical magnification (c) and (d) Pattern generator optical surface at 50X and 100X optical magnification.

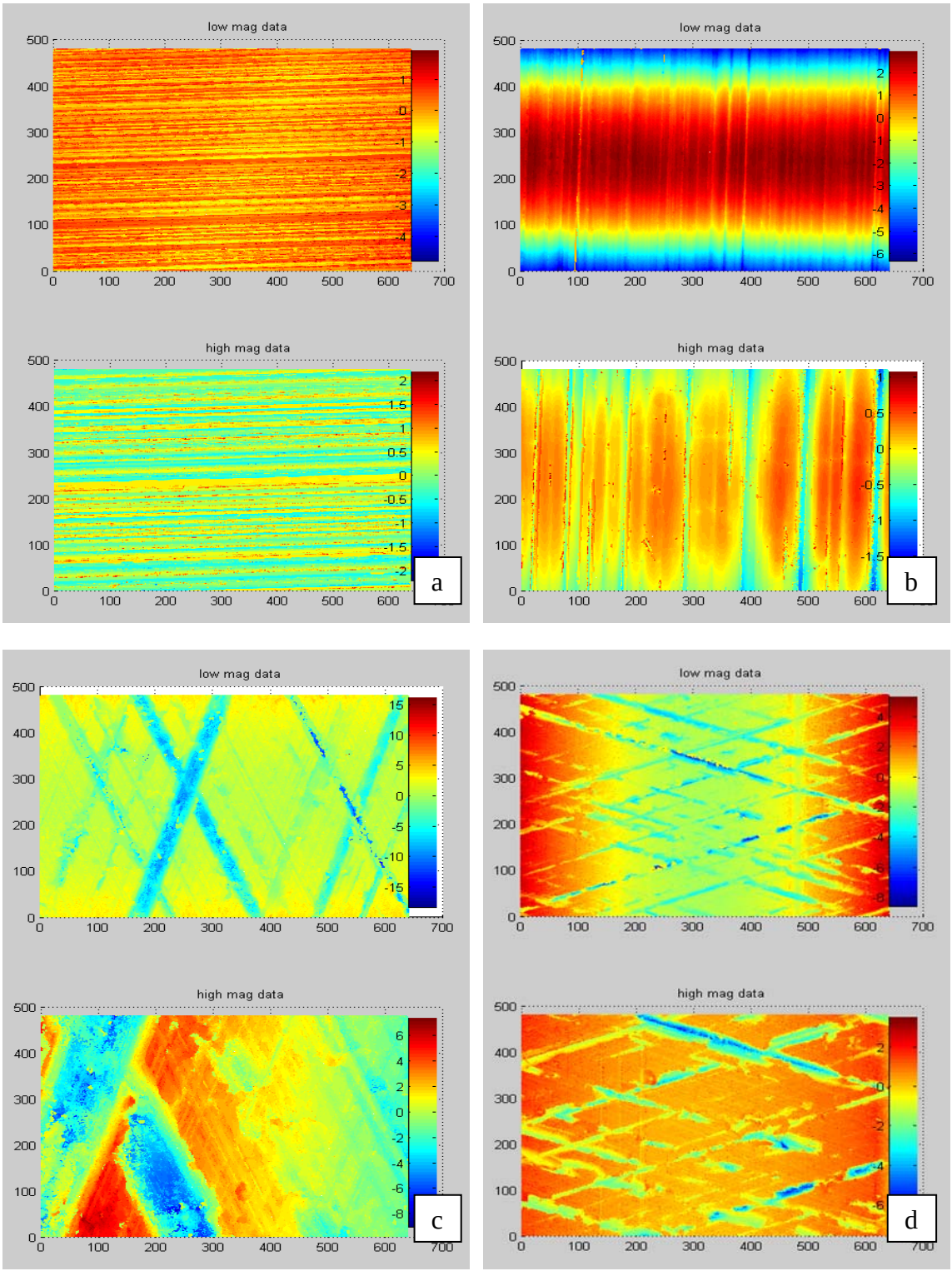

FIGURE 4.4.3: Four systematic surfaces considered (a) line generator optical surface at 10X and 20X optical magnification (b) Turned surface at 5X and 20X optical magnification (c) Honed surface at 5X and 20X optical magnification (d) Honed surface at 5X and 10X optical magnification.

TABLE 4.4.1: Multi-scale performance metric for 12 datasets.

				MS-SSIM											
				Rl,F	Rl,F	Rl,F	Rl,F	Rl,F	Rl,F	Rh,F	Rh,F	Rh,F	Rh,F	Rh,F	Rh,F
	Data	fusion method		R11(1)	R11(2)	R11(3)	R11(4)	R11(5)	R11(6)	R12(1)	R12(2)	R12(3)	R12(4)	R12(5)	R12(6)
STRUCTURED DIRECTIONAL SURFACES	1	RE	3D	0.97231	0.99679	0.99553	0.99122	**0.9933**	0.86604	1	**0.99094**	**0.9864**	**0.98163**	**0.99103**	0.81289
			3DH	**0.97712**	**0.97265**	**0.96936**	**0.9612**	0.94523	0.86604	1	0.96469	0.91062	0.90752	0.89274	0.81289
		REI	3D	0.97231	**0.99574**	**0.99432**	**0.99181**	**0.99329**	**0.95908**	1	**0.99108**	**0.99152**	**0.99082**	**0.99431**	**0.96259**
			3DH	**0.97712**	0.85136	0.85213	0.90022	0.90556	**0.95908**	1	0.85851	0.77444	0.80843	0.92352	**0.96259**
		WGC	3D	0.97231	**0.99333**	**0.98382**	**0.95746**	**0.93989**	0.64242	1	**0.98963**	**0.97791**	**0.9539**	**0.94091**	0.59898
			3DH	**0.97712**	0.56768	0.52067	0.58589	0.64957	0.64242	1	0.55405	0.48895	0.55429	0.61961	0.59898
	2	RE	3D	0.2007	**0.43849**	0.38758	**0.95576**	0.91813	**0.93114**	1	1	1	0.61329	0.74829	0.77558
			3DH	**0.2906**	0.40867	**0.42335**	0.91007	**0.94664**	**0.93114**	1	1	1	**0.70469**	**0.79435**	0.77558
		REI	3D	0.2007	**0.43849**	0.38758	**0.92567**	**0.92701**	0.87568	1	1	1	0.62762	**0.79636**	**0.89354**
			3DH	**0.2906**	0.40867	**0.42335**	0.86752	0.86615	0.87568	1	1	1	**0.70992**	0.81846	**0.89354**
		WGC	3D	0.2007	**0.43849**	0.38758	**0.70823**	**0.67425**	0.65568	1	1	1	**0.51824**	**0.69279**	0.69971
			3DH	**0.2906**	0.40867	**0.42335**	0.51577	0.57833	0.65568	1	1	1	0.46339	0.62006	0.69971
	3	RE	3D	0.56864	0.91031	0.94743	0.98296	**0.99101**	0.92935	1	0.92243	0.95609	**0.98337**	**0.99114**	0.92752
			3DH	**0.65533**	**0.93037**	**0.96803**	**0.98395**	0.98856	0.92935	1	**0.94567**	**0.96621**	0.98272	0.98789	0.92752
		REI	3D	0.56864	0.94446	**0.96962**	**0.99331**	**0.99768**	**0.99475**	1	**0.94186**	0.96519	**0.99243**	**0.99757**	**0.99072**
			3DH	**0.65533**	**0.94449**	0.96742	0.98998	0.99577	**0.99475**	1	0.92971	**0.96906**	0.99022	0.99573	**0.99072**
		WGC	3D	0.56864	**0.87178**	**0.8809**	**0.92136**	**0.94267**	0.61742	1	**0.9116**	**0.90589**	**0.92371**	**0.94306**	0.61664
			3DH	**0.65533**	0.74798	0.804	0.8324	0.86465	0.61742	1	0.75358	0.81889	0.83234	0.86327	0.61664
	4	RE	3D	0.59743	0.94719	0.97632	**0.99092**	**0.99366**	0.99525	1	0.94873	0.9777	**0.99088**	**0.99363**	0.99532
			3DH	**0.73361**	**0.9522**	**0.98144**	0.98952	0.99353	0.99525	1	**0.96538**	**0.98211**	0.98878	0.9934	0.99532
		REI	3D	0.59743	0.96708	0.98543	**0.99647**	**0.99816**	**0.99937**	1	**0.96579**	0.98435	**0.9964**	**0.99813**	**0.99931**
			3DH	**0.73361**	**0.97337**	**0.98945**	0.99485	0.99811	**0.99937**	1	0.96296	**0.98583**	0.99426	0.99762	**0.99931**
		WGC	3D	0.59743	**0.91753**	0.92882	**0.95481**	**0.95919**	0.97209	1	**0.93943**	0.941	**0.95619**	**0.95808**	0.97222
			3DH	**0.73361**	0.91649	**0.94247**	0.94176	0.95059	0.97209	1	0.91987	**0.9425**	0.93838	0.9497	0.97222
STRUCTURED NON-DIRECTIONAL SURFACES	1	RE	3D	0.49623	0.91662	0.95937	0.97927	**0.98937**	0.97532	1	0.91	0.95505	0.97729	**0.98886**	0.97249
			3DH	**0.60818**	**0.94382**	**0.96192**	**0.97994**	0.98714	0.97532	1	**0.93988**	**0.96095**	**0.9777**	0.98717	0.97249
		REI	3D	0.49623	0.94139	**0.97298**	**0.98865**	**0.99617**	**0.98332**	1	0.95246	**0.97943**	**0.99074**	**0.99665**	0.98994
			3DH	**0.60818**	**0.95503**	0.97097	0.98809	0.99551	**0.98332**	1	**0.9606**	0.97746	0.99043	0.99665	0.98994
		WGC	3D	0.49623	0.88922	**0.91328**	**0.941**	**0.97168**	0.94808	1	0.92728	**0.95027**	**0.96377**	**0.98053**	0.97544
			3DH	**0.60818**	**0.89338**	0.89839	0.93785	0.96869	0.94808	1	**0.9391**	0.94908	0.96057	0.98005	0.97544
	2	RE	3D	0.64934	0.9129	0.9726	0.99555	**0.9982**	0.99647	1	0.9358	0.97108	0.99528	**0.99815**	0.99646
			3DH	**0.70737**	**0.95425**	**0.98201**	**0.99595**	0.99746	0.99647	1	**0.95171**	**0.98556**	**0.99563**	0.99726	0.99646
		REI	3D	0.64934	0.9394	0.98228	0.99723	**0.9993**	**0.99874**	1	0.95759	0.9872	0.99767	**0.99935**	**0.99905**
			3DH	**0.70737**	**0.95589**	**0.98496**	**0.99753**	0.99896	**0.99874**	1	**0.96663**	**0.99083**	**0.99779**	0.9989	**0.99905**
		WGC	3D	0.64934	0.88846	0.94453	**0.98482**	**0.99283**	0.99233	1	0.94292	0.96936	**0.9909**	**0.99482**	0.99605
			3DH	**0.70737**	**0.89833**	**0.95887**	0.98391	0.99151	0.99233	1	**0.95055**	**0.97382**	0.98878	0.99224	0.99605
	3	RE	3D	0.62188	0.8948	0.94913	**0.98226**	**0.98658**	0.97464	1	0.86608	0.943	**0.9826**	**0.98931**	0.98505
			3DH	**0.65515**	**0.90919**	**0.96321**	0.97948	0.98159	0.97464	1	**0.92018**	**0.96397**	0.98177	0.98639	0.98505
		REI	3D	0.62188	0.91804	0.96294	**0.98794**	**0.99425**	**0.98289**	1	0.90634	0.96629	**0.98825**	**0.99443**	**0.99737**
			3DH	**0.65515**	**0.91983**	**0.96682**	0.98703	0.99335	**0.98289**	1	**0.92237**	**0.97063**	0.98789	0.99365	**0.99737**
		WGC	3D	0.62188	**0.86096**	**0.88066**	**0.92931**	**0.95742**	0.954	1	0.86884	**0.90979**	**0.94743**	**0.96799**	0.97688
			3DH	**0.65515**	0.83165	0.87887	0.92147	0.9514	0.954	1	**0.87042**	0.90963	0.93808	0.96207	0.97688
	4	RE	3D	0.64503	0.92453	0.97738	**0.99584**	**0.99789**	0.97895	1	0.93505	0.9747	**0.9953**	**0.99774**	0.97581
			3DH	**0.70446**	**0.95847**	**0.9861**	0.99455	0.99523	0.97895	1	**0.94758**	**0.98309**	0.99429	0.99506	0.97581
		REI	3D	0.64503	0.94949	0.98576	**0.99774**	**0.99931**	**0.9914**	1	**0.95792**	0.98779	0.9977	**0.99917**	**0.99277**
			3DH	**0.70446**	**0.96226**	**0.9887**	0.99752	0.99903	**0.9914**	1	0.96742	**0.98902**	**0.99777**	0.99884	**0.99277**
		WGC	3D	0.64503	**0.90399**	**0.94833**	**0.98411**	**0.99122**	0.95764	1	**0.9396**	**0.96601**	**0.98928**	**0.99245**	0.9757
			3DH	**0.70446**	0.90009	0.93967	0.97637	0.97976	0.95764	1	0.93124	0.95679	0.9822	0.98138	0.9757
SYSTEMATIC SURFACES	1	RE	3D	0.48351	**0.90702**	**0.94641**	**0.94624**	**0.96805**	**0.93406**	1	**0.88741**	**0.9223**	**0.92386**	**0.97437**	0.81421
			3DH	**0.58078**	0.90095	0.90794	0.91545	0.94676	**0.93406**	1	0.86398	0.86441	0.85419	0.89294	0.81421
		REI	3D	0.48351	**0.93232**	**0.96757**	**0.96578**	**0.98573**	0.89082	1	**0.921**	**0.9545**	**0.96411**	**0.98857**	**0.89289**
			3DH	**0.58078**	0.92951	0.93751	0.922	0.9179	0.89082	1	0.90441	0.92785	0.92391	0.93484	**0.89289**
		WGC	3D	0.48351	**0.88238**	**0.87989**	**0.84846**	**0.94909**	0.64126	1	**0.87948**	**0.87608**	**0.89094**	**0.96844**	0.60452
			3DH	**0.58078**	0.80603	0.69243	0.57283	0.62	0.64126	1	0.80897	0.69798	0.59068	0.62788	0.60452
	2	RE	3D	0.57731	0.58843	0.79612	**0.92659**	**0.94517**	**0.84175**	1	1	1	**0.9298**	**0.94618**	**0.82144**
			3DH	**0.70003**	**0.77256**	**0.87626**	0.89331	0.86077	**0.84175**	1	1	1	0.87659	0.84965	**0.82144**
		REI	3D	0.57731	0.58843	0.79612	**0.95256**	**0.97495**	0.83134	1	1	1	**0.94954**	**0.97645**	0.80606
			3DH	**0.70003**	**0.77256**	**0.87626**	0.57516	0.69168	0.83134	1	1	1	0.57347	0.68873	0.80606
		WGC	3D	0.57731	0.58843	0.79612	**0.7893**	**0.83391**	0.40189	1	1	1	**0.81671**	**0.8539**	0.3839
			3DH	**0.70003**	**0.77256**	**0.87626**	0.26931	0.38449	0.40189	1	1	1	0.27108	0.3866	0.3839
	3	RE	3D	0.66541	0.8134	**0.93661**	**0.99132**	**0.99323**	0.87919	1	1	1	**0.98689**	**0.99175**	**0.98652**
			3DH	**0.76356**	**0.8568**	0.90215	0.87129	0.85325	0.87919	1	1	1	0.97662	0.97779	**0.98652**
		REI	3D	0.66541	0.8134	**0.93661**	**0.99495**	**0.99739**	**0.91876**	1	1	1	**0.9906**	**0.99109**	0.94797
			3DH	**0.76356**	**0.8568**	0.90215	0.88229	0.90735	**0.91876**	1	1	1	0.89874	0.94662	0.94797
		WGC	3D	0.66541	0.8134	**0.93661**	**0.97083**	**0.98372**	0.80367	1	1	1	**0.96522**	**0.97221**	0.91875
			3DH	**0.76356**	**0.8568**	0.90215	0.7749	0.76495	0.80367	1	1	1	0.87119	0.88689	0.91875
	4	RE	3D	0.57834	**0.93233**	**0.97658**	**0.98927**	**0.99429**	0.80187	1	**0.91627**	**0.97112**	**0.99088**	**0.99424**	0.79843
			3DH	**0.67905**	0.90504	0.91201	0.91285	0.86179	0.80187	1	0.82959	0.88976	0.9117	0.85413	0.79843
		REI	3D	0.57834	**0.94328**	**0.98678**	**0.99641**	**0.99782**	**0.94087**	1	**0.95272**	**0.98625**	**0.99647**	**0.99843**	**0.945**
			3DH	**0.67905**	0.79653	0.89417	0.9453	0.95994	**0.94087**	1	0.80119	0.89571	0.94729	0.96501	**0.945**
		WGC	3D	0.57834	**0.92057**	**0.95911**	**0.96975**	**0.97639**	0.46457	1	**0.92177**	**0.96086**	**0.97434**	**0.98036**	0.46705
			3DH	**0.67905**	0.42533	0.44066	0.45789	0.43809	0.46457	1	0.40808	0.43616	0.45685	0.43938	0.46705

Table 4.4.1 summarizes the MS-SSIM fusion metric results on 12 datasets. The first six column values are obtained by comparing the low magnification data with the fused data and the next six column values are obtained by comparing the high magnification data with the fused data. Within each fusion method, the better performing transformation method is shown by bold type face and within each dataset, the better performing combination is highlighted with yellow color. From the table 4.4.1, it can be seen that REI fusion method and '3D' transformation method perform better on an average. It can also be seen that '3D Hybrid' method is able to consistently preserve finer details of the low magnification data, which was the intended purpose of that method. The difference between the fused data obtained using '3D' and '3D Hybrid' method is shown in figure 4.4.4. From the figure, it can be seen that significant difference is seen at high transition areas.

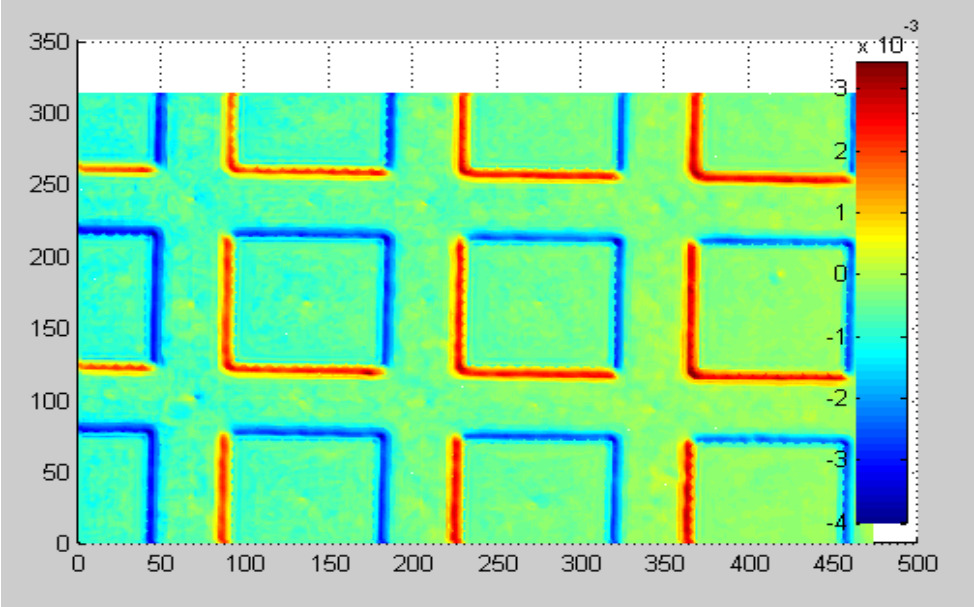

FIGURE 4.4.4: Difference between fused square grid array data obtained using 3D and '3D Hybrid' method showing artifacts near sudden transition areas.

TABLE 4.4.2: Multi-scale performance metrics for 12 datasets using '3D' transformation and 'REI' fusion method combination.

		MS-SSIM											
		Rl,F	Rl,F	Rl,F	Rl,F	Rl,F	Rl,F	Rh,F	Rh,F	Rh,F	Rh,F	Rh,F	Rh,F
	Data	R11(1)	R11(2)	R11(3)	R11(4)	R11(5)	R11(6)	R12(1)	R12(2)	R12(3)	R12(4)	R12(5)	R12(6)
STRUCTURED DIRECTIONAL SURFACES	1	0.97231	**0.99574**	**0.99432**	**0.99181**	**0.99329**	**0.95908**	1	**0.99108**	**0.99152**	**0.99082**	**0.99431**	**0.96259**
	2	0.2007	**0.43849**	0.38758	**0.92567**	**0.92701**	0.87568	1	1	1	0.62762	**0.79636**	**0.89354**
	3	0.56864	0.94446	**0.96962**	**0.99331**	**0.99768**	**0.99475**	1	**0.94186**	0.96519	**0.99243**	**0.99757**	**0.99072**
	4	0.59743	0.96708	0.98543	**0.99647**	**0.99816**	**0.99937**	1	**0.96579**	0.98435	**0.9964**	**0.99813**	**0.99931**
STRUCTURED NON-DIRECTIONAL SURFACES	1	0.49623	0.94139	**0.97298**	**0.98865**	**0.99617**	**0.98332**	1	0.95246	**0.97943**	**0.99074**	**0.99665**	0.98994
	2	0.64934	0.9394	0.98228	0.99723	**0.9993**	**0.99874**	1	0.95759	0.9872	0.99767	**0.99935**	**0.99905**
	3	0.62188	0.91804	0.96294	**0.98794**	**0.99425**	**0.98289**	1	0.90634	0.96629	**0.98825**	**0.99443**	**0.99737**
	4	0.64503	0.94949	0.98576	**0.99774**	**0.99931**	**0.9914**	1	**0.95792**	0.98779	0.9977	**0.99917**	**0.99277**
SYSTEMATIC SURFACES	1	0.48351	**0.93232**	**0.96757**	**0.96578**	**0.98573**	0.89082	1	**0.921**	**0.9545**	**0.96411**	**0.98857**	**0.89289**
	2	0.57731	0.58843	0.79612	**0.95256**	**0.97495**	0.83134	1	1	1	**0.94954**	**0.97645**	0.80606
	3	0.66541	0.8134	**0.93661**	**0.99495**	**0.99739**	**0.91876**	1	1	1	**0.9906**	**0.99109**	0.94797
	4	0.57834	**0.94328**	**0.98678**	**0.99641**	**0.99782**	**0.94087**	1	**0.95272**	**0.98625**	**0.99647**	**0.99843**	**0.945**

TABLE 4.4.3: Single-scale performance metrics for 12 datasets using '3D' transformation and 'REI' fusion method combination.

		MI			UQI			SSIM		
		Rl,F	Rh,F	Rh,Rl	Rl,F	Rh,F	Rh,Rl	Rl,F	Rh,F	Rh,Rl
	Data	R6(1)	R6(2)	R6(3)	R7(1)	R7(2)	R7(3)	R8(1)	R8(2)	R8(3)
STRUCTURED DIRECTIONAL SURFACES	1	0.95421	1.6332	0.8876	0.38342	0.55958	0.4753	0.95399	0.94036	0.90464
	2	-1.764	2.7849	-1.9051	0.33509	0.99431	0.33464	0.33457	0.99378	0.33644
	3	2.7145	4.1774	1.6381	0.42954	0.90095	0.30803	0.84771	0.96835	0.81225
	4	3.3551	4.8871	2.3255	0.45826	0.92981	0.35317	0.86437	0.98269	0.82642
STRUCTURED NON-DIRECTIONAL SURFACES	1	2.1484	4.2011	1.8842	0.43234	0.85638	0.39827	0.73501	0.98677	0.69918
	2	4.1468	5.6686	3.9126	0.52631	0.857	0.55187	0.78655	0.9911	0.77145
	3	3.487	5.3571	3.9264	0.50913	0.80669	0.46801	0.75042	0.9763	0.70235
	4	4.3492	6.0224	4.3134	0.59184	0.88238	0.59666	0.78753	0.9906	0.76761
SYSTEMATIC SURFACES	1	0.58719	3.1346	0.26262	0.68245	0.95377	0.63091	0.68669	0.97088	0.6509
	2	-0.86498	-0.66012	0.34107	0.36256	0.72014	0.43278	0.71043	0.90105	0.76596
	3	0.091405	2.1367	-0.58533	0.4371	0.90257	0.44177	0.8317	0.98443	0.82173
	4	1.2395	3.3057	0.98117	0.5136	0.94528	0.44213	0.80895	0.98735	0.78274

Table 4.4.2 summarizes the MS-SSIM values obtained on all 12 datasets using ‘REI’ fusion method and ‘3D’ transformation method. Table 4.4.3 summarizes the single-scale fusion metrics for the ‘3D’ transformation and ‘REI’ fusion combination. Table 4.4.3 shows three single-scale metrics (MI, UQI and SSIM) when the low magnification data (Rl) is compared with fused data (F), high magnification data (Rh) with fused data (F), and high magnification data with low magnification data respectively. Comparing the values between (Rh,F) and (Rh,Rl), it can be seen that the fused data has better similarity to the high magnification data compared to the low magnification data. This shows that data fusion process is able to produce a synergistic effect of preserving significant data pertaining to both the magnifications and generate a fused data which is effective in characterizing the surface when compared to both the magnification data sets separately. Figure 4.4.5 shows the fused data for structured directional surface sample datasets.

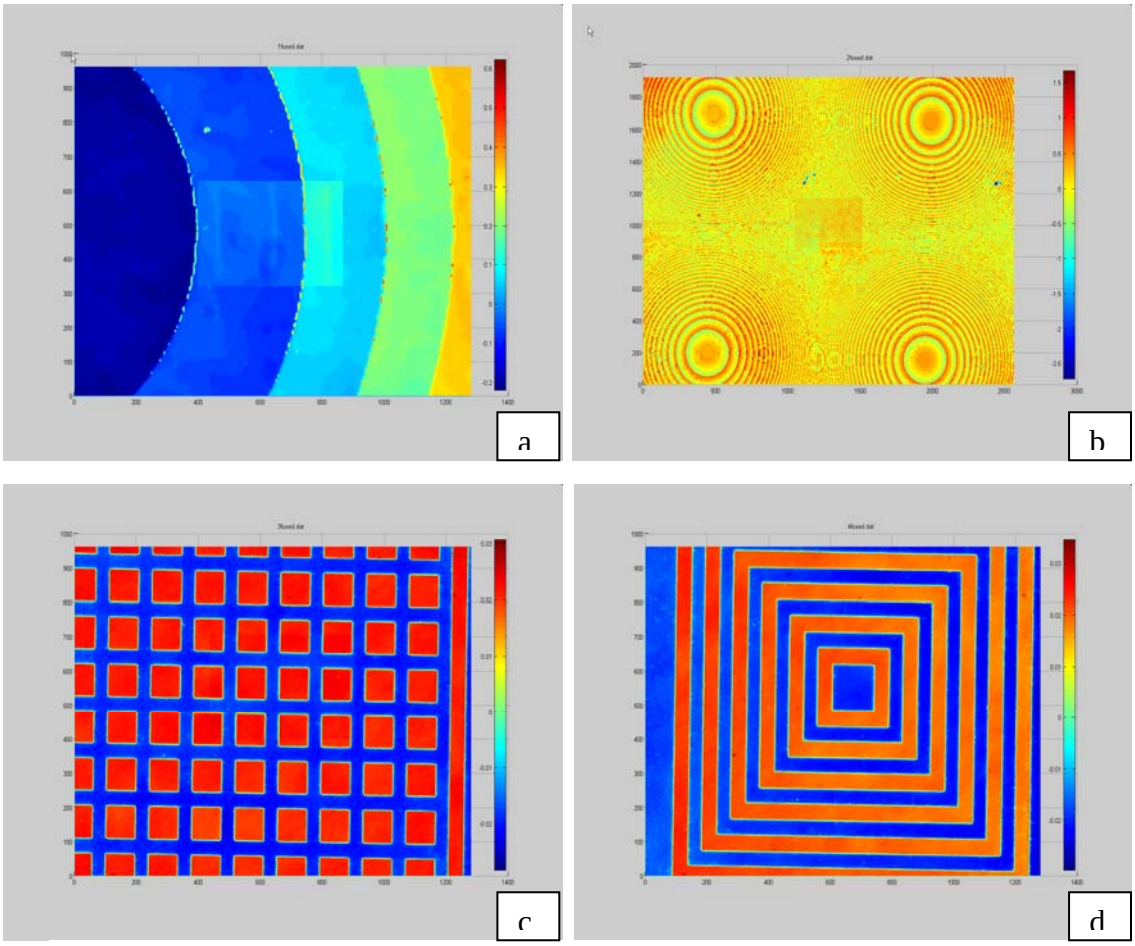

FIGURE 4.4.5: Fused data for four structured directional surfaces considered (a) Beam shaper optical surface (b) Fresnel micro-lens array (c) Square grid pattern surface (d) Concentric square pattern surface.

The fused data location for Fresnel micro-lens array data (shown in figure 4.4.5b) is shown in figure 4.4.6. Green box is used to show the location of the fused data and a red box near the fused location is shown to illustrate the resolution issues when low magnification is used.

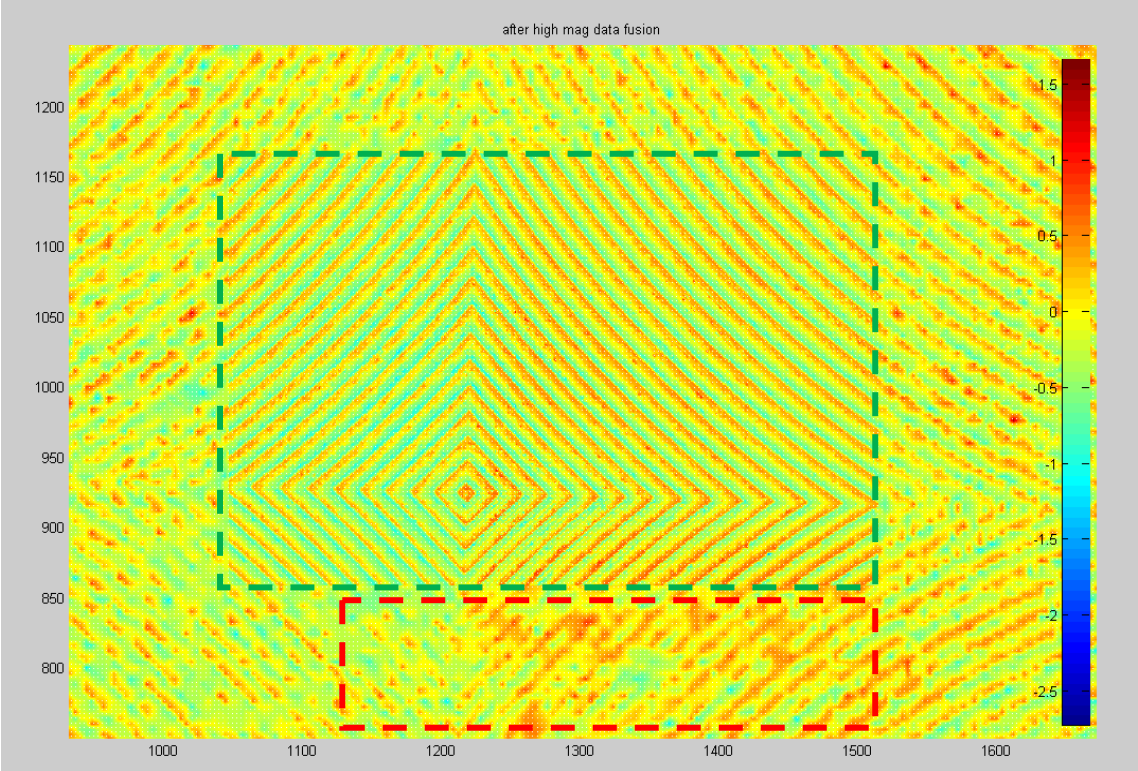

FIGURE 4.4.6: Green box showing the fused data and red box showing the resolution issues with the low magnification data on Fresnel lens.

Figure 4.4.7 and 4.4.8 show the fused data for structured non-directional and systematic surface sample datasets respectively. From figure 4.4.5a, 4.4.7 b, c, and d, it can be seen that there are visible artifacts near the edges when the fused data is replaced into the low magnification data, showing as sudden height transition between fused data and the original low magnification data. These errors are not seen on nominally planar surfaces like the ones seen in figure 4.4.7.

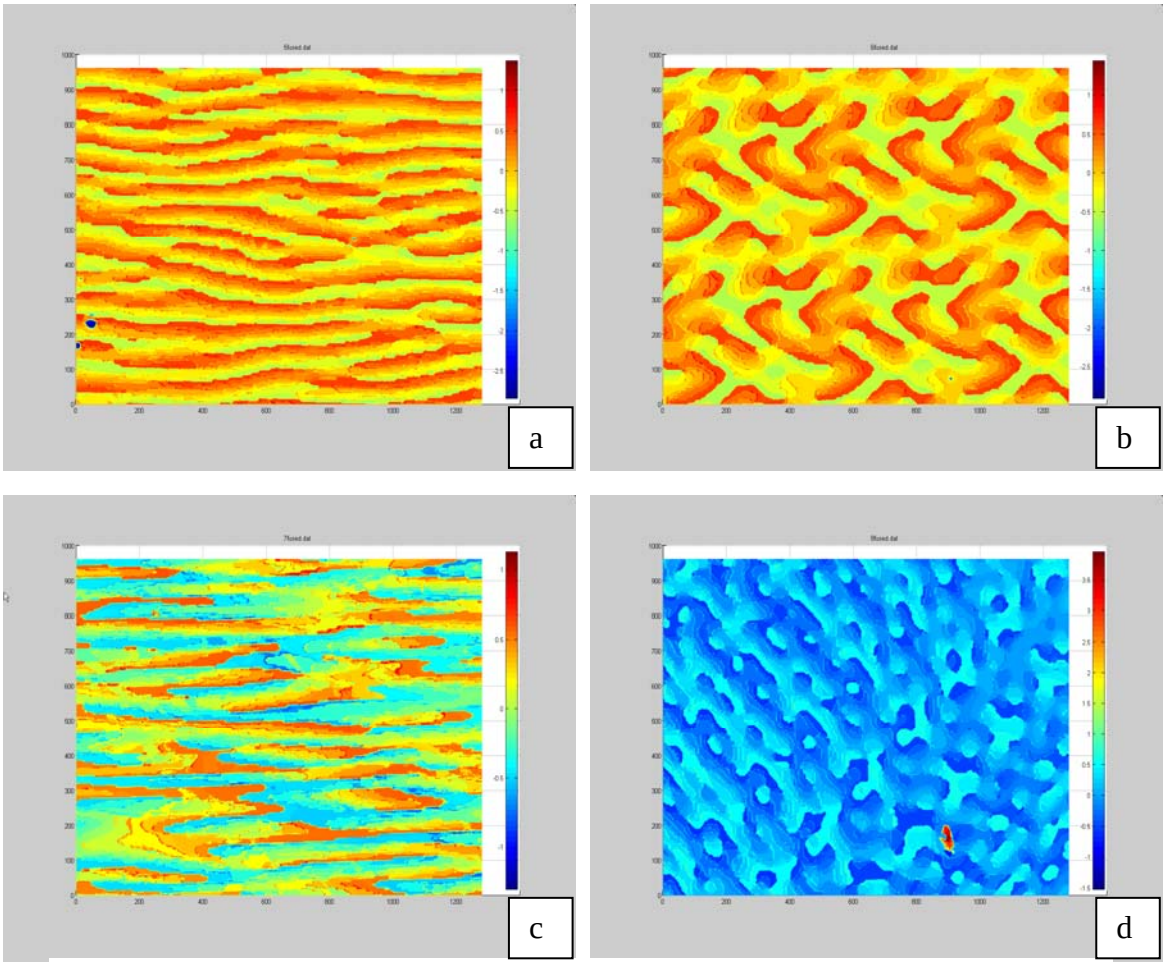

FIGURE 4.4.7: Fused data for four structured non-directional surfaces considered (a) Dipole diffuser optical surface (b) Spot array generator optical surface (c) and (d) Pattern generator optical surfaces.

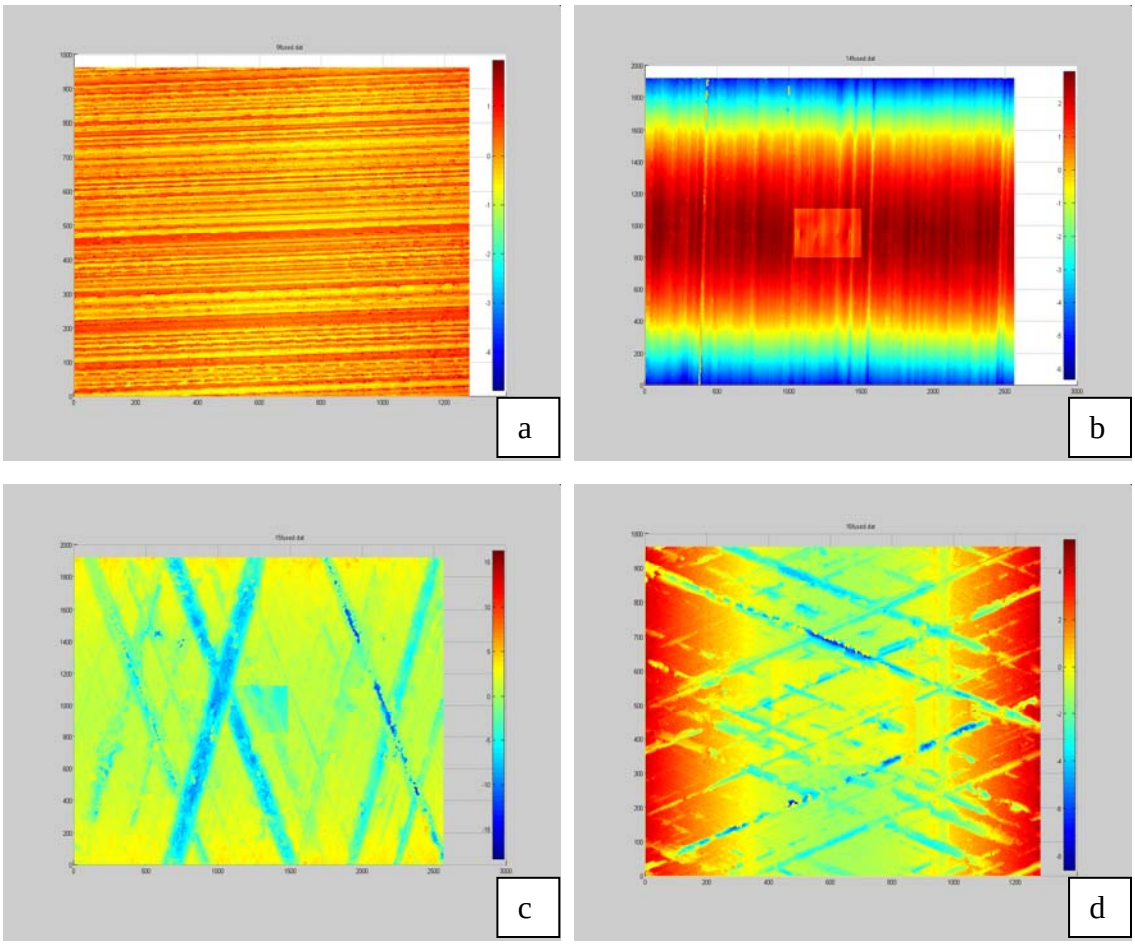

FIGURE 4.4.8: Fused data for four systematic surfaces considered (a) Line generator optical surface (b) Turned surface (c) and (d) Honed surfaces.

These visible edge artifacts are mainly due to significant change in between datasets pertaining to low frequency. From figure 4.3.3, it can be seen that both the 5X and 20X data have almost similar data at all sub-levels except the last level, which represents the lowest resolution level. The reason for this significant change in shape could be due to errors induced in shape at different magnifications, defocus and NA variations between different magnifications which were discussed in sections 2.2.6, 2.3.3 and 2.3.7 of second chapter. This effect is negligible on nominally planar surfaces and becomes significant when dealing with non-planar surfaces and surfaces with high aspect

ratio sub-regions. In order to reduce these edge artifacts and thereby accommodate non-planar surfaces, the fusion strategy has to change for sub-images containing shape information.

4.5. Summary

Different fusion metrics were compared for their performance using a set of noisy versions of datasets. Based on that study, three single-scale (MI, UQI and SSIM) and one multi-scale performance metric (MS-SSIM) were selected. Using these performance metrics, two directional surface datasets were transformed using '3D' and '3D Hybrid' methods and fused using three weighted average methods (RE, REI and WGC). Based on that study, REI method was selected as the preferred fusion method and '3D' as the preferred transformation method. Using the selected options for edge detection, transformation method and fusion method, 12 datasets were fused and their performance metrics were summarized.

Visual edge effects on non-planar surfaces were demonstrated and the need for optimized fusion strategy was discussed. In order to reduce these artifacts, a new fusion strategy will be explored that would utilize existing philosophy in surface metrology domain – separation of roughness, waviness and form. In the next chapter, surface measurement datasets will be treated specifically and specific strategies for data fusion for surface metrology datasets in particular will be developed. First, optimized strategy for fusing multiple magnification datasets of non-planar surfaces will be discussed, followed by single-scale, single-domain data fusion and single-scale multiple-domain data fusion.

CHAPTER 5: FUSION STRATEGIES FOR SURFACE METROLOGY

In the previous chapters, a generic framework for multi-scale data fusion was described along with possible options available at each individual step. Single-scale and multi-scale fusion metrics that could be used to evaluate individual options and optimize the fusion process were also described. The visual edge artifacts seen on non-planar surfaces and the need for an optimized fusion strategy to accommodate those surfaces were discussed. In this chapter, surface measurement datasets are treated specifically and specific strategies for data fusion for surface metrology datasets in particular are developed. First, optimized strategy for fusing multiple magnification datasets of non-planar surfaces is discussed, followed by single-scale, single-domain data fusion and single-scale, multiple-domain data fusion.

5.1. Multi-scale, Single-domain Data Fusion

The possible cause of edge artifacts could be due to errors induced in shape at different magnifications, defocus and NA variations between different magnifications, which were discussed in sections 2.2.6, 2.3.3 and 2.3.7 of second chapter. This effect is very prominent on surfaces that are nominally flat on most areas and have a high aspect ratio feature which is measured using higher magnification or sampling interval.

In order to reduce these edge artifacts and thereby accommodate non-planar surfaces, the fusion strategy has to change for sub-images containing shape information. The framework for multi-scale data fusion for surface metrology datasets is shown in figure 5.1.1. It retains most of the steps that were discussed for a generic multi-scale data fusion process, but deviates only for the data fusion step.

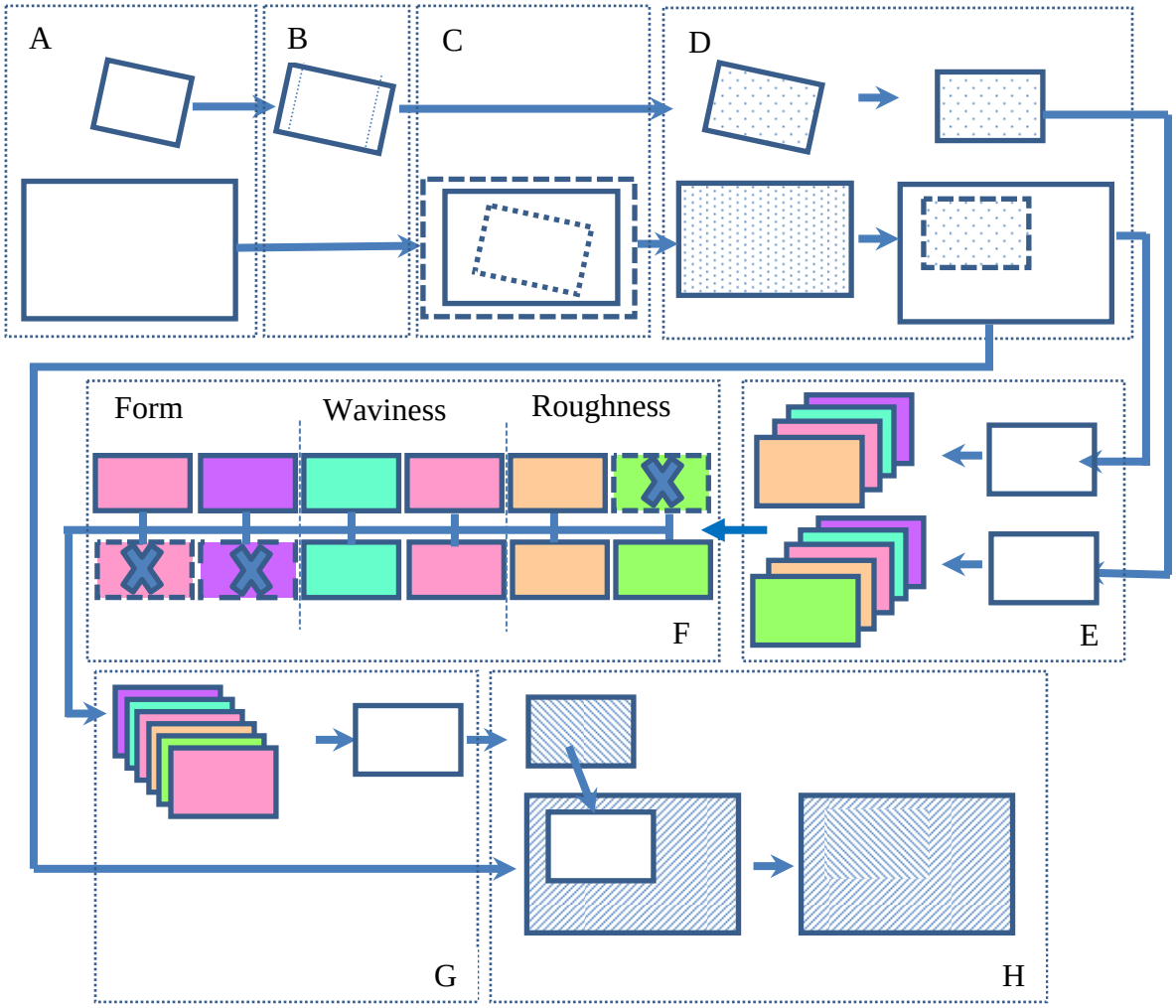

FIGURE 5.1.1: Schematic of FWR multi-scale data fusion for surface metrology datasets (A) Original Data (B) Pre-condition (outlier removal, resample and resize) (C) Coarse registration (D) Fine registration after control point detection (E) Multi scale decomposition on selected same size area from both data (F) Multi scale Fusion (G) Inverse Transform on fused sub-datasets to obtain fused data (H) Fused data replaced to the original location.

5.1.1. Pre-conditioning

Most naturally occurring surfaces and man-made surfaces could be analyzed in multi-scale format provided the data doesn't have too many outliers and missing data. It is permissible to fill sporadic missing data with linear interpolation techniques, but if the missing data is in big continuous areas, filling those areas with mean values or zeros is not effective. This in turn results in poor multi-scale decomposition results.

The data obtained using high sampling rate ($Data_{High}$) and low sampling rate ($Data_{Low}$) are initially leveled with respect to a reference surface if there is one or a least squares plane surface is used as a reference. The data are normalized and outliers and missing data points are replaced with mean value (since the data was previously normalized, the mean value will be very close to zero). If the data is very noisy due to vibration issues or system's dynamic noise level, it is recommended to de-noise the data by statistical methods either in Fourier domain or wavelet domain [164, 165]. Either one of the data set is resampled to ensure that the ratio of their sampling interval is a power of two. The datasets are also resized to have the array size a power of two, if DWT is the chosen decomposition method. Figure 5.1.2a shows the original 5X magnification data of the honed surface and figure 5.1.2b shows the resampled version of the 5X magnification data to match the sampling interval of the 20X magnification data.

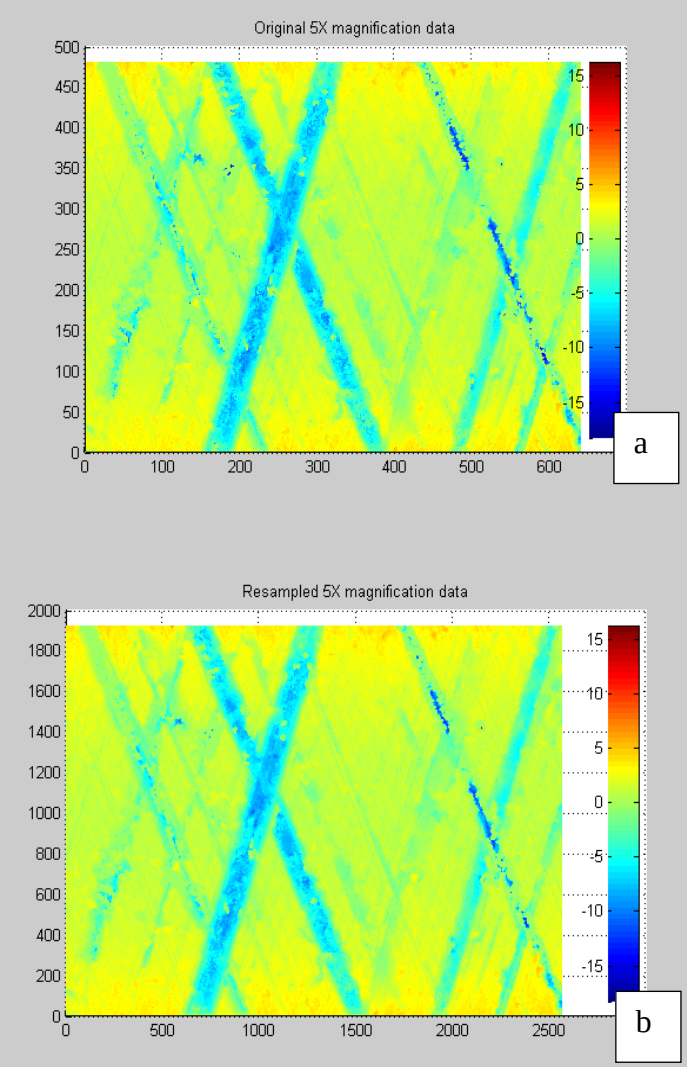

FIGURE 5.1.2: (a) 5X magnification data of honed surface (b) Resampled version to match 20X magnification data's sampling interval.

5.1.2. Coarse Registration

Data $_{Low}$ is up sampled to match the sampling interval of Data $_{High}$ using linear interpolation method to generate Data $_{LowHighRes}$. Coarse registration is performed using normalized cross correlation function on Data $_{LowHighRes}$ with Data $_{High}$ as template and then based the peak location, a sub-set image Data $_{LowClip}$ (similar to the area of Data $_{High}$, along with a border region to accommodate angular variation between both the datasets)

is generated from Data $_{Low}$. Figure 5.1.3 shows the 3D mesh representation of the calculated NCC values and the black circled location indicates the maximum value of the NCC, denoting the possible matching location of 20X magnification data on to 5X magnification data.

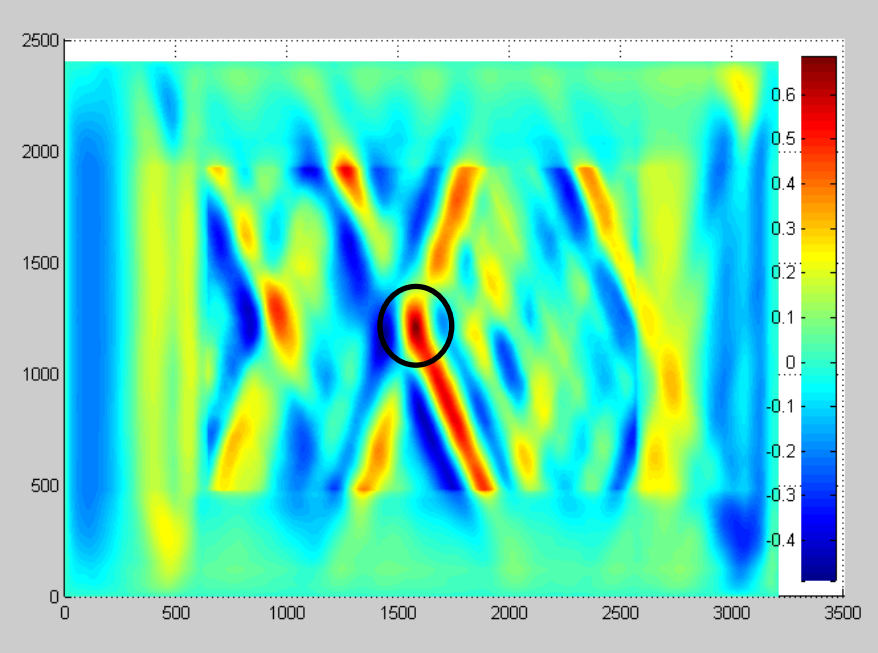

FIGURE 5.1.3: 3D mesh of NCC for 20X magnification data on 5X magnification data.

5.1.3. Fine Registration

For effective fine registration, it is recommended to perform segmentation and edge detection using single 'Watershed' method. Figure 5.1.4 shows the data points used for fine registration – green colored data points obtained from 20X magnification data and blue colored data points from 5X magnification data. Magenta colored data points were obtained after realignment using ICP finite difference method.

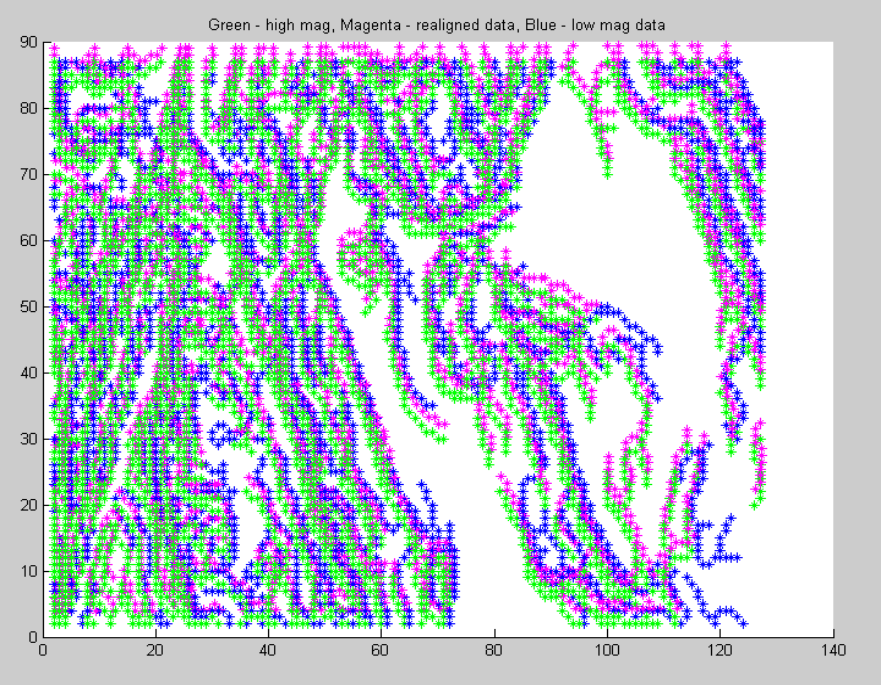

FIGURE 5.1.4: Green data points obtained from 20X magnification data, blue data points obtained from 5X magnification data and magenta data points are the realigned location of green data points.

Using the transformation parameters, $Data_{High}$ is aligned to $Data_{Low}$. A new data $Data_{LowClipNew}$ is generated from $Data_{Low}$ based on t_x and t_y values, and up sampled (to match the sampling interval of $Data_{High}$) to get $Data_{LowClipNewRes}$. Figure 5.1.5a shows $Data_{LowClipNewRes}$ and figure 5.1.5b shows the realigned $Data_{High}$ for honed surface sample.

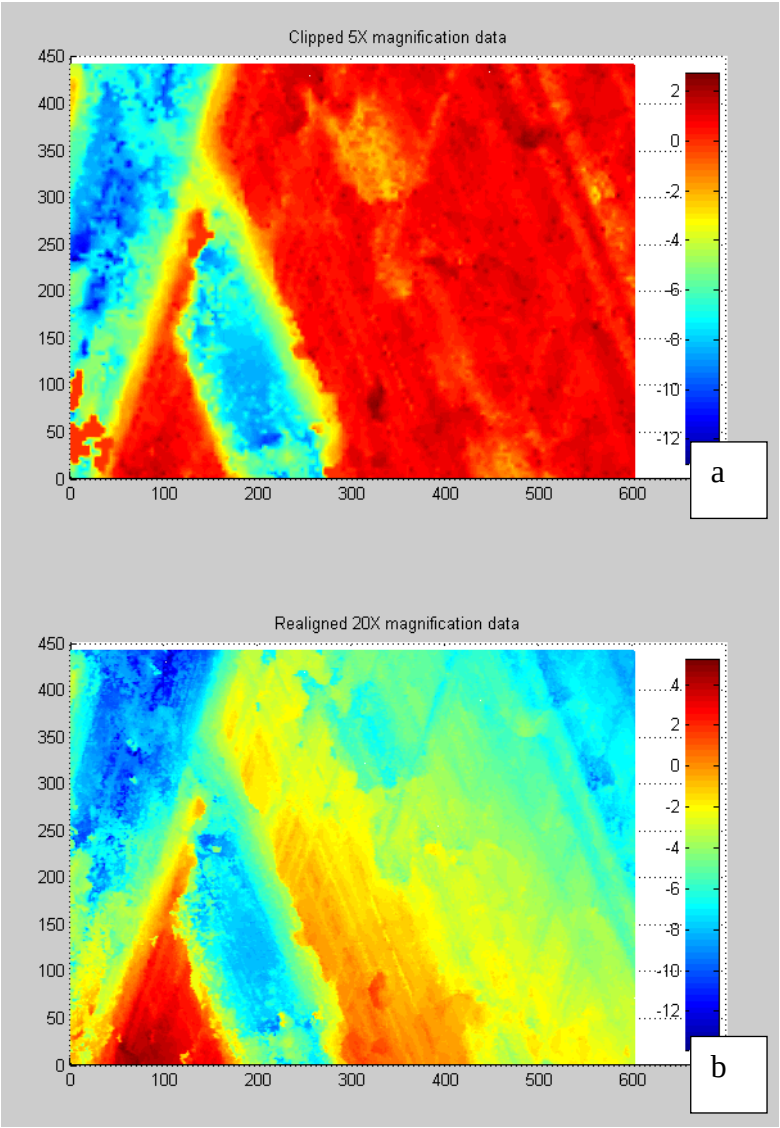

FIGURE 5.1.5: (a) Clipped 5X magnification data
(b) Realigned 20X magnification data.

5.1.4. Multi-scale Decomposition

For multi-scale decomposition, à trous DWP method with B3 spline as mother wavelet was chosen and six level of decomposition is performed to obtain two sets of six wavelet planes for $Data_{LowClipNewRes}$ and $Data_{High}$.

5.1.5. Data Fusion

The six wavelet planes obtained are matched as shown in figure 5.1.6. The planes are then categorized in a fashion similar to separation of roughness, waviness and form. The first two planes are considered to represent roughness and next two planes to represent waviness and last two planes to represent form. The first two wavelet planes of $Data_{LowClipNewRes}$ were obtained by interpolation and therefore they are not considered for fusion. For planes representing form, only the planes of $Data_{LowClipNewRes}$ are considered so as to match overall from of $Data_{Low}$, into which the fused data is going to be placed.

For the planes belonging to waviness and roughness and that were not obtained by interpolation, data fusion is performed at pixel level using REI weighted average approach. This strategy specific to surface metrology domain is named FWR method to represent the usage of separation of surface data to ‘Form, Waviness and Roughness’.

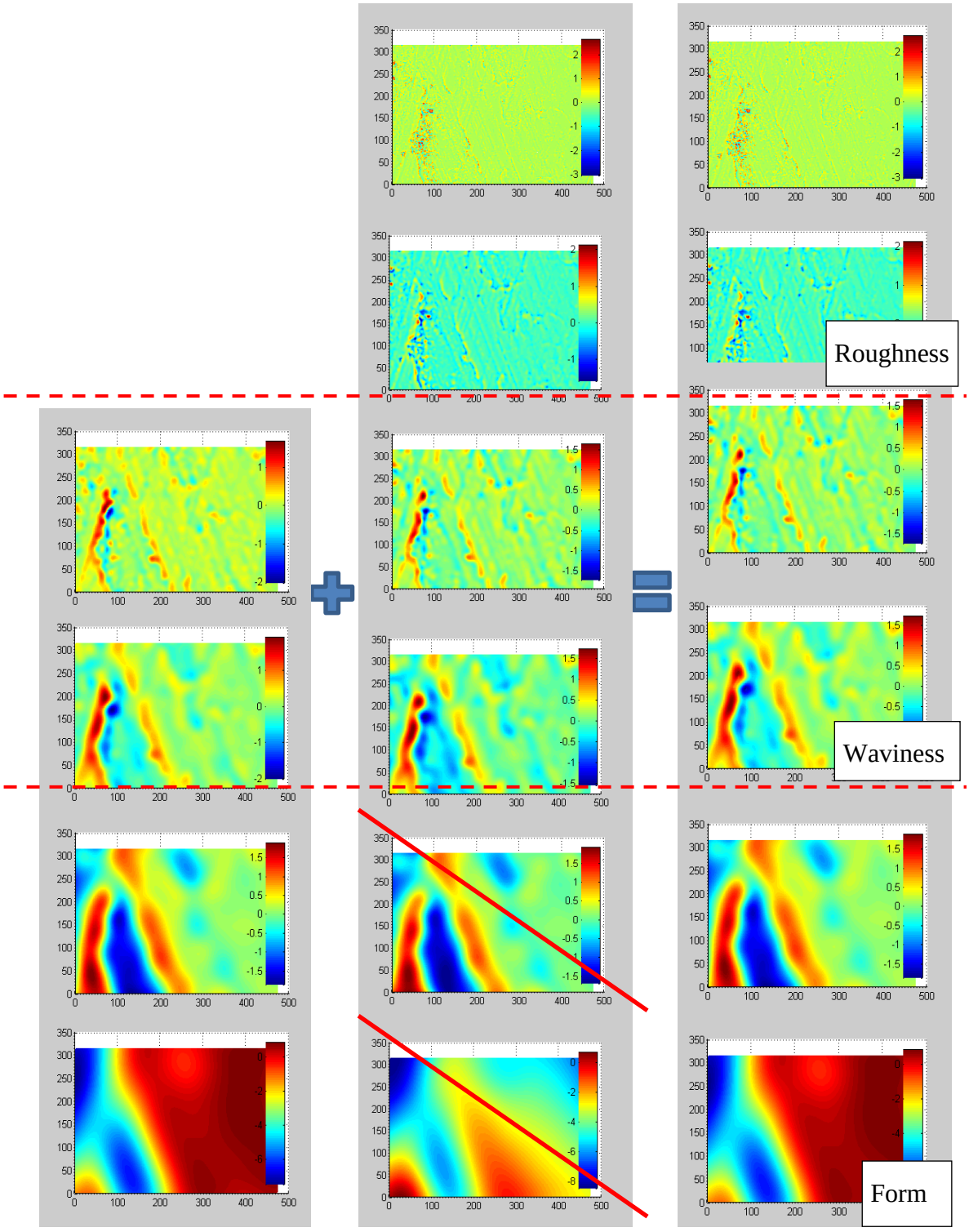

FIGURE 5.1.6: Two set of six wavelet planes fused to obtain new set of six wavelet planes using the FWR method.

5.1.6. Inverse Transform

The six fused wavelet planes are inverse transformed to obtain the fused data, which is then replaced into the corresponding location in $Data_{LowHighRes}$ (up sampled version of $Data_{Low}$). Figure 5.1.7 shows the fused data using the new proposed FWR method, on beam shaper optical surface data and surface obtained from turning process, which has shown edge artifacts when the generic fusion strategy was followed.

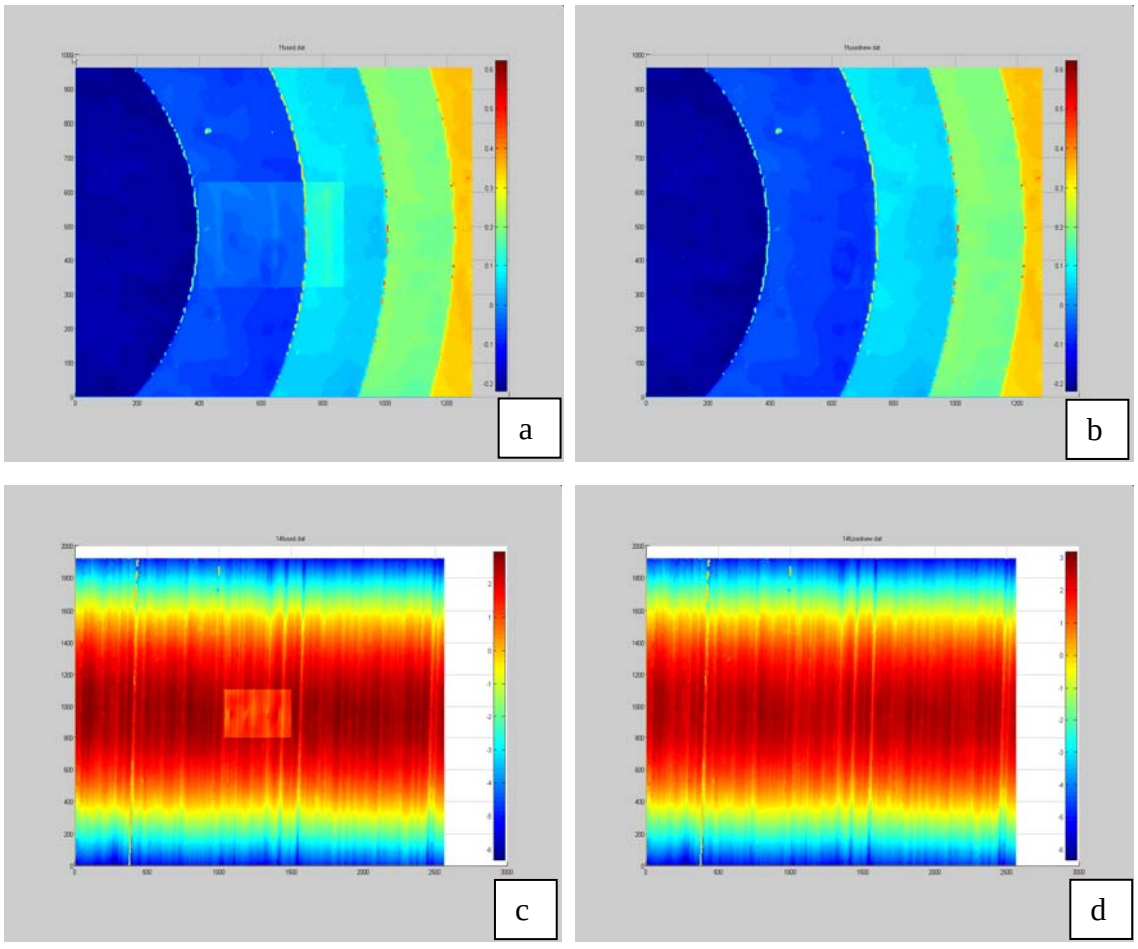

FIGURE 5.1.7: Fused data for beam shaper optical surface (a) using all frames (b) using FWR method; Fused data for turned surface (c) using all frames (d) using FWR method.

Figure 5.1.8 shows similar results obtained on two honed surface samples obtained using the generic fusion strategy and the FWR method. It can be seen from figure 5.1.7 b and d, and 5.1.8 b and d that FWR method is able to avoid edge artifacts.

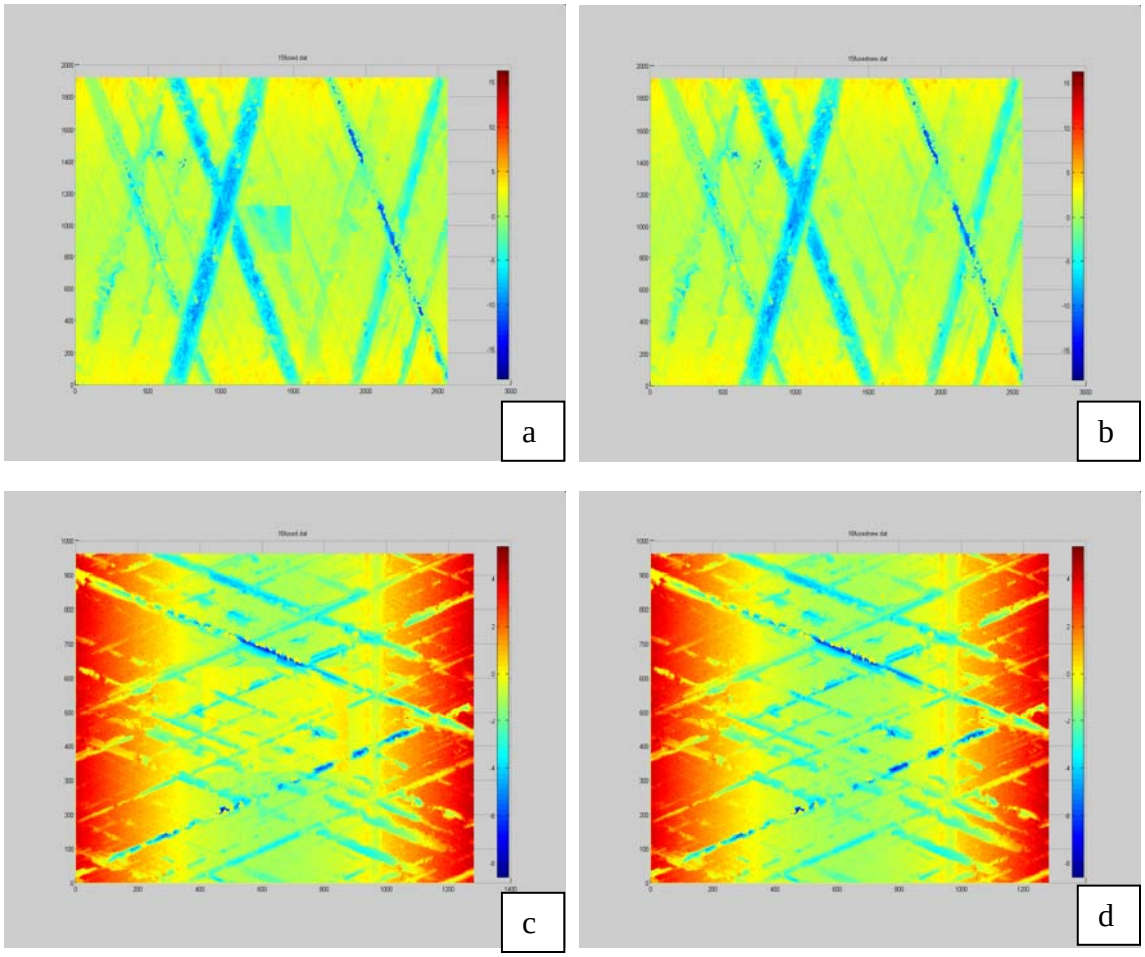

FIGURE 5.1.8: Fused data for honed surface (a and c) using all frames (b an d) using FWR method.

In order to demonstrate the robustness of this method, as an example, a 10X magnification measurement on a formed location on a surface of a one cent coin is fused with a 5X magnification measurement, as shown in figure 5.1.9.

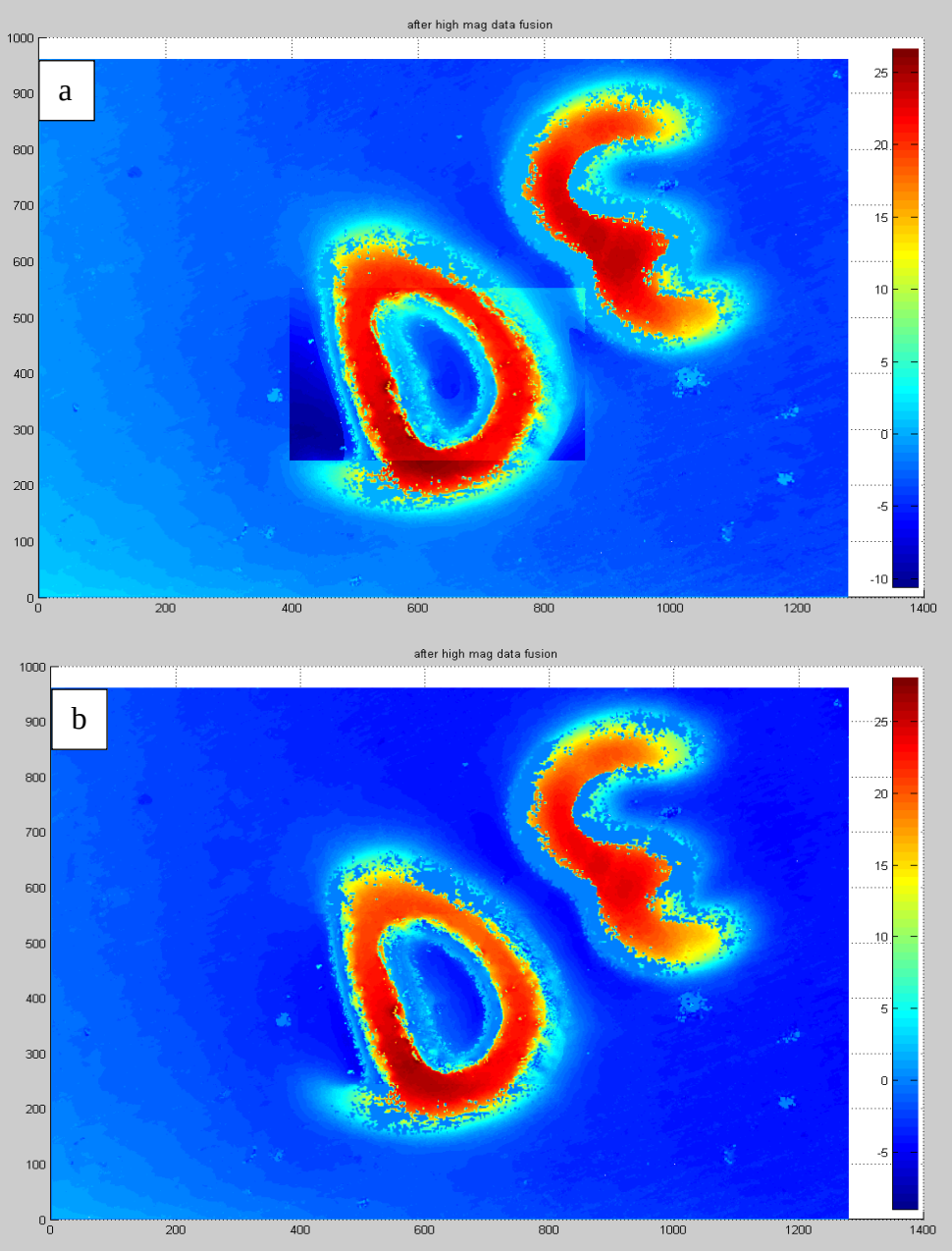

FIGURE 5.1.9: (a) Fused data obtained when all planes are considered for fusion (b) Fused data obtained using FWR method.

Figure 5.1.9a is obtained when all the six planes were treated equally and fused, showing poor transition with the 5X magnification data. Figure 5.1.9b is obtained when the roughness and waviness planes are fused and the form planes are taken from the 5X magnification data, showing good transition between the fused data and the 5X magnification data.

Having successfully demonstrated the fusion of multiple magnification datasets on different surface types, as a next step, fusion pertaining to single-scale, single-domain data is explored.

5.2. Single-scale, Single-domain Data Fusion

Single-scale, single-domain data fusion is particularly useful in situations where different light settings could be used to obtain more data. Consider the measurements obtained on spherical surface on the hard disk drive suspension, which was detailed in chapter 1. Figure 5.2.1 shows the 3D data obtained using NT8000 ® system with 10x objective and 20% light setting. Figure 5.2.2 shows data obtained at 35% light setting. Due to camera saturation, this setting results in 'No Data' condition on most areas except the side slope regions. In order to merge these two data sets, all finite data points from both data sets are taken as control points. The data obtained using 20% light setting was considered as the reference data (A) as this data has more information regarding the flat surface. ICP finite difference method was used to align control points from data obtained using 35% light setting (B) to A. The aligned control points are shown in figure 5.2.3.

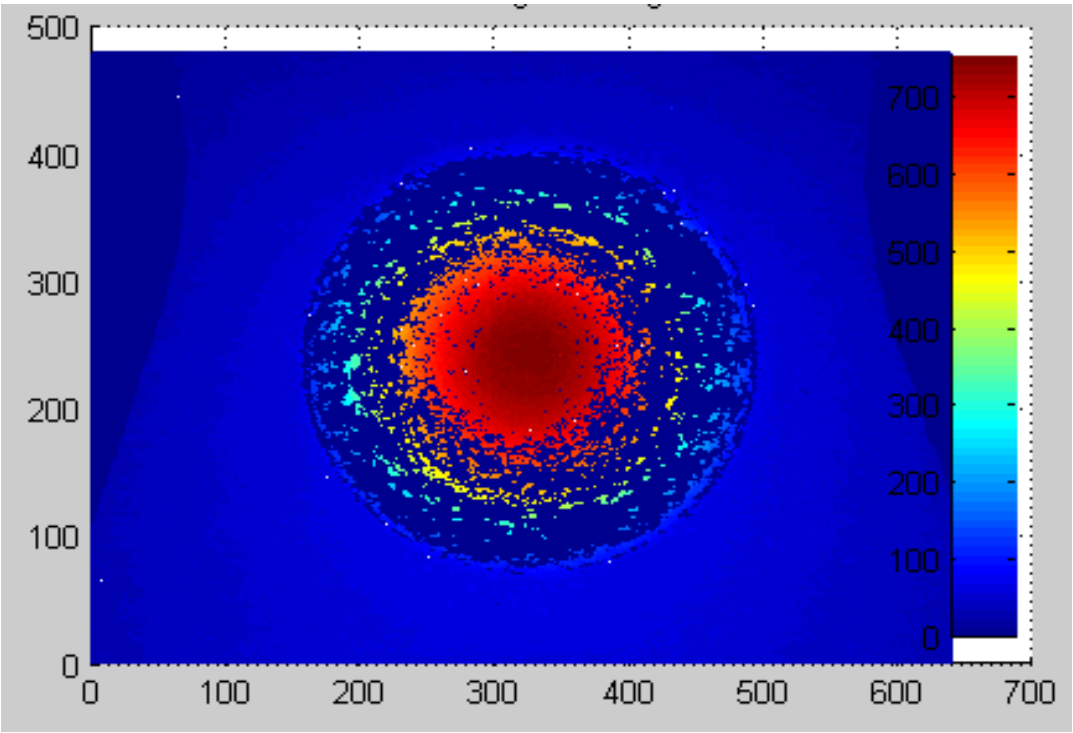

FIGURE 5.2.1: 3D surface plot of the spherical surface at 20% light setting.

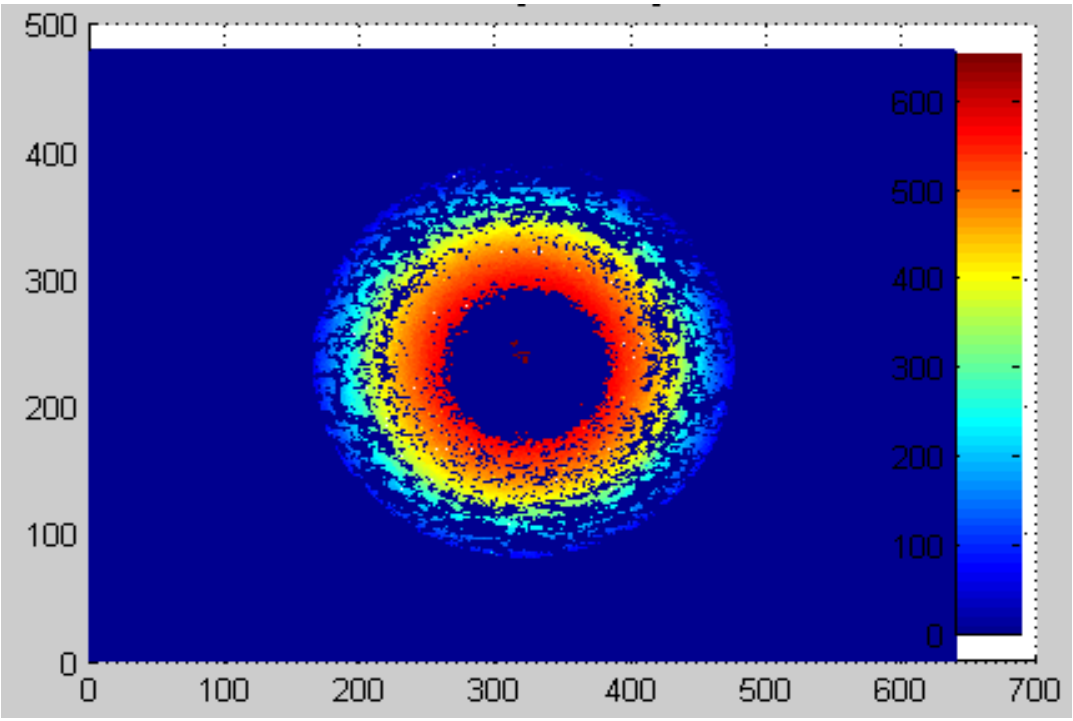

FIGURE 5.2.2: 3D surface plot of the spherical surface at 35% light setting.

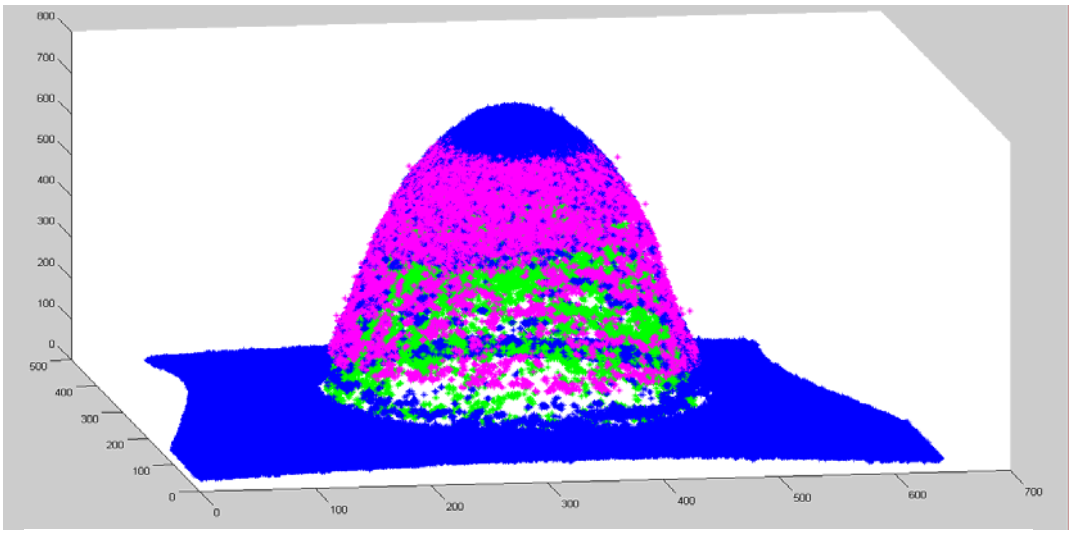

FIGURE 5.2.3: Control points (Blue – from data A, Green – from data B, Magenta – data of B after alignment).

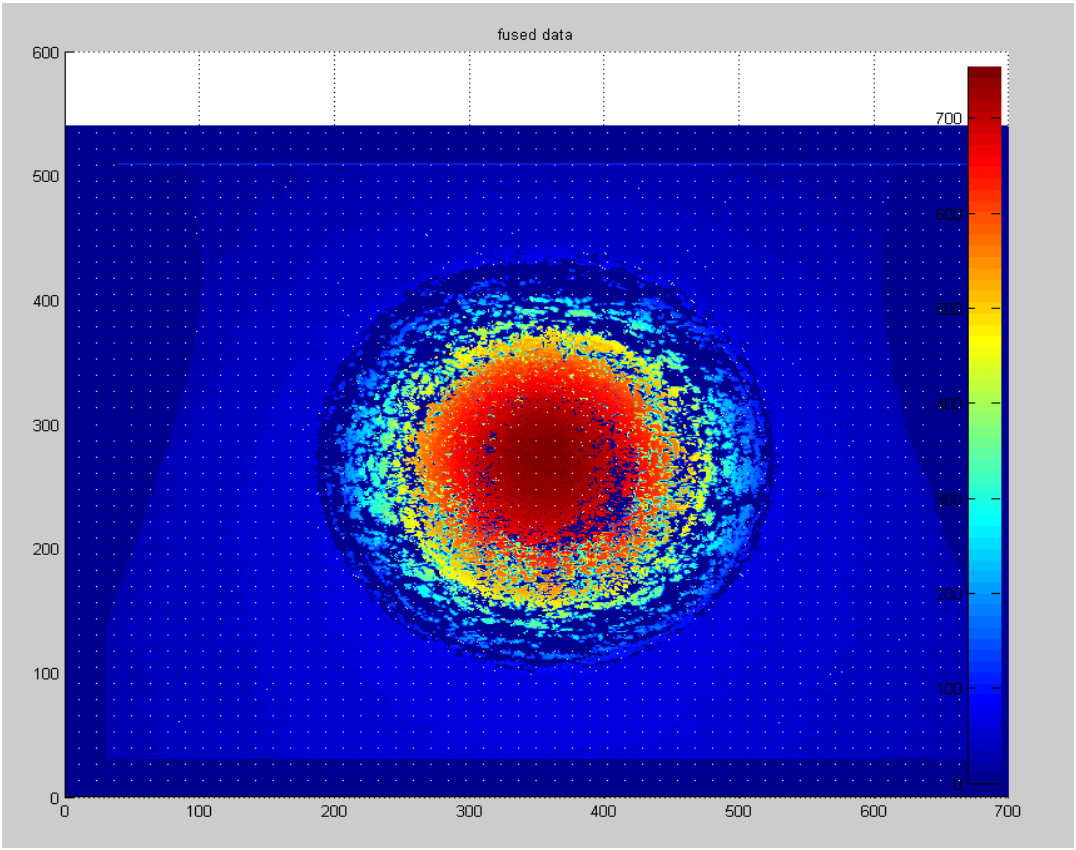

FIGURE 5.2.4: Fused 3D data.

Since the main surface that is under consideration is a single scale spherical surface and there is lot of missing data, multi scale decomposition of these data is not preferable. On a single scale, individual pixel level fusion is performed using maxima rule F(i,j) = Max [A(i, j), B(i, j)], where F(i, j) is a pixel in the fused data and A(i, j), B(i, j) are the corresponding pixels in both data. Since the missing data were replaced with either mean value of the data or zero, using average is not preferable. The fused data is shown in figure 5.2.4.

Having successfully demonstrated single-scale, single-domain data fusion, the next step is to fuse the data obtained from two domains. For this, data shown in figure 5.2.4 (with spacing of 0.9702 μm) is fused with 2D image shown in figure 5.2.5 obtained at 10X magnification with the pixel size of 0.832 μm.

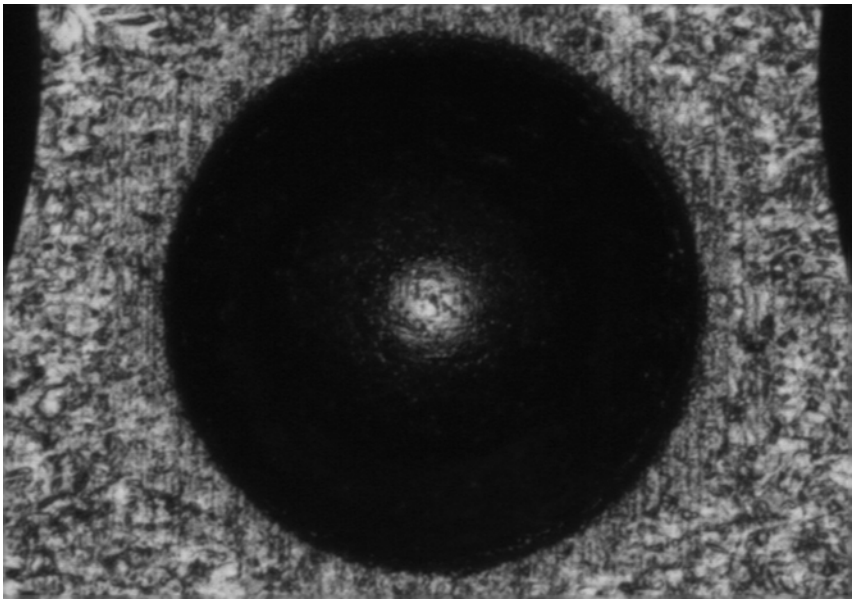

FIGURE 5.2.5: 2D image.

This method of data fusion is considered as single-scale (as the data sets have closely matching sampling size) and multi-domain (as both 2D and 3D data are considered) data fusion, which will be explained in detail in the next section.

5.3. Single-scale, Multi-domain Data Fusion

In order to fuse data obtained from two different domains, the data has to be converted to one common domain. For this, the 3D data (shown in figure 5.2.4) is converted to height based gray scale image, as shown in figure 5.3.1. Then the image is resampled using linear interpolation method to match the pixel size of the 2D image. Since the 2D image is not entirely height based and is rather a combination of slope and height, the control points have to be selected with care. From both the images, it can be seen that the edge of the flat surface and the false edge generated at the transition between the flat surface and the spherical surface are present in both images. Therefore these two edges are taken as control points and ICP finite difference algorithm is used for aligning the images, but the rotation about x and y axes are set to zero. After alignment, data fusion is performed at pixel level using the maxima rule $F(i,j) = \text{Max}\,[A(i, j), B(i, j)]$, where $F(i, j)$ is a pixel in the fused data and $A(i, j)$, $B(i, j)$ are the corresponding pixels in images. The fused image is shown in figure 5.3.2.

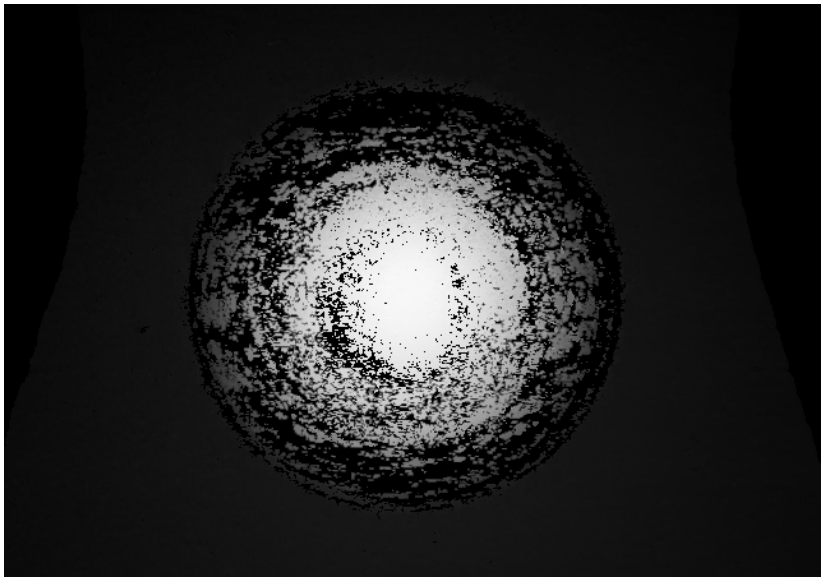

FIGURE 5.3.1: Fused 3D data converted to gray scale image.

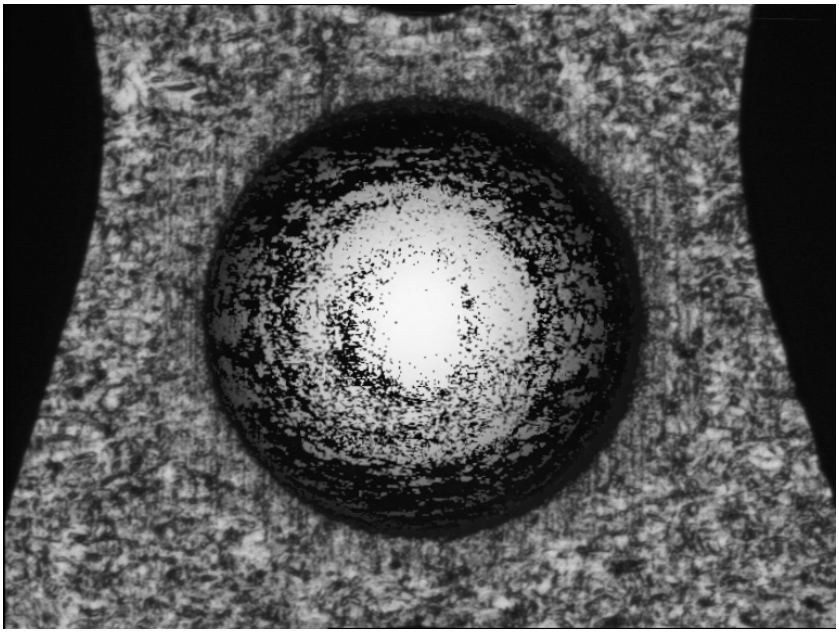

FIGURE 5.3.2: 2D Image fused with 3D data converted to gray scale image.

The fused data shown in figure 5.3.2 is then fused to the image obtained at 2.5X at a pixel size of 3.569 µm (shown in figure 5.3.3a) using the basic data fusion steps described in first chapter. It is possible to up sample 2.5X magnification image to match 10X magnification image, but for memory limitations, the concept is shown with down sampling 10X magnification image to match 2.5X magnification image.

As a first step, the image containing the 3D data with the sample size of 0.832 µm (shown in figure 5.3.3b) is down sampled to 3.569 µm (as shown in figure 5.3.3c). As a second step, normalized cross correlation function is used to find the approximate location of the high magnification image inside the low magnification image and the corresponding low magnification section is trimmed for further analysis, as shown in figure 5.3.3d. 'Canny' edge finder is used to find the control points in the images 'c' and 'd' shown in figure 5.3.3. ICP finite difference method is used to find the alignment between the two control points, with the rotations along x and y axes set to zero. Based on the obtained transformation matrix, image 'c' is rotated about z axis and the intensity

values are adjusted. Then data fusion is performed at pixel level using the maxima rule F(i,j) = Max [A(i, j), B(i, j)], where F(i, j) is a pixel in the fused data and A(i, j), B(i, j) are the corresponding pixels in the low magnification and high magnification images. The final image after 3D data fusion is shown in figure 5.3.4.

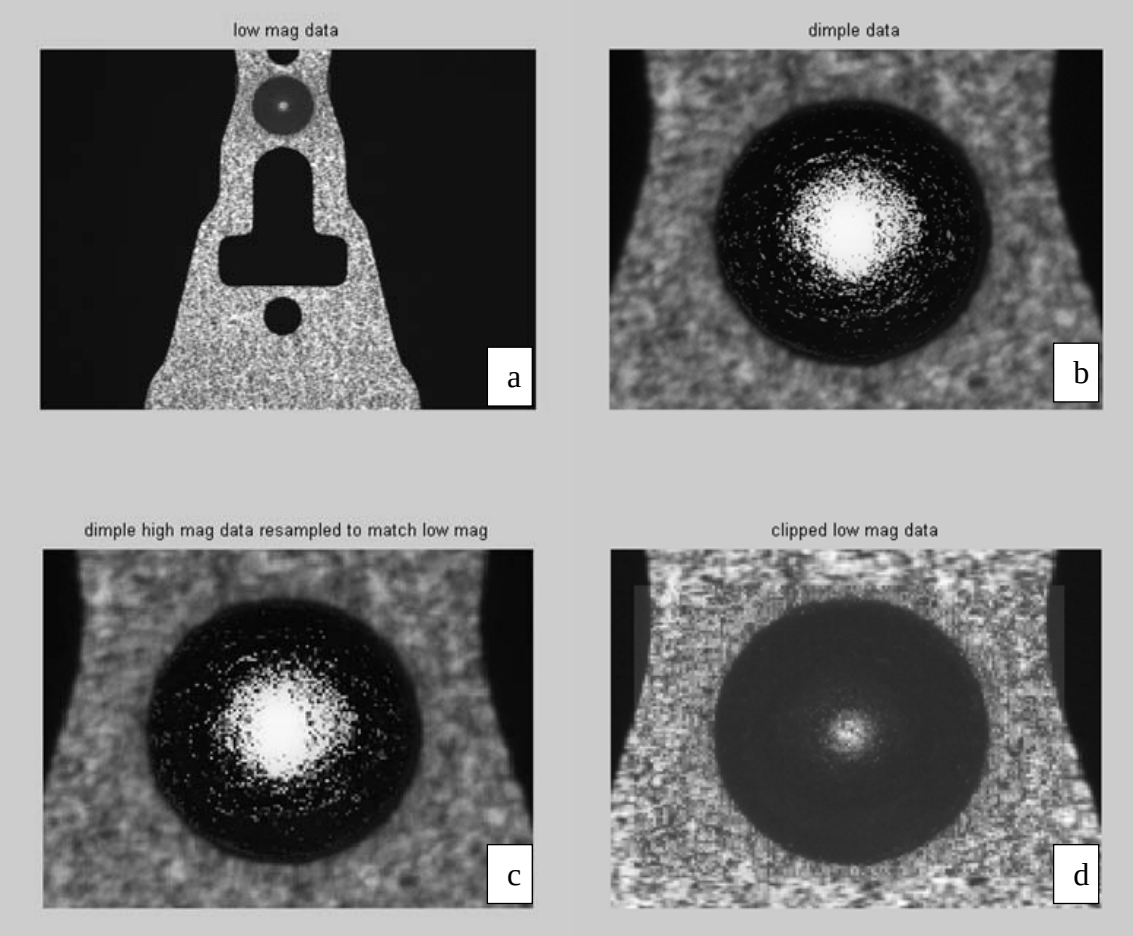

FIGURE 5.3.3: (a) 2.5x mag image (b) 10x mag image fused with 3D data (c) down sampled version of ‘b’ (d) trimmed region of ‘a’ that matches ‘c’

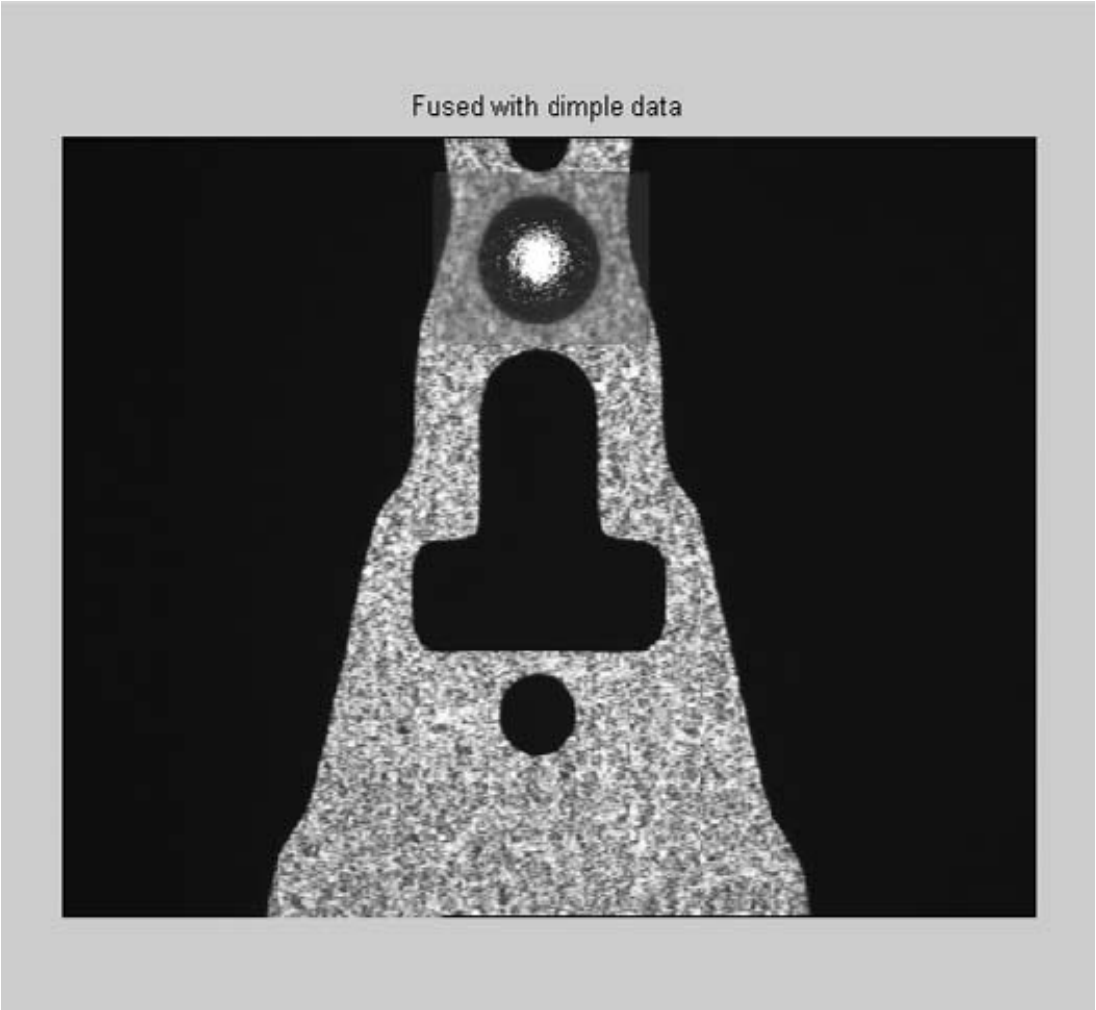

FIGURE 5.3.4: Image after 3D data fusion.

With the effective data fusion, the following are accomplished:

- The datum features (hole and slot) are imaged using a vision system at lower magnification enabling measurement time reduction and stage error minimization
- The spherical feature is characterized using CSI measurement data, enabling more surface being characterized and better correlation to actual shape
- The GD&T requirement of measuring the spherical feature's apex point with respect to the datum features.

5.4. Summary

A new fusion strategy ‘FWR method’ specific to surface metrology domain was proposed and its effectiveness was demonstrated on several non-planar and high aspect ratio surfaces. Fusion strategy for single-scale data sets obtained using different instrument settings was demonstrated on two 3D surface measurements obtained on a spherical feature on a hard disk drive suspension. Then fusion strategy for single-scale datasets obtained using different instruments was demonstrated using images obtained from a vision CMM and the previously fused 3D surface data.

With the successful deployment of these fusion strategies, it was demonstrated that data fusion can be effectively used for better characterization of features and perform datum based dimensional measurements covering a wider lateral range, with less measurement time and more data fidelity.

CHAPTER 6: SUMMARY AND RECOMMENDATIONS

A major trend in manufacturing is towards miniaturization which leads to convergence of the traditional research fields to create interdisciplinary research areas. For example, a successful lab-on-chip design requires expertise in four domains: micro-biology, micro-fluidics, micro-tribology and micro-optics. Interdisciplinary research efforts have started focusing on the development of multi-scale models and development of multi-scale surfaces to optimize the performance. In bio-medical research, knowledge of surfaces at different scales helps in better understanding of how different sizes and types of cells interact with each other and how bio-molecules get absorbed onto surfaces.

Along with the growing demand of multi-scale surface analysis for development of mathematical models, there has also been an increasing development of designer multi-scale surfaces, exhibiting specific properties at different scales for a specific purpose. For these multi-scale surfaces, traditional method of separation of surface into roughness, waviness and form, and using only the roughness data for surface characterization is not effective. Many of the varying aspect ratio surfaces need different resolution capabilities at different locations. Multi-scale surfaces require multi-scale measurement and characterization.

Apart from the capability to perform measurements at different scales and resolve features with varying aspect ratios, the system should be also capable of correlating the measurements across multiple scales and provide a multi-scale data, which could be used for validating multi-scale models and ensure the functional performance of the surface. Multi-scale surface analysis demands metrology tools that can cover a wide range of measurement range and resolution. In order to address this demand, various instrumentation development efforts are being carried out.

To expand the system's measurement area in Amplitude-Wavelength space, various magnifications or technologies could be used. Most of the instrumentation development has been using this approach, where different sub-instruments are connected together into a single frame. The sensors communicate with each other, but the data is not necessarily merged together. These systems enable the user to obtain different surface maps using various technologies, but user doesn't readily have the ability to combine all the obtained data into one single dataset. For effectively characterizing the multi-scale surface, all the datasets need to be aligned with respect to each other. It is not sufficient to just perform measurements are multiple scales, but also be capable of characterizing the entire multi-scale surface.

Researchers and instrument developers have developed instruments that are able to perform measurements at multiple scales but lack the much required multi-scale characterization capability. This kind of approach is cost prohibitive in an industrial setting to obtain bridge systems to cater to their ever changing measurement requirements. The effective approach is to obtain measurements from different available tools and then use a virtual offline software based tool to manipulate, merge and retrieve

data. This software based data fusion is actively used in satellite imaging, remote sensing and medical imaging to name a few. Data fusion by averaging temporal smooth surface data is already commonplace for subtracting system optical error in CSI systems. It is also used in triangulation systems and Imaging Confocal Microscopy (ICM) systems. Data fusion is generally performed on data obtained using same magnification. Our approach requires a fusion tool for data obtained using multiple magnifications. The primary focus was "to explore possible multi-scale data fusion strategies and options for surface metrology domain and to develop enabling software tools in order to obtain effective multi-scale surface characterization, maximizing fidelity while minimizing measurement cost and time".

Fusion strategies for surface datasets can be treated as four different categories:

- *Single-scale, single-domain data,* where data sets obtained from the same instrument but with multiple light settings are considered.
- *Single-scale, multi-domain data,* where data sets obtained from different instruments but approximately same sampling interval are considered.
- *Multi-scale, single-domain data,* where data sets obtained from similar technology instruments but with different sampling intervals are considered.
- *Multi-scale, multi-domain data,* where data sets obtained from multiple technology instruments and different sampling intervals are considered.

Existing approach in the dimensional metrology domain performs fusion based on shape primitives. Data in the surface metrology domain typically do not have extensive shape primitives. Hence a window based pixel level fusion approach was explored for the surface metrology domain. Pyramid based multi-scale decomposition and fusion

strategy was chosen and À Trous Discrete Wavelet Frame (DWF) method was explored for potential use.

The basic steps involved in a multi-scale data fusion process are coarse registration, fine registration, multi-scale decomposition, fusion and inverse transformation. For each step, multiple options are available along with the potential confusion of which performance metric to be used for evaluating the different options.

First simulation study was conducted to evaluate the impact of different noise levels, misalignment and defocus on various process steps. For this study different types of surface samples were taken and multi-scale noise and defocus were induced. The simulation study demonstrated that coarse and fine registration can register data to within one pixel accuracy. 'Watershed' edge detection method showed consistent performance at different noise levels and misalignment compared to 'Canny' and 'Sobel' edge detection methods on sub-images obtained by multi-scale decomposition. The performance results of 'Watershed' edge detection method are shown in table 6.1.1.

TABLE 6.1.1: Performance results of 'Watershed' edge detection method on single-scale images.

Watershed Edge Detection Method				
Sl.No	Test Type	Translation Error Std. Dev. (in pixels)		Avg. Computation Time (in Sec)
		X	Y	
1	With no misalignment	0.245	0.268	69
2	With 1 pixel misalignment	0.266	0.297	82
3	With 4 pixel misalignment	1.059	0.542	171
4	With 4 pixel misalignment and blurr	0.808	0.461	261

Second simulation study was conducted to evaluate available weighted average based fusion methods. Various single-scale and multi-scale performance metrics were calculated for the previously registered data sets by comparing the original data to the

noisy version. Based on that study it was determined that the following single-scale based metrics - Mutual Information (MI), Universal Quality Index (UQI) and Structural Similarity Index (SSIM) were preferred and for multi-scale evaluation, SSIM could be used. Instead of averaging SSIM values obtained from all individual sub-images, it is recommended to treat those individually.

Third study was conducted to select the preferred weighted averaging based data fusion method. Three methods of data fusion (Regional Energy (RE), Regional Edge Intensity (REI), and Combination of Wavelet coefficients and local Gradients (WGC) and two methods of transformation (3D and 3D Hybrid) were used on twelve data sets with four each of directional, non-directional and systematic type surfaces. Fusion metrics selected using the second simulation study was used to evaluate each of the transformation and data fusion method combination. Based on the study, it was shown that REI is the preferred fusion method and 3D is the preferred transformation method. REI method uses a window based activity level measurement called edge intensity, which is used to calculate corresponding weightage factors. After n-level of decomposition, if *f(i, j)* refers to the data point in a sub image and *R (m, n)* a *m x n* window. Then the edge intensity of *R(m, n)* is defined by

$$E_{R(m,n)} = \sum_{i=1}^{n}\sum_{j=1}^{m}\left|\frac{(f(i,j)-\overline{m}}{m\times n-1}\right|,$$

where $\overline{m} = \sum_{i=1}^{n}\sum_{j=1}^{m}\frac{f(i,j)}{m\times n}$

The weights are calculated using the formula

$$W_{A(i,j)} = \frac{E_{A_{R(i,j)}}}{(E_{A_{R(i,j)}} + E_{B_{R(i,j)}})}$$

$$W_{B(i,j)} = \frac{E_{B_{R(i,j)}}}{(E_{A_{R(i,j)}} + E_{B_{R(i,j)}})}$$

The new pixel value is obtained by

$$f(i,j) = W_{A(i,j)} \times A(i,j) + W_{B(i,j)} \times B(i,j)$$

The fused data, when it was replaced into the low magnification data, it displayed visual edge effects on some non-planar data sets, as shown in figure 6.1.1. This necessitated further study to evaluate alternate fusion strategies.

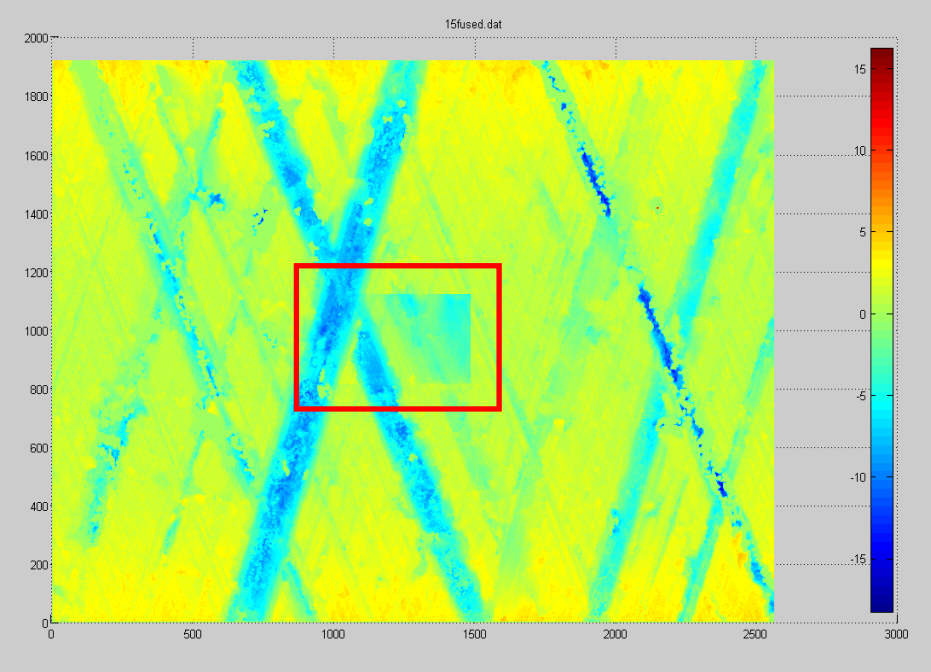

FIGURE 6.1.1: Fused data for a sample honed surface showing shape error.

An optimized fusion strategy (FWR method) for surface metrology domain (shown in figure 6.1.2) was proposed where the sub-images obtained from DWF were separated into three regimes – form, waviness and roughness, and fusion was not performed on sub-images in the form regime. This approach effectively eliminated the edge effects.

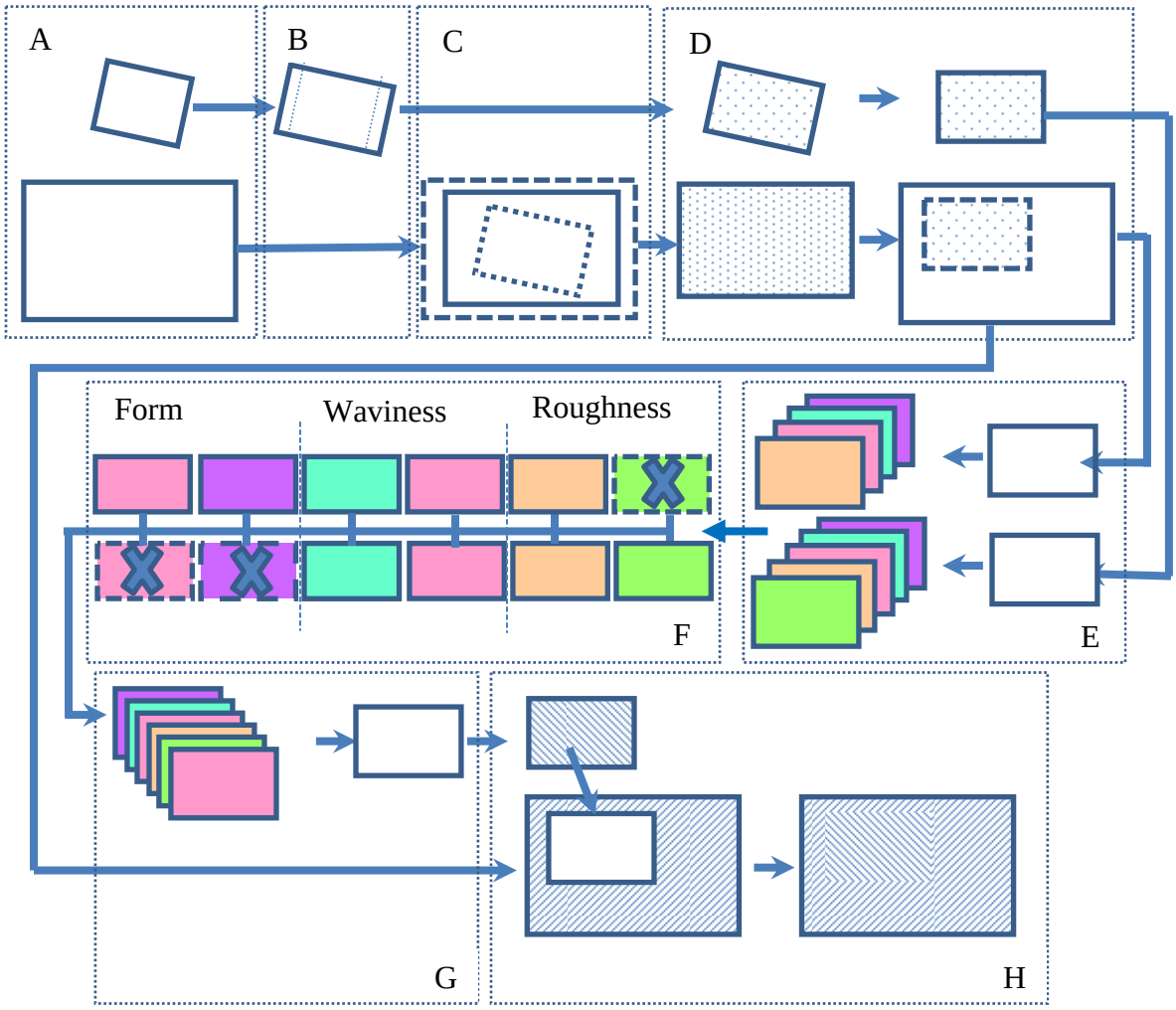

FIGURE 6.1.2: Schematic of FWR multi-scale data fusion for surface metrology datasets (A) Original Data (B) Pre-condition (outlier removal, resample and resize) (C) Coarse registration (D) Fine registration after control point detection (E) Multi scale decomposition on selected same size area from both data (F) Multi scale Fusion (G) Inverse Transform on fused sub-datasets to obtain fused data (H) Fused data replaced to the original location.

The optimal strategy for surface metrology domain was established along with the preferred options for various process steps and shown that it is possible to fuse data to pixel-level accuracy and extract synergy by merging data.

Two specific scenarios for fusion was also discussed, first one involving datasets obtained from same instrument at different light setting and the second one involving one data obtained from a CSI system and another from a Vision CMM (shown in figure 6.1.3).

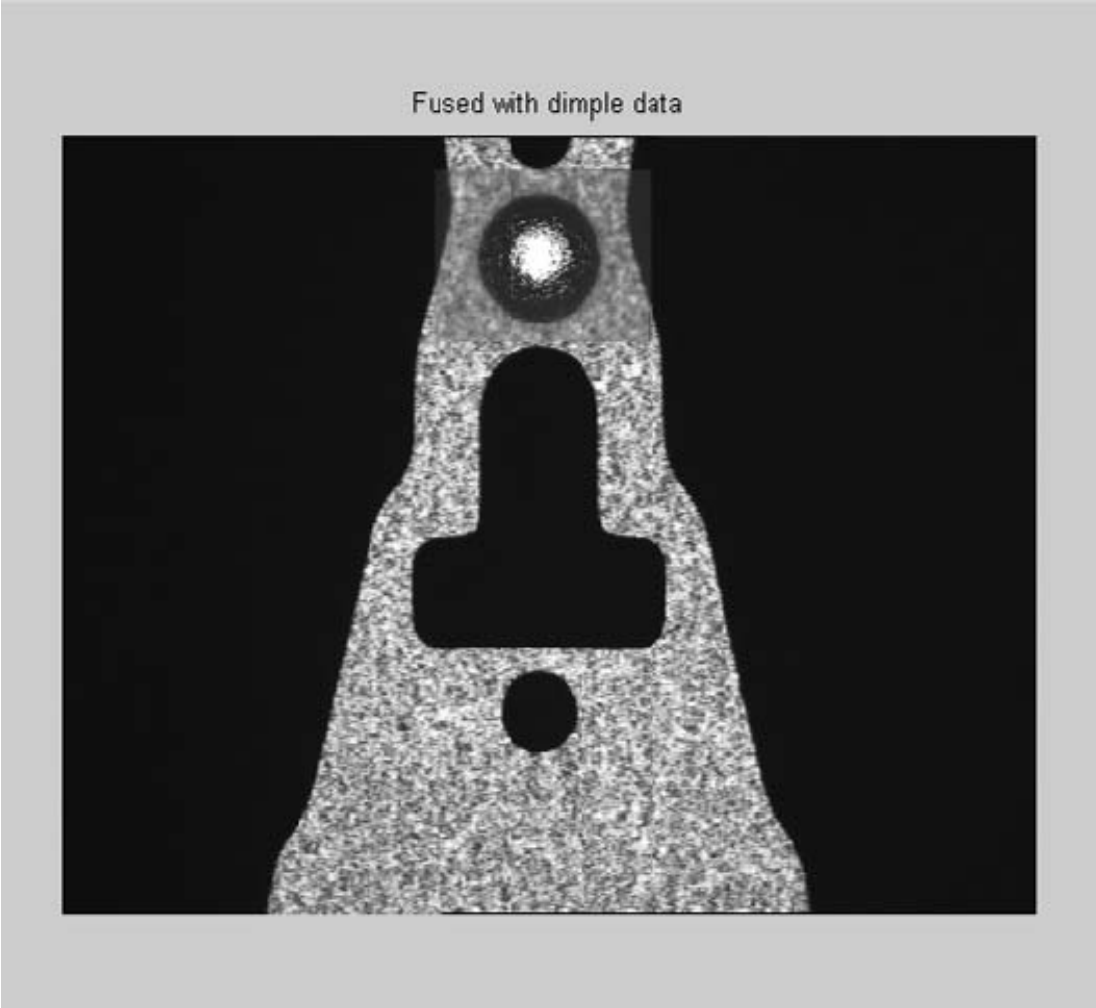

FIGURE 6.1.3: Image after 3D data fusion.

With those two case studies, it was demonstrated that using the data fusion approach, the datum features can be effectively characterized at a lower resolution using one system (Vision CMM) and the actual features of interest could be characterized at a higher resolution using another system (CSI) with higher capability while minimizing the measurement time.

6.1. Contributions

The major contributions of this research effort are:

- Development of multi-scale data fusion strategies specific for surface metrology domain, to enable effective multi-scale characterization.
- An optimized multi-scale data fusion strategy ‘FWR method’ for accommodating non-planar surfaces was developed and successfully demonstrated on both high aspect ratio surfaces and non-planar surfaces.
- Three simulation studies were conducted to select robust options at individual process steps. The following options were selected based on these three studies –
    - Coarse registration: Normalized cross-correlation is capable of handling multiple noise types and align to one pixel accuracy
    - Fine registration – Segmentation: Single level, ‘Watershed’ method was the robust method
    - Multi-scale decomposition: 3D transformation method was the most robust method
    - Data fusion: Regional Edge Intensity based weighted average fusion method performed well on multiple types of datasets.

- Fusion metrics: Mutual Information, Universal Quality Index and Structural Similarity performed well on multiple types of datasets.

- 3D Hybrid DWF transformation method was developed and demonstrated to show better edge preservation capability, which would be of great use for analyzing high aspect ratio surfaces.
- 2D DWF transformation method was demonstrated to be better for defect characterization, as shown in figure 6.1.4.

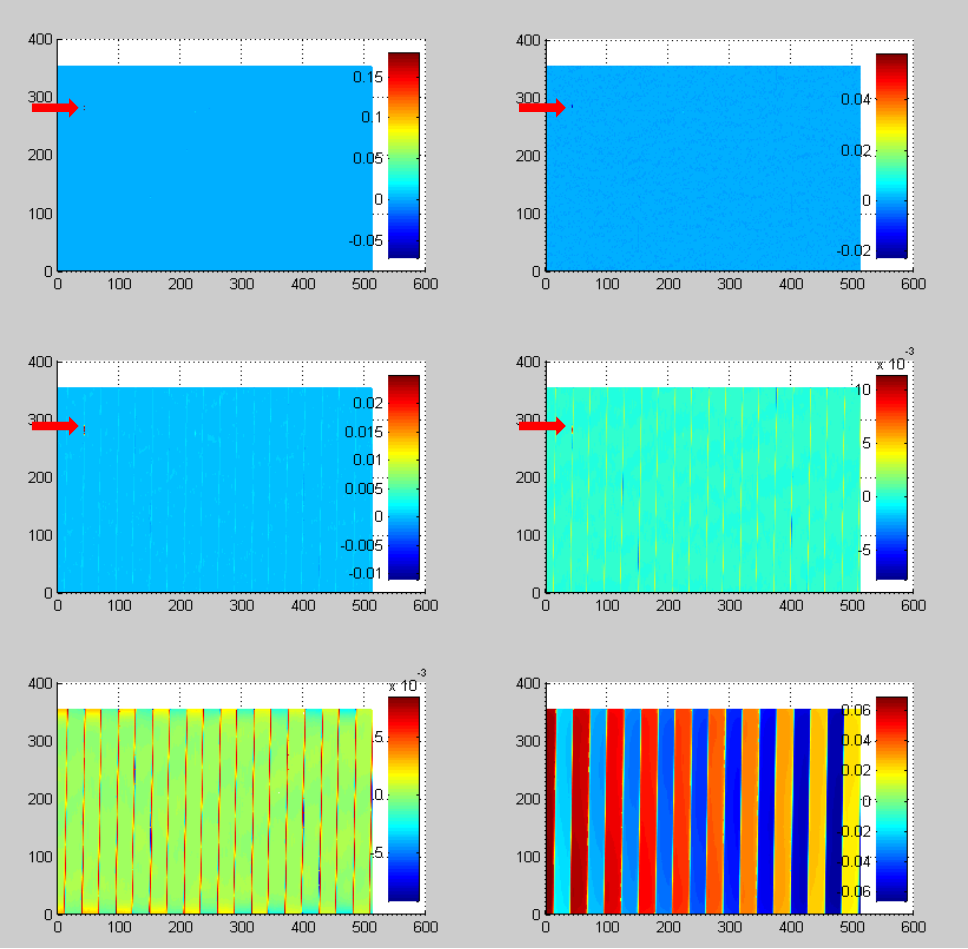

FIGURE 6.1.4: Square wave spacing specimen sub datasets obtained using 2D method.

- A novel concept of multi-parameter and multi-domain based masking for effective segmentation of structured surfaces was demonstrated using a three sided pyramid patterned surface as a specific case study (shown in figure 6.1.5). Table 6.1.2 shows the average and standard deviation of angle made by individual facets with respect to the horizontal plane

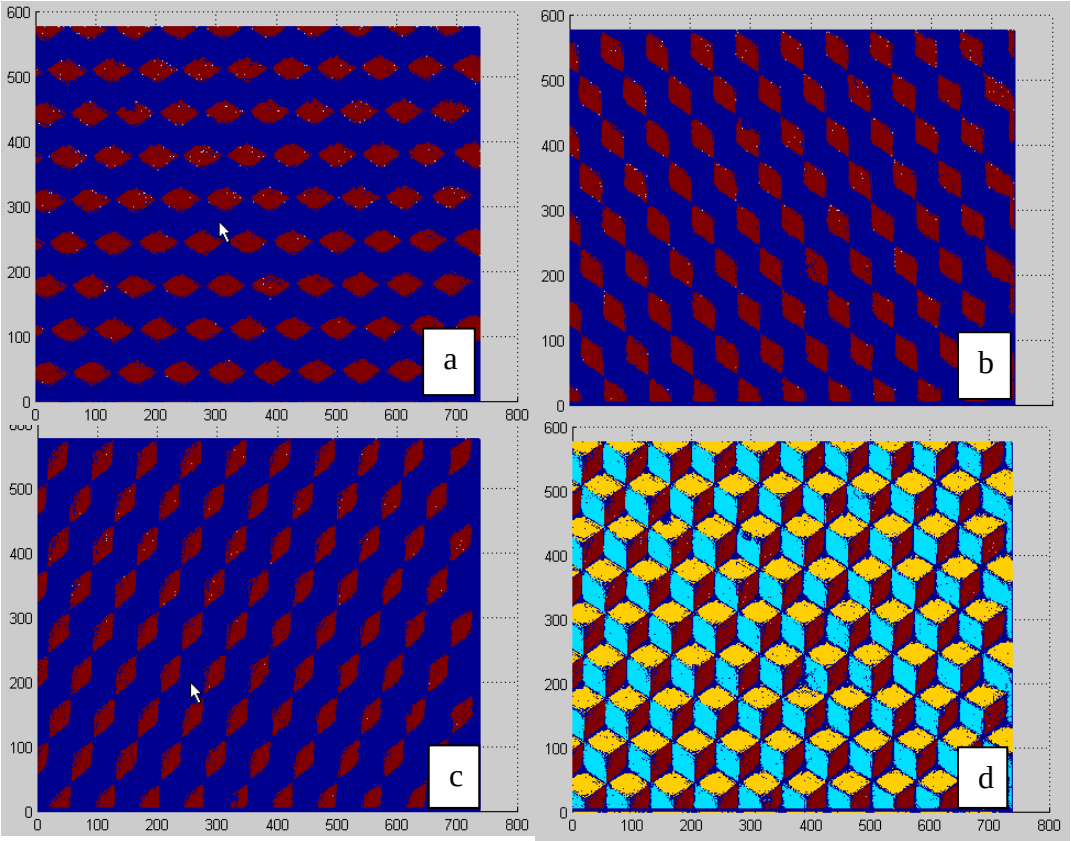

FIGURE 6.1.5: (a-c) Three individual facets (d) all three facets shown together.

Table 6.1.2: Average and standard deviations of calculated normals for facets.

Facets		Angle (Degrees)	
		Average	Std. dev.
1	**Red**	2.693	0.130
2	**Yellow**	2.641	0.211
3	**Blue**	3.088	0.178

TABLE 6.1.3: Summary of CSI error sources and their possible impacts.

Sl. No	Error Source	Symbol	1 Sigma in µm		Comments
			Z	XY	
1	Standard step ht repeatability	RHT	0.0065	0.0800	Basic system capability in measuring heights
2	Z stage repeatability	RZ	0.0800	0.1300	Impacts non-referenced surface measurements
3	Autofocus repeatability	AFR	0.1900	0.1900	Impacts panel/wafer level measurements with built-in autofocus routines
4	Focus (High Mag)	FMG	0.0050		Shows up as stable system-to-system bias
5	Reference Mirror + Optical Relay	RMOR	0.0001		Impacts stitching
6	Scan Length	SL	1.0020x		Impacts all z measurements taken using scan lengths other than what was used for calibration
7	Numerical Aperture Correction	NAC	1.0002x		Impacts all z measurements taken using objectives other than what was used for calibration
8	Algorithm	ALG	0.0400		Impacts all z measurements taken algorithm settings other than what was used for calibration
9	Dynamic Noise	DN	0.0050		
10	Z stage non-linearity	ZNL	0.0004		Impacts shape/form measurement
11	Scan Location	SSL	0.0250		Impacts all z measurements in combination with (2)
12	Dissimilar Materials	DM	0.0050		Impacts z measurements while measuring optically dissimilar materials
13	Environmental Impacts	E	0.0020	0.0500	Impacts Gage repeatability and reproducibility and long term stability
14	Camera Non-linear warping	NLWC		0.0400	Impacts within field-of-view dimensional measurements
14	objective turret repositioning error	OTRE		3.8000	Impacts dimensional measurements involving multiple magnifications
15	zoom turret repositioning error	ZTRE		0.0400	Impacts dimensional measurements involving multiple magnifications
16	XY stage repositioning error	XY		2.0000	Impacts dimensional measurements involving multiple field-of-views
17	Surface fitting residual	SF	0.2500		Impacts surface roughness parameter measurements on non-planar surfaces
18	Stitching error	S	0.0008	0.7700	Impacts dimensional measurements involving multiple field-of-views

- In order to better understand the CSI system, a comprehensive list of possible error sources was compiled along with the development of possible test plan that could be used to quantify the errors. Table 6.1.3 summarizes the error sources along with their impact on X, Y and Z axis measurements and comments on when those error sources need to be considered.

This research effort explored the fusion strategies for surface metrology domain and narrowed the focus on DWF based multi-scale decomposition. This research opens up the possibility of further efforts on different nuances involved with multi-scale data fusion, which will be briefly discussed in the next section.

6.2. Recommendations

The research effort explored the fusion strategies for surface metrology domain and narrowed the focus on DWT and DWF based multi-scale decomposition Within DWT method, 'Coiflets' were selected based on proven performance on metrology datasets. Within DWF method, B-3 spline was selected for their simplicity and performance. Further study could be made on other potential wavelets like Newland's harmonic wavelets. Curvelets [166] and ridgelets [167] also show good potential for further study.

CSI systems were the main instruments considered for this study. Research could be easily expanded to Scanning Electron Microscopes (SEMs) to cover a wider range.

Datasets were induced with defocus effect using 'Coiflet' wavelets for simplicity. Further study can be done to explore the actual optical transfer function of individual instrument and used correspondingly.

Three edge detection methods were considered for this study – ‘Canny’, ‘Sobel’ and ‘Watershed’. Other potential wavelet based edge detection algorithms [168] could also compared for their performance.

For fine registration method, different variants of ICP algorithm could be explored to optimize the computation time.

REFERENCES

[1] Muralikrishnan B, Raja J. Process diagnostics and functional correlation in surface metrology: novel techniques, case studies and analysis system development. Measurement. 2004; 36: 175-183.

[2] Peruru H, Raja J. Characterization and selection of surface texture measurement instruments and manufacturing processes for a function. Annual ASPE Proceedings. 2007.

[3] Sayles RS. How two- and three-dimensional surface metrology data are being used to improve the tribological performance and life of some common machine elements. Tribology International. 2001; 34: 299-305.

[4] Taniguchi N. Current status in, and future trends of, Ultraprecision machining and ultrafine materials processing. Annals of the CIRP. Vol. 32, Issue 2 (1983):573-582.

[5] Hofstadler SA, et al. TIGER: the universal biosensor. International Journal of Mass Spectrometry. 2005; 242: 23-41.

[6] Carneiro K, Kunzmann H, et al. Position paper on "the need for measurement and testing in nanotechnology" compiled by the high level expert group on measurement and testing. 2002. Available from: http://ec.europo.eu/research/fp5/pdf/hleggrowth-nanotechnology.pdf

[7] Whitehouse D., A new look at surface metrology, Wear Vol 266 (2009) 560-565.

[8] Semiconductor.net [Internet] [cited November 23, 2009]. Available from: http://www.semiconductor.net/article/207352-Researchers_Develop_Forward_Looking_Polymer_With_Immediate_Applications.php

[9] Htch.com [Internet]. Hutchinson Technology Inc.; c2011 [cited February 1, 2011]. Available from: http://www.htch.com/diskdrive-products.asp.

[10] Hansen HN, Carneiro K, Haitjema H, Chiffre LD. Dimensional Micro and Nano Metrology. Annals of CIRP. 2006; 55 (Pt 2):721-743.

[11] Blunt L, Bills P, Jiang X, Hardaker C, Chakrabarty G. The role of tribology and metrology in the latest development of bio-materials. Wear. 2008.

[12] Ramsden, et al. The design and manufacture of Biomedical surfaces. Annals of CIRP.2007; 56 (Pt 2): 687-711.

[13] Werner S, et al. The effect of microstructures surfaces and laminin-derived peptide coatings on sift tissue interactions with titanium dental implants. Biomaterials.2009; 30: 2291-2301.

[14] Kassies R, Van Der Werf KO, Lenfrink A, Hunter CN, Olsen JD, Subramaniam V, Otto C. Combined AFM and confocal fluoresecence microscope for applications in bio-technology. Journal of Microscopy, Vol. 217, 2005, 109-116.

[15] Lal R, Proksch R. Multimodal atomic force microscopy: biological imaging using atomic force microscopy combined with light fluorescence and confocal microscopies and electrophysiologic recording. Int. J. Imag. Sys. Tech. 8: 293-300.

[16] Gradinaru CC, Martinson P, Aartsma TJ, Schmidt T. Simultaneous atomic-force and two-photon fluorescence imaging of biological specimens in vivo. Ultramicroscopy. 2004; 99: 235-245.

[17] Ito Y. Surface micropatterning to regulate cell functions. Biomaterials. 1999; 20: 2333-2342.

[18] Yao L, et al. Effect of functionalized micropatterned PLGA on guided neurite growth. Acta Biomaterialia.2009; 5: 580-588.

[19] Hoi Ting H. Au, Cheng I, Chowdhury MF, Radisic M. Interactive effects of surface topography and pulsatile electrical field stimulation on orientation and elongation of fibroblasts and cardiomyocytes. Biomaterials. 2007; 28: 4277-4293.

[20] Mendez-Vilas A, Bruque JM, Gonzalez-Martin ML. Sensitivity of surface roughness parameters to changes in the density of scanning points in multi-scale AFM studies. Application to a biomaterial surface. Ultramicroscopy. 2007; 107: 617-625.

[21] Mason F. Multisensor measurement – making sense of it all. Quality Magazine. 2003 March: 72-76.

[22] Newswise.com [Internet]. [cited Nov 29 2009] Available from: http://www.newswise.com/articles/next-generation-nano-ct-system-will-enhance-nano-scale-research.

[23] Brennan.mse.ufl.edu [Internet].Brennan Research Group, University of Florida; [cited February 1, 2011].Available from: http://brennan.mse.ufl.edu/Research/surfaces.html

[24] Holmberg K, Ronkainen H, Laukkanen A, Wallin K, Friction and wear of coated surface – scales, modeling and simulation of tribomechanisms, Surface & Coatings Technology 202 (2007) 1034-1049.

[25] Greenwood JA, Williamson JBP, The contact of nominally flat surfaces, Proceedings of Royal Society, (1966), A295, 300-319.

[26] Whitehouse DJ, Archard JF, The properties of random surfaces of significance in their contact, Proceedings of Royal Society, (1970), A316, 97-121.

[27] Jackson RL, Streator JL, A multi-scale model for contact between rough surfaces, Wear 261 (2006) 1337-1347.

[28] Majumdar A, Bhushan B, Fractal model of elastic-plastic contact between rough surfaces, ASME Journal of Tribology, 113 (1), (1991), 1-11.

[29] Bigerelle M, Najjar D, Iost D, Multiscale functional analysis of wear – A fractal model of the grinding process, Wear 258 (2005) 232-239.

[30] Bora CK, Flater EE, Street MD, Redmond JM, Starr MJ, Carpick RW, Plesha ME, Multiscale roughness and modeling of MEMS interfaces, Tribology Letters, Vol. 19, No.1, May 2005 37-48.

[31] Koch K, Bhushan B, Barthlott W, Multifunctional surface structures of plants: An inspiration for biomimetics, Progress in Material Science 54 (2009) 137-178.

[32] Byun et al, Wetting characteristics of insect wing surfaces, Journal of Bionic Engineering 6 (2009) 63-70.

[33] Northern MT, Turner KL, Meso-scale adhesion testing of integrated micro- and nano-scale structures, Sensors and Actuators A 130-131 (2006) 583-587.

[34] Bewiogua et al, Surface technology for Automotive engineering, CIRP Annals, Manufacturing Technology 2009.

[35] Mandelbrot BB, The Fractal Geometry of Nature, San Fransisco, Freeman, New York, 1982.

[36] Scott RS, Ungar PS, Bergstrom TS, Brown CA, Childs BE, Teaford MT, Walker A, Dental microwear texture analysis: technical considerations, Journal of Human Evolution 51 (2006) 339-349.

[37] Celli A, Tucci A, Esposito L, Palmonari C, Fractal analysis of cracks in alumina-zirconia composites, Journal of the European Ceramic Society 23 (2003) 469-479.

[38] Whitehouse DJ, Fractal or fiction, Wear 249 (2001) 345-353.

[39] Brown CA, Siegmann S, Fundamental Scales of Adhesion and Area-scale Fractal Analysis, Metrology and Properties of Engineering Surfaces, 8th International Conference, Huddersfield, 26-27 April 2000.

[40] Raja J, Muralikrishnan B, Fu S, Recent advances in separation of roughness, waviness and form, Journal of the International Societies for Precision Engineering and Nanotechnology, 26 (2002) 222-235.

[41] Grabon W, Pawlus P, Sep J, Tribological characteristics of one-process and two-process cylinder liner honed surfaces under reciprocating sliding conditions, Tribology International 43 (2010) 1882-1892.

[42] ASME B46.1-2002 Surface Texture, Surface Roughness, Waviness and Lay.

[43] Stout KJ, Blunt L, A contribution to the debate on surface classifications – random, systematic, unstructured, structured and engineered, International Journal of Machine Tools & Manufacture 41 (2001) 2039-2044.

[44] Evans CJ, Bryan JB, 'Structured', 'Textured' or 'Engineered' Surfaces, Keynote Paper, Annals of CIRP 48 (2) (1999).

[45] Fresnel Technologies Inc. [Internet] [cited March 16, 2011] Available from : http://www.fresneltech.com/visible.html

[46] Frtofamerica.com [Internet]. FRT of America, LLC; [cited February 2, 2011]. Available from: http://www.frtofamerica.com/us/products/microglider-series/microglider/

[47] Werthinc.com [Internet]. Werth Messtechnik; [cited February 2, 2011]. Available from: www.werthinc.com.

[48] Topfer SCN, Nehse U, Linb G. Automated inspections for dimensional micro- and nanometrology. Measurement. 2007; 40: 243-254.

[49] Kayser D, Bothe T, Osten W. Scaled topometry in a multisensor approach. Society of photo-optical instrumentation engineers. 43 (10): 2469-2477.

[50] Osten W, Kayser D, Bothe T, Juptner W. High resolution measurement of extended technical surfaces with scalable topometry. Proceedings of SPIE. 2000; 4101.

[51] Solarius-inc.com [Internet]. Solarius Development Inc; c2003-07 [cited February 2, 2011]. Available from: http://www.solarius-inc.com/html/sensofar.html.

[52] Zygo.com [Internet]. ZYGO Metrology Services Division; [cited February 2, 2011]. http://www.zygo.com/?/met/profilers/.

[53] Bruker [Internet]. Bruker AXS; c2011 [Updated on January 1, 2011; cited February 2, 2011].Available from: http://www.bruker-axs.de/stylus_and_optical_metrology.html.

[54] WITec GmbH [Internet]. [cited February 2, 2011], Available from: http://www.witec.de/en/products/raman/alpha500/

[55] Geomagic [Internet] [cited February 2, 2011], Available from: http://www.geomagic.com/en/products/studio/

[56] Viewmm.com [Internet]. VIEW Micro-Metrology; c2011 [cited February 2, 2011]. Available from: http://www.viewmm.com/pinnacle_250.jsp.

[57] https://www.veeco.com/library/nanoscale_world/AFM_Research_Spotlights.aspx ?spotid=948&numcom=0&cat=1 [cited November 23, 2009].

[58] Artigas R, Pinto A, Laguarta F, Three-dimensional micro-measurements on smooth and rough surfaces with a new confocal optical profiler, Proceedings of SPIE Vol. 3824, 93-104, Optical Measurement Systems for Industrial Inspection.

[59] Shaw L, Weckenmann A. Optical 3D- Characterization for multiscale workpieces. 10th International Symposium on Measurement and Quality Control. 2010, September: 5-9.

[60] Weckenmann A, Jiang X, Sommer KD, Neuschaefer-Rube U, Seewig J, Shaw L, Estler T. Multisensor data fusion in dimensional metrology. Annals of CIRP – Manufacturing Technology. 2009; 58: 701-721.

[61] Hui, et al. Image fusion and 3D surface reconstruction of microparts using complex valued wavelet transforms. Proceedings of IEEE, ICIP. 2006: 2137-2140.

[62] Data fusion lexicon, Data Fusion Subpanel of the Joint Directors of Laboratories. Technical Panel for C3. U.S. Department of Defense. 1991.

[63] Ranchin T, Wald L. Data fusion of remotely sensed images using the wavelet transform: The ARSIS solution. SPIE. 3169: 272-280.

[64] Erdogan M, Maras HM, Yilmax A, Ozerbil OT. Resolution merge of 1:35.000 scale aerial photographs with LANDSAT 7 ETM imagery. The International Archives of the Photogrammetry, Remote Sensing and Spatial Information Scinces. Beijing 2008; XXXVII (B7): 1281-1285.

[65] Starck JL, Murtagh F, Bijaoui A. Image Processing and Data Analysis: The Multiscale Approach. Cambridge University Press, 2003.

[66] Wang MY, Fitzpatrick JM, Maurer CR. Design of fiducials for accurate registration of CT and MR volume images. Jr., Medical Imaging 1995: Image Processing, Proc. of SPIE. 1995; 2434: 96-108.

[67] Condeco J, Christensen LH, Rosen BG. Software relocation of 3D surface topography measurements. International Journal of Machine tools and Manufacture. 2001; 41: 2095-2101.

[68] Zitova B, Flusser J. Image registration methods: a survey. Image and Vision Computing. 2008; 21: 977-1000.

[69] Xie Z, Xu S, Li X. A high-accuracy method for fine registration of overlapping point clouds. Image and Vision Computing.2010; 28: 563-570.

[70] Besl PJ, McKay ND. A Method for Registration of 3-D Shapes. IEEE Transactions on Pattern Analysis and Machine Intelligence. Feb 1992; 14 (No. 2): 239-256.

[71] Liu Y. Improving ICP with easy implementation for free-form surface matching. Pattern Recognition. 2004; 37: 211-226.

[72] Rusinkiewicz S, Levoy M. Efficient Variants of the ICP Algorithm. Proceedings of Third International Conference on 3D Digital Imaging and Modeling. June 2001; 145-152.

[73] Witkin AP, Tenenbaum JM. On the role of structure in vision. Human and Machine Vision, Academic Press, New York. 1983: 481-544.

[74] Rosenfield A, Thurston M, Edge and curve detection for visual scene analysis, IEEE Trans. Comput., C-20 (1971) 562-569.

[75] Besrour R, Lachiri Z, Ellouze N, Using multiscale product for ECG characterization, Research letters in signal processing, Volume 2009, Article ID 209395.

[76] Yao J, Chen J, Chow C. Breast Tumor Analysis in Dynamic Contrast Enhanced MRI Using Texture Features and Wavelet Transform. IEEE Journal of selected topics in Signal Processing. Feb 2009; 3 (No. 1).

[77] Graps A. An introduction to wavelets. Computational Science & Engineering, IEEE; Summer 1995; 2(2): 50-61.

[78] Gabor D, Theory of communication, Journal of the IEE, 93, 429-441.

[79] Newland DE, Harmonic wavelet analysis, Proceedings of Royal Society of London A (1993) 443, 203-225.

[80] CNR-IMATI [Internet] [cited February 1, 2011]. Course on Wavelets and self-similarity: Theory and application. Lecture 1. Available from: http://www.mi.imati.cnr.it/conferences/brani_05.html

[81] Robertson DC, Camps OI, Mayer J, Wavelets and power system transients: feature detection and classification, Proceedings of SPIE 2242 (1994) 474-487.

[82] Fu S, Muralikrishnan B, Raja J, Engineering surface analysis with different wavelet bases, ASME Journal of Manufacturing Science and Engineering, 125(4) (2003), 844-852.

[83] Mezghani S, El Mansori M, Massaq A, Ghidossi P, Correlation between surface topography and tribological mechanisms of the belt-finishing process using multi scale finishing process signature, Mecanique 336 (2008) 794-799.

[84] Wang A, Sun H, Guan Y. The Application of Wavelet Transform to Multi-modality Medical Image Fusion. Proceedings of the 2006 IEEE International Conference on Networking, Sensing and Control; 2006: 270-274.

[85] Chibani Y. Additive integration of SAR features into multispectral SPOT images by means of the à trous wavelet decomposition. ISPRS Journal of Photogrammetry & Remote Sensing. 2006; 60: 306-314.

[86] Zhang Z, Blum RS. Fusion schemes with a performance study for a digital camera application. Proc. of IEEE. Aug 1999; 87 (No. 8).

[87] Daubechies I. Ten lectures on wavelets. Society for Industrial and Applied Mathematics (SIAM). Philadelphia, 1992.

[88] Burt PJ, Adelson AE. The Laplacian pyramid as a compact image code. IEEE Transactions on Communications. 1983; 31: 532-540.

[89] Mallat S. A theory for multi resolution signal decomposition: the wavelet representation. IEEE Transactions on Pattern Analysis and Machine Intelligence. 1989; 11: 674-693.

[90] Shensa MJ. Discrete wavelet transforms: wedding the à trous and Mallat algorithms. IEEE Transactions on Signal Processing.1992; 40: 2464-2482.

[91] Grossman A, Morlet J. Decomposition of Hardy functions into square integrable wavelets of constant shape. SIAM Journal of Mathematical Analysis.1984; 15: 723-736.

[92] Li H, Guo L, Liu H, Current research on wavelet-based image fusion algorithms, Multisensor, Multisource Information Fusion: Architectures, Algorithms, and Applications 2005 Proceedings of the SPIE, Vol. 5813 (2005) 360-367.

[93] npl.co.uk [Internet] National Physical Laboratory [cited March 16, 2011] Good Practice Guide No. 108: Guide to the Measurement of Smooth Surface Topography using Coherence Scanning Interferometry, Available from:

http://www.npl.co.uk/engineering-measurements/dimensional/dimensional-measurements/publications/dimensional-good-practice-guides

[94] npl.co.uk [Internet] National Physical Laboratory [cited March 16, 2011] Good Practice Guide No. 116: Guide to the Measurement of Rough Surface Topography using Coherence Scanning Interferometry, Available from: http://www.npl.co.uk/engineering-measurements/dimensional/dimensional-measurements/publications/dimensional-good-practice-guides

[95] ISO/WD 25178-604 Geometrical Product Specification (GPS) – Surface texture: Areal – Part 604: Nominal characteristics of non-contact (coherence scanning interferometry) instruments.

[96] Giusca CL, Leach RK, Calibration of the metrological characteristics of areal surface topography measuring instruments, Proceedings of the 2nd International Conference on Surface Metrology 2010, WPI, USA pp. 145-153.

[97] NewView 7000 Accesory Guide, OMP-0543G [Internet]. ZYGO Corporation; c2010 [cited February 7, 2011]. Available from: http://www.zygo.com/met/profilers/newview7000/nv_acc.pdf

[98] Step height standard [Internet]. VLSI Standards Incorporated; c2011 [cited February 7,2011] Available from: www.vlsistandards.com/products/dimensional/step.asp? SID=100

[99] Zygo.com [Internet]. ZYGO Metrology Services Division; [cited February 2, 2011]. Zygo Application notes OMP-0484A on lateral calibration standard

[100] Optical Dimensional Standard [Internet]. National Physical Laboratory [cited February 7, 2011] Available from: http://www.npl.co.uk/engineering-measurements/dimensional/dimensional-measurements/products-and-services/optical-dimensional-standard

[101] ISO 5436-1:2000 Geometrical Product Specification (GPS) – Surface texture: Profile method; Measurement standards – Part 1: Material measures.

[102] Surface reference standards [Internet]. Rubert & Co Ltd [cited February 7, 2011]. Available from: http://www.rubert.co.uk/Reference.htm

[103] De Groot PJ. Vibrations in phase-shifting interferometry. J Opt. Soc. Am A. Feb 1995;12 (2): 354-365.

[104] Spindle Error Analyze [Internet]; Lion Precision [cited February 7, 2011]. Available from: http://www.lionprecision.com/sea/sea.html.

[105] Harasaki A, Wyant JC. Fringe modulation skewing effect in white-light vertical scanning interferometry. Appl. Opt. May 2000; 39 (13): 2101-2106.

[106] Pavlicek P, Soubusta J. Measurement of the influence of dispersion on white light interferometry. Appl Opt. Feb 2004; 43 (4): 766-770.

[107] Sheppard CJR, Wilson T. Effect of spherical aberration on the imaging properties of scanning optical microscopes. Appl Opt. April 1979;18 (7): 1058-1063.

[108] Schwider J, Burow R, Elssner KE, Grzanna J, Spolaczyk R, Merckel K. Digital wave-front measuring interferometry: some systematic error sources. Appl Opt. Nov 1983; 22(21): 3421 – 3432.

[109] Visionpro.com [Internet] Sherlock software from VisionPro Technologies [cited March 16, 2011] Available from: http://www.visionpro.com.sg/pdt-software-ipd.html

[110] Biegen JF. Calibration requirements for Mirau and Linnik microscope interferometers. Appl Opt. June 1989; 28(11): 1972-1974.

[111] Sheppard CJR, Larkin KG. Effect of numerical aperture on interference fringe spacing. Appl Opt. August 1995; 34(22): 4731-4734.

[112] Schulz G, Elssner KE. Errors in phase-measurement interferometry with high numerical apertures. Appl Opt. Nov 1991;30 (31): 4500-4507.

[113] Creath K. Calibration of numerical aperture effects in interferometric microscope objectives. Appl Opt. August 1989; 28(15): 3333-3338.

[114] DeGroot PJ, Colonna de Lega X, Kramer J, Turzhitsky M, Determination of fringe order in white light interference microscopy, Applied Optics, Vol. 41, No. 22 (2002) 4571-4578.

[115] Schmit J, Wyant JC, Harasaki A. Improved vertical scanning interferometry. Appl. Opt. May 2000; 39(13): 2107-2115.

[116] Sandoz P. Wavelet transform as a processing tool in white-light interferometry. Optics Letters. July 1997; 22 (14): 1065-1067.

[117] Larkin KG. Efficient nonlinear algorithm for envelope detection in white light interferometry. J. Opt. Soc. Am. A. April 1996 13 (4): 832-843.

[118] Creath K. Error source in phase-measuring interferometry. SPIE; 1992; 1720: 428-435.

[119] Pavlicek P, Soubusta J. Theoretical measurement uncertainty of white light interferometry on rough surfaces. Appl Opt. 42(10): 1809-1813.

[120] Rhee HG, Vorburger TV, Lee JW, Fu J. Discrepancies between roughness measurements obtained with phase shifting and white light interferometry. Appl Opt. Oct 2005; 44 (28): 5919-5927.

[121] Kiyono S, Gao W, Zhang S, Aramaki T. Self-calibration of a scanning white light interferometer microscope. Opt Eng. 39 (10) 2720-2725.

[122] Kang MG, Lee SY, Kim SW. Self-compensation of PZT errors in white light scanning interferometry. Journal of the Optical Society of Korea. Sep 1999; 3(2): 35-40.

[123] Kim SW, Kang MG, Lee SY. White light phase-shifting interferometry with self-compensation of PZT scanning errors. Optical Engineering for sensing and nanotechnology. ICOSN'99: Proceedings of SPIE: 3740. June 1999; Yokohama, Japan. 16-19.

[124] Schwider J, Dressel T, Manzke B. Some considerations of reduction of reference phase error in phase-stepping interferometry. Appl Opt. Feb 1999; 38(4): 655-660.

[125] Olszak A, Schmit J. High stability white light interferometry with reference signal for real-time correction of scanning errors. Society of Photo-Optical Instrumentation Engineers, Opt Eng. 42(1) 54-59.

[126] Doi T, Vorburger T, Sullivan P. Effects of defocus and algorithm on optical step height calibration. Precision Engineering. 1999; 23: 135-143.

[127] Chakmakjian S, Biegen J, de Groot PJ. Simultaneous focus and coherence scanning in interference microscopy. Technical Digest, International Workshop on Interferometry. Riken, Japan. 1996; 171: 171-172.

[128] Doi T, Toyoda K, Tanimura Y. Effects of phase changes on reflection and their wavelength dependence in optical profilometry. Appl Opt. Oct 1997; 36(29): 7157-7161.

[129] Harasaki A, Schmit J, Wyant JC. Offset of coherent envelope position due to phase change on reflection. Appl Opt. May 2001; 40(13): 2102-2106.

[130] Yoo S, Kim SW. Self-calibration algorithm for testing out-of-plane errors of two-dimensional profiling stages. International Journal of Machine Tools & Manufacture. 2004; 44: 767-774.

[131] Ye J, Takac M, Berglund CN, Owen G, Pease RF. An exact algorithm for self-calibration of two-dimensional precision metrology stages. Precision Engineering. 1997; 20:16-32.

[132] Gao W, Qiang X, Kiyono S. Self-calibration of lateral non-linearities of an interference microscope. Measurement. 2003; 34: 245-253.

[133] Zhang Z. A Flexible new technique for camera calibration. Microsoft Research, Microsoft Corporation; Dec 1998; Report No.: MSR-TR-98-71.

[134] Wei GQ, Ma SD. Implicit and explicit camera calibration: Theory and experiments. IEEE Transactions on Pattern Analysis and Machine Intelligence. May 1994; 16(5): 469-480.

[135] Tsai RY. A versatile camera calibration technique for high-accuracy 3d machine vision metrology using off-the-shelf TV cameras and lenses. IEEE Journal of Robotics and Automation. Aug 1987; RA-3(4): 323-344.

[136] Ferri C, Faraway J, Brousseau E. Calibration of a white light interferometer for the measurement of micro-scale dimensions. Int. J Adv. Manuf. Technol., Special Issue, 10 May 2009.

[137] Koops K.R. Improved calibration of an interference microscope. Proceedings of SPIE, 2001; 4401: 298-304.

[138] Creath K, Hariharan P. Phase-shifting errors in interferometric tests with high-numerical-aperute reference surfaces. Appl Opt. Jan 1994;33 (1): 24-25.

[139] Creath K, Gilliand YA, Hariharan P. Interferometric testing of a high-numerical-aperture convex surfaces. Appl Opt. May 1994; 33(13): 2585-2588.

[140] Creath K. Spatial resolution limits of an optical profiler. Optics in complex systems SPIE. 1990; 1319: 318-319.

[141] Huihui L, Lei G, Hang L, Evaluation of multisensor image fusion using different wavelet transform, Wavelet application in industrial processing III, Proceedings of SPIE Vol. 6001, 600103 (2005).

[142] Raol JR, Multi-Sensor Data Fusion with MATLAB, CRC Press, 2009, Ch.11: Performance evaluation of image based data fusion systems.

[143] Mathworks.com [Internet] [Cited on September 18 2010]. Available from: http://www.mathworks.com/matlabcentral/fileexchange/24301-finite-iterative-closest-point

[144] Mathia TG, Pawlus P, Wieczorowski M, Recent trends in surface metrology, Wear 2010 (Article in press)

[145] Ramasamy SK, Kasper A. Expanding white light interferometer capabilities to be used as a μCMM. Proceedings of 25th ASPE Annual Meeting.

[146] Verma R, Raja J, Characterization of engineered surfaces, Journal of Physics: Conference Series 13, 2005, 5-8.

[147] Kong LB, Cheung CF, Jiang XQ, Lee WB, To S, Blunt L, Scott P, Characterization of surface generation of optical microstructures using a pattern and feature parametric analysis method, Precision Engineering 34(2010) 755-766.

[148] Senin N, Ziliotti M, Groppetti R, Three-dimensional surface topograph segmentation through clustering, Wear 262, 2007, 395-410.

[149] Scott PJ, Pattern analysis and metrology: the extraction of stable features from observable measurements, Proc. R. Soc. London A, 2004, 460, 2845-2864.

[150] ISO/TC 213 Draft N 755, Geometrical Product Specifications (GPS) – Surface Texture: Areal- Part 3: Specification Operators.

[151] Dimkovski Z, Anderberg C, Rosen B.-G, Ohlsson R, Thomas TR, Quantification of the cold worked material inside the deep honing grooves on cylinder liner surfaces and its effect on wear, Wear 267 (2009) 2235-2242.

[152] Xin B, Multiscale analysis of rough groove textures for three-dimensional optical measurements, Optical Engineering 48(7) 073602, July 2009.

[153] Russ JC, The Image Processing Handbook, Ch.7: Segmentation and Thresholding, 397-441, 5th edition, CRC Press.

[154] Ramasamy SK, Raja J, Boudreau BD, Characterization of structured surfaces using multi-parameter masking and segmentation approach, Proc. of 2011 ASPE Spring Topical Meeting on Structured and Freeform Surfaces.

[155] Otsu N, A threshold selection method from gray-level histograms, IEEE Transactions on Systems, Man, and Cybernetics, Vol. 9, No. 1, 1979, 62-66.

[156] Zhang X, Li D, À Trous wavelet decomposition applied to image edge detection, Geographic Information Sciences, Vol. 7, No. 2, 2001, 119-123.

[157] Haralick RM, Shapiro LG, Computer and Robot Vision, Volume I, Addison-Wesley, 1992, 28-48.

[158] Wang Z, Bovik AC, A Universal Image Quality Index, IEEE Signal processing Letters, Vol. 9 (2002) 81-84.

[159] Wang Z, Simoncelli EP, Bovik AC. Multi-scale structural similarity for image quality assessment. Invited Paper, IEEE Asilomar Conference on Signals, Systems and Computers. Nov 2003.

[160] Wang Z, Bovik AC, Sheikh HR, Simoncelli EP. Image Quality Assessment: From Error Visibility to Structural Similarity. IEEE Transactions on Image Processing. 1994; 13(No. 4): 600-612.

[161] Chen H, Liu Y, Wang Y. A novel image fusion method based on wavelet packet transform. IEEE International Symposium on Knowledge Acquisition and Modeling. 2008; 462-466.

[162] Chai Y, Zhao R, Ren J. Self-adaptive image fusion based on multi-resolution decomposition using wavelet packet analysis. Proceedings of the Third International Conference on Machine Learning and Cybernetics. Shanghai, 2004; 4049-4053.

[163] Song Y, Li M, Li Q, Sun L. A new wavelet based multi-focus image fusion scheme and its application on optical microscopy. Proceedings of the 2006 IEEE International Conference on Robotics and Biomimetics. Kunming, China. 2006; 401-405.

[164] Donoho DL. De-Noising by Soft-Thresholding. IEEE Transactions on Information Theory. May 1995; 41 (No. 3): 613-627.

[165] Krim H, Tucker D, Mallat S, Donoho DL. On Denoising and Best Signal Representation. IEEE Transactions on Information Theort. November 1999; 45 (No. 7): 225-2238.

[166] Lambert P, Pires S, Ballot J, Garcia RA, StarckJL, Turck-Chieze S. Curvelet analysis of asteroseismic data. i. method description and application to simulated sun-like stars. Astrnomy and Astrophysics; 2006; 454: 1021-1027.

[167] Candes EJ, Donoho DL. Ridgelets: the key to high dimensional intermittency? Philosophical Transactions of the Royal Society of London; 1999; A 357: 2495-2509.

[168] Zhang X, Li D, À Trous wavelet decomposition applied to image edge detection, Geographic Information Sciences, vol.7 No.2, Dec 2001, 119-123.

APPENDIX A: LIST OF MATLAB FUNCTIONS

Main file to run the fusion code:

testforfusionrev3.m

Needs following files to run

nkreadzygodat.m, zygoheader.mat, zygoheaderlegend.mat
nkreadopds.m
mallat_decomposition.m
alignddata_ms.m
atrous_decomposition4.m
ICP_finite.m
fminlbfgs.m, fminsearch.m, lsqnonlin.m movepoints.m
aligndata.m
atrous_decomposition.m
fusion_fwr.m
fusion_metrics.m
joint_h.m, MI2.m, img_qi.m, ssim_index.m, rmse.m
fusion_ms_metrics.m

Other files

testfordecomplevels.m
aligndata_ms_temp.m
createnoise.m
ms_gaussian_noise.m, ms_salt_pepper_noise.m, ms_speckle_noise.m, ms_poisson_noise.m
createconvnoise.m
fusion_zipscan.m
test_coarse_alignment.m